An Investigation of Electric Propulsion in Unmanned Aerial Vehicles through a Variable-Fidelity Multidisciplinary Design Optimisation Approach

Dionisios Korovilas

Delft University of Technology

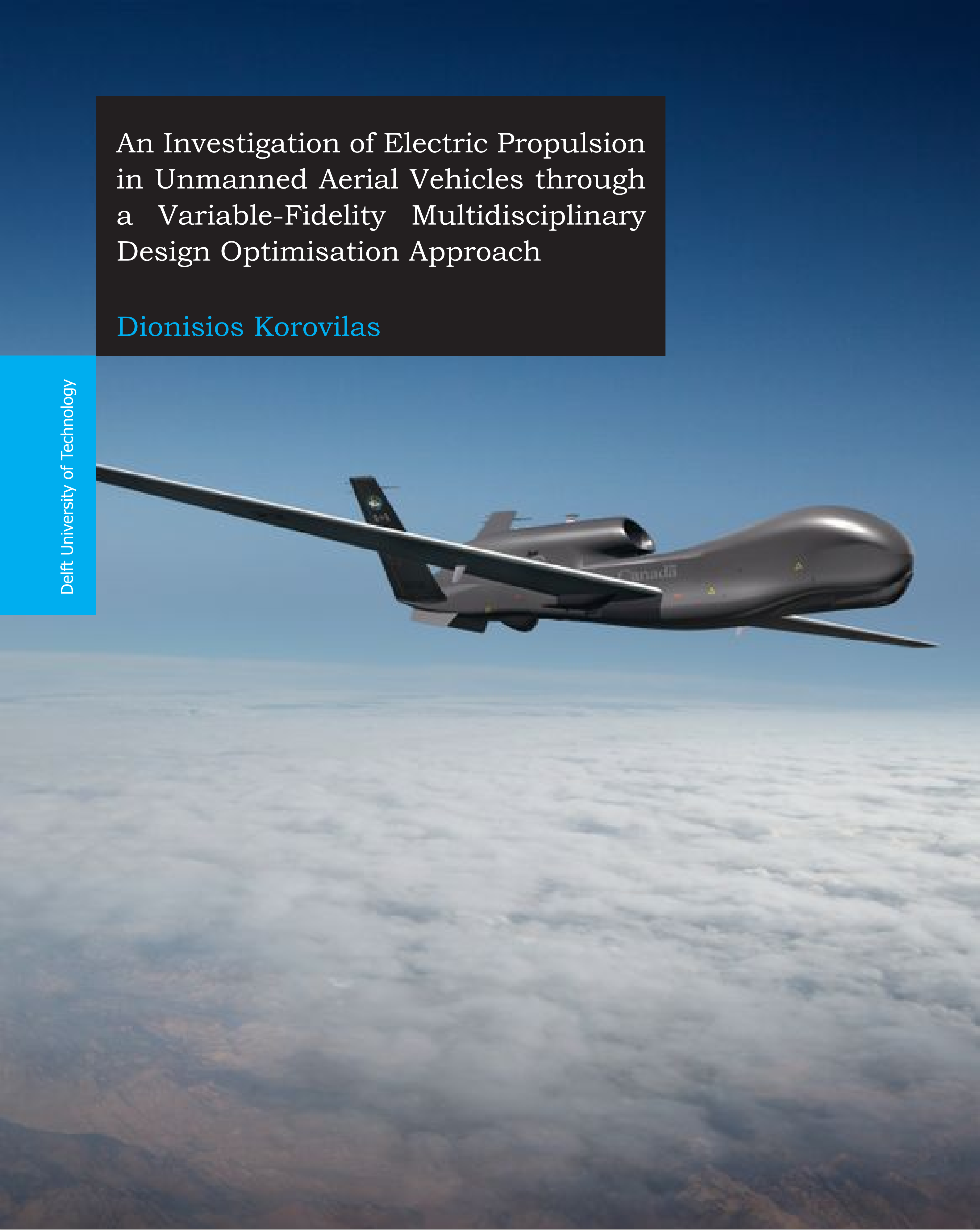

Delft
University of
Technology

Challenge the future

An Investigation of Electric Propulsion in Unmanned Aerial Vehicles through a Variable-Fidelity Multidisciplinary Design Optimisation Approach

by

Dionisios Korovilas

in partial fulfillment of the requirements for the degree of

Master of Science
in Aerospace Engineering

at the Delft University of Technology
to be defended publicly on Tuesday August 24, 2021 at 10:00 AM.

Supervisors:	Dr. Ir. Fabrizio Oliviero	TU Delft
	Dr. Ir. Dries Verstraete	University of Sydney
Thesis committee:	Prof. Dr. Ir. Leo Velduis	TU Delft
	Dr. Ir. Fabrizio Oliviero	TU Delft
	Dr. Ing. Saullo Castro	TU Delft

Cover image from [1]

Abstract

The Medium-Altitude Long-Endurance (MALE) Unmanned Aerial Vehicle (UAV) is becoming increasingly important in both military and civilian applications. Its ability to offer both reconnaissance and air-to-land direct strike capabilities without risking the operator's life has made it an indispensable tool in many military arsenals around the globe, while its large size and high altitude flight allow for heavy scientific instruments to be carried on-board for days at a time. In parallel, a growing interest is developing within the aerospace industry to shift away from hydrocarbon fuels towards electric propulsion technologies. Such a shift will not only affect the propulsion system design of UAVs, but will inevitably lead to considerable design changes on the aircraft system level. Design space studies have been conducted over the years to investigate the effects of electric propulsion systems on UAV designs - however, most of these have been centered around small-to-medium-sized UAVs, with very little research having been done on the design effects of electric propulsion systems on MALE UAV designs. As a result, MALE UAVs are still predominantly powered by conventional reciprocating engines designed for general aviation aircraft.

In seeking to fill the gap of knowledge around the electrification of MALE UAVs, a Multidisciplinary Design Optimisation (MDO) framework has been developed, which incorporates three types of propulsion system models, namely a reciprocating engine, a hydrogen fuel cell and a battery system model. The framework is used to compare the design effects imparted on the optimised shape of a MALE UAV as a result of incorporating electric propulsion solutions. Two levels of modelling fidelity have been included for the aerodynamics and structural wing weight models, in order to also investigate the effects of varying their modelling fidelity on the optimised designs.

The minimisation of the maximum take-off weight is set as the objective function of the optimisation. Five planform parameters are set as planform design variables, namely the wing span, aspect ratio, leading-edge sweep angle, taper ratio and tip twist angle. In addition, six wing structure sizing variables are included, in the case of the high-fidelity structural wing sizing model. A long-endurance reconnaissance mission is modelled, mirroring one of the most common applications of MALE UAVs. The aerodynamics module includes both low-fidelity aerodynamics relations together with a medium-fidelity higher-order panel code. The wing structure sizing model includes both low-fidelity class II weight estimation methods in addition to a finite element analysis-based wing structure sizer. The propeller is modelled with the use of propeller design codes, while the three propulsion models are based on data from real systems coupled with analytical expressions.

The results of this investigation showed a weight reduction of around 40% for the optimised aircraft design with a hydrogen fuel cell, as compared to the baseline aircraft with a conventional reciprocating engine. Moreover, the optimisation resulted in an approximately 40% smaller wing, with a wing span reduction of around 28%. Battery systems have been shown to possess insufficient levels of specific energy for the completion of a long-endurance mission, with a theoretical specific energy level of around $3000Wh/kg$ required in order to achieve the same endurance at a similar weight as the baseline reciprocating engine aircraft. The investigation further showed that the effects of modelling fidelity in the aerodynamics and structural wing weight models become more significant when the aircraft design being optimised is substantially different from the baseline configuration, such as for example when incorporating a different mission or a novel propulsion system.

Acknowledgements

This research project marks the completion of my studies at the Delft University of Technology. Throughout this time, I have had the luck and privilege of working with, studying alongside and learning from a group of extraordinary people, for whom my gratitude could never fully be expressed in these paragraphs.

I would like to extend my deepest appreciation to my supervisors, Dr. Fabrizio Oliviero and Dr. Dries Verstraete. Thank you Fabrizio for your time, guidance and persistence throughout this project. Your enduring support has been invaluable and your extensive knowledge in the field of aircraft design and multidisciplinary design optimisation has been central to the completion of this work. Dries, thank you for giving me the opportunity to join your research team at the University of Sydney, to work on a subject I thoroughly enjoy. I am grateful for our interesting discussions and for the time you took to support me during my stay in Sydney and from abroad. I would also like to thank Dr. Gianfranco La Rocca and Dr. Maurice Hoogreef for the valuable feedback they provided me with in preparation for my thesis defence.

My sincerest gratitude to my close friends Baris, Jan, Thibault and Rubén, who have been on this journey with me since day one and who continue to motivate me to this day. A special thank you to Simge, for the love, support and encouragement you have given me throughout this process and for always bringing out the best in me.

Finally, I would like to thank my family, whose unwavering love and support has always been a source of motivation and without whom this thesis would not have been possible.

Dionisios Korovilas

Contents

List of Figures

List of Tables

Glossary

AFC Alkaline Fuel Cells. 11

BLF Buckling Load Factor. 31

CFR Code of Federal Regulations. 88
CSD Concurrent Subspace Design. 15
CSSO Concurrent Subspace Optimisation. 15
CST Class Shape Transformation. 36

DSM Design Structure Matrix. 16, 27

ENFICA-FC ENvironmentally Friendly Inter City Aircraft powered by Fuel Cells. 13
ESP Engineering Sketch Pad. 37

FEA Finite Element Analysis. 29, 143
FEM Finite Element Method. 31

HALE High Altitude Long Endurance. 5

IAI Israel Aerospace Industries. 6
IDF Individual Discipline Feasible. 1, 29

KS Kreisselmeier-Steinhauser. 31

Li-Ion Lithium-ion. 9
Li-Po Lithium-ion-polymer. 9
LiS Lithium Sulphur. 9

MALE Medium Altitude Long Endurance. 1, 5, 143
MAV Micro Air Vehicles. 5
MDA Multidisciplinary Design Analysis. 15
MDF Multi Disciplinary Feasible. 29
MDO Multidisciplinary Design Optimisation. 1, 143
MPC Multi-Point Constraint. 58
MTOW Maximum Take-Off Weight. 4, 29

NAND Nested Analysis/Design. 17
NiCd Nickel-cadmium. 9

NiMH Nickel metal hydride. 9

OEW Operational Empty Weight. 50

PEMFC Proton Exchange Membrane Fuel Cells. 11

RPAS Remotely Piloted Aircraft System. 5

SOFC Solid Oxide Fuel Cell. 11

UAS Unmanned Aerial System. 3

UAV Unmanned Aerial Vehicle. 1, 143

UCAV Unmanned Combat Aerial Vehicle. 5

Nomenclature

α_{size}	Angle of attack at the wing sizing condition
η	Efficiency
η_{grav}	Gravimetric efficiency
η_{peak}	Peak power efficiency
η_{util}	Hydrogen utilisation
$\frac{P_{av}}{W_{av}}$	Power-to-weight ratio of the avionics systems
λ	Taper ratio
Λ_{LE}	Leading-edge sweep
μ	Doublet strength
ω	Rotational speed
ϕ_{xx}	Perturbation velocity potential
ϕ	Tip twist angle
ρ_{∞}	Freestream air density
ρ_{mat}	Material density
ρ_{vol}	Volumetric density
σ_{limit}	Limit stress
σ	Source strength
θ	Climb angle
A_i	Bernstein polynomial scaling factor
AR	Wing aspect ratio
$AR_{sparcap}$	Spar cap aspect ratio
b	Wing span
B_i, p	Bernstein polynomials
b_s	Wing semi-span
b_{tail}	Tailplane span
BLF	Buckling load factor
C	Engine specific parameter
C_D	Drag coefficient
C_f	Friction coefficient
C_p	Pressure coefficient

C_{D_0}	Zero-lift drag coefficient
$C_{L,des}$	Design lift coefficient
C_L	Lift coefficient
C_{nom}	Nominal discharge rate
C_P	Peukert constant
$c_{r,t}$	Tailplane root chord length
C_{rat}	Battery rated discharge rate
CV_i	Coupling variables
D	Drag
d	Fuselage diameter
d_m	Diameter of motor
D_p	Propeller diameter
E	Endurance
F	Faraday's number
F_{cont}	Factor accounting for control surfaces
F_{emp}	Empennage multiplication factor
F_{ig}	Landing-gear mass fraction
F_{mat}	Material factor
F_{mg}	Main gear on the fuselage factor
F_{ng}	Nose gear on the fuselage factor
F_{press}	Pressurized fuselage factor
F_{vt}	Vertical tail inclusion factor
FF	Form factor
$g_j(x)$	Inequality constraints
$h_k(x)$	Equality constraints
H_2	Hydrogen
H_2O	Water
h_e	Height of engine
I	Current
$J(x)$	Objective function
k_0	Parasite loss ratio
k_p	Ratio of maximum power to power at peak efficiency
k_Q	Ratio of maximum torque to torque at peak efficiency
k_W	Ratio of maximum rotational speed to rotational speed at peak efficiency

K_{inlet}	Air intake pattern parameter
K_{shp}	Multiplication factor based on shaft horsepower
l	Fuselage length
l_m	Length of motor
l_e	Length of engine
l_{tail}	Tailplane moment arm
LHV	Lower heating value
$loc_{spar,front}$	Front-most spar location
$loc_{spar,rear}$	Rear-most spar location
M_∞	Freestream Mach number
M_{tip}	Propeller tip Mach number
mac	Mean aerodynamic chord length
MR_{rib}	Vertical mesh refinement of ribs
$MR_{sparweb}$	Vertical mesh refinement of spar webs
n	Load factor
n_{cells}	Number of fuel cells
n_{H_2}	Moles of hydrogen
N_p	Number of propeller blades
N_{spar}	Number of spars
$N_{stringer}$	Number of stringers
p_{alt}	Ambient pressure at altitude
$P_{p,FC}$	Fuel cell peak power
$P^*_{p,FC}$	Fuel cell peak power target variable
P_{PL}	Power required by the payload
P_p	Peak power
P^*_p	Engine/motor peak power target variable
p_{SL}	Ambient pressure at sea level
Q_b	Battery capacity
Q^*_b	Battery capacity target variable
Q_{nom}	Nominal battery capacity
Q_{peak}	Peak power torque
R	Resistance
RPM_{peak}	Peak power RPM
S_{exp}	Exposed area

S_{ref}	Reference planform area
S_{tail}	Tailplane reference area
S_{wet}	Wetted area
$spac_{rib}$	Span-wise rib spacing
T	Thrust
t_{min}	Minimum gauge thickness
t_{skin}	Skin thickness
$t_{sparcap,r}$	Root sparcap thickness
$t_{sparcap,t}$	Tip sparcap thickness
t_{spar}	Spar thickness
$t_{stringer,r}$	Root stringer thickness
$t_{stringer,t}$	Tip stringer thickness
V_{∞}	Freestream velocity
V	Voltage
V_c	Climb rate
$V_{available}$	Available volume for fuel
V_d	Engine displacement
$V_{required}$	Volume required for fuel
W_m	Motor weight
W_p	Propeller weight
W_{ai}	Air induction weight
W_{auto}	Autopilot system weight
W_{av}	Avionics system weight
W_{batt}	Battery weight
$W_{carried}$	Weight of the components located inside the fuselage
W_{elec}	Electrical systems weight
W_{emp}	Empennage weight
W_{engine}	Engine/motor weight
W_{eqMax}	Maximum equivalent airspeed
w_e	Width of engine
W_{feq}	Fixed equipment weight
$W_{fuel,sys}$	Fuel system weight
W_{fus}	Fuselage weight
W_f	Fuel weight

W_f^*	Fuel weight target variable
W_{lg}	Landing gear weight
W_{OEW}	Operational empty weight
W_{OEW}^*	Operational empty weight target variable
W_{PL}	Payload weight
$W_{prop,sys}$	Propulsion system auxiliary weight
W_{prop}	Propulsion system weight
W_{struc}	Structural weight of the airframe
W_{tank}	Tank weight
W_{wing}	Wing weight
W_{wire}	Electrical wiring weight
x_L	Lower optimisation bound
x_U	Upper optimisation bound
$\left(\frac{t}{c}\right)_r$	Root thickness-to-chord ratio
$W_{f,loiter}^*$	Weight of the remaining fuel at the mid-loiter point target value
W_{MTOW}	Maximum take-off weight

1

Introduction

The Medium-Altitude Long-Endurance (MALE) Unmanned Aerial Vehicle (UAV) is seeing growing importance in today's world, in both civilian and military applications. Its large size, comparable to that of general aviation aircraft, together with its long endurance, in the order of days, allow it to carry heavy payloads and instrumentation for extended periods of time, without the need for a human pilot. However, in a world where electric UAVs are increasingly becoming the norm, the MALE UAV is still primarily powered by hydrocarbon fuels and its design is very much constrained by existing general aviation reciprocating engines, which are designed for a different set of requirements altogether. A substantial amount of research has been conducted around the design effects resulting from incorporating electric propulsion solutions in small and medium-sized UAVs but also in large UAVs of the High-Altitude Long-Endurance (HALE) type. Despite this, however, to date limited work has been undertaken to investigate how incorporating these novel propulsion system will affect the aircraft-level design of MALE UAVs.

Dries Verstraete of the University of Sydney has been one of the first to investigate electric propulsion solutions in MALE UAVs, with his work titled 'Multi-disciplinary optimisation of medium altitude long endurance UAVs' [13]. In this work, he developed a Multidisciplinary Design Optimisation (MDO) framework, which incorporated reciprocating engine and hydrogen fuel cell propulsion models. The MDO framework was used to optimise the design of a MALE UAV for both types of propulsion system. Verstraete showed that hydrogen propulsion has the potential to significantly reduce the weight of MALE UAVs, while also enabling longer endurances. Despite these significant findings, the study represents a first iteration in the body of knowledge around the design effects of electric propulsion solutions on MALE UAVs and can be extended and improved upon in a number of ways.

The current study is an extension of the work undertaken by Verstraete, with its objective being the development of an improved MDO framework for the comparison of optimised MALE UAV designs with different propulsion systems but also for the investigation of how varying levels of modelling fidelity affect said optimised designs. Among others, the key improvements of the new framework include the incorporation of higher-fidelity aerodynamics models in place of the low-fidelity methods used previously, the inclusion of a higher-fidelity structural wing sizing method in place of the low-fidelity class II weight estimations used previously and an improved propeller model which is based on propeller design codes. Moreover, a new MDO workflow has been developed, based on the sequenced Individual Discipline Feasible (IDF) formulation, which sees the number of design variables increased from two to 11, in order to explore a wider area of the design space, which is particularly important when investigating design effects of novel propulsion solutions.

This report is structured as follows: a literature review is provided in Chapter 2. The motivation and objective of this research is expanded upon in Chapter 3. Chapter 4 provides a detailed overview of the methodology of the study. The case study used for this investigation is discussed in Chapter 5. Results are presented in Chapter 6, while a thorough discussion of the findings is provided in Chapter 7. Finally, the conclusions and recommendation of this work are outlined in Chapter 8.

2

Literature Review

This chapter aims to introduce the reader to the fields of UAV design and propulsion and to summarise the state of the art in these fields, including related multidisciplinary design optimisation studies existing in literature. Section 2.1 will discuss UAV designs and applications, Section 2.2 will review typical UAV propulsion solutions, while Section 2.3 will review previous research on UAV designs, including multidisciplinary design optimisation studies.

2.1. Unmanned Aerial Vehicles

This section introduces the modern UAV, its classifications, and its applications in today's world. The relevance of this section to the investigation lies in the need to gain knowledge on UAVs in order to:

1. Clearly define what is and what is not a UAV
2. Classify UAVs on a number of characteristics
3. Help identify which class of UAV to use for the case study

Section 2.1.1 gives a definition of the term UAV, Section 2.1.2 provides various classifications of unmanned aircraft and Section 2.1.3 gives an overview of military and civil UAV applications.

2.1.1. Definition

Many definitions of the term 'unmanned aerial vehicle' exist. The Cambridge Dictionary defines a UAV as *'An aircraft that is operated from a distance, without a person being present on it'* [28]. NASA goes further, defining it as *'A powered, aerial vehicle that does not carry a human operator, uses aerodynamic forces to provide vehicle lift, can fly autonomously or be piloted remotely, can be expendable or recoverable, and can carry a lethal or nonlethal payload'* [29]. Based on these definitions, UAVs can be described by certain key features, namely: a) no pilot on-board. b) powered, c) may or may not be autonomous, d) may or may not be expendable, e) may or may not carry lethal payload.

A UAV is actually a constituent of an Unmanned Aerial System (UAS). Unmanned Aerial Systems are made up of three segments: the aircraft segment, the control segment and the communications segment [5]. A schematic example of a UAS is shown in Figure 2.1. The current investigation will focus exclusively on the aircraft segment of a UAS - the UAV itself.

2.1.2. Classification

Categorising unmanned aerial vehicles in a standardised way has been a challenge for developers and users alike. Rapid advancements in technology have introduced many different types of UAVs to the market in recent decades, which have blurred the lines between previously established categories. Historically, the development of unmanned technologies has been led by military bodies, most notably those of the United States and Israel. As such, over time the UAV community has adopted some of their classification systems. One such common system is the US Air Force 'Tier System', which classifies

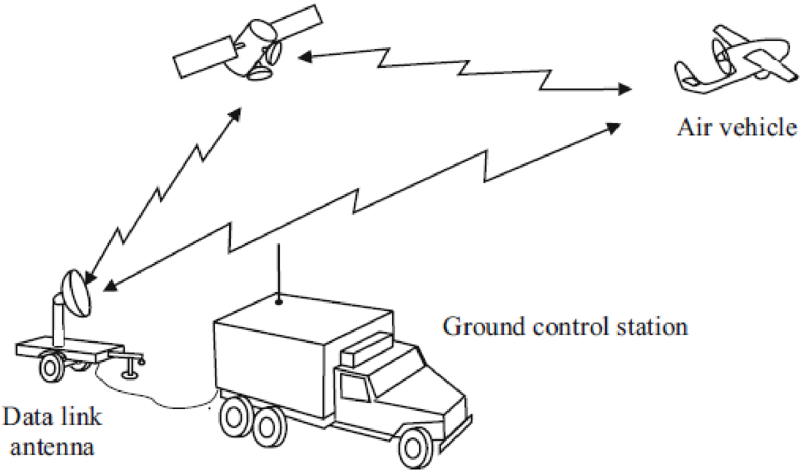

Figure 2.1: Schematic example of an Unmanned Aerial System [2]

UAVs based on altitude and endurance [2]. The Tier System is presented in Table 2.1.

Table 2.1: US Air Force Tier System for UAV classification [2]

Tier	Description	Example
N/A	Small/micro UAV	Black Hornet Nano
I	Low altitude, long endurance (LALE)	XMobots Apoena
II	Medium altitude, long endurance (MALE)	MQ-1 Predator
II+	High altitude, long endurance (HALE) conventional	RQ-4 Global Hawk
III-	High altitude, long endurance (HALE) low-observable	RQ-3 DarkStar

A more encompassing classification is presented by van Blyenburgh [20] based on size, altitude and endurance. An excerpt from this classification system is given in Table 2.2 for a few classes, with added Maximum Take-Off Weights (MTOWs) from Dalamagkidis [21]. Although van Blyenburgh's [20] is a journal article from 1999, the same classification system is used in a more recent presentation of his from 2006 [30]. Van Blyenburgh [20] has also been cited in more recent publications, including Bendea et al. [31] in 2008 and Dalamagkidis [21] in 2015, hence seems to be a classification system which is used within the UAV community until today. This classification will be the reference for the current investigation. It should be noted however, that there is no consensus on precise UAV classifications and different authors have different MTOW, altitude and endurance criteria for the classes given in Table 2.2. These class characteristics are to be taken as indicative guidelines for the purpose of UAV differentiation, rather than strict criteria.

2.1.3. Applications

There is a growing demand for UAVs in both military and civil applications, as new ways to make use of unmanned systems are discovered and the systems evolve to better meet user needs. The following subsections provide an overview of military and civil applications respectively.

Military

Unmanned systems were born out of military requirements. Elmer Sperry's early work on gyrostabilisers just before the First World War was quickly noticed by the US Navy and eventually led to the development of the Hewitt-Sperry Automatic Airplane, also known as an 'aerial torpedo' [32]. Since then, military needs have led to the advancement of UAV technologies, transforming them from simple

Table 2.2: Classification of UAVs based on size, MTOW, altitude and endurance [20] [21].

Category	Abbreviation	MTOW [kg]	Flight Altitude [m]	Endurance [hr]	Example
Micro Air Vehicles	MAV	<5	250	1	MicroStar
Small/Mini	-	<30	350	<2	SurveyCopter
Close Range	CR	25-150	3,000	2-4	Observer
Short Range	SR	50-250	3,000	3-6	Mirach 26
Medium Range	MR	150-500	5,000	6-10	Shadow 200
Low Altitude Long Endurance	LALE	15-25	3,000	>24	Aerosonde
Medium Altitude Long Endurance	MALE	1,000-1,500	5,000 - 8,000	24-48	Predator
High Altitude Long Endurance	HALE	2,500-5,000	15,000 - 20,000	24-48	Global Hawk

bomb-carrying devices to vehicles which can house an array of payloads, be controlled from anywhere around the globe and remain airborne for days at a time. Their modern military applications focus on missions characterised by the 3Ds: dull, dirty or dangerous for a human pilot [33].

The most common military application of UAVs today is surveillance/reconnaissance. UAVs across the size spectrum are used for this, with Medium-Altitude Long-Endurance (MALE) and High-Altitude Long-Endurance (HALE) UAVs typically employed for long duration missions requiring top-down view, whereas smaller devices such as Micro Air Vehicles (MAVs) and mini UAVs are used for low, close-quarters surveillance, including inside buildings.

A second military application which has been covered extensively by the media in recent years is the use of UAVs in combat operations. Termed Unmanned Combat Aerial Vehicles (UCAVs), these devices are typically of the MALE type and are equipped with aircraft ordnance such as AGM-114 Hellfire missiles. The MALE General Atomics MQ-1 Predator and its successor the MQ-9 Reaper have been used extensively by the United States in combat operations around the world, including in Iraq and Afghanistan.

MALE UAVs have found much popularity with military services around the world. Unlike HALEs or UAVs of smaller classes, MALEs operate at an altitude which allows for both surveillance and direct strike capabilities. The MQ-1 Predator was initially designed as an unmanned reconnaissance aircraft and was later upgraded to carry two Hellfire missiles, giving it dual capability and making it one of the most popular unmanned tools in the United States military arsenal. The Turkish military sought to have a domestic MALE aircraft and in response, Turkish Aerospace Industries rolled-out the Anka MALE UAV in 2010 [34]. European military services have also recognised the importance of the MALE unmanned aircraft, whom until now have relied on American and Israeli MALE models. In September 2016 a two-year definition study began by Airbus Defence and Space, Dassault Aviation and Leonardo-Finmeccanica under the title 'European MALE Remotely Piloted Aircraft System (RPAS)', previously known as 'MALE 2020' [35]. The aim of the European MALE RPAS project is to 'improve sovereignty and independence' of European nations with respect to unmanned aircraft. Further to the east, the publishing company Jane's reported in July 2017 that Russia has unveiled a MALE UAV, the Orion-E [36]. Clearly, the MALE UAV has found popularity in the military arena and is an important asset for any advanced military force.

Civil

Unmanned aircraft have seen a surge in popularity in civil applications over the past two decades. A study by Herrick [37] in 2000 revealed that UAV manufacturers were increasingly being approached by new potential customers after the visibility UAVs gained during military operations in the Balkans. Even as early as 2000, potential civil applications of unmanned vehicles were apparent. Herrick [37] listed law enforcement, science and agriculture as three key civil fields of interest, with potential applications including border patrol, drug interdiction and monitoring, fire survey and control, coastal surveillance, telecommunications and atmospheric research. Views on the potential of UAVs in the civil sector were shared by manufacturers too. Israel Aerospace Industries (IAI), Israel's largest aerospace manufacturer and an important player in the unmanned aircraft market, published a paper in 2002 reflecting many of the same applications [38].

Since then, many of these predictions have become a reality. In 2002, IAI flew its Heron MALE UAV in Kiruna, Sweden, demonstrating its civil application capabilities along with its synthetic-aperture radar and electro-optic payload [39]. The same company demonstrated automobile tracking, crowd control and waterway activity observation in 2004 with the Bird Eye 500 UAV over Amsterdam in the Netherlands [39]. Aerosonde Ltd developed the AAI Aerosonde, a UAV designed for civil purposes which is used for weather surveying and environmental monitoring [40].

Although there have been many demonstrations for civil applications and an increasing number of UAVs employed for various civil missions over the years, the civilian market for UAVs is currently not as large as was initially anticipated. The reason for this has been, and still is, a lack of legislation and regulations governing the flight of civilian UAVs in unrestricted airspace [41]. This situation is predicted to change soon, as governments and regulatory bodies are increasing their efforts to providing regulatory guidelines for the use of civil UAVs.

Despite the current lack of regulation, the MALE UAV has seen considerable use by government agencies and research bodies in the past two decades. NASA uses the Altair, a Reaper variant for civil purposes, for Earth science research and developed a program with the US Department of Agriculture to use it for forest fire monitoring [42]. In 2007 General Atomics delivered Ikhana, another Reaper variant, to NASA, which was used to support wildfire observation [43]. The Reaper's younger brother, the Predator, has two variants called Altus I and Altus II, the former being used by the Naval Postgraduate School while the latter being used by NASA [44]. In Turkey, IAI Heron MALE UAVs were purchased for border surveillance [34]. MALE UAVs offer clear advantages over smaller UAV types due to their ability to carry relatively heavy payload required by research missions, combined with their extended endurance.

2.2. UAV Propulsion Systems

This section discusses propulsion systems traditionally employed by various UAV classes and the current state of the art of each propulsion system, focusing on MALE UAV applications. The relevance of this section to the current investigation lies in the need to understand UAV propulsion systems in order to:

1. Formulate hypotheses on which propulsion systems will most likely lead to feasible designs in the MDO case study
2. Interpret the results of the case study in terms of why each optimised design looks the way it does
3. Provide recommendations for future design improvements based on current academic research in the field of UAV propulsion

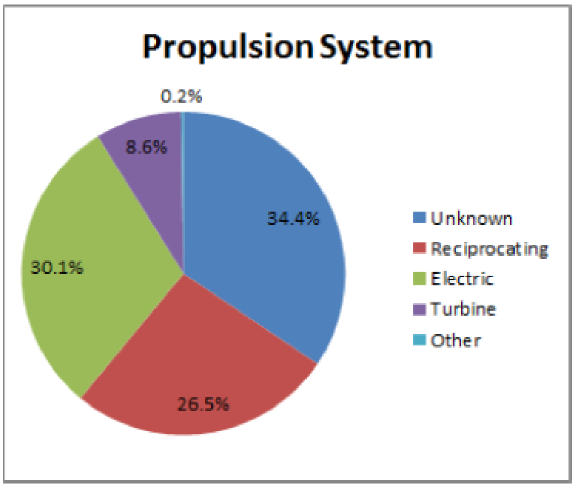

Figure 2.2: Share of propulsion system types among UAVs [3].

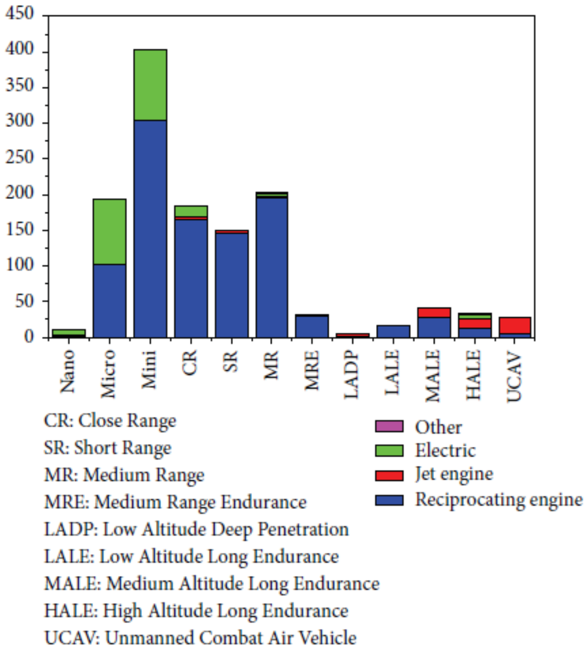

Figure 2.3: Propulsion systems typically used on UAVs of different classes [4].

To put the upcoming sections into context, Figure 2.2 indicates the share of propulsion system types among UAVs of all classes. Electric propulsion seems to be most popular at 30.1%, due to the many different mini UAVs and MAVs which use these systems. Reciprocating engines follow with 26.5%, followed by gas turbine solutions at 8.6%. Figure 2.3 shows which types of propulsion systems are typically used on UAVs of different classes. Electric solutions are mainly reserved for small UAV applications and light HALE aircraft, while reciprocating engines make up a large portion of medium and large UAV propulsion systems. Gas turbine solutions are used almost exclusively on MALE, HALE and UCAVs. Interestingly, MALE UAVs use either reciprocating engines or gas turbines but no electric solutions, even though higher-altitude aircraft in the HALE category do.

Section 2.2.1 presents reciprocating engines, while Section 2.2.2 discusses electric propulsion solutions powered by batteries and fuel cells.

2.2.1. Reciprocating engines

Reciprocating engines have for a long time been the standard for both manned and unmanned aircraft. Unlike large and expensive manned aircraft projects, where engines are often designed for particular aircraft models, in the unmanned aircraft world it is the aircraft which is designed around available engines [45]. To avoid the prohibitive costs of new engine design projects, manufacturers choose to modify engines from other sources, ranging from lawn mowers to motorcycles for low-power UAVs and automobiles to general aviation aircraft for MALE and HALE types. Although this method results in faster design cycles, it leads to sub-optimal designs, as these engines have been designed for different power levels and throttle settings in their original application. Unmanned aircraft manufacturers must thus settle for the closest available option, leading to a potential loss of aircraft performance.

Reciprocating engines are the most common propulsion method for UAVs in the MTOW range of 9-1133 kg [27]. They can be categorised into four-stroke, two-stroke and rotary types. Four-stroke and two-stroke engines are discussed in this section, as they are more common than the rotary type.

Reciprocating piston engines are a relatively inexpensive propulsive solution, as their technology is well understood. They are a frequent choice among UAV designers, because of their low cost, ease of implementation and a lack of small gas turbine alternatives [22]. Due to their linear motion they do result in significant vibration however, which may hamper operations with high-accuracy payload. More advantages and disadvantages of reciprocating piston engines are provided in Table 2.3.

Table 2.3: Advantages and disadvantages of reciprocating piston engines [22] [5].

Advantages	Disadvantages
Inexpensive	Vibration
Widely understood technology	Noise
Potentially lightweight	Many moving parts
Potentially compact	Requires seals and lubrication
Easy to obtain and implement (off-the-shelf)	Non-constant torque delivery

Reciprocating piston engines power a variety of UAVs. They are very common solutions for medium and large UAVs but may also be found in smaller vehicles, such as the Honeywell MAV [5]. Today, most MALE UAVs are powered by piston engines, with the four-stroke Rotax 914 being a popular option among UAV manufacturers [45]. This is because MALEs require higher endurance than can be delivered by most current electric propulsion solutions at that scale but are also small enough and fly low enough not to require large gas turbines. Some large MALE UAVs are powered by turboprops however, such as the General Atomics MQ-9 Reaper (also known as the Predator B). Typical MALE piston engine power outputs are around the 100 kW mark, with the popular Rotax 914 producing 84 kW of power. Many MALE piston engines employ turbochargers, which compress air before it enters the engine, allowing for typical MALE UAV service ceilings of around 25,000 feet. Turboprop systems are usually employed for the few large MALE UAVs which operate above this altitude.

The jet age turned aviation research focus away from reciprocating engines and towards gas turbine solutions, which in turn are currently being overtaken by electric propulsion investigations. This stagnated progress in reciprocating engines for aircraft applications, allowing only incremental advancements rather than breakthrough developments and leaving the majority of piston engine research to the automotive industry. Recently, however, aviation diesel engines have seen a resurgence in interest since they were first used as aircraft engines in the 1920s, sparked in part by reduced availability of aviation gasoline (avgas). Diesel engines offer many advantages over avgas engines, including lower specific fuel consumption, higher engine efficiency and higher reliability [45]. However, their low power-to-weight ratio and high cost has prevented their widespread adoption.

2.2.2. Electric propulsion systems

Electric propulsion systems first appeared on UAVs in the late 1970s, much later than internal combustion engines [27]. Today they are very popular options for small unmanned aircraft like MAVs and are increasingly being investigated for application in larger unmanned aircraft. In an electric propulsion system, the propulsor (the motor-propeller combination) is separated from the power source (the battery, fuel cells or photovoltaic cells). Electric motors convert electrical energy from the source into rotational motion through electromagnetism. Two types of electric motors exist: brushed and brushless. In a brushed motor, a stationary permanent magnet (the stator) concentrates magnetic field flux density, causing an electromagnet (the rotor, which receives current through brushes) to rotate. Brushless motors have stationary electromagnets and rotating permanent magnets, allowing them to be purely inductive. As a result, brushless motors produce less friction and are thus more efficient.

Electric propulsion systems offer many advantages over internal combustion engines. Unlike the latter, electric motors start and stop instantaneously, require minimal maintenance and produce almost no noise. One of their few disadvantages is also the reason they are not as widely used in more applications, including MALE UAVs: most electric power sources currently cannot provide long endurance flight. Because of their sources' low specific energy as compared to hydrocarbon fuels, electric motor systems are restricted to UAVs which typically weigh less than 9kg, at power outputs of less than 1kW [27]. A more extensive list of electric propulsion advantages and disadvantages is provided in Table 2.4. Battery, fuel cell and photovoltaic power sources are discussed in the upcoming sections.

Table 2.4: Advantages and disadvantages of electric propulsion systems [5] [23].

Advantages	Disadvantages
Low maintenance	No power source currently available with sufficient endurance for many UAV applications
High efficiency	Potential sensitivity to liquids
Fast start-up and shut down	Electromagnetic interference
Low noise	
Easily scalable	

Batteries

Batteries are self-contained electrochemical devices. They consist of a single or multiple voltaic cells, which consist of an anode and a cathode, connected by a conductive electrolyte. As may be seen in Figure 2.4, anions flow to the anode while cations flow to the cathode. With an electrical load placed between the two, current begins to flow. Both single-use (primary) and rechargeable (secondary) batteries are used in unmanned vehicle applications, with primary batteries offering superior performance in the form of higher specific energy. However, secondary cells are the standard for non-expendable UAVs due to the prohibitive cost of continuously replacing primary batteries.

Several battery chemistries have been used over time. Nickel-cadmium (NiCd) batteries were popular in the 1980s and 1990s. These were briefly replaced by nickel metal hydride (NiMH) batteries towards the end of the 1990s. Since then, the dominant battery types have been lithium-ion (Li-Ion) and lithium-ion-polymer (Li-Po), as they both have a higher specific energy than the rest and are more environmentally friendly to dispose of. Lithium sulphur (LiS) is an up-and-coming battery chemistry, which promises ever higher specific energy than Li-Ion and Li-Po batteries [27].

Advantages of batteries over other electric power sources include their lack of an external consumable, their high efficiency and virtually no noise. Their primary disadvantage is their low specific energy compared to consumable fuels like hydrocarbons or hydrogen. To put this in perspective, aviation jet turbine fuel (Jet A-1) has a specific energy of 42.8 MJ/kg, while Li-Po batteries can only reach specific energies of less than one MJ/kg [46] [27]. Although better than Li-Ion and Li-Po, LiS batteries with their predicted 2.3 MJ/kg still cannot compete with liquid consumable fuels [47]. More advantages and disadvantages of batteries for UAV use are presented in Table 2.5.

Current research relating to batteries is focused around improving their energy densities and specific energies. This research is mainly driven by the transportation and consumer products industries and

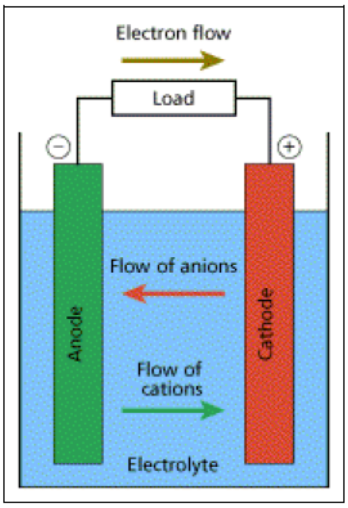

Figure 2.4: Schematic of a voltaic cell [5].

Table 2.5: Advantages and disadvantages of batteries [5].

Advantages	Disadvantages
No external consumables	Currently very low specific energy
Efficient	Hazardous internal chemicals
Silent	Currently limited recharge rates
No waste products	Heating due to internal resistance

is outside the scope of this report. More relevant discussions pertain to past and future applications of battery-based electric propulsion on unmanned aircraft and the endurances achieved by these systems.

Historically, UAVs operating purely on battery power have been limited to the MAV and mini-UAV classes, examples being the EMT Aladin, AeroVironment Wasp and Lockheed Martin Desert Hawk. All three of these vehicles employ Li-Ion batteries and have endurances around the one hour mark, a typical value for pure battery-powered systems of their size [5]. Larger UAV systems which incorporate batteries typically do so in a hybrid propulsion system, though the use of photovoltaic cells and batteries. An example of such a UAV is the Helios, a HALE solar-powered UAV with lithium batteries for night operation, which set a sustained horizontal flight altitude record of 96,863ft in 2001 [48]. A second example is the QinetiQ Zephyr 7, a HALE solar-powered 53kg unmanned aircraft fitted with lithium sulphur batteries [49]. In 2010 the Zephyr set the current world endurance record for an unmanned vehicle, staying aloft for 14 days and 21 minutes. Looking at the MALE class, Panagiotou et al. [50] undertook a conceptual design study of a MALE solar-battery hybrid UAV, claimed to operate at 23,000ft for over 48 hours, with up to 50kg of payload.

What these examples show is that although current batteries have low specific energies and can only provide short endurance flight for pure battery-powered systems, they are crucial to the achievement of long endurance electric flight when incorporated into a hybrid system. This is even the case for large UAVs like MALEs and HALEs, which at best would have endurances of only a few hours on purely battery-powered systems. Apart from solar-battery hybrids, the use of batteries may prove crucial for the successful adoption of fuel cell systems by UAV manufacturers as well. This will be discussed in the upcoming section on fuel cells.

Fuel cells

To achieve longer endurances than are allowable by current batteries, research has increasingly focused on fuel cells as electric power generators. A fuel cell consumes an externally-stored fuel such as hydrogen but does not suffer from the inefficiencies involved in combustion processes. Rather, a catalyst converts the H_2 into a positive hydrogen atom and a free electron. The ion passes through the electrolyte to the cathode, creating a potential difference, and combines with oxygen and the free electron to become H_2O. A schematic of the process is given in Figure 2.5. The fuel cell's key difference to a battery is that its fuel is externally stored, meaning a fuel cell can operate for as long as the fuel is provided. With a high energy fuel like hydrogen, this can result in long endurance operation, provided enough hydrogen is easily stored on-board. Common storage methods are in gaseous form, cryogenic liquid form and chemical hydride storage. Various types of fuel cells exist, including alkaline fuel cells (AFC), proton exchange membrane fuel cells (PEMFC), and solid oxide fuel cells (SOFC) to name a few [51]. PEMFCs are the most promising type for applications on UAVs and are thus the focus of this discussion [5] [52].

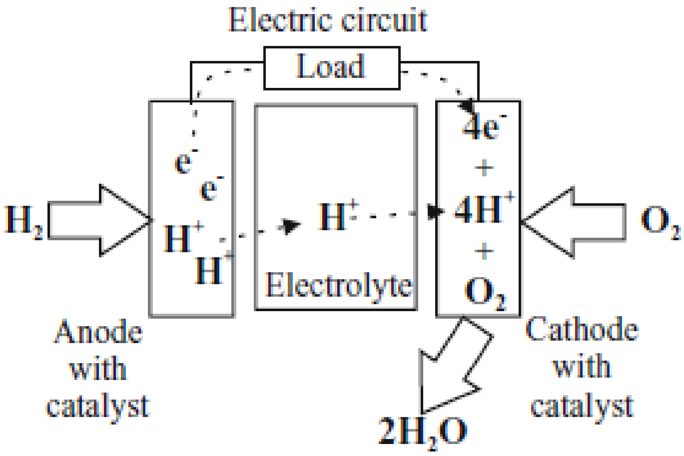

Figure 2.5: Schematic of a hydrogen fuel cell [2].

Advantages of hydrogen fuel cells include higher efficiency than internal combustion engines, higher specific energy than batteries (around 700-1000 Wh/kg as compared to less than 220 Wh/kg for batteries) and easy scalability [53] [27]. Like batteries, they have no harmful emissions, as their sole by-product is water. Fuel cells also come with many drawbacks however, including increased complexity, high acquisitions costs and a very low energy density fuel. Hydrogen has a low density and it must thus be pressurised (gaseous or cryogenic liquid form) to allow for feasible aircraft designs, resulting in the need for reinforced pressurised tanks and thus increased weight. Fuel cells also need humidity and water management systems, so the membrane remains hydrated and water is collected, further increasing complexity, weight and cost. A more extensive list of advantages and disadvantages of fuel cells is presented in Table 2.6.

Table 2.6: Advantages and disadvantages of fuel cells [5].

Advantages	Disadvantages
Higher specific energy than batteries	Very low energy density of hydrogen
Higher efficiency than internal combustion engines	Expensive
Reversible reaction has regenerative properties	Complex
Water is the only reaction product	Requires humidity and water management
Easily scalable	Not yet matured technology

Although fuel cell research dates back to the early 1800s and PEMFC technology was developed as early as the 1950s, the concept of fuel cell use for unmanned aircraft is relatively new [52]. The first use of fuel cells for UAV power and propulsion was demonstrated by AeroVironment in 2003 using a PEMFC [24]. From then until 2007, Bradley et al. [24] list a total of 10 PEMFC and one SOFC UAV demonstrations, shown in Table 2.7 along with their corresponding endurances. By 2012, Dicks [54] reported 20 fuel cell-powered UAV flights had been demonstrated. The late adoption of fuel cells to UAVs and aviation in general, compared to stationary power generation and automotive propulsion, is likely the result of aviation's demanding requirements on fuel cell designs. Bradley et al. [55] identify the need for compact reactant storage systems, air compression systems for high altitude flight and water and thermal management strategies at altitude as three key requirements aviation applications impose on fuel cell design. Until recently however, designers and developers of fuel cell systems have catered to the needs of the stationary power generation and automotive sectors, not so much to those of the aviation industry, meaning typical fuel cell designs do not include aircraft-specific design considerations [55].

Table 2.7: Published fuel cell-powered UAV demonstrations until 2007 in chronological order [24].

Organization	Fuel cell type	Reactant storage type	Endurance (estimated)
AeroVironment Inc (2003)	PEMFC	H_2 sodium borohydride	0.2 hours
AeroVironment Inc (2005)	PEMFC	H_2 cryogenic	24 hours
Fachhochschule Wiesbaden (2005)	PEMFC	H_2 gaseous	90 seconds
Naval Research Laboratory (2006)	PEMFC	H_2 gaseous	3.3 hours
Adaptive Materials Inc (2006)	SOFC	Propane	4 hours
Georgia Institute of Technology (2006)	PEMFC	H_2 gaseous	0.75 hours
California State University (2006)	PEMFC	H_2 gaseous	0.75 hours
DLR, German Aerospace Centre, HyFish (2006)	PEMFC	H_2 gaseous	0.25 hours
California State University and Oklahoma State University (2007)	PEMFC	H_2 gaseous	12 hours
Korea Advanced Institute of Science and Technology (2007)	PEMFC	H_2 sodium borohydride	10 hours
AeroVironment Inc (2007)	PEMFC	H_2 sodium borohydride	9 hours

Indeed, it has been shown that fuel cells in particular need to be designed in an application-oriented manner, if they are to be used on UAVs. Bradley et al. [24] conducted a study in 2009, comparing the performance of a fuel cell aircraft design using automotive-type fuel cell design rules to that of an aircraft design that allows for the application-specific optimisation of fuel cell subsystem models. Their results showed that the aircraft design with the application-specific optimised fuel cell resulted in a 26.8% increase in endurance, from 26.5 hours to 33.6 hours.

Another important consideration of fuel cell use on UAVs is the propulsive power profile demanded. UAVs and aircraft in general are characterised by long durations of moderate power required during cruise, with high power peaks during take-off, acceleration and landing. Although high in specific energy, fuel cells have a low specific power and suffer from slow dynamic response [56]. In an attempt to overcome this issue, research has recently been done to investigate the viability of fuel cell-battery hybrids. Batteries have a low specific energy but high specific power, meaning they could be used for short-duration high-power transients, while the fuel cells are used to maintain long endurance cruise flight. Dries Verstraete has published numerous papers describing such fuel cell-battery hybrid investigations, most of which have been in conjunction with the Defence Science and Technology Group of the Australian Department of Defence [57] [58] [56] [23] [59]. In Gong and Verstraete [58], the authors set out to determine the role of a battery in a hybrid electrical fuel cell UAV propulsion system. The setup consisted of the AeroPak fuel cell-battery hybrid propulsion system, manufactured by Horizon Energy Systems. The fuel cell had 35 cells and two lithium polymer 3S 1350 mAh battery packs were used. A power management board was used to distribute the load between the two sources. Through test bench experimentation, the authors concluded the battery to be *'vital to the high power response of the AeroPak fuel cell system'* [58]. The battery provided nearly 60% of power at the peak output power of 600 W. According to the authors, *'This enables the AeroPak system to have a much greater power density compared to a pure fuel cell system and ensures versatility in high power stages of UAV flight such as take off and climb'* [58].

Not all authors agree on the necessity of hybridising fuel cells with batteries, however. Swider-Lyons et al. [60] demonstrated 24-hour pure fuel cell flight on the 16 kg Ion Tiger UAV, while carrying 2.3 kg of payload. The 550 W fuel cell powered the vehicle through both cruise (300 W) and power peaks due to winds (550 W). Estimates and simulations were then conducted to determine whether replacing the 550 W fuel cell with a 300 W fuel cell and batteries which could provide the remaining 250 W for peak periods would bring weight savings and extend endurance. The authors' estimates predicted that the weight of the batteries would out-weight the decrease in weight from a 550 W fuel cell to a 300 W fuel cell, resulting in an overall weight increase. Furthermore, simulations did not predict an increase in endurance with a hybrid system. However, it is still the case that batteries have a superior dynamic response to fuel cells, something which was not addressed in this paper.

So far, the discussion on fuel cells has focused on small UAVs, where researchers expect the first marketed applications to arise. As discussed however, fuel cells are characterised by their ability to provide long endurance for flights which have a low number of transients. A perfect application of such flight is long endurance surveillance/reconnaissance which is typically undertaken by aircraft of the MALE or HALE type. Fuel cell research exists for very lightweight HALE types, typically in hybrid form with solar panels, but to the best of the author's knowledge no fuel cell research exists for heavy MALE UAVs. The reason for this does not seem to be a consensus that fuel cells will never be able to power such large and heavy systems, as research and even demonstrations have taken place for fuel cell-powered general aviation aircraft. Rather, it seems researchers in the unmanned arena have focused on the earliest-applicable UAV types, since fuel cells for unmanned aircraft applications are still very new technologies. At the moment, the best way to gauge the potential of fuel cell technology for MALE UAVs is to examine general aviation research and demonstrations.

Three key projects investigating the potential of fuel cells for general aviation include Boeing's fuel cell demonstrator airplane [61], the German Aerospace Centre's (DLR) Antares DLR-H2 demonstrator [62] and the EU-funded ENvironmentally Friendly Inter City Aircraft powered by Fuel Cells (ENFICA-FC) project [53]. In February and March 2008, Boeing conducted test flights with the first manned fuel cell-powered aircraft in history. A Diamond HK36 Super Dimona motor-glider fitted with a 24kW PEMFC and Li-Ion batteries capable of providing another 75kW of power maintained an altitude of 1,000 m for about 26 minutes purely by means of the PEMFC (the batteries were used for take-off and landing). The MTOW was 860 kg. Had all the hydrogen and battery capacity on board been utilised, Boeing estimates a total theoretical endurance of around 1 hour. A similar project using the Antares 20E motor-glider was undertaken by DLR, with the aircraft having an MTOW of 825 kg. ENFICA-FC is an EU-funded project led by the University of Torino, involving the powering of a two-seater Rapid200 aircraft (not motor-glider) by a fuel cell-battery hybrid system (20kW + 20kW). In 2010 the aircraft demonstrated a successful flight test, with a take-off weight of 554 kg for a duration of 39 minutes.

These three demonstrator projects showcase the potential of fuel cells for general aviation aircraft and by extension MALE UAV applications, which have similar take-off weights. Although the demonstrators flew around the 1 hour mark with current fuel cell technology (around 700-1000 Wh/kg), Romeo et al. [53] predict this figure to increase to 10,000 kWh/kg in 10-15 years and up to 20,000 kWh/kg in 20-30 years, which would allow for the 24 hours endurance of current combustion engine MALEs. This specific energy figure does seem optimistic however, considering firstly that Romeo et al. provide no evidence of this and secondly that the authors are on the ENFICA-FC team and may be expressing a degree of wishful thinking. Nevertheless, fuel cells are in their very early stages of adoption to the aviation sector and the future looks promising even for large UAVs.

2.3. MDO Applications and Design Studies of UAVs

This section discusses the use of MDO in UAV design applications. The relevance of this section to the current investigation lies in the need to be aware of previous UAV MDO studies in order to:

1. Understand the relevance of MDO to UAV design
2. Become acquainted with common themes in MDO UAV design
3. Document proven and peer-reviewed methods of previous studies which may be useful for the current investigation
4. Document relevant results and observations of interest of previous studies
5. Determine whether previous work exists on the use of MDO as a propulsion system comparison method

Section 2.3.1 provides a brief overview of MDO, while Section 2.3.2 discusses previous UAV design studies where MDO was applied.

2.3.1. An overview of MDO

The designing of engineering products is often a complex task. This is particularly true in the field of aviation, where aircraft design is characterised by many different disciplines, including aerodynamics, structures, propulsion, guidance and control systems and aeroacoustics. Experts from these different disciplines work sequentially to design an aircraft which meets their discipline's requirements. For example, the aerodynamic designers would be tasked with providing an outline aircraft shape, which would then serve as the outer boundary for the structural designers. In most cases, disciplines have conflicting requirements. For example, experts from the field of propulsion may wish to store more fuel in the wing, to allow for longer ranges. This directly affects the wing's structural characteristics, requiring more reinforcement to support the increased load. Aircraft design is thus inherently characterised by the need to find a compromise in satisfying the various disciplines' requirements, in order to achieve the overarching objective(s).

As an alternative to the sequential design process, aircraft designers and researchers are increasingly incorporating multidisciplinary design optimisation (MDO) into their work. MDO involves translating the aircraft design process into a mathematical optimisation problem which incorporates the various disciplines, to explore the overall design space and determine the 'optimal' design relative to a predetermined criterion. The advantage of MDO over traditional design processes is that the different disciplines are incorporated in the design process in a synergistic manner, allowing for their interactions to be accounted for. Disadvantages of MDO include the need to correctly setup the optimisation problem and potentially high computational expense, although many methods have emerged which reduce this, as will be discussed later.

In brief, the general formulation of an MDO may be represented as a nonlinear constrained optimisation, defined within an n number of disciplines d_n:

$$
\begin{aligned}
&\underset{x}{Minimize}: && J(x) = f(d_1, d_2, \dots d_n)\\
&Subject\ to: && \\
&& g_j(x) \le 0 \quad & for\ j = 1, 2, \dots, m\\
&& h_k(x) = 0 \quad & for\ k = 1, 2, \dots, l\\
&& x_i^L \le x_i \le x_i^U \ & for\ i = 1, 2, \dots, n
\end{aligned}
\tag{2.1}
$$

Here, $J(x)$ is the objective function to be minimised, subject to the inequality constraints $g_j(x)$ and the equality constraints $h_k(x)$. x represents the design vector, which contains the design variable to be altered during the optimisation (the inputs). The design variables are allowed to vary between their lower and upped bounds, x_L and x_U respectively. Not shown in the formulation are the state variables, contained in the state vector y. These are variables affected by a change in the design variables and are used to describe the performance of a design. What differs between a general unconstrained optimisation problem and an MDO is the number of disciplines d_n. In an MDO, the evaluation of the objective and the constraints often do not depend directly on the design variables, but rather on the effects the design variables impart on the many disciplines involved and their respective state variables.

2.3.2. Applications of MDO to UAV design studies

MDO is commonly used in transport-class design cases which feature a high degree of novelty, such as blended-wing-body or closed-wing configurations. So what is the need to apply MDO to the design of UAVs? Sóbester and Keane outline two main reasons [63]. Firstly, the UAV has not reached the high level of maturity which exists in the design of commercial aircraft, where designs are driven by vast amounts of historical data. Secondly, UAVs are not subject to the stringent regulations existent in commercial aviation, where passenger accommodation systems add weight, complexity and design restrictions. As a result, the design space for UAVs is very large compared to manned aircraft. This design freedom requires a method to help the designer quickly identify relevant areas of interest in the vast design space; this method is MDO.

Since the late 1990's, numerous UAV design studies have been undertaken which incorporated MDO, albeit in much smaller numbers than manned aircraft design studies [64]. Common themes include:

1. Flexible/deformable/morphing UAV bodies [65], [66], [67], [68]
2. Novel/unconventional optimisation algorithms applied to UAV case studies [69], [70], [71]
3. UCAV design optimisation [72], [73]
4. UAV optimisation with electric propulsion systems [6], [7], [74], [75], [76], [77]
5. MALE and HALE optimisation [78], [79], [80], [64], [8], [81]

The following two sections will explore literature around UAV optimisation with electric propulsion systems and MALE and HALE optimisation.

UAV optimisation with electric propulsion systems

Energy sources which have been incorporated in MDO UAV studies include batteries, fuel cells, solar cells and hybrids. Batill et al. [6] was one of the first research studies of this kind and looks at the optimisation of a small (approximately $3kg$) battery-powered UAV aircraft. Bradley and colleagues Moffitt, Mavris and Parekh have undertaken multiple studies which use MDO or MDA (multidisciplinary design analysis, essentially MDO without optimisation) in the design of fuel cell-powered UAVs. These include Moffitt et al. [7], which used MDO to search the design space for a medium-sized $(25-100kg)$, long endurance fuel cell UAV, Moffitt et al. [74], which describes an MDA method to design a small (approximately $25kg$) fuel cell UAV, and Moffitt et al. [75], which introduces variable fidelity procedures into the optimisation of a small (approximately $25kg$) fuel cell UAV. Hung et al. [76] focus on the mission optimisation of an internal combustion-electric hybrid, using multi-objective evolutionary algorithms, while Bryson et al. [77] conducted optimisation investigations with similar small $(25kg)$ hybrid unmanned vehicles, but included aeroacoustic and propulsion acoustic shielding modelling into the framework, to help design for noise abatement in the conceptual design stage. The studies of Batill et al. and Moffitt et al. are of particular interest to the current study, as they contains methodologies and results which may be useful.

Optimisation with batteries In the study of Batill et al., titled 'Multidisciplinary design optimisation of an electric-powered unmanned air vehicle', the authors aimed to use an optimisation framework known as Concurrent Subspace Design (CSD) to undertake the preliminary design of an electric battery-powered UAV. The CSD framework is built upon the Concurrent Subspace Optimisation (CSSO) architecture, described in Martins and Lambe [82], and involves the use of neural network-based response surface approximations, which help improve computational efficiency. The objective was to minimise the take-off weight W_{TO}, using both mixed and continuous design variables of wing and fuselage geometry along with battery and electric motor design variables.

An interesting methodological implementation the authors used is to order the discipline analyses in such a way as to minimise the number of feedback loops, helping to reduce computational expense. This notion of discipline analysis ordering is exhibited in other MDO studies, including a relevant one by Moffitt et al. [7] which will be discussed in the upcoming section on optimisation with fuel cells. The authors used the order shown in the Design Structure Matrix (DSM) of Figure 2.6.

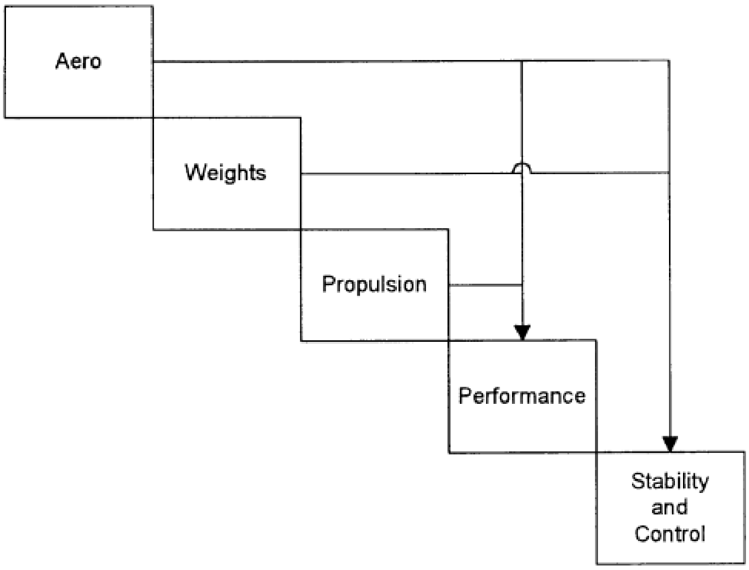

Figure 2.6: The DSM of Batill et al. [6], ordering discipline analyses for feedback minimisation.

The results of the optimisation are shown in Figure 2.7. The optimisation resulted in a lower aspect ratio wing and higher aspect ratio horizontal tail, both of which had an increased sweep. This is in line with theory, as the optimiser may have been attempting to reduce wing weight by reducing its span.

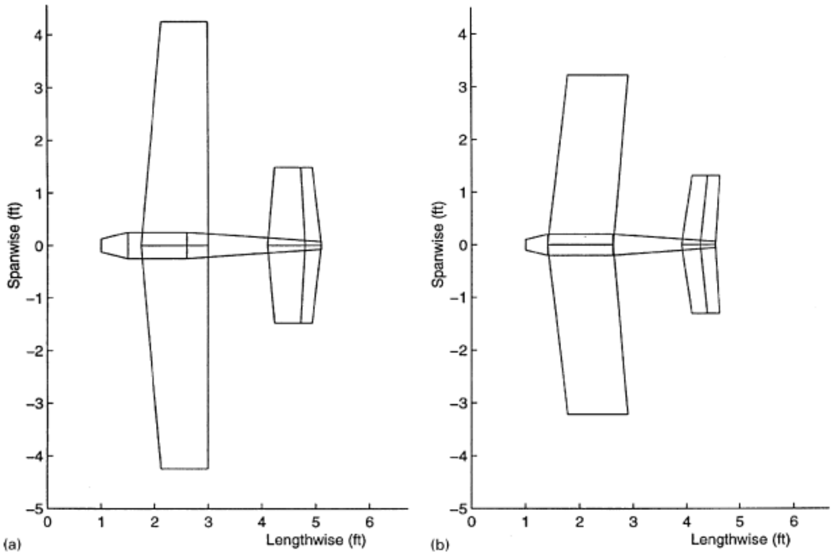

Figure 2.7: Initial (left) and optimised (right) designs of the small battery-powered UAV [6].

To benchmark the CSD framework performance, the authors made additional runs using the gradient-based Nested Analysis/Design (NAND) algorithm and the CSD framework. Only 12 variables were used, all of which were continuous, as gradient-based optimisation algorithms cannot be applied to mixed continuous discrete problems. The CSD runs resulted in lower weight than the NAND runs with much fewer analyses runs required, showcasing the strength of CSD.

Optimisation with fuel cells Although similar methods were used in the three studies of Moffitt and colleagues, Moffitt et al. [7] contains the most useful information and is discussed in depth here. The study, titled 'Design Space Exploration of Small-Scale PEM Fuel Cell Long Endurance Aircraft', was conducted to explore the design space for medium (25-100 kg), low altitude UAVs powered by PEM fuel cells, with ranges of up to 5000 km and endurances of up to 64 hours.

As shown in Equation 2.2, the objective function was the weighted sum of range R and take-off mass m_{TO}. $\kappa_R = 62.137$ and $\kappa_m = 66.14$ were used, allowing range to be about an order of magnitude more important than take-off mass. V_c refers to the climb rate and M_{tip} to the propeller tip Mach number. 11 design variables were used, including the number of motors/propellers, hydrogen tank radius & operating pressure and propeller diameter. Rather than undertaking a mixed continuous discrete optimisation, the authors opted to conduct 4 continuous variable optimisations, over the 4 discrete numbers of propellers/motors (1-4). The full list of design variables is given in Figure 2.8, along with the DSM showing the 7 contributing discipline analyses. As was also mentioned in Batill et al. [6], Moffitt et al. [7] highlight that the order of disciplines in the DSM is important and that intelligent structuring of the DSM leads to better computational efficiency. In their study, their DSM structure resulted in 79 forward-fed variables and only 7 backward-fed ones. Interestingly, both Batill et al. [6] and Moffitt et al. [7] have aerodynamic and structural/weight analyses near the beginning, while propulsion and performance are towards the end. This makes logical sense, as aerodynamics and weight govern how much power/thrust is required and thus the performance characteristics of the aircraft.

$$\begin{aligned} &\underset{x}{Minimize}: && J(x) = -\frac{R}{\kappa_R} + \frac{m_{TO}}{\kappa_m} \\ &Subject\ to: && 75 \leq V_c \quad (m/min) \\ & && M_{tip} \leq 0.85 \end{aligned} \tag{2.2}$$

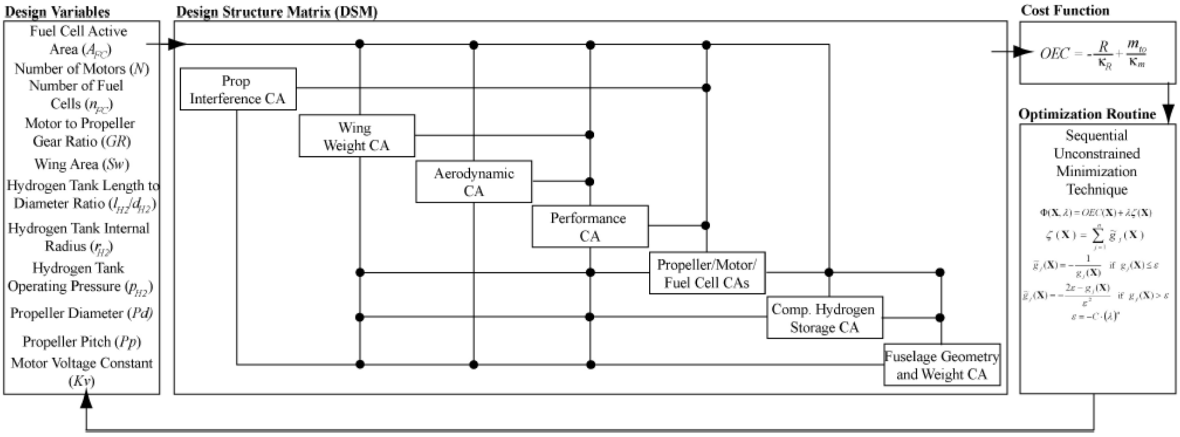

Figure 2.8: The DSM of Moffitt et al. [7].

The fuel cell was represented as a static polarisation curve, which shows the relationship between a fuel cell stack's voltage and its current [56]. This is a typical method to represent a fuel cell's performance and was also used in Verstraete and colleagues' work, which was discussed in Section 2.2.2. According to Moffitt et al. [74] polarisation curves capture the performance characteristics and fuel consumption of fuel cells with good fidelity.

In the compressed hydrogen storage contributing analysis, the authors assumed a composite, aluminium-lined cylindrical tank. They state the aluminium layer is required in composite tanks to help reduce hydrogen leaking. They assumed the aluminium layer had a constant thickness, did not contribute to the strength of the tank but did contribute to its weight. The amount of hydrogen fuel required for the mission in moles n_{H_2} may be calculated using Equation 2.3 (assuming all the hydrogen stored in the tank may be extracted), with n_{cells} being the number of cells, I being the current, F being Faraday's number, η_{util} being the hydrogen utilisation and E being the endurance.

$$n_{H_2} = \frac{n_{cells} \cdot I}{2 \cdot F \cdot \eta_{util}} \cdot E \tag{2.3}$$

The tank storage volume V needed for this amount of hydrogen under pressure P may be determined using the Redlich-Kwong equation, given in Equation 2.4. Here, R is the gas constant and T represents the tank storage temperature.

$$\begin{aligned} P &= \frac{R \cdot T}{V-b} - \frac{a}{T^{1/2} \cdot V \cdot (V+b)} \\ a &= 0.1425 \\ b &= 1.817 \cdot 10^{-5} \end{aligned} \tag{2.4}$$

The results showed an increase in range but also in mass. This was the result of the weighing factors in the objective function, with more importance having been placed on the range. To achieve this increased range, the wing area increased drastically, which in turn increased the mass. The authors do not specify how the area increased, however it would make sense that the span saw a drastic increase, to be able to achieve long ranges.

From the multi-engine optimisation runs, the best performing aircraft was the one with 2 propellers and is shown in Figure 2.9. The optimiser produced a high aspect ratio, tapered wing, and a long but relatively slim hydrogen tank. The range of the 2 engine optimal aircraft is longer than that of the single-engine optimal at the expense of a much higher mass.

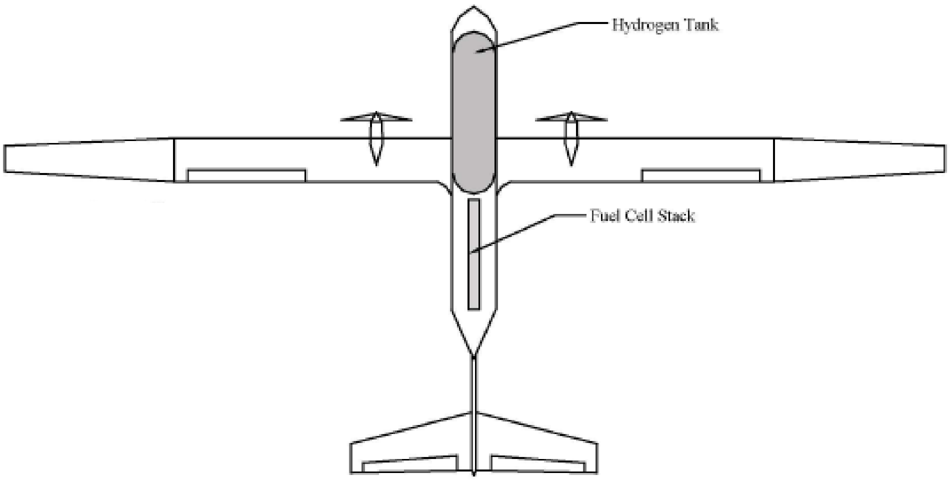

Figure 2.9: Optimal fuel cell aircraft design in Moffitt et al. [7].

MALE and HALE optimisation

Various MDO studies of MALE and HALE UAVs exist. These include studies relating to morphing structures by Ajaj et al. [78], where a low-fidelity MDO platform was used to maximise lift-over-drag ratio and later rolling moment to yawing moment ratio of a 800 kg MALE UAV with active aeroelastic structures. Ajaj et al. [79] also looked at a variable span concept and conducted two consecutive optimisations on axial stiffness minimisation, followed by structural mass minimisation of the wing partition under study. Collaborative design environment projects like the European AGILE project have included MALE UAVs as optimisation tool case studies. Prakasha et al. [80] tested their collaborative design environment by minimising mission fuel and maximum take-off mass of a MALE UAV. Studies aiming to maximise MALE endurance include one by Rajagopal et al. [64], who undertook a conceptual design study of a MALE UAV wing through an MDO framework to achieve long endurance. Rajagopal and Ganguli [8] conducted a similar study but used a two step optimisation process, by first optimising the 2D airfoil for endurance, then optimising the wing planform for endurance maximisation and wing weight minimisation, using Kringing meta-models. Morrisey and McDonald [81] optimised a HALE UAV with a very large aspect ratio featuring a pinned-wing concept for weight minimisation, finding up to 17.3% of weight reduction through their MDO platform.

Because of its relevance, the paper of Rajagopal and Ganguli [8] will be discussed in more detail. The study, titled 'Multidisciplinary Design Optimization of Long Endurance Unmanned Aerial Vehicle Wing', considers a 1800 kg, twin-piston-engine tractor configuration MALE UAV, designed to loiter at an altitude of between 20,000 ft and 25,000 ft and a Mach number of 0.13. The problem was split into two parts. Firstly, a single-objective, single-discipline aerodynamic optimisation of the 2D airfoil was conducted, with the objective function being the endurance minimisation parameter, given by Equation 2.5. The multi-objective genetic algorithm NSGA-II was used.

$$J(x) = \frac{{C_l}^{(3/2)}}{C_d} \tag{2.5}$$

Once the optimised airfoil was determined, it was fed into the second optimisation. This was a multi-objective, multi-disciplinary optimisation problem with the objectives being the maximisation of the endurance parameter and the minimisation of wing weight, as seen in Equation 2.6. Both 2D and planform optimisations used the panel method code XFLR5, while the planform optimisation also used CATIA for geometry modelling, PATRAN for mesh generation and NASTRAN for the finite element analysis.

$$J(x) = \begin{bmatrix} \frac{{C_l}^{(3/2)}}{C_d} \\ -W_{wing} \end{bmatrix} \tag{2.6}$$

The authors made sure to normalise all values of design variables. This is important, as it translates to a much smoother optimisation problem, which helps increase accuracy and robustness [83].
The results of the study are shown in Figure 2.10 in the form of five points on a Pareto front. The y-axis label is to be read upwards and states 'Endurance Parameter'. Point 1 on the Pareto front corresponds to a lightweight solution and point 5 corresponds to a high endurance solution, with points in between corresponding to equally optimal solutions which do not maximise endurance or weight individually. Clearly then, wing weight and endurance are competing parameters. Interestingly, point 4 does not sit on the Pareto front curve produced by the other four points. This suggests point 4 is actually not a global optimum, as either weight and/or endurance have room for improvement. The optimiser might have thus found a local optimum at point 4, rather than a global one. However, this is simply the current author's educated speculation, as no comment was made by the authors of the study regarding the location of point 4 being inside the Pareto front, something which should have been clarified.

Figures 2.11 and 2.12 give the normalised aspect ratio and taper ratio for the points on the Pareto front. Clearly, as endurance becomes the dominant objective function, both aspect ratio and taper ratio tend towards their maximum values, as was seen in previous studies.

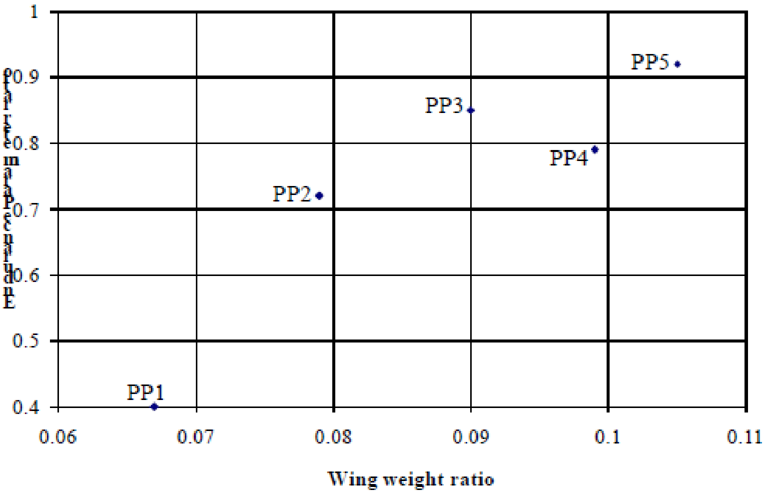

Figure 2.10: Points on the Pareto front of endurance parameter against wing weight ratio from Rajagopal and Ganguli [8].

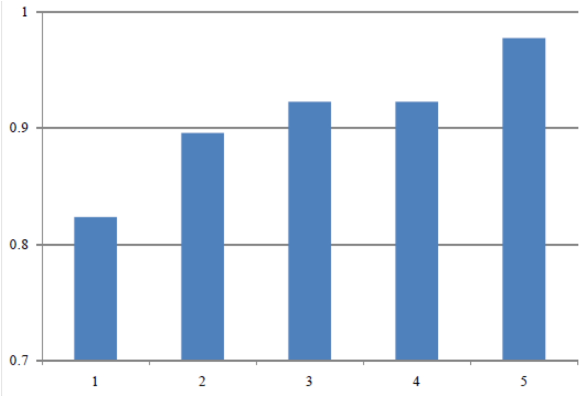

Figure 2.11: Normalised aspect ratio variation along Pareto points in [8].

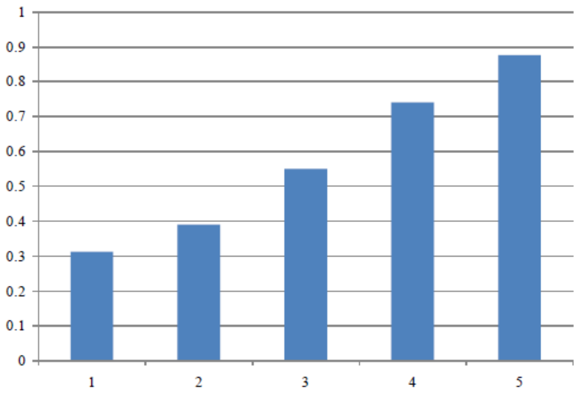

Figure 2.12: Normalised taper ratio variation along Pareto points in [8].

3

Research Objective and Motivation

3.1. Motivation

In Section 2.1, the growing importance of UAVs in the modern world was highlighted. In particular, the MALE UAV has proven to be one of the most significant classes of UAVs, both in military and civil applications. Its ability to offer both reconnaissance and air-to-land direct strike capabilities without risking the operator's life has made it an indispensable tool in many military arsenals around the globe, while its large size and high altitude flight allow for heavy scientific instruments to be carried onboard. As a result, governments and designers are racing to develop new MALE models, with European nations developing the RPAS and Russia prototyping the Orion-E.

In Section 2.2, propulsion systems of unmanned vehicles were discussed. It has been shown that electric propulsion systems, particularly those involving hydrogen fuel cells, are relatively new to large UAVs. MALE UAVs in particular have historically seen almost no application of electric propulsion and are still powered by internal combustion engines to meet their long endurance needs. This significantly limits the potential of MALE UAVs, as they are currently designed around existing piston engines, which results in their design being constrained by them. However, with aircraft electrification on the horizon, electric-based solutions are showing promise, particularly fuel cells which have proven to deliver days of power at a time. Incorporating novel propulsion solutions will allow for propulsion systems to be tailored to the needs of the UAV design, unleashing the UAV's full design potential. However, enabling this paradigm shift requires knowledge of the system-level design effects and trade-offs which result from integrating electric propulsion systems into MALE UAVs. It is therefore imperative that these design effects are studied and understood before widespread MALE UAV electrification can take place.

In Section 2.3, the UAV's unique need for MDO methods in determining design effects was described. This need was shown to be the result of two main reasons, as described by Sóbester and Keane [63]: firstly, the UAV has not reached the high level of maturity which exists in the design of commercial aircraft, where designs are driven by vast amounts of historical data. Secondly, UAVs are not subject to the stringent regulations existent in commercial aviation, where passenger accommodation systems add weight, complexity and design restrictions. As a result, the design space for UAVs is very large compared to manned aircraft and requires a method to help the designer quickly identify relevant design areas of interest; this method is MDO.

The intersection of the points discussed in the three paragraphs above presents an important area of research: considering the importance of MALE UAVs in today's world, together with the promise shown by electric propulsion for long endurance applications, the existence of a feasible design space and the subsequent aircraft-level design effects of implementing these novel propulsion technologies into MALE UAVs must be studied and understood, in order to support designers and researchers in the paradigm shift of electrification. Such UAV design studies are uniquely positioned for the application of MDO, as a result of a lack of regulatory constraints and the extensive design space inherent in UAV design.

Literature surrounding this field has been presented in Section 2.3, with research falling into two main categories: MDO studies concerning UAVs with electric propulsion systems (battery-powered, hydrogen fuel cell-powered and hybrids) and MDO studies concerning the optimisation of MALE UAV designs. Interestingly, there is sparse overlap between these two streams of research. It was found that work around electric UAV design optimisation through MDO skews heavily towards small and medium-size UAVs, with most of the presented studies being in the $25kg$ range. This would make logical sense, as electric propulsion has historically been limited by low specific energies (in the case of battery-powered systems) and low energy densities (in the case of hydrogen fuel cell-powered systems). This has led researches to first investigate electric propulsion applications on smaller UAVs, where there would be higher chances of success.

Clearly then, a gap exists in the body of knowledge of MALE UAV design. Research is required to identify whether a feasible design space exists for electric MALE UAVs and what system-level effects electric propulsion systems have on the design of the MALE UAV. Considering the importance of MALE UAVs in today's world and the promise shown by electric propulsion, the result of such an investigation may be of interest to researchers and designers alike.

3.2. Research Objective

This study is an extension of the work of, and conducted under the joint supervision of, Associate Professor Dries Verstraete of the University of Sydney, with the aim of filling this gap. Verstraete has been one of the first to develop a MDO framework in order to compare design effects of different propulsion systems on MALE UAVs, through his work titled 'Multi-disciplinary optimisation of medium altitude long endurance UAVs' [13]. In this study, he investigated the optimal design of a MALE UAV powered by a piston engine and compared it to the optimal design of the same MALE UAV powered by hydrogen fuel cells. He concluded that hydrogen fuel cells offer an improved alternative to a piston engine, in terms of a reduced take-off weight and extended endurance. In doing so, Verstraete has demonstrated promising results for the possibility of using clean energy sources to power MALE UAVs.

Verstraete's MDO framework represents a first iteration in the quest to fill the gap of knowledge around the design effects of electric propulsion solutions on MALE UAVs and his work can be extended through various improvements. Firstly, his framework contains a low-fidelity aerodynamic method, namely the digital USAF Stability and Control Data Compendium (DATCOM). Considering that any loss of fidelity in the aerodynamic modelling is magnified across the very long flight time of the modelled mission, it would be beneficial to investigate how much the results vary when using a higher-fidelity method. Secondly, low-fidelity weight estimation methods have been incorporated, namely class II empirical methods. While this may be sufficient for many of the aircraft components, the wing contributes significantly to the aircraft weight and would thus benefit from an increase in modelling fidelity. Thirdly, the propeller model utilises relations derived from UAVs and model aircraft which are typically smaller than most MALE UAVs. The incorporation of a new propeller method, such as a propeller design code, could prove helpful in attaining more accurate propeller performance calculations. Fourthly, two planform parameters have been set as design variables in the MDO, namely the wing area and aspect ratio. The use of more design variables opens up the extensive design space of UAVs, which is important to explore when switching to novel propulsion technologies. Incorporating more planform parameters as design variables could thus potentially unlock new design optima.

The current study is the next iteration in understanding the design effects of electric propulsion technologies on MALE UAVs. Its purpose is to improve on Verstraete's MDO framework, in order to arrive to a more complete picture of what various optimised electric MALE UAV designs may look like but also to investigate what effects the modelling fidelity has on these designs. Rather than taking the complete framework of Verstraete and building upon it, it was decided with Associate Professor Verstraete that a separate framework shall be developed, such that the current author may arrive at his own conclusions. Naturally, codes of various modules have been shared and used in the development of the current work, in the interest of time. These include the medium-fidelity piston engine, battery and hydrogen fuel cell models. The mission, performance codes and class II weight estimation methods used in the current study are also based on those provided by Verstraete. Among other improvements, all of the key improvements detailed in the previous paragraph are included in the scope of this study, namely a higher-fidelity method for the aerodynamics discipline (in addition to a new low-fidelity method), a higher-fidelity method for the wing weight estimation (in parallel to the class II weight estimation relations), a propeller design code and a new MDO architecture which includes a wider variety of design variables and constraints. As the new framework contains both low-fidelity and high-fidelity methods for the aerodynamics and wing weight estimation disciplines, a key outcome of this study is to investigate the effects modelling fidelity has on the optimal UAV shape.

With these considerations in mind, the research objective is formulated as follows:

The objective of this research is to develop an improved multidisciplinary design optimisation framework featuring both low and high fidelity aerodynamics and structural wing weight models and use it to investigate the impact that modelling fidelity and electric propulsion systems have on the optimised shape of a medium-altitude long-endurance unmanned aerial vehicle.

The sub-questions which must be answered in order to meet the research objective include:

1. *What are the effects on the optimised shape of a MALE UAV resulting from improving the fidelity of the aerodynamics and structural wing weight models?*
2. *Does a feasible design space exist for MALE UAVs with electric propulsion systems?*
3. *If a feasible design space does exist, what are the effects on the optimised shape of a MALE UAV resulting from incorporating electric propulsion systems?*

It should be noted that a key requirement set by Associate Professor Verstraete on the current study was that all modelling software shall be free/open source, with the exception of MATLAB as the interfacing language and optimiser. As such, the modelling software selected for use in this study have been limited to non-proprietary options.

4

Methodology

This chapter details the methodological approach taken towards the development of an MDO framework for UAV propulsion system comparison using a variable-fidelity approach. The chapter begins with Section 4.1, in which the technical scope of the framework is discussed. In Section 4.2, the design structure matrix is introduced, the optimisation problem is specified and an introduction is given on the relevant discipline analyses. The remaining sections of the chapter each go into more detail about the methodology applied for each specific discipline module. More specifically, the selected mission is introduced and discussed in Section 4.3. The methodology around parametrisation and geometry is elaborated upon in Section 4.4. The low and high-fidelity aerodynamics methods are discussed in Section 4.5. In Section 4.6, the methodology employed in the propeller module is discussed. The weights module is covered in Section 4.7, including both the low and high-fidelity wing weight estimation techniques. In Section 4.8, the methods of each of the three propulsion systems investigated in this study are discussed, while lastly, the performance module is elaborated upon in Section 4.9.

4.1. Scope of MDO Framework

Designing an aircraft requires the incorporation of a multitude of disciplines, each with their own considerations. The designer's task is to work towards balancing the considerations of these disciplines, in such a way as to meet the design requirements set out by the customer. As a result, before a design study can commence, a clear outline of relevant disciplines which will be considered must be produced. This research will focus on the core technical design disciplines, as shown in Figure 4.1, namely parametrisation and geometry, aerodynamics, propeller design, weights, propulsion systems and performance.

Cost, stability and control and application-specific considerations lie outside the scope of this study. The justification for this decision is that, firstly, although cost is one of the driving factors in the design of an aircraft, its relevance within this study does not align with the technical disciplines. Secondly, although important from a technical perspective, stability and control considerations are not accounted for as limiting the technical scope of the project is required, in the interest of time. Lastly, application-specific considerations are not relevant within the study, as the study focuses on a class of UAV, rather than intended applications. The effect of these disciplines on the design of a MALE UAV is thus recommended as an extension to the current study, for future work.

Within the propulsion discipline, three types of propulsion systems fall within the scope of this study. These are:

- Reciprocating piston engine propulsion
- Hydrogen fuel cell powered electric motor propulsion
- Battery powered electric motor propulsion

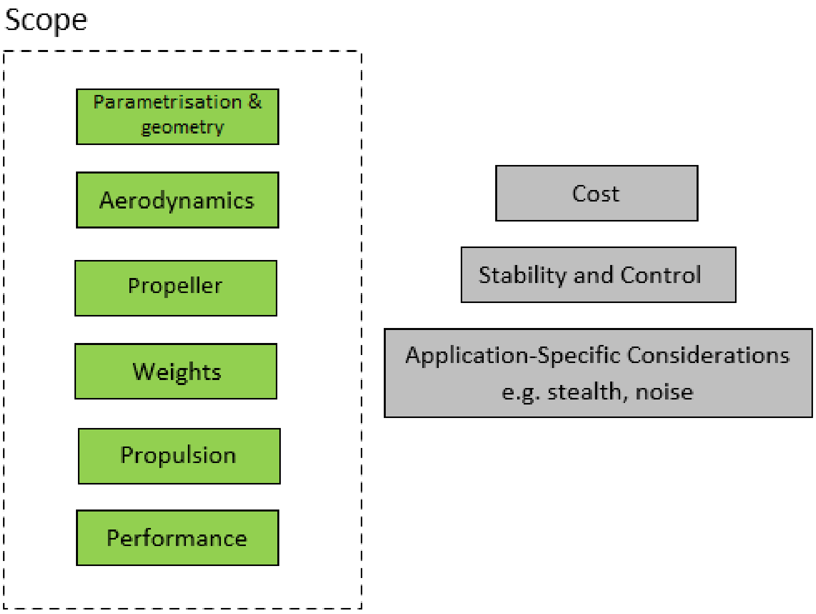

Figure 4.1: Design disciplines in and out of scope of this study

The selection of propulsion systems reflects the current and potential future market for MALE UAVs. As was highlighted in Section 2.2 of Chapter 2: Literature Review, reciprocating engines are historically and currently the most common choice for powering MALE UAVs, while fuel cell powered and battery powered electric motors are two electric alternatives which are increasingly gaining traction in design studies, as was highlighted in Section 2.2 and Section 2.3. Gas turbine propulsion, typically reserved for larger HALEs, along with hybrid propulsion solutions, are outside the scope of the current investigation. This is because, at the time of this study, the modelling of only the three aforementioned propulsion technologies is readily available to the current author. For the inclusion of more technologies, such as gas turbines or hybrid systems, the current author would need to increase the scope of the study, to include the development of such propulsion models. This is not feasible within the available time-frame and is thus suggested as a future extension of the current study.

The in-scope disciplines of Figure 4.1 are each given their own module within the framework, where their discipline-specific analyses are executed. Together, these modules are collectively referred to here as the 'discipline analyses'. The discipline analyses simulate the aircraft behaviour and each output key discipline characteristics, referred to here as 'coupling variable responses', $\vec{y}$. The discipline analyses are executed each time the objective function is required and thus form the core part of the MDO, providing the optimiser with the values of the response coupling variables and thus the objective function and constraints. The upcoming sections of this chapter each detail the methodological approach of each module of the discipline analyses. As a result, the methods and processes described in this chapter refer to the automated process that is followed every time the optimiser calls the discipline analyses.

4.2. Design Structure Matrix, Optimisation Problem Specification & Discipline Analyses

Before going into detail about the modelling of each discipline, this section describes the interrelation of said disciplines and details the selected optimisation problem, which is built around the discipline analyses.

4.2.1. Design structure matrix

The first step in describing the MDO framework is detailing the Design Structure Matrix (DSM). The DSM is a graphical tool which is used to showcase the interrelations between the discipline analyses within the context of the optimisation. The DSM of this investigation is given in Figure 4.2. It has been made as propulsion-system-agnostic as possible, to encompass the three propulsion technologies investigated in this research. The arrows represent the flow of information during a single optimisation iteration. The design variables $\vec{x}$ are given in the top-right corner, with their arrow pointing to all disciplines, highlighting the fact that each discipline takes the design variables as inputs. The objective function $J(\vec{x})$ and constraints are given in the bottom-left corner, as they are fed from the end of the discipline analyses, back to the optimiser, for another loop to begin. This DSM is to be used by the reader in the two upcoming sections, Sections 4.2.2 and 4.2.3, to help understand the optimisation parameters (including the design variables, objective function and constraints), along with each module of the discipline analyses.

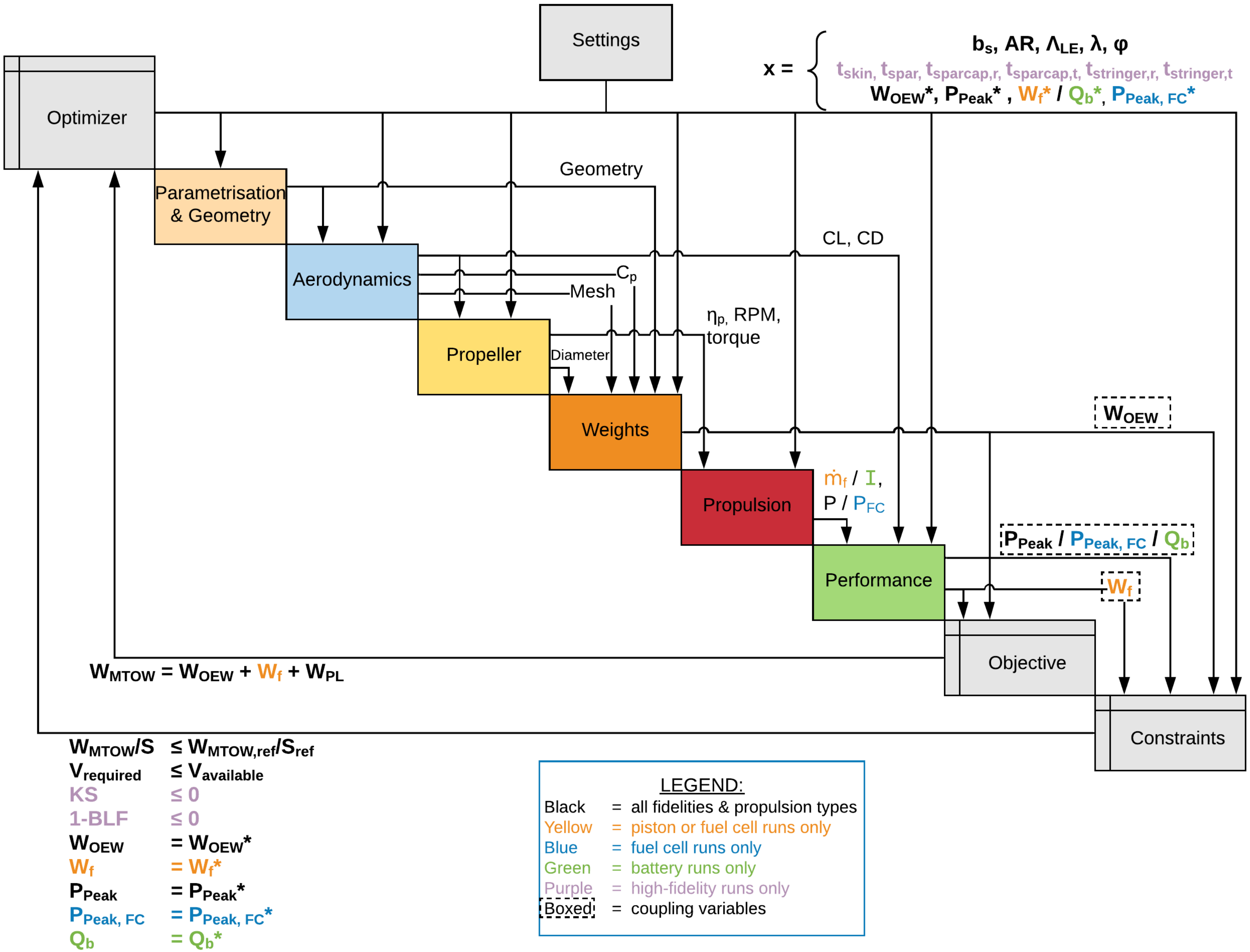

Figure 4.2: Design Structure Matrix of the current study.

4.2.2. Optimisation problem specification

The top-most and two bottom-most components (in grey colour) in the DSM of Figure 4.2 represent the optimisation scheme which encompasses the discipline analyses. This includes the objective function, the design vector, the equality and inequality constraints and the optimisation algorithm, while the architecture of all these elements represents the selected MDO formulation.

MDO formulation

The framework follows the sequenced Individual Discipline Feasible (IDF) formulation [84]. This is a hybrid of a pure Multi Disciplinary Feasible (MDF) and pure IDF formulation, wherein only a selection of disciplines are decoupled, while the rest retain their coupled relationships. To achieve this, first the problem has been expressed in a pure MDF formulation. Next, the sequence of disciplines has been rearranged to minimise the number of feedback variables, exposing the disciplines requiring inter-disciplinary consistency. Lastly, only these inter-disciplinary consistency relationships have been decoupled, and their coupling variable responses $\vec{y}$ have been mirrored in the design vector as coupling variable targets $\vec{y}^{\,t}$. Here, the 'Weights', 'Propulsion' and 'Performance' disciplines have been decoupled, with W_{OEW}, W_f/Q_b and $P_{peak,FC}$ generating target coupling variables. This formulation has been selected as it does not require inter-disciplinary consistency in each optimisation iteration, as in MDF, while at the same time not requiring all response coupling variables to be mirrored in the design vector as target coupling variables, as in IDF, ultimately resulting in a much more computationally efficiency framework for this specific application.

Objective function

The objective function has been selected as the minimisation of the Maximum Take-Off Weight (MTOW), given mathematically in Equation 4.1 as a function of the operational empty weight W_{OEW}, fuel weight W_f and payload weight W_{PL}. W_{OEW} and W_f are two key response coupling variables while the payload weight W_{PL} is typically known prior to the design of an aircraft and hence it is set as a constant prior to the MDO initialisation. With reconnaissance flights being a common application of MALE UAVs, the maximisation of endurance was also considered as an appropriate objective function. However, MTOW was ultimately selected, in order to align this study with the initial low-fidelity study of Verstraete [13], which the current study expands upon and which also uses MTOW as the objective.

$$J(\vec{x}) = W_{MTOW}(\vec{x}) = W_{OEW}(\vec{x}) + W_f(\vec{x}) + W_{PL} \tag{4.1}$$

Design vector

The design vector $\vec{x}$ consists of five wing planform variables, six wing structure sizing variables and three or four target coupling variables, depending on whether the reciprocating engine or electric motor propulsion systems are being run. The six wing structure sizing variables are only activated when using the high-fidelity Finite Element Analysis (FEA)-based wing structure sizing method. The low-fidelity wing structure sizing method is empirical-based and does not require these sizing variables. Further information on the different fidelity methods will be provided in Section 4.7. The design variables are:

- **Planform variables:**
  - Wing semi-span b_s
  - Aspect ratio AR
  - Leading-edge sweep Λ_{LE}
  - Taper ratio λ
  - Tip twist angle ϕ
- **Wing structure sizing variables:**
  - Skin thickness t_{skin}
  - Spar thickness t_{spar}
  - Root sparcap thickness $t_{sparcap,r}$
  - Tip sparcap thickness $t_{sparcap,t}$
  - Root stringer thickness $t_{stringer,r}$
  - Tip stringer thickness $t_{stringer,t}$

- **Target coupling variables:**
    - Operational empty weight W_{OEW}^{*}
    - Engine/motor peak power P_p^{*}
    - Fuel weight W_f^{*} (reciprocating and fuel cell only)
    - Fuel cell peak power $P_{p,FC}^{*}$ (fuel cell only)
    - Battery capacity Q_b^{*} (battery only)

All design variables corresponding to their propulsion system are given in Table 4.1. The five planform variables were selected as they represent some of the most significant wing parameters, with wing design crucial to the long-endurance performance of MALE UAVs. The six wing structure sizing variables were selected as they were found to have the most impact on the weight and structural integrity of the wing. This choice of wing structure sizing design variables is further discussed in Section 4.7.2. Finally, the target coupling variables mirror the variables required for inter-disciplinary consistency in a pure MDF formulation. With the use of the sequenced IDF formulation instead, these surrogate variables are required as inputs into each iteration.

Table 4.1: Design variables for the three propulsion types. Wing sizing variables are only active in the high-fidelity method.

	Planform Variables	Wing Structure Sizing Variables	Coupling Variables
Reciprocating	b_s AR Λ_{LE} λ ϕ	t_{skin} t_{spar} $t_{sparcap,r}$ $t_{sparcap,t}$ $t_{stringer,r}$ $t_{stringer,t}$	W_{OEW}^{*} W_f^{*} P_p^{*}
Fuel Cell	b_s AR Λ_{LE} λ ϕ	t_{skin} t_{spar} $t_{sparcap,r}$ $t_{sparcap,t}$ $t_{stringer,r}$ $t_{stringer,t}$	W_{OEW}^{*} W_f^{*} P_p^{*} $P_{p,FC}^{*}$
Battery	b_s AR Λ_{LE} λ ϕ	t_{skin} t_{spar} $t_{sparcap,r}$ $t_{sparcap,t}$ $t_{stringer,r}$ $t_{stringer,t}$	W_{OEW}^{*} Q_b^{*} P_p^{*}

Inequality constraints

Four inequality constraints have been applied, the last two of which only apply to the high-fidelity FEA-based wing structure sizing method:

- **Wing loading constraint:** The wing loading $\frac{W_{MTOW}(\vec{x})}{S(\vec{x})}$ shall be less than or equal to that of the reference aircraft, to maintain similar take-off performance, as given in Equation 4.2

$$\frac{W_{MTOW}(\vec{x})}{S(\vec{x})} = \frac{W_{OEW}(\vec{x}) + W_f(\vec{x}) + W_{PL}}{S(\vec{x})} \leq \frac{W_{MTOW,ref}}{S_{ref}} \tag{4.2}$$

- **Fuel volume constraint:** The available volume for fuel $V_{available}(\vec{x})$ shall be greater than or equal to the volume required for fuel $V_{required}(\vec{x})$, as given in Equation 4.3. For the reciprocating engine case, the fuel is assumed to be stored in the wing and thus the available volume for fuel $V_{available}(\vec{x})$ is taken as the volume between the front and rear spar (25% and 75% chord respectively), from the aircraft centerline to 75% of the semi-span. For the fuel cell case, the fuel is assumed to be stored in a cylindrical tank with spherical caps inside the fuselage, between 30% and 90% along its length (to allow for payload space forward of the tank and space for the electric motor aft of the tank). Hence, the available volume for fuel $V_{available}(\vec{x})$ is the available space between the 30% and 90% points along the fuselage length, while $V_{required}(\vec{x})$ is the volume required by the cylindrical tank itself (not only the hydrogen fuel volume). For the battery case, the battery pack is assumed to be located in both the wing and fuselage if required, hence $V_{available}(\vec{x})$ is the available space in both the wing and fuselage, as previously described, while $V_{required}(\vec{x})$ is the volume of the required battery pack.

$$V_{required}(\vec{x}) \leq V_{available}(\vec{x}) \tag{4.3}$$

- **Wing von Mises stress constraint (high-fidelity wing structure sizing method only):** The wing stress at the sizing condition shall be less than the limit stress σ_{limit}, which is the yield strength of the material divided by a safety factor. To apply this condition effectively when dealing with a large number of nodes in a FEA framework, the Kreisselmeier-Steinhauser (KS) function is used for constraint aggregation, as in Equation 4.4 [85].

$$KS(g_j(\vec{x})) = g_{max}(\vec{x}) + \frac{1}{\rho}\ln\left[\sum_{j}^{n_g} e^{\rho(g_j(\vec{x}) - g_{max}(\vec{x}))}\right] \leq 0 \tag{4.4}$$

where:

$$g_j = \frac{\sigma_j(\vec{x})}{\sigma_{limit}} - 1 \tag{4.5}$$

for every Finite Element Method (FEM) node j.

- **Wing buckling constraint (high-fidelity wing structure sizing method only):** The wing Buckling Load Factor (BLF) shall be greater than or equal to one, as per Equation 4.6. This signifies that the load currently being applied to the wing would need to be increased by a factor greater than one in order for buckling to occur.

$$1 - BLF(\vec{x}) \leq 0 \tag{4.6}$$

Equality constraints

With the optimisation taking the form of a sequenced IDF scheme, the target coupling variables given in Table 4.1 must converge with their respective response coupling variables by the end of the optimisation for consistency to be achieved. Therefore, the equality constraints of the problem take the form:

$$CV_i(\vec{x}) = CV_i^*(\vec{x}) \tag{4.7}$$

for each target coupling variable $CV_i^*(\vec{x})$ given in Table 4.1 and its corresponding response coupling variable $CV_i(\vec{x})$.

Optimisation algorithm

The optimisation is conducted using the 'fmincon' nonlinear programming solver of the MATLAB Optimization Toolbox [86]. Fmincon is a gradient-based solver which supports equality and inequality constraints. As gradient-based solvers use local information (gradients), the returned optimal solution will most likely be a local optimum, rather than a global optimum. The exploration and use of more complex global optimisation solvers is outside the scope of this investigation and is thus a recommended improvement. The algorithm of choice in this study is the 'interior-point' algorithm, as it is the recommended one from the five available options according to MathWorks [86].

Optimisation Problem Formalisation

The optimisation problem explained thus far may be formalised as shown on the next page. The case with the low-fidelity wing structure sizing method is on the left, while the case with the high-fidelity FEA-based wing structure sizing method is on the right. The design vector and equality constraints depend on the propulsion system as a result of the coupling variables CV_i. In this framework, the objective function, constraints and design vector have all been normalised with respect to their initial values.

$$
\begin{array}{ll}
\mathit{Minimise:} & J(\vec{x}) = W_{MTOW}(\vec{x}) = W_{OEW}(\vec{x}) + W_f(\vec{x}) + W_{PL} \\
\mathit{Subject\ to:} & CV_i(\vec{x}) = CV_i^{*}(\vec{x}) \\
 & \frac{W_{MTOW}(\vec{x})}{S(\vec{x})} = \frac{W_{OEW}(\vec{x})+W_f(\vec{x})+W_{PL}}{S(\vec{x})} \leq \frac{W_{MTOW,ref}}{S_{ref}} \\
 & V_{required}(\vec{x}) \leq V_{available}(\vec{x}) \\
\mathit{where:} & \vec{x} = [b,\ AR,\ \Lambda_{LE},\ \lambda,\ \phi,\ CV_i] \\
\mathit{for:} & CV_i = [W_{OEW},\ W_f,\ P_p] \quad \mathit{if\ reciprocating} \\
 & CV_i = [W_{OEW},\ W_f,\ P_p,\ P_{p,FC}] \quad \mathit{if\ fuel\ cell} \\
 & CV_i = [W_{OEW},\ Q_b,\ P_p] \quad \mathit{if\ battery}
\end{array}
$$

$$
\begin{array}{l}
J(\vec{x}) = W_{MTOW}(\vec{x}) = W_{OEW}(\vec{x}) + W_f(\vec{x}) + W_{PL} \\
CV_i(\vec{x}) = CV_i^{*}(\vec{x}) \\
\frac{W_{MTOW}(\vec{x})}{S(\vec{x})} = \frac{W_{OEW}(\vec{x})+W_f(\vec{x})+W_{PL}}{S(\vec{x})} \leq \frac{W_{MTOW,ref}}{S_{ref}} \\
V_{required}(\vec{x}) \leq V_{available}(\vec{x}) \\
KS(g_j(\vec{x})) = g_{max}(\vec{x}) + \frac{1}{\rho}\ln\left[\sum_{j}^{n_g} e^{\rho(g_j(\vec{x})-g_{max}(\vec{x}))}\right] \leq 0 \\
1 - BLF(\vec{x}) \leq 0 \\
\vec{x} = [b,\ AR,\ \Lambda_{LE},\ \lambda,\ \phi,\ CV_i,\ \dots \\
\quad t_{skin},\ t_{spar},\ t_{sparcap,r},\ \dots \\
\quad t_{sparcap,t},\ t_{stringer,r},\ t_{stringer,t}] \\
CV_i = [W_{OEW},\ W_f,\ P_p] \quad \mathit{if\ reciprocating} \\
CV_i = [W_{OEW},\ W_f,\ P_p,\ P_{p,FC}] \quad \mathit{if\ fuel\ cell} \\
CV_i = [W_{OEW},\ Q_b,\ P_p] \quad \mathit{if\ battery}
\end{array}
$$

4.2.3. Discipline analyses

All of the coloured components in the DSM of Figure 4.2 represent the various discipline modules. Each one is introduced below, along with the relevant inputs and outputs. Each subsequent section of this chapter goes into detail about the methodological approach of each module individually.

Parametrisation & geometry

The purpose of this module is to generate a parametrised geometrical representation of the aircraft from the given settings and current design variables at every iteration. This parametrised geometry feeds into the aerodynamics and weight modules, for the construction of meshes, to be used in the high-fidelity panel code and FEA.

Aerodynamics

The aerodynamics module takes in the given settings, current design variables and the parametrised geometry. It contains two levels of fidelity, a low-fidelity method and a high-fidelity method, which may be selected by the user as required. For the high-fidelity method, the aerodynamics module generates a mesh of the aircraft and runs this mesh though an aerodynamics panel code, to model the aerodynamic performance of a given iteration of the aircraft. The outputs of this module are:

- Drag polars at various relevant altitudes, which are used in the propulsion module to calculate required energy resources
- The pressure coefficient (C_p) distribution over the wing, at the defined wing-sizing condition, which is required by the FEA (high-fidelity method)
- The external wing mesh upon which the mesh used by the FEA is built (high-fidelity method)

Propeller

With MALE UAVs being nearly universally propeller-driven due to their low subsonic flight speeds, the current framework incorporates a propeller module for its propulsor analysis. The propeller module has been intentionally defined separately from the propulsion module, as the propulsion module contains three different options of propulsion system, whereas the propeller inputs and outputs remain the same regardless of which propulsion system is active. Although visualised as one block in Figure 4.2, the propeller module is divided into two parts. In the first part, the module takes the given settings, design variables and aerodynamics performance properties in order to generate a propeller design for a given iteration of the aircraft. The output of this part is the propeller design itself and the propeller diameter, which is fed to the weights module. The second part of the propeller module is within the mission analysis, wherein the performance module calls the previously-designed propeller and runs it at each discrete mission segment. The outputs of this part are the propeller efficiency, rotational speed and torque at each mission segment, which are required by the propulsion module for engine/motor matching and energy resource calculations.

Weights

The weights module is one of two modules which outputs a direct component of W_{MTOW} - the W_{OEW}. It takes a multitude of inputs, including settings, design variables, geometric variables, wing C_p distribution, the external wing mesh and propeller diameter, to calculate a plethora of aircraft component weights. These weights together comprise the module's single main response coupling variable of W_{OEW}. This is fed to the optimiser as one of the variables which make up the objective of MTOW. The value of W_{OEW} is also passed onto the constraints module, to calculate the current equality constraint violation of Equation 4.7 for the W_{OEW}^* coupling variable.

Propulsion

In a similar fashion to the propeller module, the propulsion module is split into two parts. In the first part, it takes in settings and all power-related coupling variables, and sizes the engine/motor/fuel cell/battery. This is done prior to the mission analysis, in a similar fashion to how the propeller is designed prior to the mission analysis. The second part of the propulsion module is called by the performance module, within the mission analysis. Here, the propeller performance parameters (efficiency, rotational speed and torque) are taken as inputs from the propeller module and the engine performance parameters are evaluated at each discrete mission segment. The output of this part of the module is the fuel flow (piston or fuel cell case) or electric current (battery case), which is required by the performance module at each mission calculation point to calculate energy resource requirements. The second output is the reciprocating engine/motor power P and fuel cell power P_{FC} (fuel cell case), which is required by the performance module to calculate engine/motor/fuel cell peak power.

Performance

The final module is the performance module. The performance module forms the core of the mission analysis, where its purpose is to model the defined aircraft mission of Figure 4.3 at a discreet number of points, in order to calculate key response coupling variables. It does so by continuously calling the second parts of the propeller and propulsion modules at each discrete mission segment, and receives from them the fuel flow (piston or fuel cell case) or electric current (battery case). It accumulates these parameters throughout the entire mission, to provide the remaining variables of:

- Engine/electric motor peak power P_{peak}
- Fuel weight W_f (piston engine or fuel cell case)
- Fuel cell peak power $P_{peak,FC}$ (fuel cell case)
- Battery capacity Q_b (battery case)

All the outputs of this module are fed to the constraints module in order to calculate the current equality constraint violation of Equation 4.7 for the coupling variables. W_f is also fed to the optimiser for the calculation of MTOW in the reciprocating engine and fuel cell cases.

4.3. Mission Specification

Although the mission specification is not a discipline module in its own right, and its reporting would typically belong to Chapter 5: Case Study, it is described here in order to aid in the understanding of the subsequent discipline analyses' methodology sections.

In order to produce a fair comparison between the different propulsion system and different fidelity runs, the modelling of a common mission is required. The mission is selected to match that of the preceding study of Verstraete [13], which closely resembles a reconnaissance mission of the General Atomics RQ-1 Predator [17]. As will be described in Chapter 5, the Predator UAV is selected as the case study for the current investigation, and so this mission matches the case study. The modelled mission is divided into the eight main phases typical of a reconnaissance mission, shown in Figure 4.3, namely:

- Takeoff
- Climb
- Cruise (Ingress)
- Loiter
- Cruise (Egress)
- Descent
- Landing Loiter
- Landing

A distinction is made between cruise and loiter flight. Loiter is the main mission phase, characterised by low speed and an active reconnaissance payload, while cruise is the flight phase that brings the aircraft into and out of the area of interest, termed ingress and egress respectively. It should be noted that Figure 4.3 does not show the loiter and land loiter distances travelled, for the sake of clarity. Instead, their holding patterns are represented by stars.

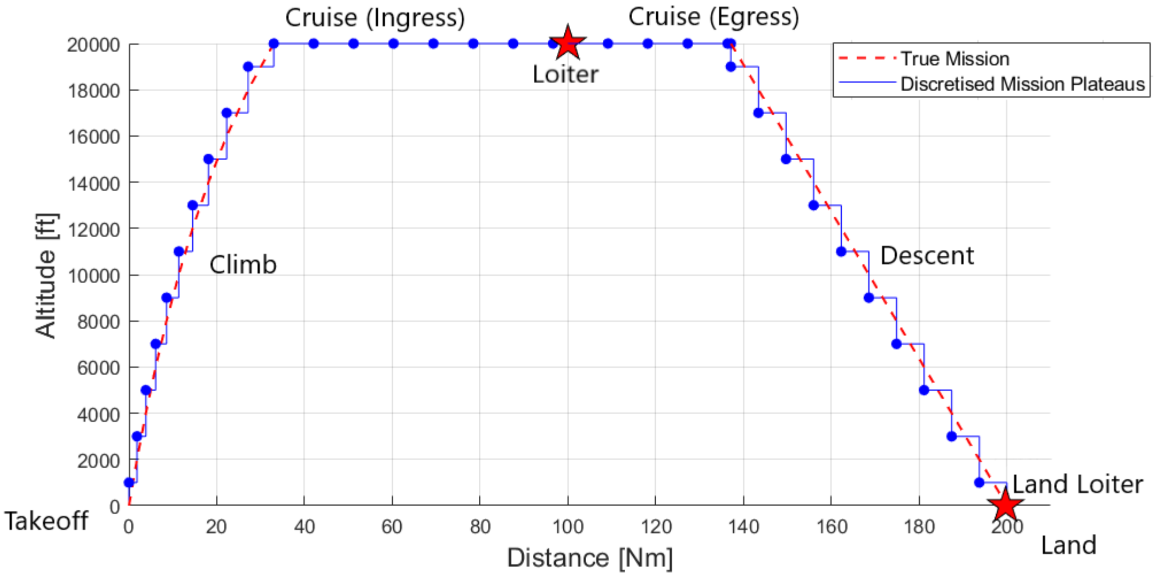

Figure 4.3: True mission and modelled discritised mission segments.

In order to model the mission and calculate aircraft performance parameters across it, each mission phase is discritised into a number of segments, represented by the blue marked line in Figure 4.3.

Throughout the remainder of this document, the term 'segments' refers to each discrete section of a mission phase, not the mission phase itself. The performance, propulsion and propeller modules are run for each segment, in order to calculate energy and power requirements over a given segment. Together, these three modules form the so-called 'mission analysis', which will be referenced throughout this document. The mid-segment altitude is used for the segment calculations, denoted by the blue markers in Figure 4.3. All flight phases are discritised into 10 segments, except for the land loiter phase, which is discritised into only two segments, as a result of its short five minute duration.

Table 4.2: Key MALE reconnaissance mission parameters [13]

Altitude [ft]	Loiter Endurance [hr]	In/Egress Distance [Nm]	Climb Speed [kt]	Cruise Speed [kt]	Loiter Speed [kt]	Sea-Level Rate of Climb [m/s]	Top-of-Climb Rate of Climb [m/s]	Descent Angle [^{o}]	Land Loiter Altitude [ft]	Land Loiter Duration [min]
20,000	24	100	65	80	65	6.5	2.7	3	100	5

Table 4.2 contains the key mission constants. The rate of climb varies linearly over the climb segments, decreasing with altitude from the sea-level rate of climb, to the top-of-climb rate of climb. The horizontal distances traversed during the climb and descent phases are included in the ingress and egress distances and thus subtracted from the cruise phase distances, as can be seen by their reduced number of cruise segments in Figure 4.3.

4.4. Parametrisation and Geometry

The purpose of the parametrisation and geometry module is to provide the discipline analyses with a parametrised geometrical representation of the aircraft, for a given optimisation iteration. The module is split into two main sections, for the parametrisation of the wing and the parametrisation of the fuselage.

4.4.1. Wing parametrisation

The wing is parametrised using the Class Shape Transformation (CST) method, developed by Brenda Kulfan and John Busseletti at Boeing [87]. This method is formed on the basis of 'class functions' and 'shape functions'. Class functions describe an underlying baseline shape, which helps distinguish classes of bodies that are fundamentally different. Shape functions on the other hand, provide the means to tailor the shape to match that of the specific body in question. In the case of airfoils, the CST method is particularly useful, as the same class function exponents may be used to describe many airfoils, while the shape functions are effective at parametrically describing a given airfoil's unique characteristics, including the leading edge radius and sharpness of the trailing edge. The CST method is defined by Equation 4.8:

$$\frac{z}{c}\left(\frac{x}{c}\right) = C_{N2}^{N1}\left(\frac{x}{c}\right) \cdot S\left(\frac{x}{c}\right) + \frac{x}{c} \cdot \frac{\Delta z}{c} \tag{4.8}$$

where $C_{N2}^{N1}\left(\frac{x}{c}\right)$ represents the normalised class function, $S\left(\frac{x}{c}\right)$ represents the normalised shape function and $\frac{x}{c} \cdot \frac{\Delta z}{c}$ represents the trailing edge thickness. The class function is defined as:

$$C_{N2}^{N1}\left(\frac{x}{c}\right) = \left(\frac{x}{c}\right)^{N1}\left(1 - \frac{x}{c}\right)^{N2} \tag{4.9}$$

where $N1$ and $N2$ are the class exponents for the front and the read of the shape respectively, meaning in the case of an airfoil, the choice of $N1$ shapes the leading edge while that of $N2$ shapes the trailing edge. Settings $N1 = 0.5$ and $N2 = 1$ produces a generic airfoil shape, as shown on the right of Figure 4.4.

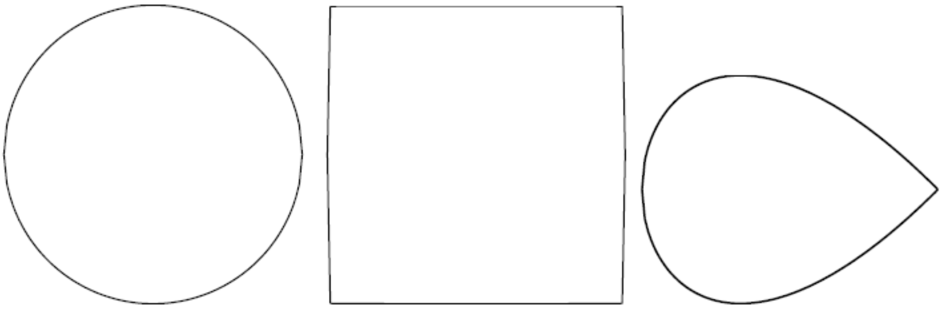

(a) $N1$=0.5,$N2$=0.5 (b) $N1$=0.001, $N2$=0.001 (c) $N1$=0.5, $N2$=1

Figure 4.4: Three distinct shapes each described by a unique pair of class function exponents [9]

.

The shape function takes the form of Bernstein polynomials $B_{i,p}\left(\frac{x}{c}\right)$, scaled by a vector A_i to provide the body's unique shape, and is defined by Equation 4.10:

$$S\left(\frac{x}{c}\right) = \sum_{i=0}^{n} A_i \cdot B_{i,p}\left(\frac{x}{c}\right) \tag{4.10}$$

A specific airfoil can be parametrised by selecting the appropriate scaling factors of A_i, for the upper surface and the lower surface. In the current study, this selection is done by means of an optimisation to minimise the least-squares error between the CST-generated points and the true airfoil coordinates, prior to initiating the MDO. The length of the scaling vectors for the top and bottom surfaces is chosen as three, which is sufficient to reproduce airfoil shapes well. An example of a parametrised NACA 4412 airfoil is shown in Figure 4.5.

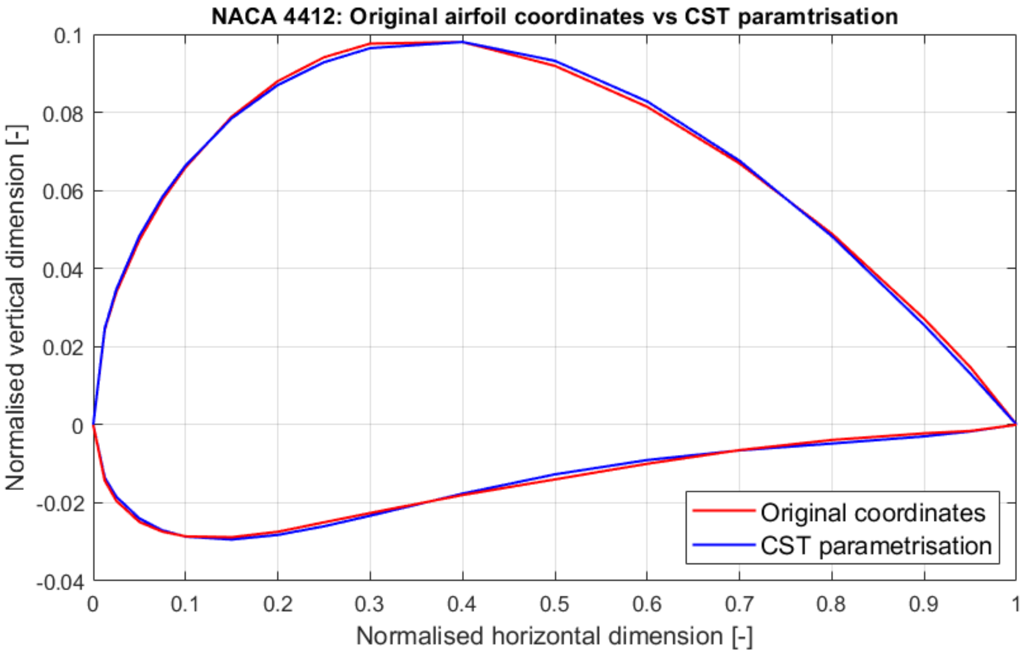

Figure 4.5: NACA 4412: Original coordinates vs CST parametrisation with $N1 = 0.5$, $N2 = 1.0$, $A_{up} = [0.222, 0.283, 0.266]$, $A_{lo} = [-0.126, 0.011, -0.040]$

4.4.2. Fuselage parametrisation

While the CST method may also be used to parametrise fuselage cross-sections, the use of superellipses is preferred for fuselage parametrisation in this study. This is because superellises provide sufficient control over the shape of a fuselage but require the selection of a smaller number of parameters. The equation for a superellipse is given as [10]:

$$\left|\frac{x}{a}\right|^{n} + \left|\frac{y}{b}\right|^{m} = 1 \quad n,\ m > 0 \tag{4.11}$$

Here, n and m are tuning exponents which are used to control the gradient of the curves at the y and x-intercepts, as may be seen in Figure 4.6. a and b are the x and y scaling factors, hence non-dimensionalising superellipses is done with $a = b = 1$, leaving only two tuning parameters to be determined for a given fuselage cross-sectional shape.

In this study, similarly to the determination of the three CST tuning parameters, the two superllipse tuning exponents are determined by means of minimising the least-squares error between the fuselage cross-section coordinates and the superellipse parametrisation, for a given fuselage cross-section. An example of a non-dimensional parametrised cross-sectional half of the Predator UAV at length location 1.12m is shown in Figure 4.7.

4.4.3. Geometry

With wing and fuselage cross-sections parametrised, a complete geometrical representation of these bodies now needs to be generated automatically for every iteration of the MDO. This is done using the Engineering Sketch Pad (ESP), an open source, browser-based solid modelling tool, developed at MIT for intended use in the MDO community [88]. The strength of ESP lies in its ability to construct solid models rapidly in comparison with other modelling tools which were tested. This is particularly

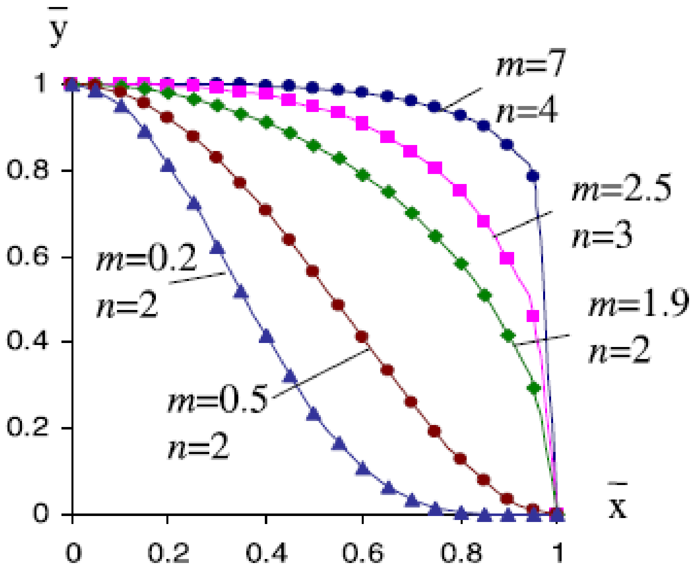

Figure 4.6: Examples of superellipse quadrants with varying tuning exponents [10]

.

important when used within an MDO framework, where computational cost is exacerbated due to the highly-iterative nature of optimisation. Speed is the key reason why ESP has been selected for this study.

ESP supports the CST parametrisation method natively, hence requires only the class and shape parameters as inputs to describe the shape of an airfoil. Support for superellipse parametrisation also exists, but is not flexible enough to allow for accurate fuselage representations. Therefore, fuselage cross-sections are passed to ESP by first constructing them externally to ESP using the superellipse function, scaling them and feeding ESP sampled coordinates. Three airfoils are generated in ESP at the wing root and tip locations, along with an intermediate location set by the user, to facilitate the possibility of a mid-wing crank. The airfoils are scaled and the wing geometry is generated using the 'loft' function. In a similar fashion, 10 fuselage cross-sections are correctly positioned and the fuselage geometry is generated by means of the 'blend' function. The number and location of fuselage cross-sections is selected to capture the full fuselage shape along its length-wise direction. The two bodies are joined together through the 'union' function. To reduce computational cost in this module and downstream, only half of the aircraft geometry is modelled. An example of a geometric solid model of the Predator UAV is shown in Figures 4.8 and 4.9.

One drawback of the current implementation of ESP is the lack of modelling of the tailplane. Both ESP and downstream modules generated issues with an additional body being modelled. As a result, it was decided to not include the tailplane in the solid model. Its aerodynamic and structural weight properties have been accounted for through empirical relations downstream in the framework. This is considered a limitation of the current study. Furthermore, although the functionality for the parametrisation of the fuselage has been developed and is included in the framework, it was ultimately decided not to include fuselage sizing parameters as design variables in the current MDO investigation, in order to limit computational cost in the interest of time. In future, further studies can be undertaken which incorporate the fuselage sizing in the MDO, as the functionality is readily available within the current framework.

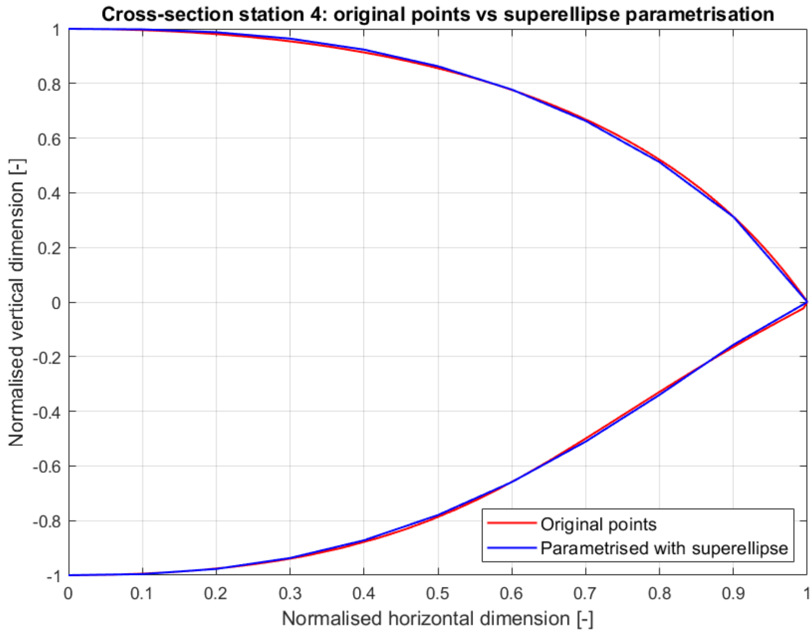

Figure 4.7: Predator $l = 1.12m$ cross-section: Original coordinates vs superellipse parametrisation with $n_{up} = 2.60$, $m_{up} = 1.23$, $n_{lo} = 2.49$, $m_{lo} = 0.79$

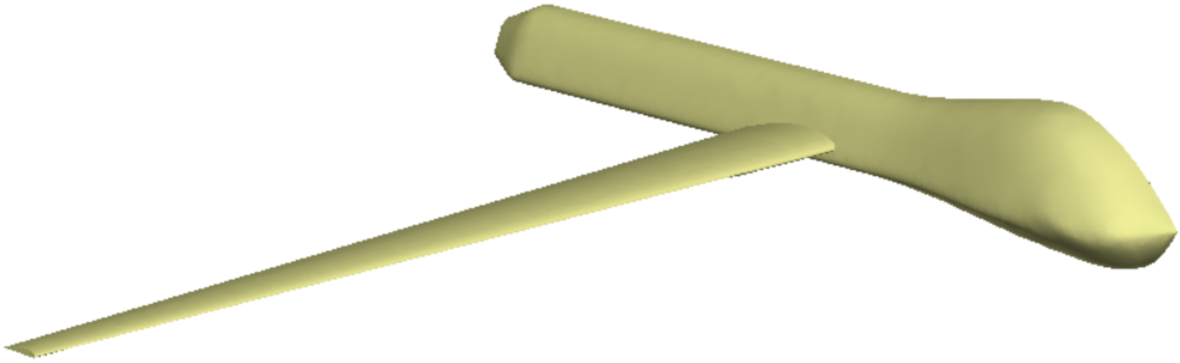

Figure 4.8: A solid model of half the Predator UAV in ESP

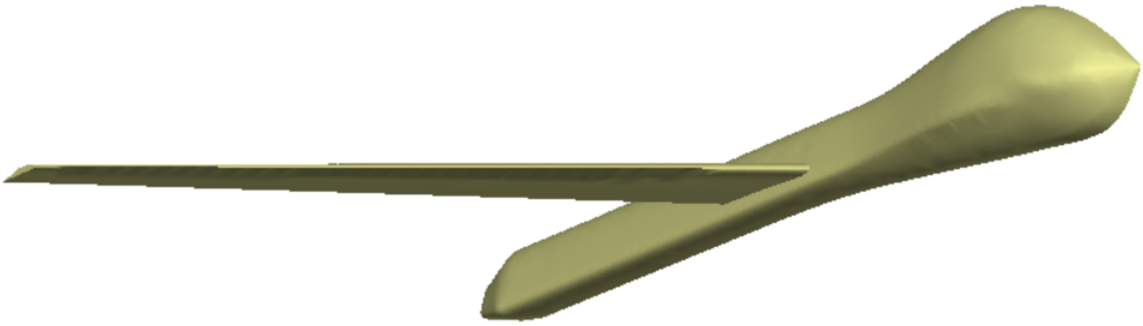

Figure 4.9: A solid model of half the Predator UAV in ESP

4.5. Aerodynamics

The purpose of the aerodynamics module is to model the aerodynamic performance of the aircraft, for a given set of design variables. An aircraft's aerodynamic performance has a very significant impact on its fuel consumption and thus its MTOW. This impact is especially pronounced for long-endurance missions, where the smallest improvement in aerodynamic efficiency can lead to a substantial reduction in fuel burn over a long period of time, allowing for a reduced design MTOW and/or improved mission performance. This is also why many MALE UAVs typically feature long, slender wings - their long span, high aspect ratio planform allow for improved aerodynamic performance and thus increased endurance. This make aerodynamic design one of the key disciplines throughout the aircraft design process.

Furthermore, the current framework features five planform parameters as design variables. For the gradient-based optimiser to correctly traverse to a reliable minimum, it is imperative that the aerodynamic performance model accurately captures the sensitivity of its parameters to changes in these planform design variables. It was thus decided to include the aerodynamics discipline in the fidelity-enhancement exercise. The aerodynamics module thus features a low-fidelity method and a high-fidelity method, which will allow for the comparison of fidelities on the optimisation result.

The output of the aerodynamics module includes:

- Lift curves and drag polars at various relevant altitudes, which are used in the propulsion module to calculate required energy resources
- The pressure coefficient (C_p) distribution over the wing, at the defined wing-sizing condition, which is required by the FEA (only for the high-fidelity case)
- The external wing surface mesh upon which the mesh used by the FEA is built (only for the high-fidelity case)

4.5.1. Low-fidelity method

The drag polar is the sole output of the low-fidelity aerodynamics module. The drag polar is determined by determining the drag contributions of each component on the aircraft. In the case of a MALE UAV, this typically includes:

- Wing drag
- Fuselage drag
- Horizontal tailplane drag
- Vertical tailplane drag

Total aircraft drag is calculated by means of Equation 4.12

$$C_D = C_{D_0} + \frac{{C_L}^2}{\pi AR\, e} \tag{4.12}$$

where C_{D_0} is the zero-lift drag and the second term is the induced drag. No wave drag is present at the low subsonic speeds of a MALE UAV. The zero-lift drag is estimated using classical flat plate skin friction formulas [89] and consists of the zero-lift drag of all four components. The zero-lift drag of the components is estimated by means of Equation 4.13:

$$C_{D_0} \cong C_f \frac{S_{wet}}{S_{ref}} FF \tag{4.13}$$

Here, C_f represents the friction coefficient, S_{wet} the wetted area, S_{ref} the reference area, while FF represents the form factor, used to account for the form drag. C_f is taken as 0.0055 for a single-engine light aircraft [90]. The wetted area for planar surfaces such as the wing and tailplane components is given by Equation 4.14 [91]:

$$S_{wet,P} = 2 \cdot S_{exp}\left(1 + 0.25\left(\frac{t}{c}\right)_r \cdot \frac{1 + \tau \cdot \lambda}{1 + \lambda}\right) \tag{4.14}$$

with S_{exp} being the exposed area, $\left(\frac{t}{c}\right)_r$ being the root thickness-to-chord ratio, λ being the taper ratio and $\tau = \frac{\left(\frac{t}{c}\right)_t}{\left(\frac{t}{c}\right)_r}$, while the wetted area of streamlines bodies such as the fuselage is given by Equation 4.15 [91]:

$$S_{wet,B} = \pi \cdot d_f \cdot l_f\left(1 - \frac{2}{\lambda_B}\right)^{\frac{2}{3}}\left(1 + \frac{1}{{\lambda_B}^2}\right) \tag{4.15}$$

with λ_B being the body's fineness ratio, $\frac{l}{d}$. The form factor of a planar surface is given by Equation 4.16 [89]:

$$FF = 1 + 2.7\left(\frac{t}{c}\right) + 100\left(\frac{t}{c}\right)^4 \tag{4.16}$$

while for bodies like the fuselage [89]:

$$FF = 1 + 1.5\left(\frac{d}{l}\right)^{1.5} + 7\left(\frac{d}{l}\right)^3 \tag{4.17}$$

For the calculation of the induced drag of the lift-generating components, the Oswald factor e is calculated using the MATLAB function developed by Sartorius [92], which is based on the methodology of Shevell [93]:

$$e = \frac{1 - 0.02 \cdot AR^{0.7} \cdot \Lambda^{2.2}}{\frac{1}{u \cdot s} + \pi \cdot AR \cdot 0.375 \cdot C_{D_0}} \tag{4.18}$$

where:

$$s = 1 - 1.9316 \cdot \left(\frac{d}{b}\right)^2 \tag{4.19}$$

with d being the fuselage diameter, b being the wing span and $0.98 < u < 1$ being the planform efficiency, taken here as the worst-case scenario of $u = 0.98$.

4.5.2. High-fidelity method

The drag polar, pressure coefficient distribution over the wing at the sizing condition and external wing surface mesh are the three outputs of the high-fidelity aerodynamics module. To obtain these outputs, the high-fidelity method employs the higher-order aerodynamic panel code PANAIR, developed by Boeing [94] [95]. PANAIR was initially created in the late 1970s to provide the NASA Aimes Research Center with the capability to solve for the fluid flow around three-dimensional arbitrary bodies, at either subsonic or supersonic Mach numbers. As a result, it is a relatively old but capable program and has been selected in this framework because of its superior performance over more modern 'lower-order' panel codes.

PANAIR methodology

PANAIR is used to solve boundary value problems involving the Prandtl-Glauert equation of Equation 4.20 [96]:

$$\tilde{\nabla}^2\phi = (1 - {M_\infty}^2)\phi_{xx} + \phi_{yy} + \phi_{zz} = 0 \tag{4.20}$$

with M_∞ being the freestream Mach number and ϕ representing the perturbation velocity potential. The Prandrl-Glauert equation is derived from the Navier-Stokes equations by employing the following main assumptions:

- The flow is inviscid
- The flow is irrotational
- The flow is linear
- The flow is steady

These simplifying assumptions have the effect of neglecting the physical phenomena of skin-friction drag and separation, which must be accounted for by other means. The ultimate objective of panel codes like PANAIR is to determine the pressure distribution over the surface of a body, through the determination of the local fluid velocity.

PANAIR may be considered a mid-to-high-fidelity aerodynamic modelling tool. Its increased fidelity as compared to the more typical 'low order' panel methods stems from its higher-order characteristics. Panel codes operate by employing distributions of sources and doublets across the discretised panels, the strengths of which must be solved for. While the strengths of these sources and doublets are constant in lower-order panel methods, in higher-order panel method sources are defined as having linearly-varying strengths, while doublets as having quadratically-varying strengths [95]. In this way, higher-order methods overcome common issues of lower-order panelling methods, including allowance of continuous doublet strengths across panel boundaries, and thus provide a more accurate representation of the flow.

PANAIR allows for the representation and analysis of bodies of arbitrary geometry, through their discretisation into surface panels of user-selected refinement. Moreover, additionally to the modelling of meshes of physical bodies, PANAIR allows for the inclusion of 'wake networks', which are used to model wakes downstream of the physical body itself. However, before being able to use a panel code like PANAIR, the geometrically continuous body must first be discritised into a collection of panels.

Mesh generation

Mesh generation is done automatically using SALOME, an open source pre-processing and post-processing platform used for numerical simulations, developed by Open Cascade, Électricité de France and the French Alternative Energies and Atomic Energy Commission [97]. For every objective function run of the optimisation, the .brep file produced by the solid modelling tool ESP during parametrisation is input into SALOME. SALOME is then run in batch mode through a Python script developed by Clar [98].

The first step in this Python-driven meshing process is the partitioning of the external solid surface into multiple different areas, each having four sides. PANAIR mandates the use of quadrilateral-element meshes, hence any surface that is meshed in SALOME should contain four sides to accommodate for this. While the upper and lower surfaces of the wing are already quadrilateral polygons, the modelled fuselage is a single surface and hence requires partitioning. This is done in the SALOME Python script by defining six new edges, seen in Figure 4.10, as follows:

- Horizontally from the front edge of the fuselage to the leading edge of the wing
- Horizontally from the rear edge of the fuselage to the trailing edge of the wing
- Vertically from the upper edge of the fuselage to the leading edge of the wing
- Vertically from the leading edge of the wing to the lower edge of the fuselage
- Vertically from the upper edge of the fuselage to the trailing edge of the wing
- Vertically from the trailing edge of the wing to the lower edge of the fuselage

As shown in Figure 4.10, the addition of these 6 edges results in the partitioning of the fuselage from a single surface into 6 distinct surface, each having 4 sides. It should be noted that a side exists at the nose of the fuselage, as seen by the circled close-up.

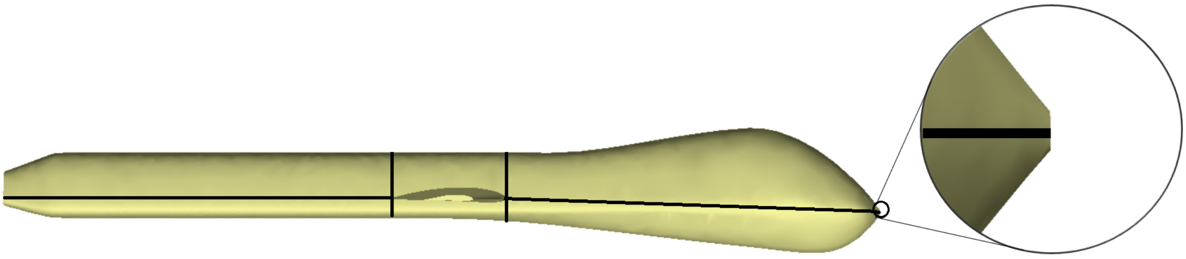

Figure 4.10: Partitioned fuselage into quadrilateral solid surfaces

With the fuselage partitioned, each surface is individually meshed with quadrilateral elements, as seen in the example of Figure 4.11. The fuselage and wing meshes may be refined by increasing the number of elements in their two orthogonal directions. For the fuselage, these directions are the longitudinal direction and the circumferential direction, while for the wing these directions are the chord-wise and span-wise directions. In order to maintain mesh continuity at the wing-fuselage boundary, the central area of the fuselage must contain the same number of panels longitudinally, as the wing does in the chord-wise direction. As a result, the fuselage mesh is effectively split into three sections: forward, centre and aft. This implies that, while the three sections share the same refinement in the circumferential direction, the forward and aft fuselage meshes may be controlled individually in the longitudinal direction. As a result, the wing mesh refinement is controlled by two parameters, namely the number of panels in the chord-wise and span-wise directions, while the fuselage mesh refinement is controlled by three parameters, namely the number of panels in the longitudinal direction for the front and aft sections and the number of panels in the circumferential direction. Mesh refinement with these five parameters is set by the user in the MDO input files prior to initiating the optimisation.

The advantages of this partitioning method includes the possibility of each mesh group being controlled independently. For example, the mesh refinement of the wing may be increased as compared to that of the fuselage, to focus computational resources on areas critical to the evaluation of the aerodynamic parameters. Finally, a network of wake elements is generated, completing the mesh.

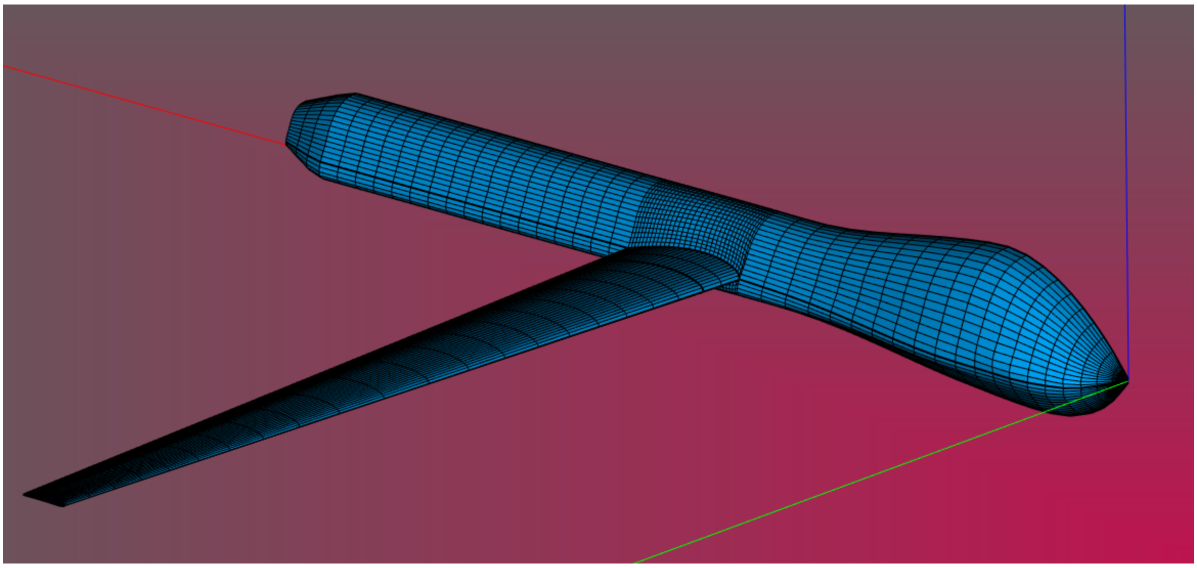

Figure 4.11: An example of a meshed aircraft model using SALOME

Deriving the drag polar and C_p distribution

With the mesh ready, it is now fed to PANAIR, along with the specific flight conditions under which PANAIR will be run, including the angle of attack α, the altitude and the free-stream Mach number M_∞.

As PANAIR was developed privately by Boeing under contract to the NASA Aimes Research Center, it was not initially intended for public distribution and thus has an unconventional and complex input format. To overcome this, the PANAIR pre-processing program PANIN was later developed and is used in this framework to consolidate the PANAIR inputs into the required format [99].

The MATLAB scripts handling PANIN and PANAIR pre-processing and post-processing have been developed by Clar [98], who also developed a MDO platform which incorporated PANAIR, in parallel to the current author. The methods of these files are elaborated upon below. The first step in generating the input file with PANIN is transforming the meshed aircraft geometry and wakes to the Langley Wireframe Geometry Standard (LaWGS), the standard numerical input model format at the Langley Research Center [100]. The second step is the definition of the boundary conditions, as follows [98]:

- Geometry panels: Impermeability Boundary Conditions (IBCs)
- Wake panels: Vorticity matching Kutta condition and doublet matching condition
- Fuselage base panels: Base surface condition

IBCs are one of the fundamental types of boundary conditions imposed in aerodynamic panel methods, which imply that there is no flow through the surface of the panel [101]. This is defined mathematically as:

$$\vec{V} \cdot \hat{n} = 0 \tag{4.21}$$

which may be interpreted as the flow velocity component normal to the flow is 0. The wake boundary condition refers to the requirement that the pressure difference across the trailing edge should be 0, known as the Kutta condition [101].

With the geometry having been defined in the LaWGS format, along with the imposition of the boundary conditions, PANIN consolidates this information into a PANAIR input file. PANAIR is now executed with this input file, to solve a system of linear algebraic equation of the form [102]:

$$[AIC]\{\lambda\} = \{b\} \tag{4.22}$$

Here, $\{\lambda\}$ is a vector containing the unknown source and doublet strengths to be solved for, while $\{b\}$ is a vector containing the boundary condition terms. $[AIC]$ denotes the 'aerodynamic influence coefficient' matrix, whose entries describe the effect of a given source or doublet on a given boundary condition. With the source and doublet strengths solved for, post-processing is undertaken to ultimately determine the pressure coefficient distribution C_p, lift C_L and inviscid drag C_D. To do so, the perturbation velocity over each panel must first be calculated as [98]:

$$\vec{v} = \begin{bmatrix} u \\ v \\ w \end{bmatrix} = \nabla\mu + \sigma \cdot \vec{n} = \begin{bmatrix} \frac{\partial \mu}{\partial x} \\ \frac{\partial \mu}{\partial y} \\ \frac{\partial \mu}{\partial z} \end{bmatrix} + \sigma \cdot \vec{n} \tag{4.23}$$

where σ and μ represent the source and doublet strengths respectively. The pressure coefficient distribution over the panels follows from the perturbation velocity as [98]:

$$C_p = -2 \cdot u - \left((1 - M_\infty^2) \cdot u^2 + v^2 + w^2\right) \tag{4.24}$$

Finally, the lift and drag coefficients at the given angle of attack at which PANAIR is run are derived from the normal force and axial force coefficients of Equations 4.25 and 4.26 [98].

$$C_N = -\frac{2}{S} \sum_i C_p \cdot A_i \cdot n_z \tag{4.25}$$

$$C_A = -\frac{2}{S} \sum_i C_p \cdot A_i \cdot n_x \tag{4.26}$$

$$C_L = C_N \cdot \cos(\alpha) - C_A \cdot \sin(\alpha) \tag{4.27}$$

$$C_D = C_N \cdot \sin(\alpha) + C_A \cdot \cos(\alpha) \tag{4.28}$$

where S is the reference wing area and A_i represents the panel area of panel i.

As the tailplane is not currently modelled in the parametrisation and geometry module, as was discussed in Section 4.2.3, the drag contributions of the horizontal and vertical tailplane surfaces are accounted for by using the same methodology as the low-fidelity aerodynamic method, namely Equations 4.12 to 4.19. Furthermore, the skin friction drag of the wing and fuselage is also incorporated this way. These contributions are added to the drag derived from PANAIR, to give the total aircraft drag.

Deriving the drag polar The aforementioned methodological steps describe a single run of PANAIR, at a single angle of attack and flight condition, which yields a single value of lift and drag respectively. To determine the first output of the aerodynamics module, the drag polar at a given altitude and Mach number, PANAIR is required to be run for at least three different angles of attack, to allow for a quadratic fitting of the three resulting values of C_D, in the form of:

$$C_D = k_0 + k_1 \cdot \alpha + k_2 \cdot \alpha^2 \tag{4.29}$$

To verify that the number of sample points above three does not affect the drag polar, quadratic fittings were conducted with sample points for up to 12 angles of attack. All polars were virtually identical regardless of the number of sample points. Therefore, for the determination of a drag polar at a given flight condition in this framework, PANAIR is run three times, for $\alpha = [0°,\ 5°,\ 10°]$ and the resulting C_D values are fitted with a quadratic of the form of Equation 4.29. Ideally, a drag polar would be generated for each individual discrete mission segment of Figure 4.3. As will be discussed in Section 4.9, only two drag polars are evaluated in this study, due to computational limitations: at sea-level and at maximum altitude. Therefore, during each optimisation iteration, PANAIR is run three times at sea-level, for $\alpha = [0°,\ 5°,\ 10°]$ and three times at maximum altitude, for $\alpha = [0°,\ 5°,\ 10°]$ - a total of six runs, for the generation of two drag polars.

Deriving the C_p distribution Once the drag polars have been generated, the second output of the aerodynamics module - the C_p distribution across the wing at the wing sizing condition - may be determined. The selection of the wing sizing condition, along with its critical load factor n, is done by constructing a V-n diagram. This activity is done manually, prior to the optimisation being executed and is specific to the case study at hand. It is thus outside the discussion scope of the discipline analyses and is instead discussed in Chapter 5: Case Study. The current section proceeds with the assumption that the sizing point has already been selected and the critical load factor n determined.

The wing sizing condition imposes a required lift coefficient $C_{L,size}$, based on the critical wing load factor n, as in Equation 4.30. A new single PANAIR run is thus required for each optimisation iteration, which will generate a C_p distribution across the wing such that it results in $C_L = C_{L,size}$. The angle of attack α_{size} that PANAIR must be run at to generate $C_{L,size}$ is determined from the $C_L - \alpha$ curve generated in the previous step. PANAIR is then run at this α_{size} and outputs the C_p distribution at the wing sizing condition by means of Equation 4.24. This C_p distribution, along with the external wing surface mesh of this single PANAIR run, is fed to the weights module for the FEM-based wing sizing.

$$C_{L,size} = \frac{n \cdot W \cdot g}{\frac{1}{2} \cdot \rho \cdot V^2 \cdot S} \tag{4.30}$$

The high-fidelity aerodynamics model has been validated by modelling the NACA RM L51F07 wing-body configuration and comparing the results against wind tunnel data. The results showed a very good fit with the data, validating the model and its implementation. More information on the validation exercise may be found in Appendix A.

4.6. Propeller

The purpose of the propeller module is to generate a new propeller design at the beginning of each objective function run and to use this design later in the mission analysis to calculate all relevant propeller performance parameters. The propeller module is thus divided into two parts: the propeller design part, which is run prior to the mission analysis, and the propeller performance evaluation part, which is run within the mission analysis at each discrete mission segment. The outputs of the propeller module include the propeller diameter, to be passed to the weights module for airframe weight calculations, and values of propeller efficiency, rotational speed and torque at each discrete mission segment, to be passed to the propulsion module for energy resource calculations.

4.6.1. Propeller design process

The first step in designing the propeller is determining its diameter. This is calculated directly, via Raymer's empirical formulation for the diameter of a propeller based on the fourth-root of the system's peak power [103]:

$$D_p = K_p \cdot \sqrt[4]{\frac{P_{peak}}{1000}} \tag{4.31}$$

where:

$$\begin{aligned} K_p &= 0.56 \quad for\ N_b = 2 \\ K_p &= 0.52 \quad for\ N_b = 3 \\ K_p &= 0.49 \quad for\ N_b > 3 \end{aligned} \tag{4.32}$$

where N_b denotes the number of propeller blades. Figure 4.12 provides the three diameter curves for a varying K_p. For the Predator UAV, which features two blades and a peak engine power of $84,600W$, the predicted diameter of $1.7m$ matches very well with its true diameter of $1.73m$ [17], validating the relation. The propeller diameter may now be passed onto the weights discipline, to determine its mass.

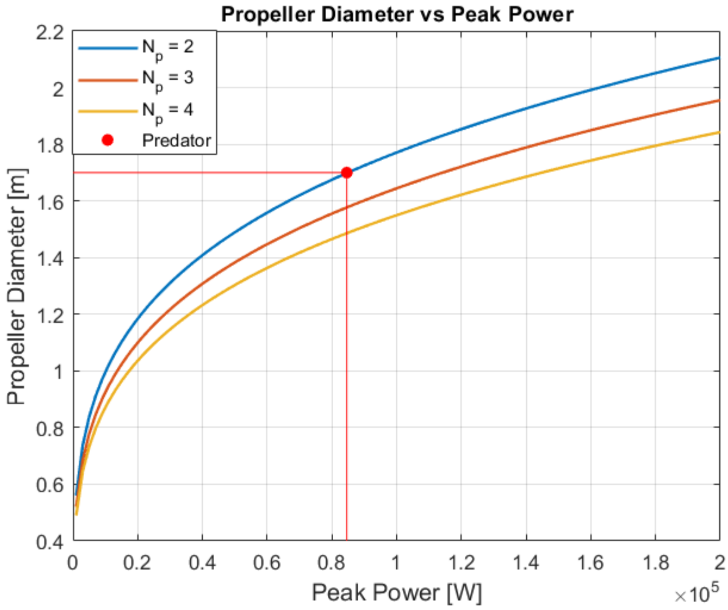

Figure 4.12: Propeller diameter vs system peak power, Predator UAV propeller diameter shown for comparison

The next step is to automatically design the propeller's geometric shape. This is done using the propeller design tool XROTOR. XROTOR is a computational tool for the design and analysis of free-tipped and ducted propellers, developed by Mark Drela of MIT [104]. Invoking the 'DESI' routine executes a calculation of the rotor chord and blade angle distributions, which achieve a minimum induced loss. The ‘DESI’ routine takes in a number of input variables:

- Altitude [km]
- Number of blades [-]
- Propeller radius [m]
- Hub radius [m]
- Hub wake displacement body radius [m]
- True airspeed [m/s]
- Advance ratio [-]
- Thrust [N]
- Propeller lift coefficient [-]

The propeller radius is derived from the propeller diameter determined earlier. The number of blades, hub radius, hub wake displacement body radius and propeller lift coefficient are all constants, set prior to the initialisation of the MDO. Altitude, airspeed, advance ratio and thrust, on the other hand, are flight-point dependant parameters and therefore one specific point in the mission must be selected as the design point of the propeller. By far the longest and most important flight phase of a MALE UAV is the loiter phase, with around 95% of the mission flight time being spent there. The middle of the loiter phase is thus selected as the propeller design point. Loiter altitude and airspeed are mission constants set prior to the initialisation of the MDO. This leaves advance ratio and thrust as the only two remaining unknown parameters.

The thrust in the middle of the loiter phase is a function of the design lift coefficient $C_{L,des}$ through the drag polar, which was derived in the aerodynamics module.

$$T = D = f(C_{L,des}) \tag{4.33}$$

The design lift coefficient depends on the aircraft weight in the middle of loiter as:

$$C_{L,des} = \frac{W_{des} \cdot g}{\frac{1}{2} \cdot \rho \cdot V_{loiter}^2 \cdot S} \tag{4.34}$$

For the case of the battery-powered electric motor propulsion system, the weight of the aircraft remains constant throughout the mission, thus $W_{des} = W_{MTOW}$. For the reciprocating engine and fuel cell-powered electric motor system, however, the aircraft weight decreases as fuel is consumed. Referring to the DSM of Figure 4.2, the propeller discipline is called before the performance discipline, as the performance discipline requires a fully-designed propeller to calculate mission performance. This entails that for a given objective function run, the weight of the consumed fuel at the mid-loiter point is not yet known when designing the propeller. In an IDF MDO scheme, this chicken-and-egg problem would call for the introduction of an additional target coupling variable: the weight of the remaining fuel at the mid-loiter point, $W^*_{f,loiter}$. To avoid the additional computational cost associated with introducing an additional target coupling variable into the MDO, the mid-loiter fuel weight is approximated as half of the fuel weight.

$$W_{des} = W^*_{OEW} + W_{PL} + \frac{W^*_f}{2} \tag{4.35}$$

This is a valid assumption, as a MALE UAV with a 24 hour loiter endurance spends $\sim 95\%$ of flight time in loiter, which reduces the net effects on fuel weight of the other phases which account for $\sim 5\%$ of flight time. To validate this assumption, discipline analyses runs were conducted and the propeller module's predicted W_{des} of Equation 4.35 was compared to the actual mid-loiter aircraft weight of the downstream performance module. The design weight error averaged 0.9%, validating the applicability of the assumption.

With the thrust determined, the advance ratio J at the design point is the sole remaining parameter required by XROTOR to design the propeller geometry. Its value is selected by allowing XROTOR to iteratively design propeller geometries based on an array of J values and select the J and corresponding propeller design which maximises propeller efficiency at the design point. An example of a propeller geometry designed by XROTOR is given in Figure 4.13.

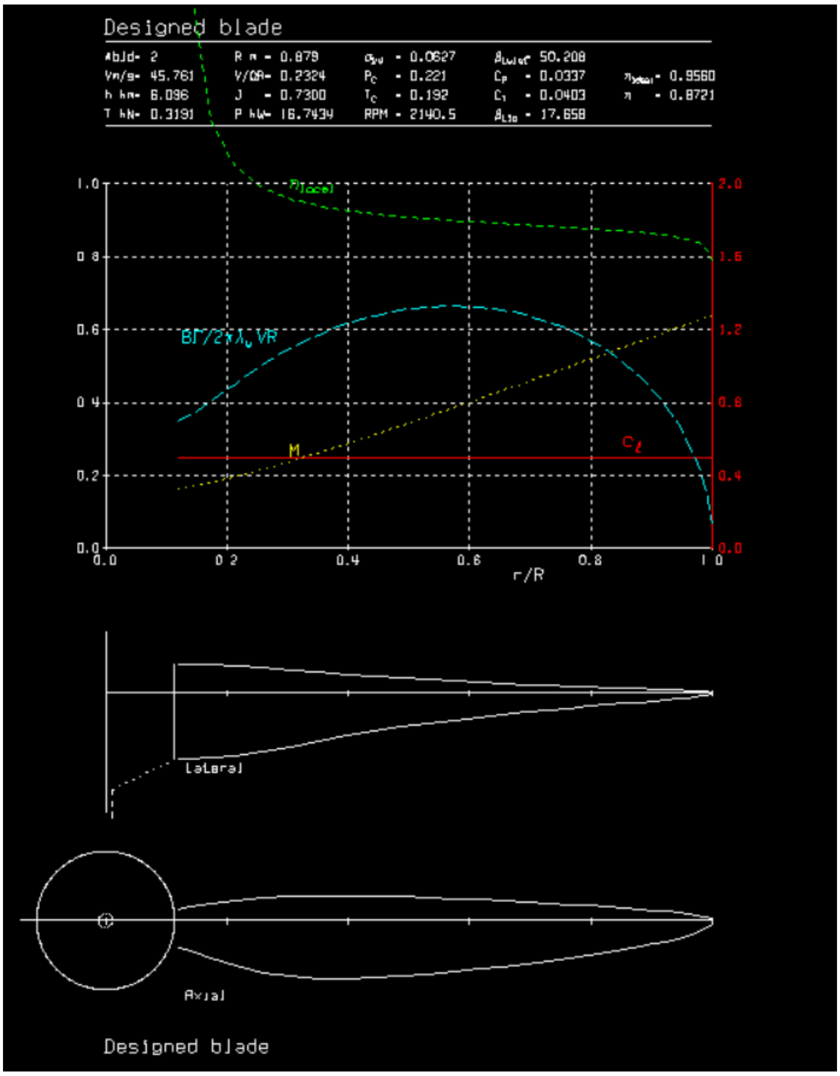
```
Designed blade
#bld= 2        R m = 0.879     σvv  = 0.0627   βtwist= 50.208
V m/s= 45.761  V/ΩR= 0.2324    Pc   = 0.221    Cp    = 0.0337   ηideal= 0.9560
h km= 6.096    J    = 0.7300   Tc   = 0.192    Ct    = 0.0403   η     = 0.8721
T kN= 0.3191   P kW= 16.7434   RPM  = 2140.5   β.75  = 17.658
```

Figure 4.13: An example of a propeller design using XROTOR

4.6.2. Propeller performance evaluation process

The propeller design may now be used downstream in the framework to provide propeller performance parameters. More specifically, the propeller discipline is called again during the mission analysis, to provide the propulsion discipline with the propeller efficiency, rotational speed and torque at every mission segment of Figure 4.3. To do so, the propeller design in loaded back into XROTOR during the mission analysis and the ‘OPER’ routine is called at every mission segment, taking in the following inputs:

- Altitude [m]
- True airspeed [m/s]
- Thrust [N]

The altitude and airspeed are mission constants for a given discreet mission segment, while thrust is calculated in the performance module using Equation 4.36.

$$T = D + W \cdot g \cdot \sin(\theta) \tag{4.36}$$

with D being the drag, W being the aircraft mass and θ being the climb angle for a given discreet mission segment. As is discussed in the performance module section, Section 4.9, the drag is determined based on the drag polars generated in the aerodynamics module, the climb angle is determined from the velocity and rate of climb at that point, while the aircraft mass is the MTOW minus any fuel that has been spent during the mission so far.

XROTOR’s ‘OPER’ routine returns the performance characteristics of the propeller at the prescribed flight condition, which include the propeller efficiency, rotational speed and torque. These parameters are then fed to the propulsion discipline for engine/motor matching and energy resource calculations. This mission analysis process is described in more detail in Section 4.9.

4.7. Weights

The purpose of the weights discipline is to calculate the mass of each physical component, structural and non-structural, on the aircraft, for a given set of optimisation design variables. The sole output of the weights discipline is the Operational Empty Weight (OEW), which is a coupling variable and one of the two components of the objective, the MTOW.

In this framework, weight estimation is conducted predominantly with the use of class II weight estimation methods. This enables the framework to capture the weights of a wide variety of components, from structural airframe elements, to avionics instrumentation, to electrical wiring, in a rapid fashion. Although empirical weight estimation methods for UAVs are few and far between, Gundlach [27] provides an extensive collection of weight estimation relations for many UAV components. Furthermore, the comparable low weight and high aspect ratio of manned sailplanes allows for the applicability of their weight estimation relations to this study. Lastly, due to the comparable size and performance of MALE UAVs to general aviation aircraft, empirical methods for general aviation aircraft are also considered appropriate as a last resort, in the absence of UAV or sailplane relations. In keeping in line with the work of Verstraete [13], upon which the current research extends, most of the same weight estimation relations are used and are discussed in the following sections.

With the wing being a major component in any aircraft, the accurate prediction of the wing weight is critical in the aircraft design process. Moreover in the current framework, the design variables are centred around wing planform parameters. Therefore it is essential that the wing weight estimation methods employed have a sufficient and appropriate sensitivity to changes in the planform design variables, so that the gradient-based optimiser may correctly traverse to an optimal design. For this reason, it was decided to include the wing weight estimation in the fidelity-enhancement exercise. The framework thus incorporates a low-fidelity wing weight estimation method, using class II weight estimation methods, and a high-fidelity wing weight estimation method, which incorporates a FEA to size the wing based on structural requirements.

The MTOW is composed of the OEW, fuel weight and payload weight as:

$$W_{MTOW} = W_{OEW} + W_f + W_{PL} \tag{4.37}$$

As discussed in Section 4.2.2, the payload weight W_{PL} is a constant, set prior to the MDO initialisation, while W_f is calculated by the performance module. The OEW is broken down into the following constituents [27]:

$$W_{OEW} = W_{struc} + W_{prop} + W_{feq} \tag{4.38}$$

where W_{struc} is the structural weight of the airframe, W_{prop} is the weight of the propulsion system and W_{feq} is the fixed equipment weight, which includes items like avionics and wiring but not payload equipment. Each constituent is further broken down as:

$$W_{struc} = W_w + W_{fus} + W_{emp} + W_{lg} \tag{4.39}$$

$$W_{prop} = W_{engine} + W_p + W_{ai} + W_{fuel,sys} + W_{prop,sys} \tag{4.40}$$

$$W_{feq} = W_{av} + W_{auto} + W_{elec} + W_{wire} \tag{4.41}$$

with: W_w - wing weight, W_{fus} - fuselage weight, W_{emp} - empennage weight, W_{lg} - landing gear weight, W_{engine} - engine/motor weight, W_p - propeller weight, W_{ai} - air induction weight, $W_{fuel,sys}$ - fuel system weight, $W_{prop,sys}$ - propulsion system auxiliary weight, W_{av} - avionics system weight, W_{auto} - autopilot system weight, W_{elec} - electrical systems weight, W_{wire} - electrical wiring weight. The weight estimation methods for these constituents are described in the next sections.

4.7.1. Wing: Low-fidelity method

In the low-fidelity method, the wing weight is estimated by taking the average value of two empirical relations. The first one is that of Gerard [105], also used by Gundlach [27], given by Equation 4.42, where n represents the load factor. This relation is based on sailplanes with wing spans between $13.4m < b < 26.4m$, which is in line with those of MALE UAVs. The second relation is taken from the unpublished report [15] of Verstraete's preceding study [13], originally citing Raymer [103], and is given by Equation 4.43.

$$W_w = 0.0038 \cdot (n \cdot W_{MTOW})^{1.06} \cdot AR^{0.38} \cdot S^{0.25} \cdot (1+\lambda)^{0.21} \cdot \left(\frac{t}{c}\right)_r^{-0.14} \quad [\text{kg}] \tag{4.42}$$

$$W_w = 1.35 \cdot S^{0.694} \cdot AR^{0.5} \cdot \left(\frac{t}{c}\right)_r^{-0.4} \cdot (1+\lambda)^{0.1} \quad [\text{kg}] \tag{4.43}$$

4.7.2. Wing: High-fidelity method

In order to calculate a more accurate wing weight, the high-fidelity wing weight estimation method departs from the empirical approach described previously and takes the form of a physics-based approach, which accounts for the specific aerodynamic loading expected to be experienced by the aircraft. This physics-based approach involves the use of the finite element method to size the wing through the variation of wing component thicknesses, driven by structural integrity requirements. Rather than incorporating a sub-optimisation routine to size the aircraft wing during every objective function call, this wing structure sizing optimisation is brought up to the top-level MDO, by incorporating the wing structure sizing variables into the main design vector, and passing the structural integrity requirements as constraints to the optimiser.

The choice of making the step from the low-fidelity, class II estimation methods of Equations 4.42 and 4.43, directly to a high-fidelity, class III method like FEA, without first incorporating a medium-fidelity method, may seem peculiar but is not without justification. Indeed, methods which are rapid and computationally inexpensive are preferred in highly-iterative frameworks such as MDO studies, when computational resources are limited. The novel nature of UAVs, however, requires a more physics-based approach to wing weight estimation, for accurate results. This is because, except for the few empirical relations used in this framework, UAVs are not well covered by a wide range of empirical relations, nor by quasi-analytical, medium-fidelity methods. So-called class II & 1/2 methods provide a good balance of computational efficiency and accuracy, with EMWET being a prominent example [106]. Despite EMWET boasting a high accuracy, with an average error margin of merely 2%, it has been validated on aircraft of conventional configurations, with MTOW ranges of $20,820kg$ (Fokker 50) to $242,670kg$ (Boeing 777-200) - orders of magnitude above the weight range of MALE UAVs. UAVs, which do not conform to the same design and regulatory requirements seen in passenger aircraft, are thus better-served by physics-based methods, assuming said methods do not impose a prohibitive computational barrier to the study.

Finite element solver

In keeping with the requirement of using exclusively open source software, it was not possible to incorporate proprietary and well-documented FEA suites such as Nastran or Abaqus. The open source FEA application CalculiX has been employed instead. CalculiX comprises of a finite element solver, CalculiX CrunchiX (CCX), developed by Guido Dhondt, and a pre- and post-processor, CalculiX GraphiX (CGX), developed by Klaus Wittig [107]. CCX provides linear and non-linear calculation capabilities, for static, dynamic and thermal problems. It has been chosen because it is open source, it is provided with documentation in English, and shares the same input file format as Abaqus, which the current author is familiar with.

Structural components

The finite element model comprises of all major structural components found in a wing. These are shown in Figure 4.14 and include:

1. Skin
2. Spar webs
3. Spar caps
4. Stringers
5. Ribs

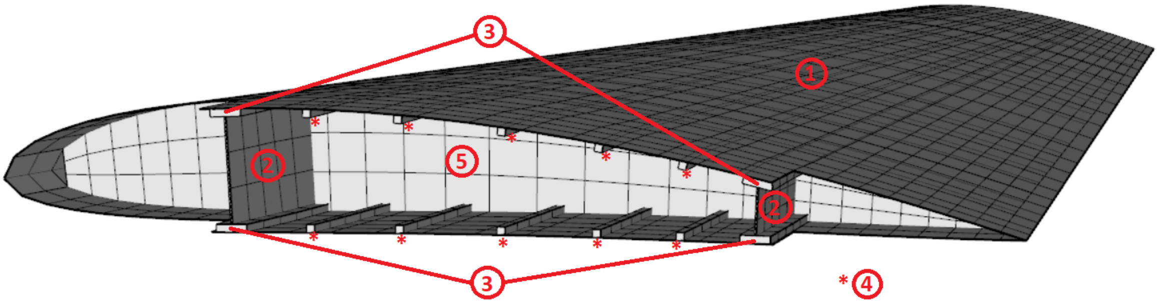

Figure 4.14: Five types of structural elements modelled in CalculiX: 1 - skin, 2 - spar webs, 3 - spar caps, 4 - stringers, 5 - ribs.

Topological parameters may be set by the user. These include the number of spars, their chord-wise locations, the spar cap aspect ratio, the number of stringers and the rib spacing. Furthermore, mesh refinement is also set by the user, for both the external wing surface and internal wing structure meshes. A list of inputs with their default values is provided in Table 4.3.

The default number of spars is set to two, to simulate the traditional two-sparred wing box. The default locations of the front and rear spar have been selected according to the ranges recommended by Roskam [108]. The default spar cap aspect ratio has been selected in order to provide the spar caps with a realistic cross-sectional shape. Initially, the default rib spacing was set at $0.914m$, as given by Roskam [108] for light aircraft. However, this spacing seemed too large, as only eight ribs would exist in the $7.425m$ semi-span Predator UAV wing. Upon inspection of the Cessna Citation II and Caproni Vizzola C22J light aircraft internal structure diagrams provided by Roskam [108], their rib spacing was determined to be in the order of $0.3m$. This spacing is more realistic and is set as a default here.

Table 4.3: Finite element wing modelling user-defined inputs and their default values.

Parameter	Description	Default Value
N_{spar}	Number of spars [-]	2
$loc_{spar,front}$	Front-most spar location (chord-wise fraction) [-]	0.25
$loc_{spar,rear}$	Rear-most spar location (chord-wise fraction) [-]	0.75
$AR_{sparcap}$	Spar cap aspect ratio (width-to-height) [-]	4
$N_{stringer}$	Number of stringers per surface [-]	5
$spac_{rib}$	Span-wise rib spacing [m]	0.3
$MR_{sparweb}$	Vertical mesh refinement of spar webs [-]	3
MR_{rib}	Vertical mesh refinement of ribs [-]	3

Sizing variables

In the current framework, the wing may be sized on the basis of 18 thickness variables, when using the default topological inputs of Table 4.3. These are:

1. **Skin: x1** Uniform skin thickness across entire wing.
2. **Spar webs: x4** Root and tip thicknesses for the two spar webs, varying linearly span-wise. Front and rear spars each have their own root and tip thicknesses, for a total of four variables.
3. **Spar caps: x8** Root and tip thicknesses for the four spar caps, varying linearly span-wise. Front, rear, upper and lower spar caps each have their own root and tip thicknesses, for a total of eight variables.
4. **Stringers: x4** Root and tip thicknesses for the stringers, varying linearly span-wise. Upper and lower stringers have their own root and tip thicknesses, for a total of four variables.
5. **Ribs: x1** All ribs given the same thickness.

As was mentioned previously, the wing structure sizing is incorporated in the top-level optimisation of the MDO. This would mean the wing structure sizing alone would contribute 18 design variables, in addition to the five wing planform variables and three or four target coupling variables. 26-27 design variables is too computationally expensive for the current study. As a result, the number of wing structure sizing variables is reduced from 18 to a more appropriate number of six. This has been done by only allowing thickness variations in the span-wise direction, such that the thicknesses of a given component type are the same at the root and the same at the tip. For example, the four spar caps originally had their own individual root thickness and tip thickness - resulting in eight variables. This is changed to all four spar caps having the same thickness at the root and the same thickness at the tip, resulting in only two variables. The logic behind this is that a larger variation in thickness (and thus mass) is expected between the root and tip of structural components, rather than between their front and rear or upper and lower instances. This was verified by running the wing structure sizer for three cases: root-tip variation, front-rear variation and upper-lower variation. The root-tip variation resulted in the most weight savings.

Applying the above method reduces the spar webs, spar caps and stringers to only two variables each, which together with the skin and rib thicknesses results in eight variables in total. To further reduce the number of sizing variables from eight to six, the two elements which contribute the least to the wing mass, the spar webs and ribs, are given a further reduction in sizing variables. The spar webs are given a single thickness, meaning no variation in the span-wise direction or across their front-rear instances, while the thickness of the ribs is set as a constant. This is deemed acceptable, as they have a 7% and 6% contribution to the overall structural wing mass respectively, as is seen in Figure 4.15. These variable reductions result in the six wing structure sizing variables of:

1. **Skin: x1** Uniform skin thickness across entire wing.
2. **Spar webs: x1** Uniform spar web thickness across span and between the front and rear spars.
3. **Spar caps: x2** Root and tip thicknesses for the spar caps, varying linearly span-wise. All spar caps share the same thicknesses.
4. **Stringers: x2** Root and tip thicknesses for the stringers, varying linearly span-wise. Upper and lower stringers share the same thicknesses.

Mesh generation: Nodes

The first step in sizing the wing using a FEA is to generate the mesh upon which the FEA will be executed. This must be done in an automated fashion, such that the FEA-based wing structure sizer is run for every objective function call of the MDO. As was described in the closing paragraph of Section 4.5.2, the aerodynamics module outputs a C_p distribution over the wing at the particular sizing point, along with the external wing surface mesh which PANAIR uses to generate this C_p distribution. In order to maintain a 1-to-1 correspondence between the C_p distribution and the FEA mesh it will act upon, the

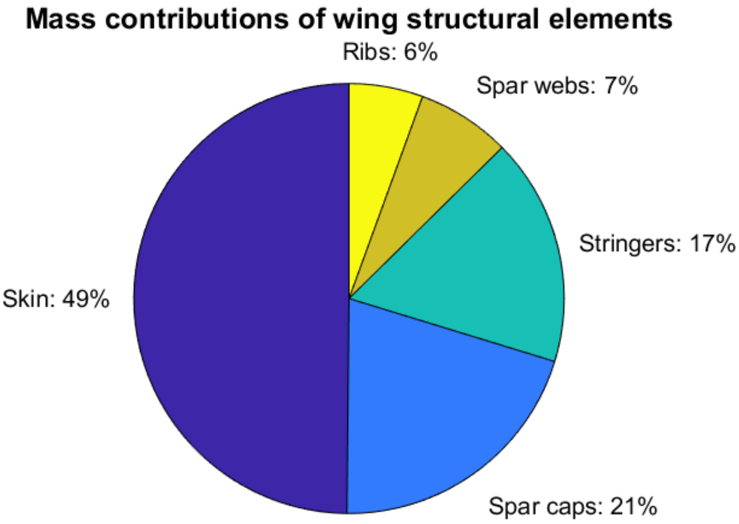

Figure 4.15: Mass contributions of the wing structure elements, showcasing the low contributions of the spar web and ribs.

mesh passed from PANAIR is reconstructed as the external wing surface mesh of the FEA. The nodes of an example of the reconstructed external wing surface mesh are shown in Figure 4.16.

Next, the mesh is extended to include the meshing of the internal wing structure. The internal structure meshing is performed automatically in MATLAB, by generating new nodes in the space enclosed by the external wing surface mesh. These internal nodes are automatically positioned based on the user-defined topological inputs of Table 4.3. As will be explained in the upcoming sections, tie constraints (a form of multi-point constraint) are used in this framework to join together different structural components. For this reason, the meshes of different structural components are defined independently of one another and are positioned accurately relative to each other. For example, in the case of the upper spar caps, the spar cap nodes are positioned below the skin nodes (onto whose elements they will be tied) with an offset, in such a way as to account for both the skin thickness and their own thickness. The internal wing structure is extended to the aircraft centerline, in order to model the wing box inside the fuselage. An example of the nodes of the internal structure are shown in Figure 4.17.

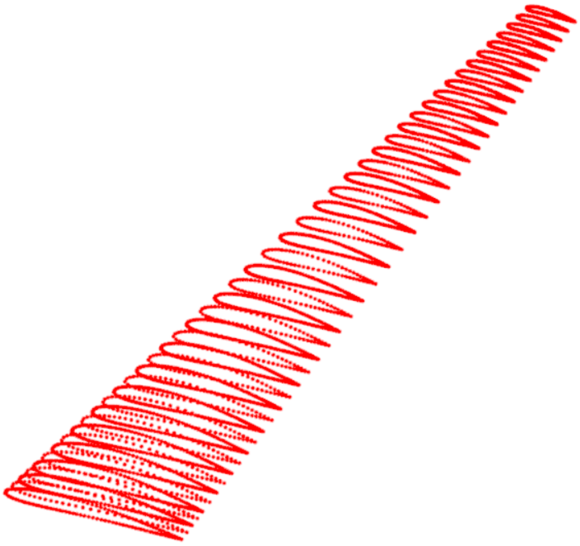

Figure 4.16: FEM nodes of the external wing surface mesh.

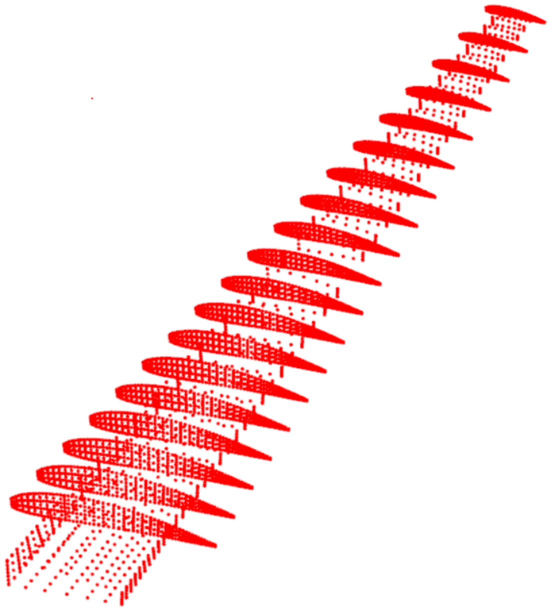

Figure 4.17: FEM nodes of the internal wing mesh.

Mesh generation: Elements

Like many finite element modelling packages, CalculiX provides a variety of element types for use in a structural FEA. These elements can be broadly categorised by three main characteristics: their dimension, the order of their shape functions and the number of their integration points. Dimensionally, 1-D, 2-D and 3-D elements are available. Due to the thin-walled nature of wing structures, 2-D shell elements are used extensively in literature for modelling the wing skin, spar webs and ribs and are also employed in this framework. For spar caps and stringers, 1-D beam elements are selected. An important point to note is that CalculiX always expands 1-D beam and 2-D shell elements into 3-D brick elements internally, prior to running the analysis. It is then upon these expanded 3-D brick elements that the FEA is conducted. The purpose of defining 1-D beam and 2-D shell elements is therefore purely for ease of input, as only a co-planar set of nodes, along with a thickness, are required for the definition of 2-D shell elements, while a set of co-linear nodes, along with cross-sectional profile dimensions, are required for defining 1-D beam elements. Examples of these expanded elements are provided in the upcoming paragraphs.

The second classification of elements is based on the order of their shape functions. This relates to the so-called 'p-refinement' of a mesh, which is explained as follows: three types of mesh refinement are typically employed in a FEA. These are increasing the number of elements, termed 'h-refinement', increasing the order of the elements' shape functions, termed p-refinement and implementing an adaptive mesh, which maintains the same number of elements and the same shape function degree, but moves the nodes [109]. While the third refinement option is not intrinsically available in CalculiX, both h-refinement and p-refinement are. Their difference is demonstrated in Figure 4.18.

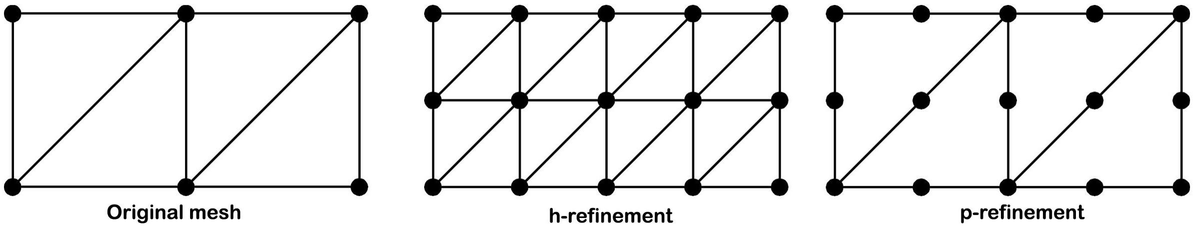

Figure 4.18: The effect of h-refinement and p-refinement on a two-element mesh with linear shape functions [11].

For all beam and shell elements, CalculiX offers two levels of p-refinement: elements with linear or quadratic shape functions. For shell elements, these are the 4-node S4/S4R and 8-node S8/S8R elements respectively, shown in Figures 4.19 and 4.20, while for beam elements these are the 2-node B31/B31R and 3-node B32/B32R elements respectively, shown in Figures 4.21 and 4.22. Also shown in these figures are the 3-D brick elements which the shell and beam elements are expanded into internally, namely the 8-node C3D8/C3D8R brick element and C3D20/C3D20R brick element.

In this framework, increasing the p-refinement has been chosen over increasing the h-refinement. The justification for this is two-fold. Firstly, it has already been mentioned that the external wing surface mesh used in the FEA is reconstructed from the wing mesh used in the PANAIR panel code. As a result, if h-refinement was desired for the finite element model, the panel code mesh would also need to be refined, leading to an unnecessary increase in computational run-time, as PANAIR is by far the most costly tool within this framework. Allowing PANAIR to generate a mesh with its own refinement requirements, passing that mesh to CalculiX and then refining it through a p-refinement is a much more computationally-efficient process in this case. This p-refinement is done in MATLAB by defining new nodes at the mid-points of the existing shell and beam nodes, prior to inputting the mesh into CalculiX. 8-node S8R and 3-node B32R elements, with quadratic shape function, are then generated, using this augmented mesh. Both these types of elements are internally expanded to C3D20R brick elements.

The second reason for preferring a p-refinement in the current framework is that Dhondt [12] recommends the use of quadratic elements, such as S8/S8R shell elements and B32/B32R beam elements, over linear elements like S4/S4R and B31/B31R types. This is because the shape functions used for quadratic elements are superior to those used for linear elements. In particular, linear elements tend to exhibit anomalous behaviour, such as shear and volumetric locking. This is often countered by software vendors by modifying the linear shape functions; however, different vendors use different methods to do so and CalculiX in particular incorporates no modifications to the linear shape functions [12].

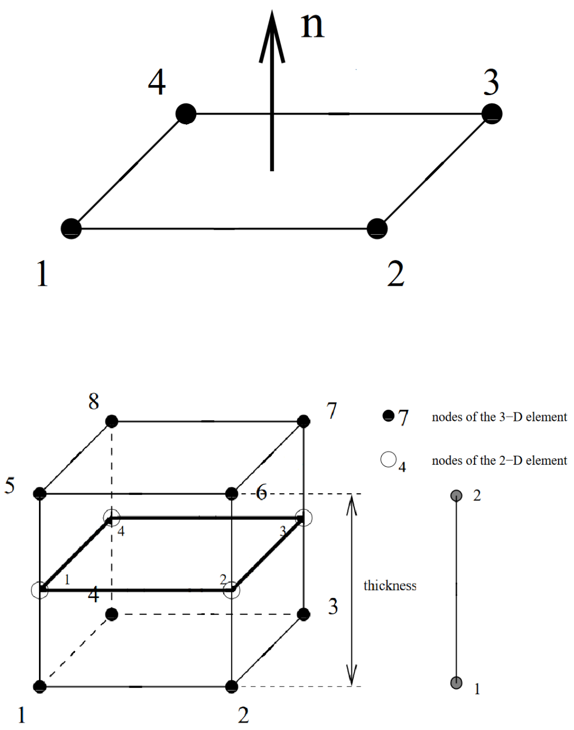

Figure 4.19: 4-node S4/S4R shell element (top) with its expanded 8-node C3D8/C3D8R brick element (bottom). In the expanded element, empty circles represent the original shell nodes, while full circles represent the expanded brick nodes [12].

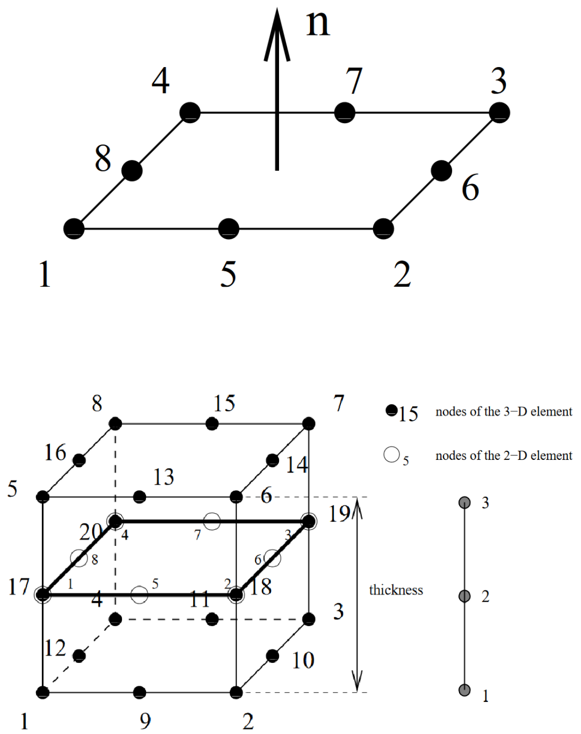

Figure 4.20: 8-node S8/S8R shell element (top) with its expanded 20-node C3D20/C3D20R bricks element (bottom). In the expanded element, empty circles represent the original shell nodes, while full circles represent the expanded brick nodes [12].

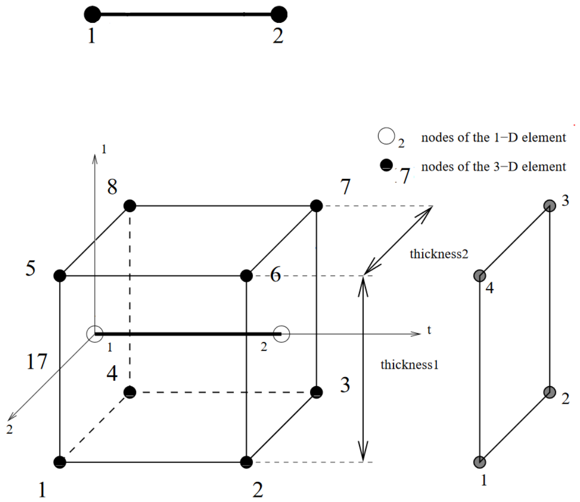

Figure 4.21: 2-node B31/B31R beam element (top) with its expanded 8-node C3D8/C3D8R brick element (bottom). In the expanded element, empty circles represent the original beam nodes, while full circles represent the expanded brick nodes [12].

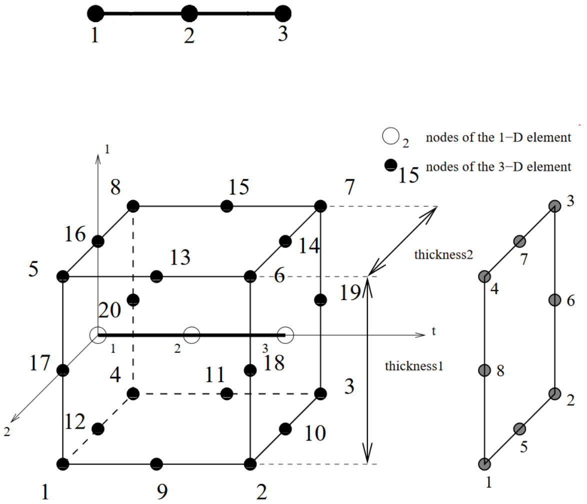

Figure 4.22: 3-node B32/C32R beam element (top) with its expanded 20-node C3D20/C3D20R bricks element (bottom). In the expanded element, empty circles represent the original beam nodes, while full circles represent the expanded brick nodes [12].

Finally, the third classification of elements is based on the number of integration points they contain. Integration points are points within an element where integrals are evaluated numerically, in order to solve the stiffness matrix. In CalculiX, any discussion around integration points is only pertinent to 3-D brick elements, as these are the elements 1-D and 2-D elements are expanded into. Two variations of elements exist based on the number of integration points: full integration and reduced integration. The 20-node C3D20 brick element, which is expanded from S8 and B32 elements, is fully integrated, containing a total of 27 integration points in a 3x3x3 scheme, as shown in Figure 4.23. Its reduced integration counterpart, the 20-node C3D20R brick element, which is expanded from S8R and B32R elements, contains a total of 8 integration points in a 2x2x2 scheme, as shown in Figure 4.24.

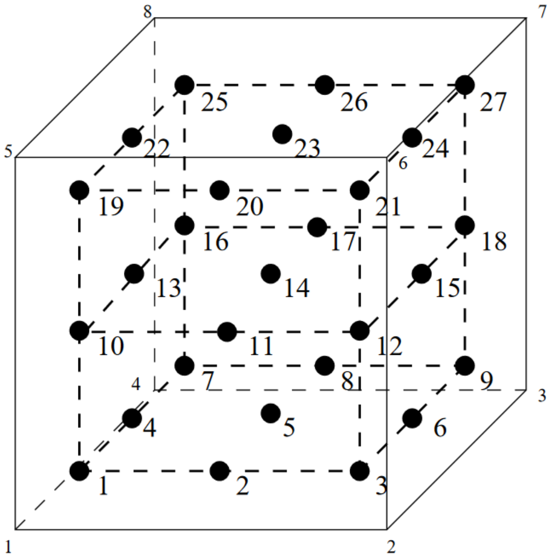

Figure 4.23: 20-node C3D20 brick element with full integration. The full circles represent the 27 integration points, in a 3x3x3 scheme [12].

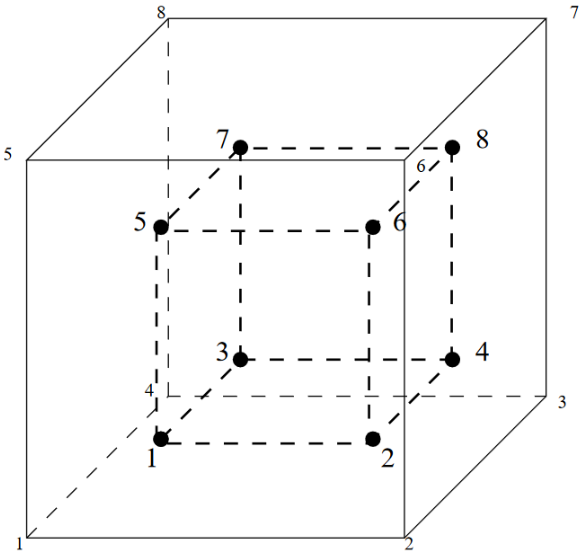

Figure 4.24: 20-node C3D20R brick element with reduced integration. The full circles represent the 8 integration points, in a 2x2x2 scheme [12].

Full integration and reduced integration brick elements have their advantages and disadvantages, depending on the application. According to Dhondt [12], C3D20 brick elements with full integration have a tendency to be too stiff in bending for applications involving thin plates or slender beams. Conversely, Dhondt states that C3D20R reduced integration elements perform well under bending, and that *"if you are setting off for a long journey and you are allowed to take only one element type with you, that's the one to take"* [12]. As a finite element analysis of a wing structure predominantly involves modelling thin plates and slender beam structures under bending loads, the C3D20R brick element with reduced integration is selected for use in this framework. This entails that the augmented mesh shall generate S8R and B32R elements in the input file, for them to be internally expanded to C3D20R elements.

Selecting the right elements is paramount to ensuring reliable results in a finite element analysis. For this reason, a verification study was conducted to ensure the claims of Dhondt on the robustness of the S8R element (and by extension the C3D20R elements, which the B32R elements also expand into) were accurate. The study showed that the use of S8R elements in CalculiX produces very similar results to those obtained through using S8R elements in Abaqus. The same was not true with the use of other linear and quadratic elements, like the S4 and S4R. More information on the verification study may be found in Appendix B.

Mesh generation: Joining meshes

As was previously mentioned, the modelling of each individual wing structure component is conducted independently of the others, meaning no two components share any nodes. The reasoning for this is now explained. Based on the selection of wing structure sizing variables including different values for root and tip thicknesses, tapering of structural components is modelled. CalculiX accommodates tapering through the *NODAL THICKNESS card. This tells the solver at run-time to ignore the single thickness value prescribed to a given set of elements and instead provide each of the elements' nodes with an individual thickness. However, CalculiX does not accommodate for the possibility of two structural components which share the same mesh, requiring a different set of nodal thicknesses. This issue is illustrated in the simple example of Figure 4.25. Here, a horizontal panel which represents the skin shares nodes with a vertical panel which represents a spar web. The horizontal panel is given a single thickness, while the vertical panel is tapered both vertically upwards and axially, into the plane of the page, using the *NODAL THICKNESS card. Because the vertical panel shares nodes with the horizontal one, the horizontal panel inevitably takes on the prescribed nodal thicknesses on those shared nodes. In the case of the wing structure, this would mean the skin, spar caps and spar webs would all have the same thickness along the line of shared nodes.

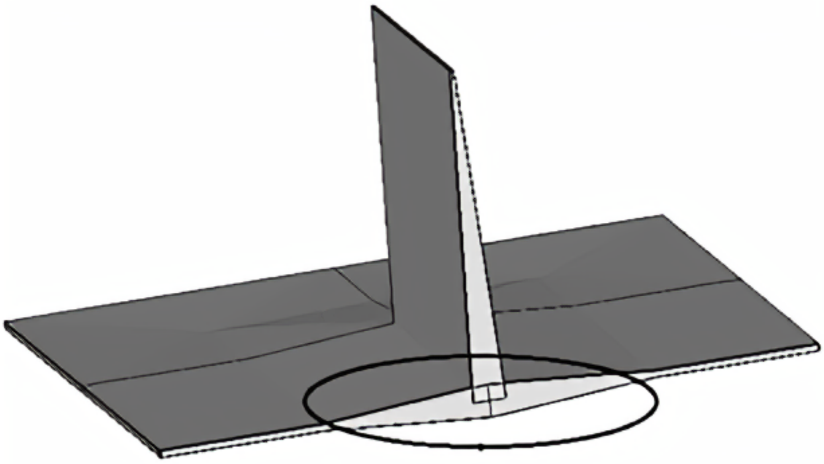

Figure 4.25: An example of orthogonal elements sharing the same nodes, inevitably sharing the same thickness with the application of *NODAL THICKNESS.

This is the reason why each structural component is modelled separately and then joined together using the *TIE card. *TIE applies Multi-Point Constraints (MPCs) between the nodes of the slave surface and the face of the master surface, effectively tying them together. The following tie relationships are employed, with the master of each relationship being listed first:

- Skin - spar caps
- Spar caps - spar web
- Skin - stringers
- Skin - ribs

Hence, the spar caps act as both a slave to the skin and a master to the spar webs. During each run of the wing structure sizer, prior to the tie constraints being activated, the positioning of each component is automatically offset to account for its own thickness and the thickness of the component it is being tied to, such that the two faces are perfectly aligned when the tie constraint is activated during the analysis.

Similarly to the element selection, the tie constraint has be verified against that of Abaqus and shows an acceptable match. Details around the tie constraint verification are provided in Appendix B.

The resulting wing model is given in Figure 4.26, while the internal structure is shown in Figure 4.27.

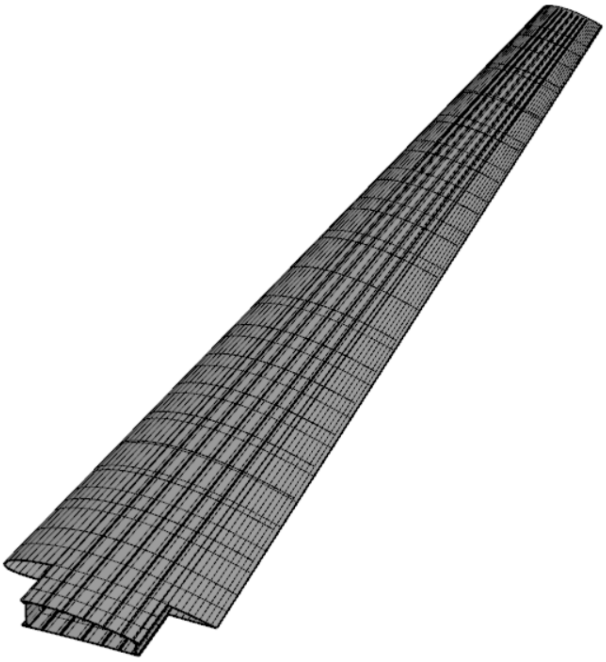

Figure 4.26: The complete FEM of the wing.

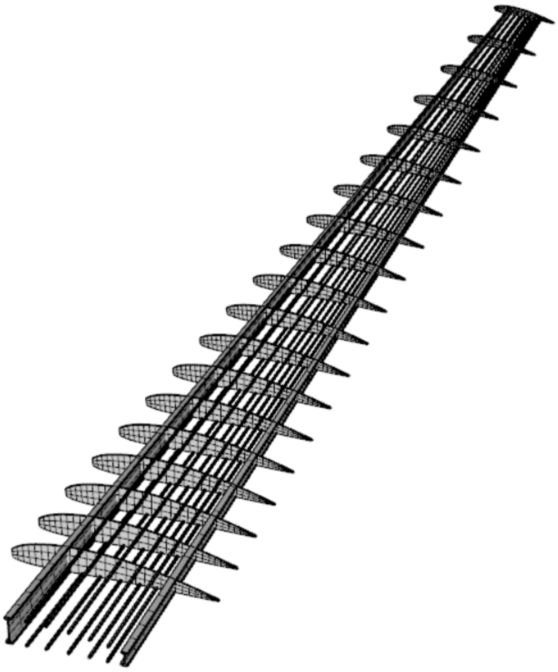

Figure 4.27: The FEM of the wing internal structure.

Boundary conditions

Replicating the boundary conditions of the wing FEM as closely as possible to the true aircraft is paramount to ensuring accuracy of the analysis. One type of boundary condition which is often prescribed in wing-loading finite element models is clamping the wing along the internal root (namely, at the fuselage centerline, or the symmetry plane of the model), which amounts to fixing the translational and rotational degrees of freedom of the wing internal root. However, in reality the wing is connected to the aircraft structure both at its internal root and at the wing-fuselage juncture. Therefore, the boundary conditions are set following the approach of Dorbath et al. [110], who model the wing in a similar fashion to the current author - the portion of the wing which sits outside of the fuselage is modelled in full, while only the wingbox is modelled inside the fuselage. In their study, Dorbath et al. [110] fix the nodes of the wingbox along the symmetry plane in the spanwise direction, while fixing the nodes of the entire wing cross-section at the wing-fuselage junction, in the vertical and flight directions. Following the same approach, the boundary conditions applied in this framework consist of fixing the following degrees of freedom:

- Symmetry plane:
  - Degree of freedom 2 - translation in the span-wise direction
  - Degree of freedom 4 - rotation about the fuselage axis
  - Degree of freedom 6 - rotation about the vertical axis
- Wing-fuselage juncture:
  - Degree of freedom 1 - translation in the flight direction
  - Degree of freedom 3 - translation in the vertical direction
  - Degree of freedom 5 - rotation about the span-wise axis

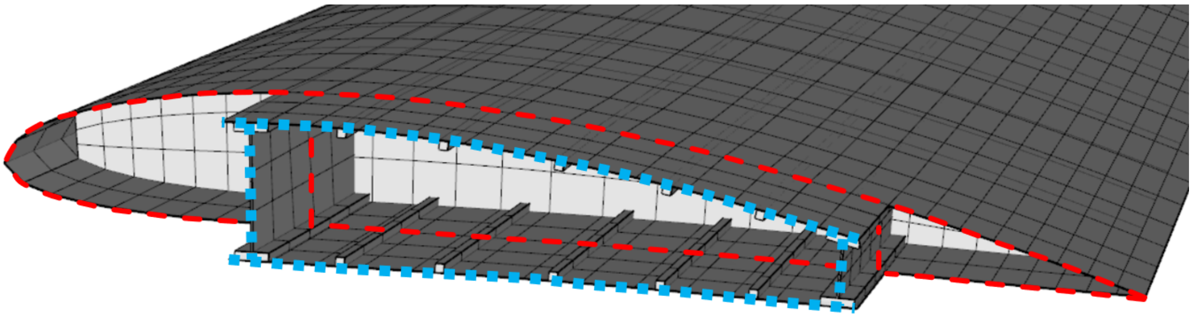

Figure 4.28: The boundary conditions applied to the wing model. The blue contour represents the symmetry plane boundary conditions, while the red contour represents the wing-fuselage juncture boundary conditions.

Applied loads

Three main loads act on the wing of an aircraft during flight. These are the aerodynamic loads generated by the wing, the weight of the wing itself and the weight of the fuel contained in the wing. All three loads have been modelled in this framework, with the fuel weight only applying to the reciprocating engine case. However, it was ultimately decided to not include the fuel weight relief in the case study, so as to size the wing in a more conservative manner. Regardless, all three methods are described here for the sake of completeness.

Aerodynamic loading The aerodynamic loading is fed from the PANAIR panel code of the aerodynamics module in the form of a pressure coefficient C_p distribution. As was described in Section 4.5.2, the C_p distribution at the wing sizing condition is determined by a run of PANAIR using the critical load factor n. The selection of the wing sizing condition, along with its critical load factor n, is done by constructing a V-n diagram. This activity is done manually, prior to the optimisation being executed and is specific to the case study at hand. It is thus outside the scope of the discipline analyses and is instead discussed in Chapter 5: Case Study.

The first step in applying the aerodynamic loading is to dimensionalise the C_p distribution using the dynamic pressure, as per the definition of the C_p in Equation 4.44. The freestream density ρ_∞ and velocity V_∞ are constants which have been determined during the selection of the wing sizing condition using the V-n diagram (see Chapter 5: Case Study for more information).

$$C_p = \frac{p - p_\infty}{\frac{1}{2}\rho_\infty V_\infty^2} \tag{4.44}$$

The dimensionalisation of the C_p distribution results in the distribution of the pressure differential $p - p_\infty$ over the wing. This pressure differential distribution is fed to CalculiX, using the *DLOAD card. *DLOAD is used to specify the application of a distributed pressure load over the mesh. With *DLOAD, CalculiX will multiply the input pressure differential $p - p_\infty$ acting on each element face, by the area of that element, to give a uniform force over the element face, acting perpendicularly.

Wing weight loading The inertia relief induced by the weight of the wing structure itself is accounted for by using an additional *DLOAD card with a GRAV label. CalculiX will load the structure based on the mass of each element and a given acceleration constant, set at $9.81 m/s$ in the negative z direction (acting downwards).

Fuel weight loading The weight of the fuel also induces an inertia relief. This is accounted for as follows: The shell elements on the lower skin surface, between the front and rear spar, and between the aircraft centerline and 75% of the semi-span, are automatically identified in MATLAB, as shown in Figure 4.29. It is assumed that the weight of the fuel acts upon these elements. Next, the total known fuel mass is multiplied by the fraction of each element's area to the total highlighted area. This gives the proportion of the fuel mass which will act upon each element, based on each element's area. The mass of the fuel which acts upon each element is then multiplied by the gravitational acceleration of $9.81 m/s$, to give the weight acting on each element. Finally, each of these weights is divided by the area of the element which they act upon. This gives a uniform pressure loading on each element surface, which acts in the negative z direction. A *DLOAD card is then used to input this pressure distribution into CalculiX. It should be noted that the fuel weight loading is only activated in the case of the reciprocating engine, when the fuel is stored in the wings. In the case study of this research, however, it was decided to deactivate the fuel weight loading for all cases, in order to size the wing in a more conservative manner. Further information on this is provided in Chapter 5.

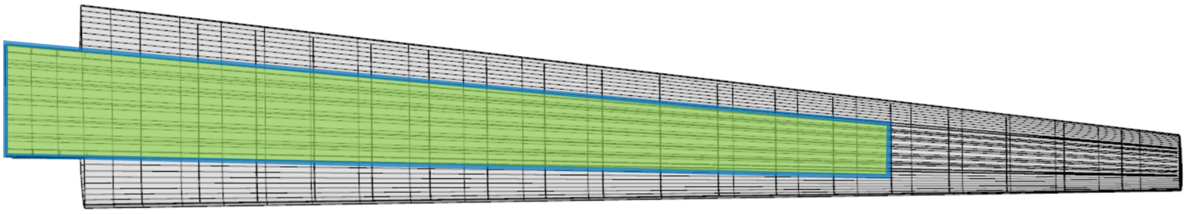

Figure 4.29: A highlighting of the lower surface shell elements between the front and rear spar, and between the aircraft centerline and 75% semi-span, where the distributed fuel loading is applied.

Material selection

The material modelled in the FEA has been selected as aluminium 2024-T3. Aluminium 2024-T3 is one of the primary materials used in airframe structures and is found extensively in the wings and fuselage [111]. The material properties of aluminium 2024-T3 are provided in Table 4.4. Unfortunately, it is not possible to model composite materials such as Carbon Fibre Reinforced Polymers (CFRP) in the current framework. This is because CalculiX has a limited implementation of anisotropic materials. The main limitation for the current framework is the fact that the *TIE function is only applicable to isotropic materials. As was previously explained, the *TIE function is what allows the structural components to be sized and is thus a key requirement of the framework. This lack of composite material modelling is considered a weakness of the current study. As a future recommendation, in order to model composite materials within the framework, a new update of CalculiX may be used to replace the current version (version 2.14). Alternatively, should the anisotropic material implementation not be expanded in future updates of CalculiX, replacing CalculiX with a more complete FEA package is recommended.

Table 4.4: Material properties of aluminium 2024-T3 [25] [26]

Young's Modulus [GPa]	Poisson's Ratio [-]	Density [kg/m3]	Yield Strength [MPa]
73.1	0.33	2770	360

Finite element analysis & structural integrity constraints

With the mesh complete, the boundary conditions set and the loads ready to be applied, the finite element analysis is executed. Two types of analyses are incorporated into the framework: A static analysis, by calling the *STATIC card, and a linear buckling analysis, by calling the *BUCKLE card. The static analysis provides the displacements and stresses at the nodes as outputs. These stresses are then input into the Kreisselmeier-Steinhauser stress-aggregation function, discussed in the next paragraph, to determine an aggregated stress constraint. The buckling analysis does the same as the static analysis but also provides the buckling load factor. The BLF is the scalar the applied load would need to be multiplied with, in order for the buckling load to occur. Hence, a $BLF >= 1$ signifies that no buckling has occurred, written in the form of a constraint as:

$$1 - BLF \leq 0 \tag{4.45}$$

As was also mentioned in Section 4.2.2, the Kreisselmeier-Steinhauser function is required in order to aggregate the stress constraints. The KS function was originally introduced by Kreisselmeier and Steinhauser [112] and contains an aggregation parameter ρ, set at $\rho = 50$, as recommended by Martins and Poon [85]. This stress constraint aggregation is necessary, as without it the framework would require that the stress at each node in the FEM does not exceed the set stress limit σ_{limit}. With the FEM containing a very large number of nodes, imposing the equivalent number of constraints on the optimiser would be infeasible. For this reason, these stresses are all aggregated into a single constraint, denoted here as the 'KS constraint' and given by Equation 4.46 [85].

$$KS(g_j(\vec{x})) = g_{max}(\vec{x}) + \frac{1}{\rho}\ln\left[\sum_{j}^{n_g} e^{\rho(g_j(\vec{x})-g_{max}(\vec{x}))}\right] \leq 0 \tag{4.46}$$

where:

$$g_j = \frac{\sigma_j(\vec{x})}{\sigma_{limit}} - 1 \tag{4.47}$$

for every FEM node j. Here, $\vec{x}$ denotes the wing structure sizing design variables. σ_{limit} is the limit stress imposed by the user. This has been selected as the aluminium 2024-T3 yield stress, divided by a safety factor of 1.33. This 33% stress buffer has been favoured over the more conventional 50%, as a conservative and fictitious critical load case has already been selected through the use of the V-n diagram, as explained in Chapter 5. Coupled with the fact that the aircraft is unmanned and not adherent to stringent safety regulations for manned aircraft, a safety factor of 1.33 was deemed more appropriate.

Lastly, with the two structural integrity constraint values determined, the final output of the FEA is the wing structure mass. This is determined from the total material volume output by CalculiX, multiplied by the material density of Table 4.4.

Secondary wing weight

The weight output by CalculiX is the weight of the primary, load-bearing structure, along with the leading and trailing edges. To determine the total wing weight, the secondary wing weight must be added to this. The secondary wing weight includes the weight of high lift devices, hydraulics and controls. Secondary wing weight is often derived through empirical relations. Many of the available relations, such as those presented by Torenbeek [113], apply only to large transport aircraft. Howe [114] provides one of the few empirical relations which are applicable to general aviation aircraft. The secondary wing weight for a single-engine, general aviation aircraft with $MTOW \leq 5,700kg$ may be estimated by means of Equation 4.48 [114]. As a sanity check on the applicability of the relation, taking the baseline Predator UAV with $W_{MTOW} = 745kg$ results in an estimated $W_{w,sec} = 18.6kg$. Considering the FEA results in a primary structure in the range of $90 - 100kg$ during trial runs of the current study, the secondary wing weight accounts for about 17% of the total wing weight. Considering also that the secondary wing weight is typically around 25-30% of the total wing weight, as stated by Torenbeek [113] for large aircraft, the relation is deemed acceptable.

$$W_{w,sec} = 0.025 \cdot W_{MTOW} \tag{4.48}$$

4.7.3. Fuselage

The fuselage weight is estimated by taking the average of two regression methods, those of Gundlach [27] and Zhang & Wang [115] given in Equations 4.49 and 4.50 respectively. The relation of Equation 4.49 is derived from a curve fit of 197 fuselages, most of which were sailplanes, rendering the relation appropriate for the current application. The relation of Equation 4.50 estimates the fuselage weight for the HALE class of UAVs, which are similar in size to the MALE UAV class considered in the current study.

$$W_{fus} = 0.5257 \cdot F_{mg} \cdot F_{ng} \cdot F_{press} \cdot F_{vt} \cdot F_{mat} \cdot l^{0.3796} \cdot (W_{carried} \cdot n)^{0.4863} \cdot V_{EqMax}^{2} \quad [\mathrm{lb}] \tag{4.49}$$

$$W_{fus} = 0.0025 \cdot K_{inlet}^{1.42} \cdot q^{0.283} \cdot W_{MTOW}^{0.95} \cdot \left(\frac{l}{d}\right)^{0.71} \quad [\mathrm{kg}] \tag{4.50}$$

For Equation 4.49, the factor definitions are provided in Table 4.5, while l is the fuselage length in feet, $W_{carried}$ represents the weight of the components located inside the fuselage in pounds, n is the load factor and V_{EqMax} is the maximum equivalent airspeed in knots. For Equation 4.50, K_{inlet} is the air intake pattern parameter (nose intake: $K_{inlet} = 1.0$, abdomen intake: $K_{inlet} = 1.05$, back intake: $K_{inlet} = 1.2$, both sides intake: $K_{inlet} = 1.3$), q is the dynamic pressure in pascals and $\frac{l}{d}$ is the fineness ratio.

Table 4.5: Factors for fuselage weight estimation relation of Gundlach [27]

Factor	Definition	Value
F_{mg}	Main gear on the fuselage factor	1 if no main gear on fuselage 1.07 if main gear on fuselage
F_{ng}	Nose gear on the fuselage factor	1 if no nose gear on fuselage 1.04 if nose gear on fuselage
F_{press}	Pressurized fuselage factor	1 if unpressurized 1.08 if pressurized
F_{vt}	Vertical tail inclusion factor	1 if vertical tail weight not included 1.1 if vertical tail weight included
F_{mat}	Material factor	1 if carbon fiber 2 if fiberglass 1 if metal 2.187 if wood 2 if unknown

4.7.4. Empennage

Similarly to the fuselage, the empennage weight is derived from the relations of Gundlach [27] and Zhang & Wang [115] and averaged.

$$W_{emp} = \frac{1}{6} \cdot F_{emp} \cdot F_{cont} \cdot S_{tail} \cdot t_{min} \cdot \rho_{mat} \quad [\mathrm{lb}] \tag{4.51}$$

$$W_{emp} = 0.022 \cdot \left(W_{MTOW}^{0.813} \cdot n^{0.813} \cdot S_{tail}^{0.584} \cdot \left(\frac{b_{tail}}{c_{r,t}}\right)^{0.033} \cdot \left(\frac{mac}{l_{tail}}\right)\right) \quad [\mathrm{kg}] \tag{4.52}$$

where F_{emp} is the empennage multiplication factor (given as 1.3 by [27]), F_{cont} is the factor accounting for control surfaces (given as 1.2 by [27]), S_{tail} is the reference area of the tail in question in square feet, t_{min} is the minimum gauge thickness in inches and ρ_{mat} is the material density in pounds per cubic foot. Moreover, b_{tail}, $c_{r,t}$, mac and l_{tail} are the span, root chord length, mean aerodynamic chord length and moment arm length respectively, all in meters, for the tail in question.

4.7.5. Landing gear

The final component of the structural weight, the landing gear weight, is also determined from the average of the weight relations given by Gundlach [27] and Zhang & Wang [115].

$$W_{lg} = F_{lg} \cdot W_{MTOW} \quad [\text{lb}] \tag{4.53}$$

$$W_{\text{lg}} = 0.165 \cdot W_{MTOW}^{0.84} \quad [\text{kg}] \tag{4.54}$$

F_{lg} represents the landing-gear mass fraction, which is given as 0.04 for aircraft that take off and land on paved runways [27].

4.7.6. Engine/Motor

The weight calculation methods of the engine, motor, fuel cells, batteries and electronic speed controller are detailed in Section 4.8.

4.7.7. Propeller

The General Dynamics propeller weight estimation method given by Roskam [116] and also used by Gundlach [27] is used in this study and given by Equation 4.55.

$$W_p = K_{shp} \cdot N_p \cdot N_b^{0.391} \cdot \left(\frac{D_p \cdot P_{peak}}{1000 \cdot N_p} \right)^{0.782} \quad [\text{lb}] \tag{4.55}$$

Here, K_{shp} is a multiplication factor based on the system's shaft horsepower ($K_{shp} = 24.0$ for turboprops with $P_{shaft} > 1,500shp$, $K_{shp} = 31.92$ for engines with $1,500shp > P_{shaft} > 50shp$, $K_{shp} = 15$ for engines with $P_{shaft} < 50shp$). N_p is the number of propellers, N_b the number of blades, D_p the propeller diameter in feet and P_{peak} the peak power in horsepower.

4.7.8. Air induction

The air induction system refers to the inlets present on the aircraft for feeding air to a reciprocating engine or fuel cell system, or to provide cooling. These are typically very small on a MALE UAV and their weight may be estimated using Equation 4.56 [27] .

$$W_{ai} = F_{ai} \cdot P_{peak} \quad [\text{lb}] \tag{4.56}$$

Values of F_{ai} for reciprocating engines are in the range of 0.08-0.24 [27]. Here, the average value of 0.16 is taken. For electric motors, values range between 0.04-0.07. Here, 0.07 is taken for the hydrogen fuel cell case, while 0.04 is taken for the battery-powered case, due to batteries not requiring air for energy conversion, only for cooling.

4.7.9. Fuel systems

For reciprocating engines, the fuel system weight includes the weight of the fuel tank, fuel lines, pumps, valves and venting. These weights may be estimated using Equation 4.57 [27].

$$W_{fuel,sys} = F_{fs} \cdot W_f^{E1} \quad [\text{lb}] \tag{4.57}$$

For a single-engine MALE UAV, $F_{fs} = 0.692$ and $E1 = 0.67$ [27].

For the fuel cell-powered electric motor case, the hydrogen fuel tank system weight is calculated separately and is discussed in Section 4.8.3.

4.7.10. Propulsion System Weight of Balance

Reciprocating engines have additional auxiliary weights that need to be accounted for, such as engine controls, oil systems and engine starters. These are captured for MALE UAVs by Equation 4.58 [27], solely for the reciprocating engine case of the current study.

$$W_{prop,sys} = F_{prop,sys} \cdot W_{engine} \quad [\text{lb}] \tag{4.58}$$

with $F_{prop,sys}$ ranging from 0.08 to 0.35 [27]. The average value of 0.215 is taken in this work.

4.7.11. Avionics and systems

Aircraft systems including avionics, instrumentation and communications are accounted for using Equation 4.59 [103].

$$W_{av} = 0.052 \cdot W_{MTOW}^{0.843} \quad [\text{lb}] \tag{4.59}$$

4.7.12. Autopilot

Empirical relations are not an adequate method for estimating the weight of autopilot systems, as their weight depends heavily on the specific UAV size in question [27]. Typical autopilot weights specific to the UAV category under consideration are used directly. For MALE UAVs, Gundlach provides a typical range of $10 - 50lb$. Here, $10lb$ is taken as the autopilot weight, in line with Verstraete [13].

4.7.13. Electrical systems

The electrical systems include power distribution units, converters and rectifiers. Their weight may be estimated by means of Equation 4.60 [27].

$$W_{elec} = 0.003 \cdot \left(P_{PL} + \frac{P_{av}}{W_{av}} \cdot W_{av}\right)^{0.8} \cdot \left(l_{fus} + b\right)^{0.7} \quad [\text{lb}] \tag{4.60}$$

Here, P_{PL} is the power required by the payload, which is a mission constant in the MDO. $\frac{P_{av}}{W_{av}}$ is the power-to-weight ratio of the avionics systems, which typically has a value of $15W/lb$ [27].

4.7.14. Wiring harnesses

The use of systems like avionics, autopilots and any other electrical systems inherently involve the use of wiring and connectors. This weight contribution may be estimated as a fraction of the system weights, using Equation 4.61 [27], where f_{wire} is taken as 0.1.

$$W_{wire} = f_{wire} \cdot (W_{av} + W_{auto} + W_{elec}) \quad [\text{lb}] \tag{4.61}$$

4.8. Propulsion

The purpose of the propulsion module within this framework is to size and model the performance of the three propulsion system types under consideration. As highlighted in Section 4.2.3, the propulsion module is divided into two parts. The first is run prior to the mission analysis, in order to size the propulsion system components, using the power-related coupling variables. The second part forms the mission analysis, together with the propeller and performance modules. More specifically, the propulsion module is called by the performance module at every discretised mission segment, to match the propeller with the engine/motor and determine the energy resource requirements and power requirements. The propulsion module takes as inputs the mission segment propeller performance (efficiency, rotational speed and torque), while its main outputs are: a) the fuel flow $\dot{m}_f$ in the cases of the reciprocating engine and fuel cell and electric current I in the case of the battery-powered electric propulsion model and b) the engine/motor power P for all cases and additionally the fuel cell power P_{FC} for the fuel cell case.

The propulsion models take the form of a 'rubber engine', where a combination of data from real engines/motors, fuel cells and batteries together with analytical expressions and empirical relations are used to scale propulsion components as required. These propulsion models are mainly based on the work of Verstraete [13], who provided the current author with his MATLAB scripts, which the propulsion scripts of the current framework are based on. The methods of the reciprocating engine, hydrogen fuel cell and electric battery models are discussed in detail below.

4.8.1. Reciprocating engine model

The two parts of the reciprocating engine model are as follows: First, the peak power operating parameters are determined, in order to size the engine for a given peak power P_p coupling variable input. This step is executed prior to initiating the mission analysis. The second part of the model is within the mission analysis, where the normalised engine maps are scaled according to the peak power parameters evaluated in the first part. This allows the off-peak performance parameters requested by the performance module to be calculated for each mission segment.

Sizing - Peak power condition

Engine sizing and performance map scaling is based on a regression analysis of 484 reciprocating engines conducted by Verstraete [13] using the scaling methods of Menon and Cadou [117]. The regression analysis includes 294 two-stroke engines and 194 four-stroke engines of sizes ranging from those in the small, UAV-enthusiast market to those in general aviation aircraft. MALE UAVs, being in the weight category of the latter, typically employ four-stroke reciprocating engines and thus only four-stroke engine relations are used in the current study.

In order to size the engine and scale its performance maps, the physical and performance parameters required from the regression analysis include:

- Mass
- Dimensions
- Peak power RPM
- Peak power torque
- Peak power efficiency

To determine these, the sole input parameter of the regression analysis is the engine peak power. Peak power is one of the coupling design variables of the MDO, due to the fact that it is both an input required by the propulsion module but also an output of the performance module, which creates a loop dependency. Within the performance module, peak power is related to the five parameters of interest by first relating it to engine displacement, which is shown to correlate well with both physical and performance parameters [117]. Peak power correlates to displacement by means of a power law regression of the form [13]:

$$V_d = a \cdot P_{peak}^b \tag{4.62}$$

with V_d being the engine displacement, P_{peak} being the peak power and a and b being the regression coefficients, taking the values of:

$$\begin{aligned} a &= 11.8987 \\ b &= 1.2242 \end{aligned} \tag{4.63}$$

for four-stroke engines [13]. Figure 4.30 provides the results of the analysis, showing a good fit for the four-stroke case, particularly for larger engines in the $50kW - 300kW$ range where MALE UAVs typically operate. The goodness of fit is provided by Verstraete as 0.9847, with a relative uncertainty of 5.2%, confirming a good correlation.

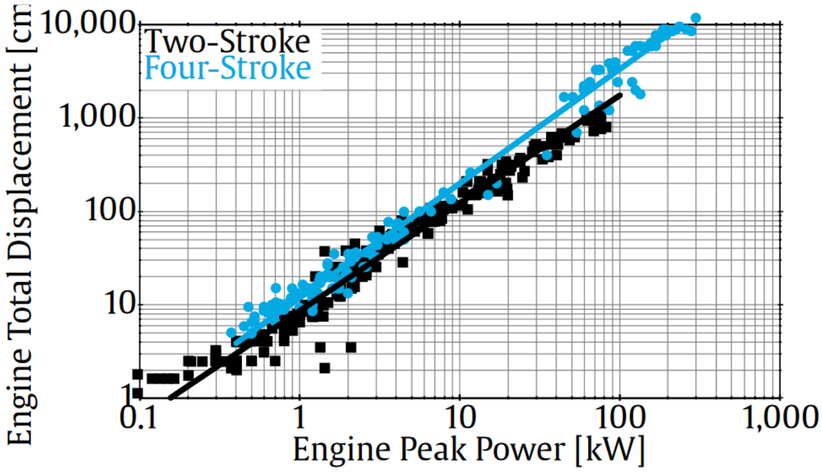

Figure 4.30: Peak power against engine displacement for 294 two-stroke engines and 194 four-stroke engines [13].

Once the engine displacement is determined from the peak power, it is used to determine values of the five parameters of interest. Through the same regression analysis, the engine mass, peak power RPM, peak power torque and peak power efficiency relate to the engine displacement through Equations 4.64 to 4.67, with the coefficients provided in Table 4.6 and the regression results shown in Figures 4.31 to 4.34 [13].

$$m_e = a \cdot V_d^b \tag{4.64}$$

$$RPM_{peak} = a \cdot V_d^b \tag{4.65}$$

$$Q_{peak} = a \cdot V_d^b \tag{4.66}$$

$$\eta_{peak} = \frac{a \cdot V_d^b}{100} \tag{4.67}$$

The remaining engine sizing parameters are the engine dimensions of length l_e, width w_e and height h_e, which relate directly to peak power through Equations 4.68 to 4.70, as were provided in the MATLAB scripts for the study of Verstraete [13].

$$l_e = 1.56 \cdot \left(\frac{P_{peak}}{745.7}\right)^{0.15} \quad [\text{ft}] \tag{4.68}$$

Table 4.6: Power law coefficients, goodness of fit values and relative uncertainty percentages for correlations of engine displacement to engine mass, peak power RPM, peak power torque and peak power efficiency [13].

	a	b	R^2	Rel. Unc.
m_e	0.0532	0.9126	0.9893	3.5%
RPM_{peak}	19175	-0.2217	0.9349	7.6%
Q_{peak}	0.0643	1.0355	0.9956	3.6%
η_{peak}	16.14	0.08	Not available	Not available

$$w_e = 1.5 \cdot \left(\frac{1.5}{200} + 0.00134\right) \cdot \frac{P_{peak}}{745.7} \quad [\text{ft}] \tag{4.69}$$

$$h_e = 1.5 \cdot \left(\frac{1.7}{200} + 0.00156\right) \cdot \frac{P_{peak}}{745.7} \quad [\text{ft}] \tag{4.70}$$

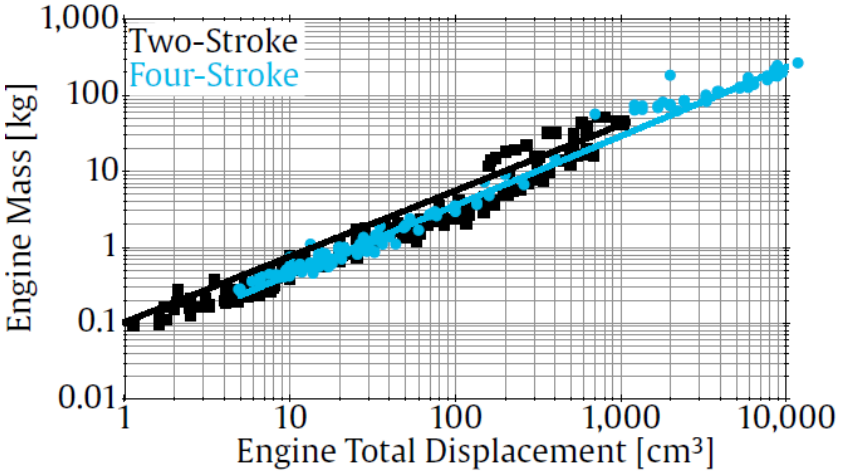

Figure 4.31: Engine displacement against engine mass for 294 two-stroke engines and 194 four-stroke engines [13].

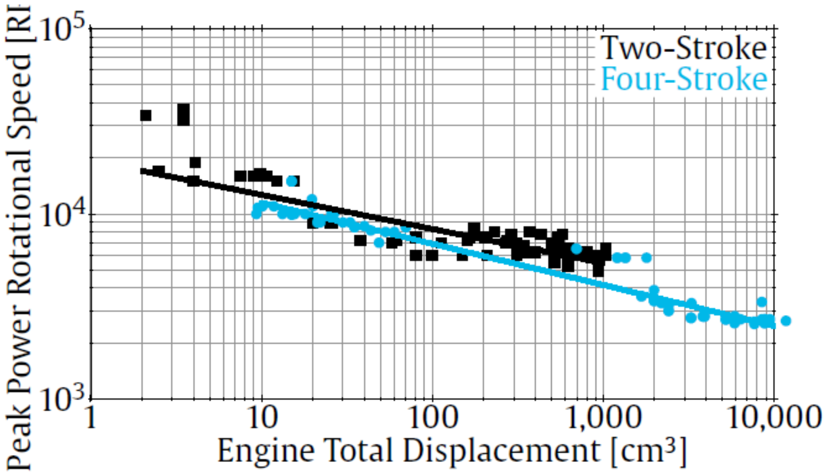

Figure 4.32: Engine displacement against peak power RPM for 294 two-stroke engines and 194 four-stroke engines [13].

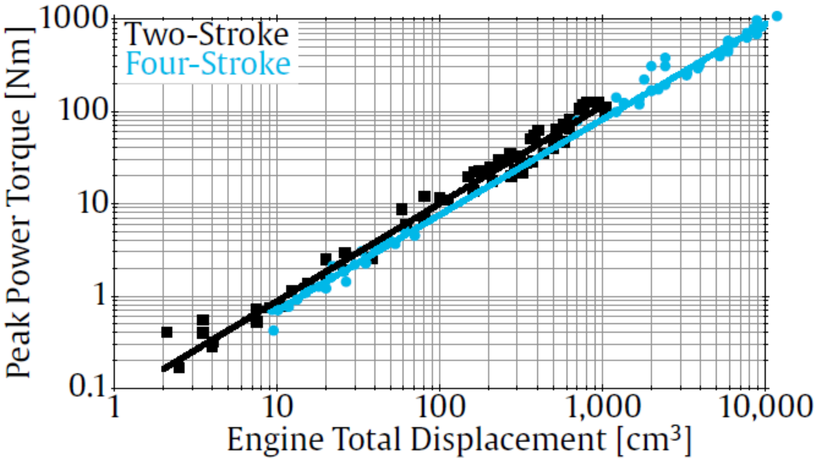

Figure 4.33: Engine displacement against peak power torque for 294 two-stroke engines and 194 four-stroke engines [13].

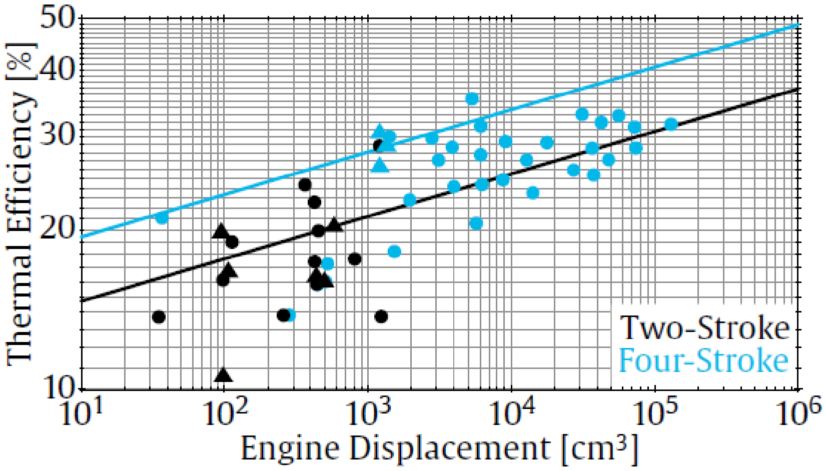

Figure 4.34: Engine displacement against peak power efficiency for 294 two-stroke engines and 194 four-stroke engines [13].

Mission performance - Off-peak condition

With the physical and performance parameters of the engine sized for the peak power condition, the second part of the reciprocating engine model involves using these peak power parameters to scale engine performance maps, in order to calculate the off-peak engine performance for each mission segment. A normalised performance map has been generated by Verstraete [13], based on a $95kW$ four-stroke engine taken from Wipke et al. [118]. The normalised performance map has then been fitted with an analytical expression of the form:

$$\eta = a_0 + a_1 x + a_2 y + a_3 xy + a_4 x^2 + a_5 y^2 + a_6 x^2 y + a_7 x \ln(x) + a_8 y \ln(y) + a_9 \ln(x) + a_{10} \ln(y) \quad (4.71)$$

with the coefficients listed in Table 4.7. This results in a normalised analytical function for engine efficiency, shown in Figure 4.35. The analytical nature of the normalised efficiency map is particularly advantageous within a gradient-based MDO framework, due to the smoothness of the function.

Table 4.7: Coefficients of the normalised engine map analytical expression fit [13].

$a0$	$a1$	$a2$	$a3$	$a4$	$a5$	$a6$	$a7$	$a8$	$a9$	$a10$
0.6824	0.7170	0.8585	-0.6433	1.2580	-2.4920	0.5358	-3.6600	3.0480	-0.4510	0.7318

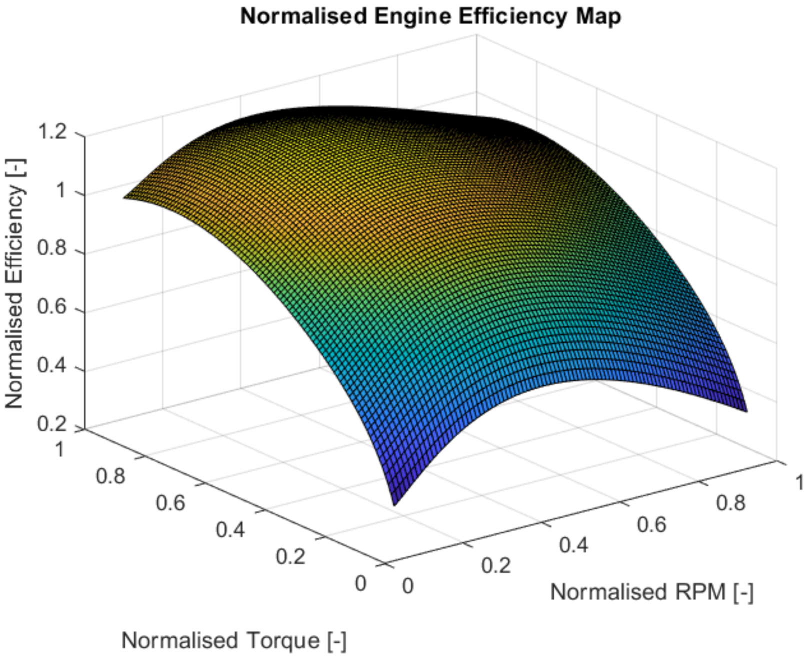

Figure 4.35: Regression-fit normalised engine efficiency map, using the coefficients of Table 4.7.

During the mission analysis, for a given mission segment, the propulsion module will scale the normalised efficiency map by the peak power performance parameters, to give the baseline scaled engine map. The engine map is then further scaled, to account for altitude effects relating to a reduced air density. Power is scaled for altitude using the Gagg-Farrar altitude drop-off factor of Equation 4.72 [13] [119], while efficiency is scaled using Equation 4.73 [13] [120].

$$\phi = \frac{\sigma - C}{1 - C} \tag{4.72}$$

$$F = \frac{\sigma \cdot (1 - D)}{(\sigma^{E} - D)} \tag{4.73}$$

where σ is the ratio of air density at altitude to that at sea level, the engine-specific parameter C is taken as 0.12, in line with Verstraete [13], $D = 0.065$ and $E = 1.117$ [13] [120].

Finally, the fuel flow $\dot{m}_f$ - the first output of the propulsion module in the reciprocating engine case - is given by:

$$\dot{m}_f = \frac{P}{\eta \cdot LHV} \tag{4.74}$$

with LHV being the lower heating value of avgas, taken as $43.7 MJ/kg$. P, the engine power required for the given segment, is the second output of the propulsion module and is derived from the rotational speed, torque and Gagg-Farrar altitude factor.

4.8.2. Electric motor model

An electric motor converts electrical energy to mechanical shaft energy and its modelling is thus required for both the hydrogen fuel cell and battery cases. It is an intermediate step towards the determination of the propulsion module output of fuel flow or electric current, as the electric motor efficiency is required by the fuel cell and battery models. In a similar fashion to the reciprocating engine case, Verstraete [13] uses a regression analysis to determine key performance characteristics of electric motors, with the exact methods detailed in the work of MacNeill and Verstraete [121]. However, the study is geared towards smaller tactical UAVs. Their regression analysis is based on data from 1,743 DC electric motors in the power range of approximately $30W$ to $30kW$, with the majority of data points below the $10kW$ mark. MALE UAVs operate at much higher power points, typical near the $100kW$ mark. It was therefore decided to diverge from the method employed by Verstraete [13] and incorporate electric motor methods which are more suitable for higher power ranges.

Sizing

As a result of the regression analysis of MacNeill and Verstraete [121] not being applicable to the MALE UAV power range, the weight of the electric motor is estimated through a constant power-to-weight ratio of $5kW/kg$, taken as the average from a number of state-of-the-art large electric motors for aerospace applications (MagniX magni250, $4kW/kg$ [122], Siemens SP260D-0, $5.2kW/kg$ [123], Siemens SP260D-A, $5.9kW/kg$ [123]). The weight of the electronic speed controller (ESC) is also based on a weight-to-power ratio, taken as $0.04kg/kW$ from Verstraete [13], cited originally from [27] [124].

The motor dimensions of diameter d_m and length l_m are modelled as a function of the motor mass W_m by Equations 4.75 and 4.76, as given in the unpublished report [15] of the preceding study [13].

$$d_m = 68.81 \cdot \sqrt[3]{W_m} \tag{4.75}$$

$$l_m = 80.68 \cdot \sqrt[3]{W_m} \tag{4.76}$$

Mission performance

The electric motor performance model of the current framework is based on the work of McDonald [14]. Here, McDonald takes the electric motor efficiency model of Larminie and Lowry [125], given by Equation 4.77, and rather than determining the loss coefficients C_i experimentally, as Larminie and Lowry suggest, expresses them in terms of the peak efficiency $\hat{\eta}$ and the corresponding torque $\hat{Q}$ and rotational speed $\hat{\omega}$ at peak efficiency. These expressions are given in Equations 4.79 to 4.82.

$$\eta = \frac{\omega Q}{\omega Q + P_L} \tag{4.77}$$

$$P_L = C_0 + C_1\omega + C_2\omega^3 + C_3Q^2 \tag{4.78}$$

$$C_0 = k_0 \frac{\hat{\omega}\hat{Q}}{6}\frac{1-\hat{\eta}}{\hat{\eta}} \tag{4.79}$$

$$C_1 = \frac{-3C_0}{2\hat{\omega}} + \frac{\hat{Q}(1-\hat{\eta})}{4\hat{\eta}} \tag{4.80}$$

$$C_2 = \frac{C_0}{2\hat{\omega}^3} + \frac{\hat{Q}(1-\hat{\eta})}{4\hat{\eta}\hat{\omega}^2} \tag{4.81}$$

$$C_3 = \frac{\hat{\omega}(1-\hat{\eta})}{2\hat{Q}\hat{\eta}} \tag{4.82}$$

Here, k_0 is defined as the parasite loss ratio, which takes a value of $0 < k_0 < 1$ [14]. A normalised parametric electric motor model is fully describable with the four parameters of $\hat{\eta}$, $\hat{Q}$, $\hat{\omega}$, k_0, while a scaled parametric model requires three additional parameters, namely the ratio of maximum torque to torque at peak efficiency, k_Q, the ratio of maximum rotational speed to rotational speed at peak efficiency, k_ω and the ratio of maximum power to power at peak efficiency, k_P.

In the current framework, peak motor efficiency $\hat{\eta}$ is set at 94%, which aligns with the peak efficiency of state-of-the-art electric motors for aerospace applications (MagniX magni250, 93% [122], UQM PowerPhase 125, 94% [126], Siemens SP260D-0 & SP260D-A, 95% [123]). $\hat{Q}$ and $\hat{\omega}$ are set by the propeller discipline as the torque and rotational speed at the design point - the loiter phase - during each optimisation iteration. k_Q is set at 3 and k_ω at 1.75, both values selected by trial and error to provide an electric motor map which is in the torque and speed range of similarly-sized motors. k_P is set during each optimisation iteration by the peak power. k_0 is taken as 0.5, the intermediate value of its range $0 < k_0 < 1$, as no further guidance is provided by McDonald [14] on its selection.

Figure 4.36 gives an example of a parametric electric motor map (smooth contours) from McDonald [14], modelled after and overlaid on the actual performance map of the $125kW$ UQM PowerPhase 125 motor (non-smooth contours). The contour values represent the efficiency at a given torque and speed combination. The parametric model matches well with the PowerPhase 125 performance map, validating McDonald's method. Figure 4.37 provides an example motor map as implemented in the current framework, for the Predator UAV case study. A loop of the discipline analyses was run and the resulting motor performance points are shown on the map for each mission segment. In this example, the in-flight mission phases have been discretised into four segments each. A clear path is discernible from the high-RPM, high-torque take-off, to a decreasing torque requirement as the aircraft climbs, to the near-peak efficiency at the loiter points and finally a low-RPM, low torque condition for the landing phase.

The efficiency of the Electronic Speed Controller (ESC) is modelled following the method used by Verstraete in the preceding study [13], but detailed in the unpublished report [15], which was originally cited from [127]. Here, the full-throttle efficiency of the ESC is given by [15] [127]:

$$\eta_{ESC,FT} = \frac{P_{out}}{P_{in}} = \frac{V - R \cdot I}{V} \tag{4.83}$$

V is the voltage coming into the ESC from the battery/fuel cell, I is the current across the ESC and R is the ESC resistance. The part-load efficiency is modelled as a reduction to the full-throttle efficiency by [15] [127]:

$$\eta_{ESC,PT} = \eta_{ESC,FT} - \frac{PTF}{V}(1 - PS) \tag{4.84}$$

Here, PS is the power setting at a given mission segment, expressed as a fraction of the full throttle. The part throttle factor PTF is taken as 210 [15] [127]. The electric motor and ESC efficiencies are multiplied to obtain the effective electric motor efficiency, which is the output of the electric motor model. To determine the output of the propulsion module - the fuel flow in the case of the fuel cell and the electric current in the case of the battery - the electric motor efficiency is fed through to the subsequent fuel cell and battery models.

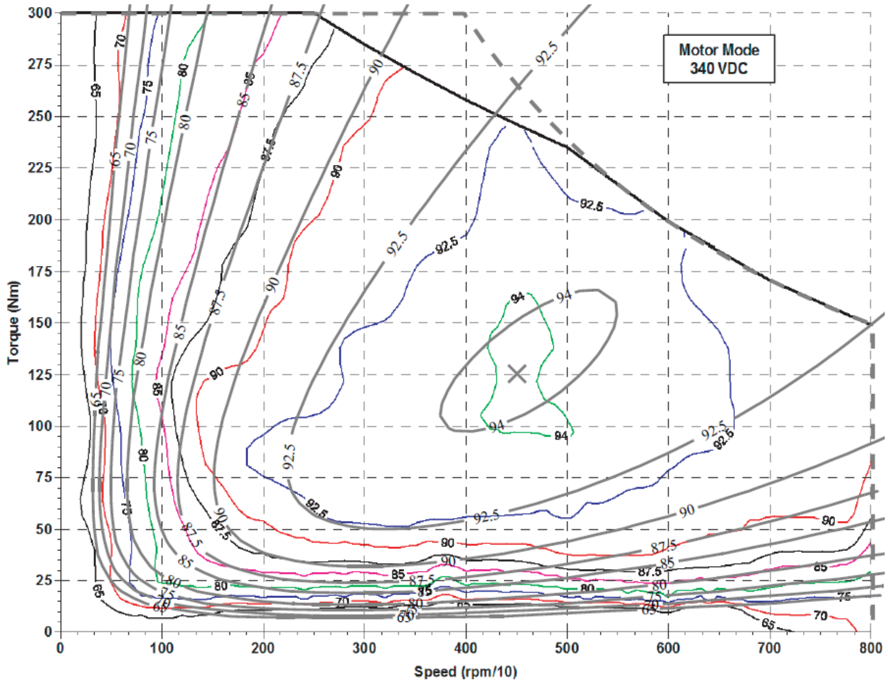

Figure 4.36: A parametric electric motor map of the UQM PowerPhase 125 motor, overlaid on its actual performance map - smooth contours represent the parametric model efficiency, while non-smooth contours are the actual performance map efficiencies [14].

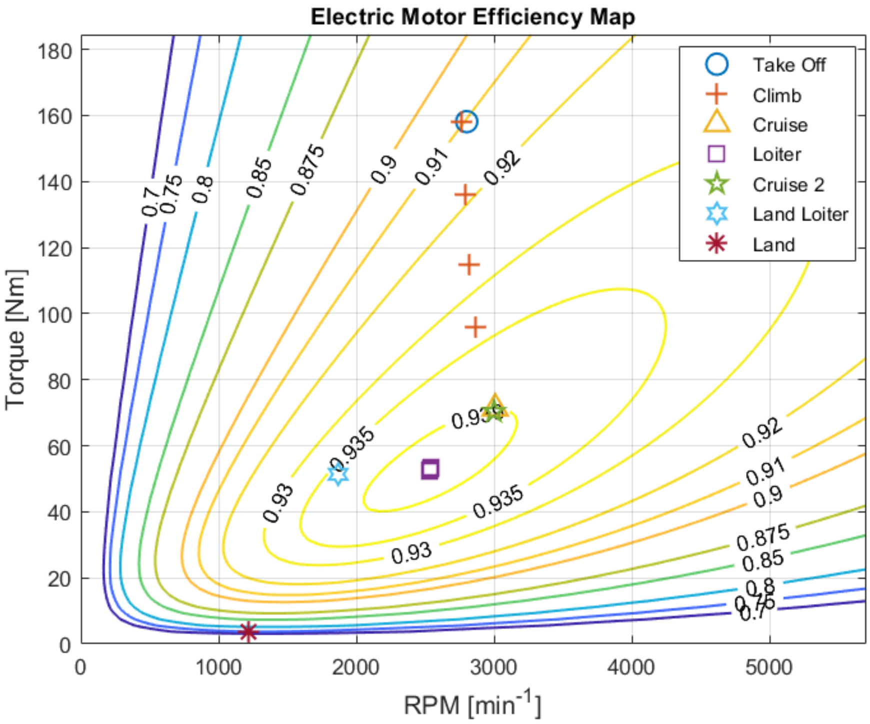

Figure 4.37: An example parametric electric motor map modelled for the Predator UAV, using the method of McDonald [14]. Mission segment performance points are shown, with the main mission phases discretised into 4 segments each.

4.8.3. Hydrogen fuel cell model

The purpose of the fuel cell model is to size the fuel cell prior to the mission analysis and determine its fuel flow during the mission analysis. Additionally, as hydrogen requires more complicated storage than traditional hydrocarbon fuels, the mass and dimensions of the storage solution are also determined.

As was discussed in Section 2.2.2, various types of fuel cells exist, such as alkaline fuel cells (AFC), proton exchange membrane fuel cells (PEMFC) and solid oxide fuel cells (SOFC). With PEMFCs being the most promising fuel cell solution for vehicular applications due to their high efficiency, high power density and low temperature of operation [52], they are modelled in this study.

Sizing

The fuel cell mass is determined by means of a specific power value. This is taken as $2.5kW/kg$, based on a $90kW$ fuel cell with a power density of $3.7W/cm^3$ [13]. The fuel cell dimensions are determined by first calculating the number of cells in the stack, by means of a linear scaling of peak power. Verstraete [13] uses fuel cell data for fuel cells ranging from $5kW$ to $180kW$ to derive the following relationship:

$$n = 3 \cdot P_{peak} \tag{4.85}$$

Through this, the stack height may be determined [13]:

$$h_{fc} = 0.857 \cdot (n - 75) + 0.25 \tag{4.86}$$

while the area is set as a function of peak power, in order to obtain the power density of $3.7W/cm^3$ [13].

Mission performance

The fuel cell efficiency is modelled as a function of two variables - the applied load and the fuel cell size. Curves of efficiency against normalised power are presented in Figure 4.38, for peak power levels between $10kW$ and $150kW$ [13] [128]. Larger fuel cells display higher efficiencies for loads below 70% peak load, while smaller fuel cells show higher efficiencies above the 70% peak power mark. In the current framework, the variation of efficiency with size is accounted for by interpolating between the four curves, for a given load.

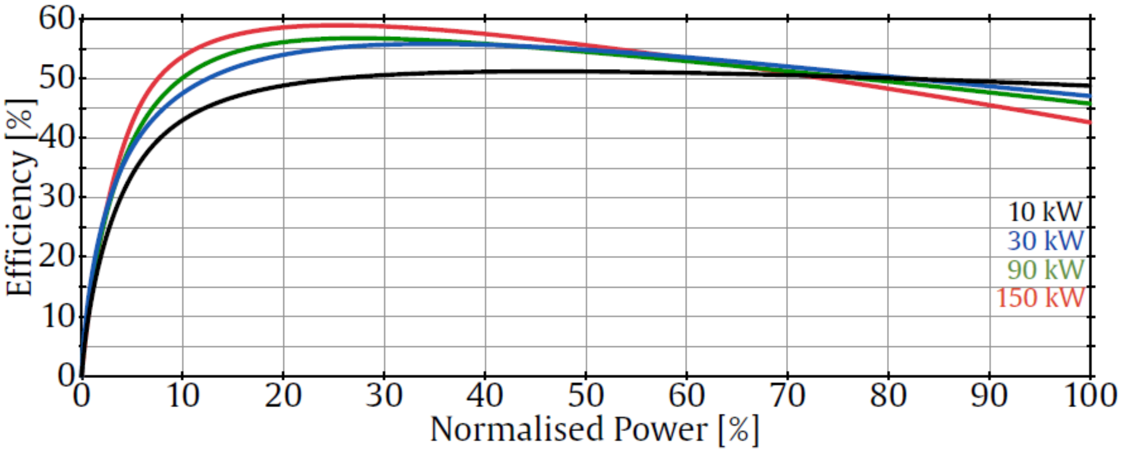

Figure 4.38: Fuel cell efficiency vs normalised power curves. Each curve represents a different fuel cell size class. [13].

As fuel cells require air for their operation, the effects of altitude on their performance must be accounted for. This is done by increasing the required fuel cell power P_{FC} at altitude to match the power it would deliver at sea-level, through the scaling factor [13]:

$$\phi = \frac{\ln(p_{SL})}{\ln(p_{alt})} \tag{4.87}$$

where p_{SL} and p_{alt} represent the ambient pressure at altitude and sea level respectively.

Finally, the fuel flow $\dot{m}_f$ - the first output of the propulsion module in the fuel cell case - is given by:

$$\dot{m}_f = \frac{P_{FC}}{\eta_{FC} \cdot LHV} \tag{4.88}$$

with LHV being the lower heating value of hydrogen, taken as $119.9MJ/kg$. P_{FC}, the power required from the fuel cell, is the second output of the propulsion module and is derived from the rotational speed, torque and motor/ESC efficiencies, together with the altitude scaling factor of Equation 4.87.

Hydrogen storage modelling

As was discussed in Section 2.2.2, hydrogen has garnered interest as a fuel because of its high specific energy. One of its main drawbacks, however, is that it suffers from a very low density. As a result, complex hydrogen storage solutions are required and are usually one of the driving factors in the design of hydrogen-powered aircraft. It is thus particularly important to model the specific hydrogen storage method in the framework. Hydrogen may be stored in solid, compressed gaseous (GH_2) and cryogenic liquid (LH_2) form. For applications in aircraft, LH_2 is often considered the most complex form of storage as a result of its requirement to maintain the hydrogen temperature at $20K$. On the other hand, liquid hydrogen has a much higher density than compressed hydrogen gas. While there is a weight penalty involved in storing hydrogen in cryogenic liquid form, according to NASA [129] this penalty is less significant than the weight and volume penalty of a pressurised GH_2 vessel. Furthermore, considering the specific long-endurance application at hand, the higher density offered by LH_2 is highly beneficial to storing the fuel volume required for such a long mission, assuming the cryogenic tank is sufficiently insulated against hydrogen boil-off. As a result, LH_2 is generally seen as providing a more feasible path to hydrogen propulsion in aviation and is thus modelled in this framework.

Figure 4.39 shows the volumetric density against the gravimetric efficiency for various solid (purple points), gaseous (black points) and liquid (blue points) hydrogen storage solutions. Here, volumetric density is defined as the mass of hydrogen contained within $1m^3$ of fuel tank volume, whereas gravimetric efficiency is the ratio of the mass of hydrogen fuel within a storage tank, to the mass of the total storage solution, inclusive of the fuel. As one would expect, both volumetric density and gravimetric efficiency increase as more hydrogen fuel is required and thus tank size increases. To capture this within the framework, the volumetric density and gravimetric efficiency of the tank are defined as functions of the hydrogen fuel mass required to complete the given mission, by Equations 4.89 and 4.90 [13].

$$\rho_{vol} = 4.759 \cdot \ln(1000 \cdot W_f) - 0.4604 \quad [\text{kg/m}^3] \tag{4.89}$$

$$\eta_{grav} = 0.06304 \cdot \ln(1000 \cdot W_f) - 0.2966 \quad [-] \tag{4.90}$$

These relations are shown as the linear regression of the liquid storage solutions - the blue line - in Figure 4.39, with an applicable range of $0.1kg$ to $100kg$ of hydrogen fuel. Considering a MALE UAV such as the avgas-powered Predator UAV which is modelled in the current study with a fuel weight of around $200kg$, and with hydrogen having roughly three times the specific energy of avgas ($119.9MJ/kg$ vs $43.7MJ/kg$), a rough estimation of the required hydrogen fuel mass lands at around $67kg$. This is within the applicable range, considering also that the actual required hydrogen fuel mass could likely fall below $67kg$ due to the weight snowball effect.

During each optimisation iteration, the required hydrogen fuel weight W_f - a coupling variable of the MDO - is used to determine the volumetric density and gravimetric efficiency of the hydrogen tank, through Equations 4.89 and 4.90 respectively. The volume and mass of the tank are then determined by the definitions of volumetric density and gravimetric efficiency:

$$V_{tank} = \frac{W_f}{\rho_{vol}} \tag{4.91}$$

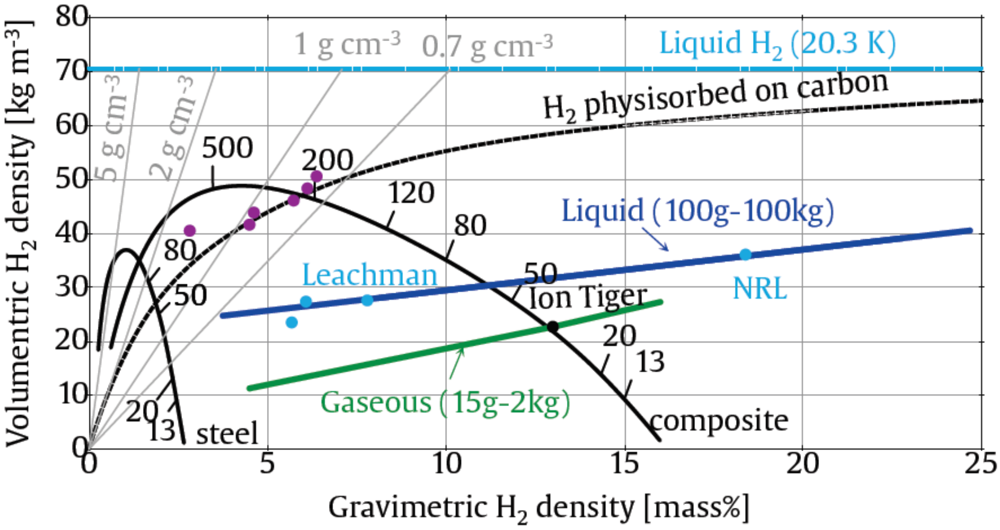

Figure 4.39: Volumetric density against gravimetric efficiency for solid (purple points), gaseous (black points) and liquid (blue points) hydrogen storage solutions [13].

$$W_{tank} = W_f \cdot \left(\frac{1}{\eta_{grav}} - 1 \right) \tag{4.92}$$

Finally, the dimensions of the tank are determined by setting a tank length-to-diameter ratio (taken as five in this study to match the length-to-diameter ratio of the rear fuselage section of the Predator UAV) and solving for the required diameter.

4.8.4. Battery model

Unlike reciprocating engines and hydrogen fuel cells, batteries do not involve the use of a physical consumable. Therefore, and as was detailed in the DSM of Figure 4.2, the determination of the energy resource requirements revolves around the calculation of the battery capacity Q_b required to complete the mission, instead of the amount of fuel W_f. In order for the performance module to be able to calculate the amount of electric charge required for a given discrete mission segment, the propulsion module must first provide the current I drawn from the battery during that mission segment. Therefore, the main performance-related output of the battery model is the current I drawn at any given mission segment, while the physical outputs are battery mass W_{batt} and volume V_{batt}.

As was discussed in Section 2.2.2, several types of batteries exist. In the current framework, however, lithium-ion batteries are modelled, as they offer the best specific energy of all current established battery technologies and are thus the standard option for use in electric vehicles. The implemented battery model follows the methodology of the preceding study of Verstraete - although the battery case is not included in the published article [13], it is detailed in the unpublished report [15].

Sizing

The battery model follows regression analyses of 1,747 lithium-ion battery packs and 18650 cells, for which corrections for the Peukert effect were made, by means of Equation 4.93 [15].

$$\frac{Q}{Q_{nom}} = \left(\frac{C_{rat}}{C_{nom}} \right)^{1-C_p} \tag{4.93}$$

with Q being the battery capacity which was used in the regression analysis, Q_{nom} being the nominal battery capacity specified by manufacturers, C_{rat} being the battery's rated discharge rate, while C_{nom} is the nominal discharge rate, which corresponds to the nominal capacity (assumed to be 1/20 as is standard practice [15]). C_p is the Peukert constant, which was set at 1.02 [15].

The resulting battery data provided by Verstraete takes the form of cell specific energy against C-rate, given in Figure 4.40 and cell specific power against cell specific energy, given in Figure 4.41. The controlling variable here is the C-rate. As the C-rate - a measure of a battery's rate of discharge - is increased, Peukert's law dictates that the overall useful capacity will decrease. This results in a lower specific energy but a higher specific power, as the allowable current increases [15]. The upper limit of the cell energy density in the data of Verstraete, about $250Wh/kg$, is in line with what is perceived in literature as the upper limit of current battery technology specific energies, cited as $265Wh/kg$ by Thapa et al. [130].

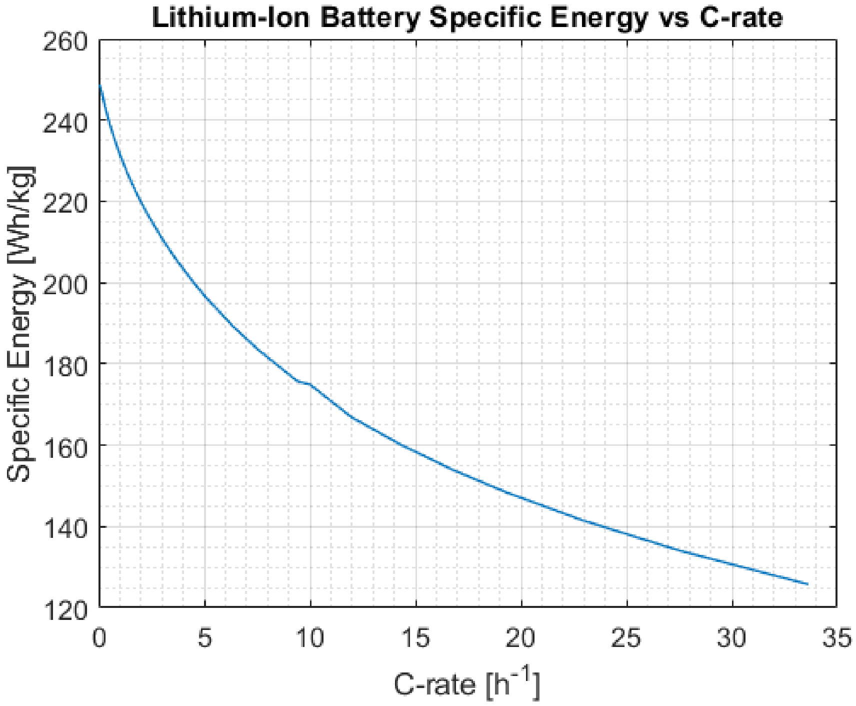

Figure 4.40: Current battery technology specific energy against C-rate, as provided by Verstraete [15].

The data shown thus far applies to the battery cell level. Battery systems for electric vehicles typically contain multiple connected lithium-ion cells in modules, together with thermal and electrical management systems. The battery module housing, thermal and electrical management systems introduce additional weight to the battery system. As a result, batteries on a system level will inherently have reduced specific energies as compared to the cell level. The current upper limit of this system-to-cell specific energy efficiency factor is given as 0.672 by Löbberding et al. [131], who analysed batteries for 25 electric road vehicles between 2010 and 2019. It should be noted, however, that efficiency factors for battery systems may vary between automotive and aeronautical applications, due to the increased importance of weight in aeronautical applications, coupled with a different array of regulatory considerations. Indeed, the Airbus Group's E-Fan electric aircraft featured a $29kWh$ battery system, with a weight of $167kg$, resulting in a system specific energy of $174Wh/kg$ [132]. With a lithium-ion 18650 cell specific energy of $207Wh/kg$, the efficiency factor is 0.84 [132].

Another fully battery-powered aircraft for which its battery specifications are known, the Pipistrel Alpha Electro, shows an identical efficiency factor. It features two $53kg$ battery packs, for a total capacity of $21kWh$, as per its information brochure [133], resulting in a system-level specific energy of $198Wh/kg$. According to the aircraft's Civil Aviation Authority of New Zealand acceptance report [134], the battery system is made up of Samsung INR18650-30Q lithium-ion 18650 cells, which according to Samsung feature a specific energy of $236Wh/kg$ [135]. The system-to-cell efficiency factor is therefore 0.84. Clearly then, electric aircraft manufacturers are currently achieving higher system-to-cell specific energy efficiency factors than automotive manufacturers. As a result, a system-to-cell efficiency factor of 0.84 is taken in the current work.

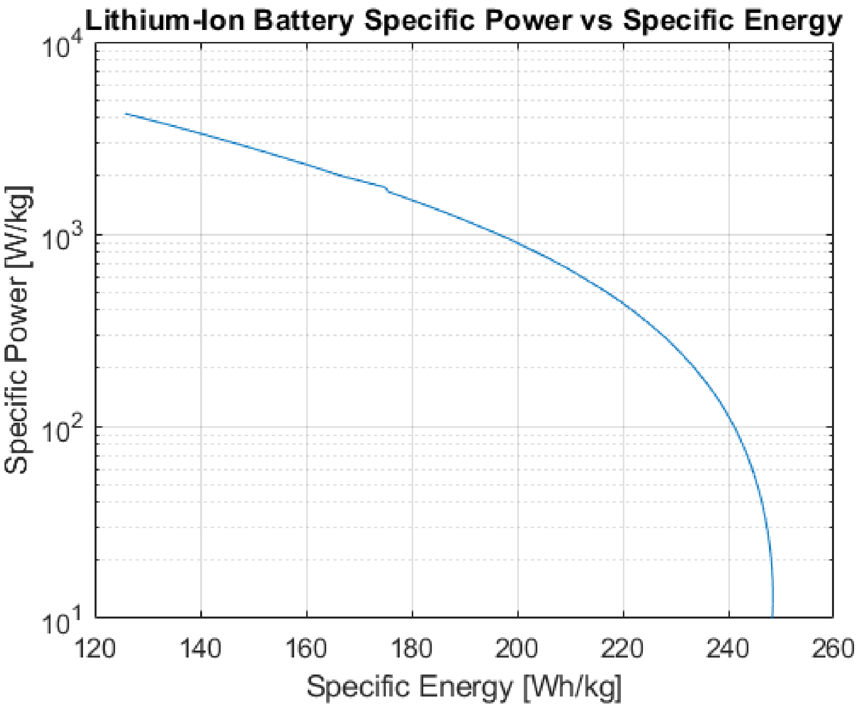

Figure 4.41: Current battery technology specific power against specific energy, as a result of a varying C-rate, as provided by Verstraete [15].

The C-rate of a given MDO iteration, together with the data presented in Figure 4.40 and the system-to-cell efficiency factor of 0.84 allow for the determination of the system battery specific energy for that iteration. The mass of the battery is then determined by dividing the capacity in Wh by the specific energy.

The volume of the battery system is determined by means of a regression analysis conducted by Verstraete [15], which showed a good correlation between the specific power and volumetric power density of a battery by means of Equation 4.94:

$$V_{batt} = \frac{W_{batt}}{2104} \quad [\mathrm{m}^3] \tag{4.94}$$

4.9. Performance

The performance module is the final module and forms the core part of the mission analysis. It is in this module where the mission described in Section 4.3 is modelled, by first discretising the mission phases into discrete segments, calculating the atmospheric and flight conditions of each segment and calling the propeller and propulsion modules to determine the fuel consumption or current drawn, along with the power required, for each segment. At the end of the mission analysis, the fuel required for each segment is summed to give the new total fuel weight, while the maximum power required during the mission is taken as the new peak power. The output of the performance module includes all the coupling variables given in Table 4.1, except for W_{OEW}, hence:

- Reciprocating engine: W_f, P_p
- Fuel Cell: W_f, P_p, $P_{p,FC}$
- Battery: Q_b, P_p

The logic of the performance module is based on the MATLAB scripts provided by Verstraete. Flow charts of the mission analysis process are given in Figures 4.42, 4.43 and 4.44 for the reciprocating engine, hydrogen fuel cell and battery cases respectively. The flow charts show the iterative steps taken in the mission analysis, for a given discrete segment. For every segment, the first step is to determine the current aircraft weight, shown in the aforementioned figures as the 'Current Weight Evaluation' process step. This is done by subtracting the weight of fuel spent so far in the mission, from the maximum take-off weight of the current optimisation iteration. For the battery case, the battery weight remains constant, as no physical consumables are used up.

The second step is to calculate the segment's flight conditions. These include local atmospheric conditions, the Mach number and the rate of climb, which is based on a linear interpolation of the sea-level and top-of-climb rates of climb, as given in Table 4.2. This step is also where the aerodynamic properties are calculated. The lift coefficient is calculated as:

$$C_L = \frac{W \cdot g}{\frac{1}{2} \cdot \rho \cdot V^2 \cdot S} \cdot \cos(\theta) \tag{4.95}$$

with θ being the climb angle. With the lift coefficient known, the drag coefficient is calculated by the standard quadratic drag polar of Equation 4.12 in the low-fidelity case. In the high-fidelity case, the drag coefficient is determined through the drag polars generated by the PANAIR panel code, as described in Section 4.5.2. Ideally, a new drag polar would be generated for each segment, as the altitude varies between segments during climb and descent. However, the generation of a single drag polar through PANAIR requires approximately 10 minutes at an acceptable mesh refinement, using the 6-core laptop computer available to the current author. With eight flight phases modelled and up to 11 segments per phase, generating a polar per segment would be prohibitively expensive. For this reason, only two drag polars are generated - one at sea-level and another at maximum altitude. This is done in the aerodynamics discipline, prior to the mission analysis, as per Section 4.5.2. During the mission analysis, the drag coefficients of sea-level and cruise/loiter segments are determined from their respective drag polar, while the drag coefficients of climb and descent segments are interpolated from the two polars, based on altitude. This approximation is considered a weakness of the current study; however, it is deemed acceptable, as less than 5% of the flight time is spent in the climb/descent phases, where drag coefficient interpolation occurs. As a future recommendation, enhanced computational resources would allow for the generation of a drag polar for each individual segment, slightly improving accuracy.

With the drag coefficient and thus the drag known, the thrust may now be calculated as:

$$T = D + W \cdot g \cdot \sin(\theta) \tag{4.96}$$

The third step of the mission analysis involves feeding the required thrust to the propeller module, to run the propeller performance model. As was described in Section 4.6.2, the propeller design, which is evaluated prior to the mission analysis, is loaded back into XROTOR and is run at the mission segment's flight conditions. This results in the outputs of propeller efficiency η_p, rotational speed and torque.

The fourth step of the mission analysis is where the methodology diverges, based on the selected propulsion model. In the reciprocating engine case, shown in Figure 4.42, propeller efficiency, rotational speed and torque are fed to the reciprocating engine model. Here, the engine efficiency and ultimately the fuel flow and power required are evaluated, by means of the methods discussed in Section 4.8.1.

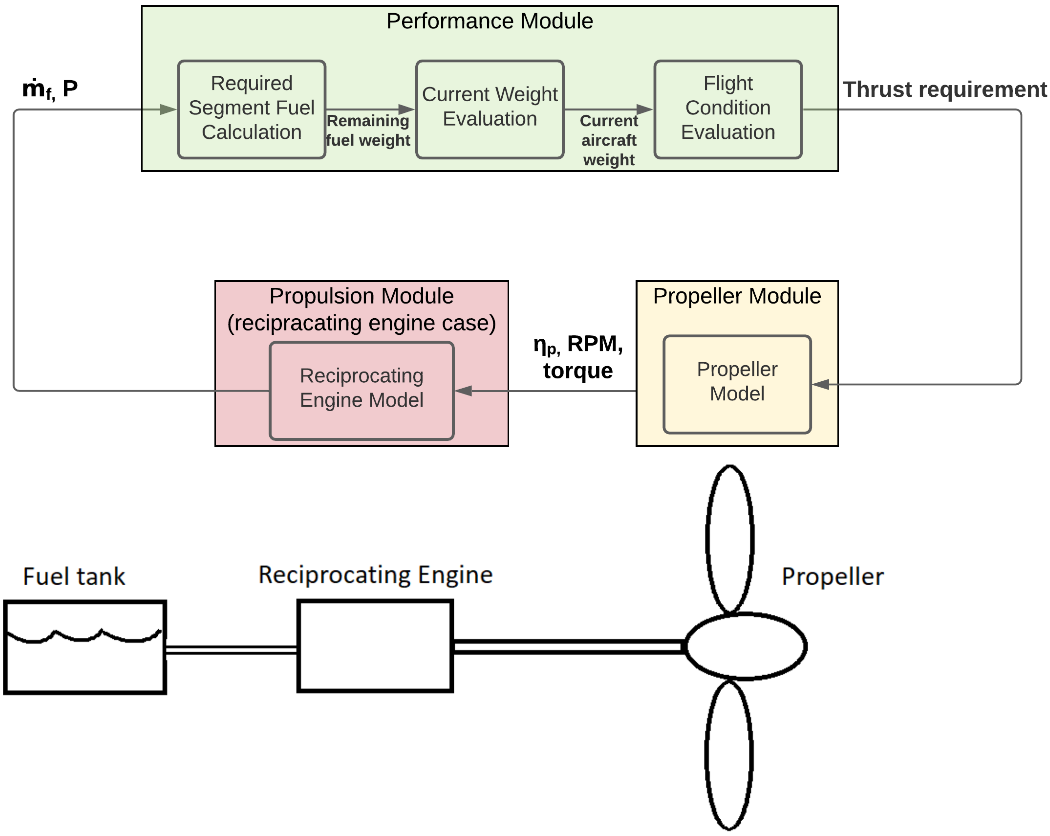

Figure 4.42: A flowchart of the mission analysis for the reciprocating engine case. The flowchart depicts the process for a given mission phase segment.

In the case of the hydrogen fuel cell coupled to an electric motor, shown in Figure 4.43, the propeller efficiency, rotational speed and torque are fed to the electric motor model. Here, the electric motor efficiency, followed by the ESC efficiency, are calculated, based on the methods described in Section 4.8.2. Their product is then passed to the fuel cell model, where the fuel cell efficiency and thus hydrogen fuel consumption and fuel cell power are calculated, based on the methods described in Section 4.8.3.

In the case of the battery coupled to an electric motor, the motor and ESC efficiencies are calculated in the same way as for the fuel cell case but are then fed to the battery model. Here, the output of the battery model, the electric current, is calculated using the methods described in Section 4.8.4 and is fed back into the performance module.

In the fifth and final step of the mission analysis loop, the propulsion module outputs of fuel consumption or electric current are fed back into the performance module, in order to calculate the required fuel weight or battery capacity for the given segment. This is done by multiplying fuel flow or electric current by the time taken to traverse the discrete mission segment. This value is then used to update the aircraft weight (in the reciprocating engine and fuel cell cases) and the loop begins again for the next discrete mission segment.

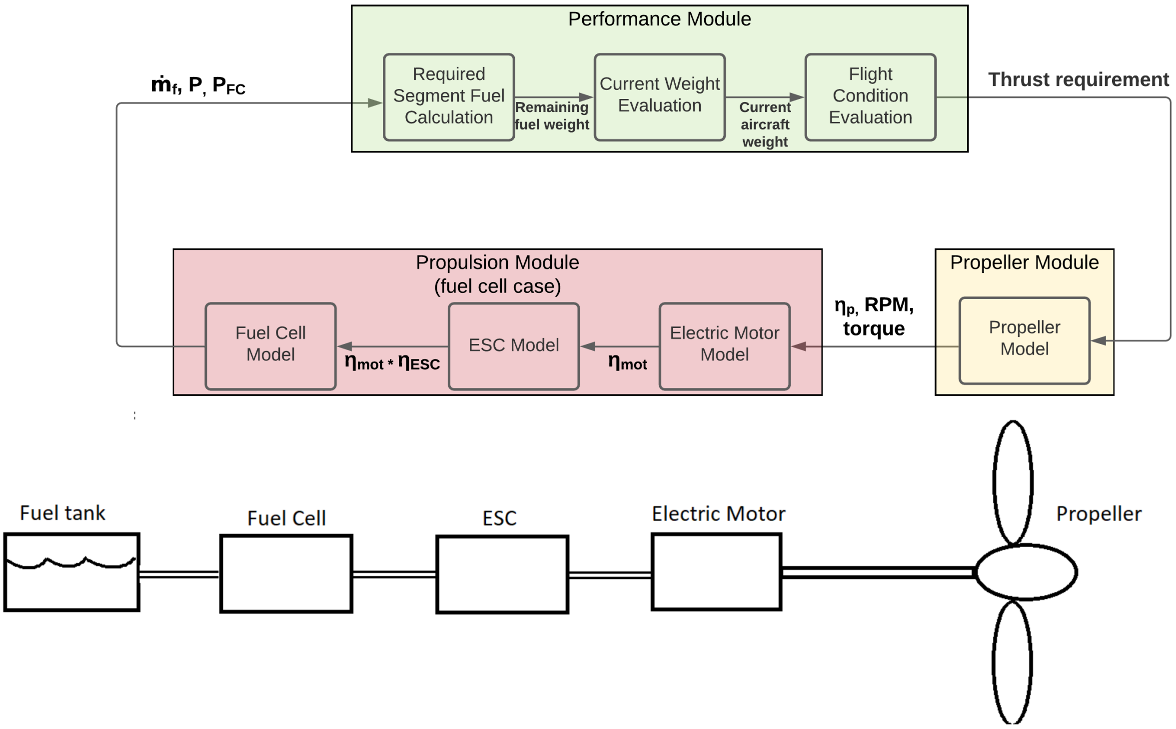

Figure 4.43: A flowchart of the mission analysis for the fuel cell case. The flowchart depicts the process for a given mission phase segment.

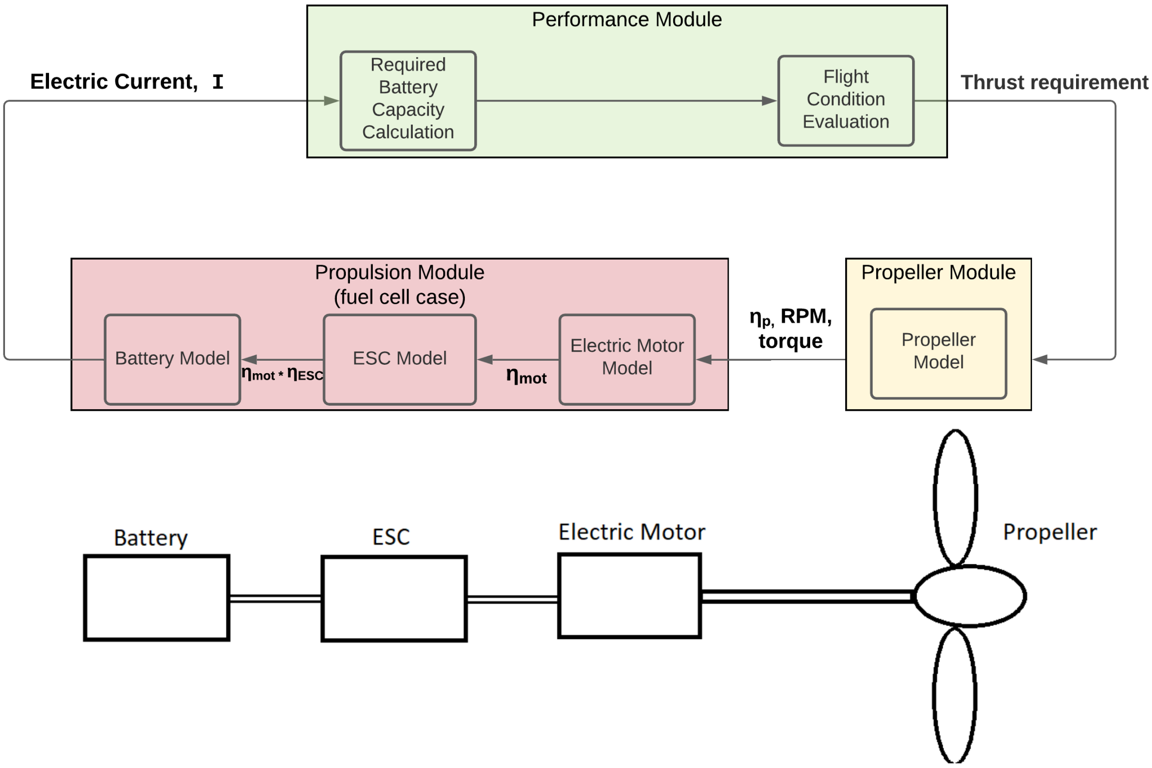

Figure 4.44: A flowchart of the mission analysis for the battery case. The flowchart depicts the process for a given mission phase segment.

Once this iterative mission analysis process has been completed for each discrete mission segment, for all phases of the mission, the total fuel weight or battery capacity required for the entire flight is evaluated, as a sum of that required for each segment, given by Equations 4.97 and 4.98 respectively. Furthermore, from the collection of required reciprocating engine/motor/fuel cell power from each mission segment, the maximum value is determined and set as the new, updated peak power response coupling variable, as per Equations 4.99 and 4.100.

$$W_f = \sum_i W_{f,i} \quad i = 1\ldots \text{ number of segments} \tag{4.97}$$

$$Q_b = \sum_i Q_{b,i} \quad i = 1\ldots \text{ number of segments} \tag{4.98}$$

$$P_p = \max(P_i) \quad i = 1\ldots \text{ number of segments} \tag{4.99}$$

$$P_{p,FC} = \max(P_{FC,i}) \quad i = 1\ldots \text{ number of segments} \tag{4.100}$$

5

Case Study: Predator UAV

This chapter provides an overview of the aircraft used as the case study within this research. Section 5.1 provides a justification for the selection of the specific aircraft, along with its key design values. Sections 5.2 through 5.5 go into detail about the aircraft-specific constants and parameters, along with the methods which sit outside of the discipline analyses and which were executed prior to the optimisation runs in order to determine the inputs.

5.1. Predator UAV Baseline Configuration

The General Atomics RQ-1 Predator UAV has been selected as a case study for the current research. The Predator is a MALE UAV designed in the 1990s by the General Atomics defence corporation. It features in many military forces around the world, taking on an aerial reconnaissance role. Subsequent iterations produced a design with reinforced wings, which allowed it to carry two AGM-114 Hellfire missiles, upgrading it to dual-role capability.

The Predator UAV has been selected as the case study for multiple reasons. Firstly, it is one of - if not the most - widely-used and widely-recognised MALE UAVs. As was highlighted in the Literature Study of Chapter 2, it has been used extensively in United States military operations in Iraq and Afghanistan and has received much media coverage in the process. Furthermore, it has a strong holding outside of the military realm, as civil variants of the aircraft were subsequently designed and are still in use. Secondly, it is a good representation of a typical MALE UAV, as it features many of the same design characteristics found on a wide range of MALE UAVs. These include a conventional configuration (as opposed to the twin-boom design of the IAI Heron), a single pusher propeller and the widely-used Rotax 914 reciprocating engine. Thirdly, as a result of its popularity, the Predator is one of the best-documented MALE UAVs. This is particularly important for this study, as most MALE UAVs are designed for military use, rendering many of their design specifications a secret. Finally, it is the aircraft modelled in the preceding study of Verstraete [13], meaning the results of the current study may be directly compared to those of Verstraete.

The values of the key characteristics and planform design variables of the Predator are provided in Table 5.1. The maximum take-off weight represents the baseline value of the objective function of the optimisation, while the operational empty weight, fuel weight and peak power represent the baseline values of the target coupling variables of the optimisation. The target design W_{MTOW} in Table 5.1 is achieved through the summation of W_{OEW} and W_f from Jane [17] and the user-defined payload weight, W_{PL}. In this study, W_{PL} is taken as $100kg$. This allows the Predator to carry its Versatron Skyball EO/IR payload ($30kg$), together with its Lynx SAR payload ($52kg$) and leaves a margin for any additional required payload. [120] [13].

In the following sections, the case-study-specific parameters of each of the disciplines are discussed, in the same discipline order as Chapter 4: Methodology.

Table 5.1: Values of the key characteristics and design variables of the baseline Predator UAV [17].

W_{MTOW} [kg]	W_{OEW} [kg]	W_f [kg]	P_p [W]	b_s [m]	AR [-]	Λ_{LE} [^{o}]	λ [-]	ϕ [^{o}]
745	350	295	84,600	7.425	19.26	2.7	0.364	N/A

5.2. Mission Specification

For the purpose of clarity throughout Chapter 4: Methodology, the Predator UAV mission specification has already been discussed in Section 4.3.

5.3. Parametrisation and Geometry

As was described in Section 4.4.2, the fuselage parametrisation is done using superellipses. In order to model the fuselage of the Predator using superellipses, the coordinates of the fuselage cross-sections are required. These cross-sectional coordinates have been obtained as follows: Firstly, a CAD model of the Predator has been downloaded from the free CAD-sharing platform GrabCAD [16]. It should be noted that this is not an official model, as no such official model is available to the public. However, it visually resembles the Predator to a very high degree and is deemed acceptable for use in this study. Next, the .STEP file of the model has been imported into the open source computer graphics software Blender [136], shown in Figure 5.1. 10 planes have been used to intersect the fuselage at strategic locations, such that the planes are concentrated in areas of high curvature in the longitudinal direction, as shown in Figure 5.2. The intersection of the aircraft model with the planes has been taken, resulting in the 10 fuselage cross-sections shown in Figure 5.3. The external coordinates of these cross-sections have then been used to fit superellipses by means of minimising the least-squares error.

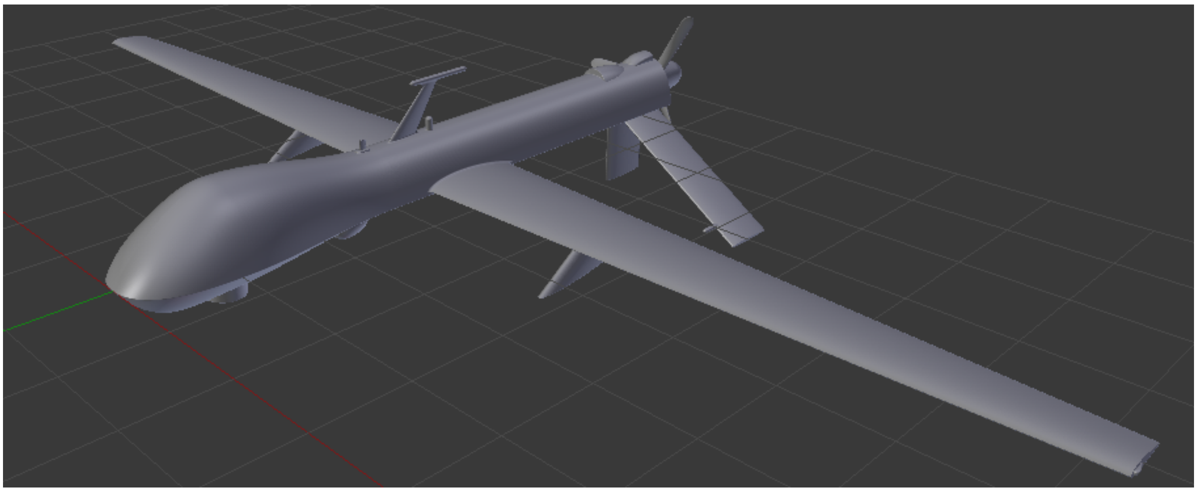

Figure 5.1: A Predator CAD model taken from GrabCAD [16].

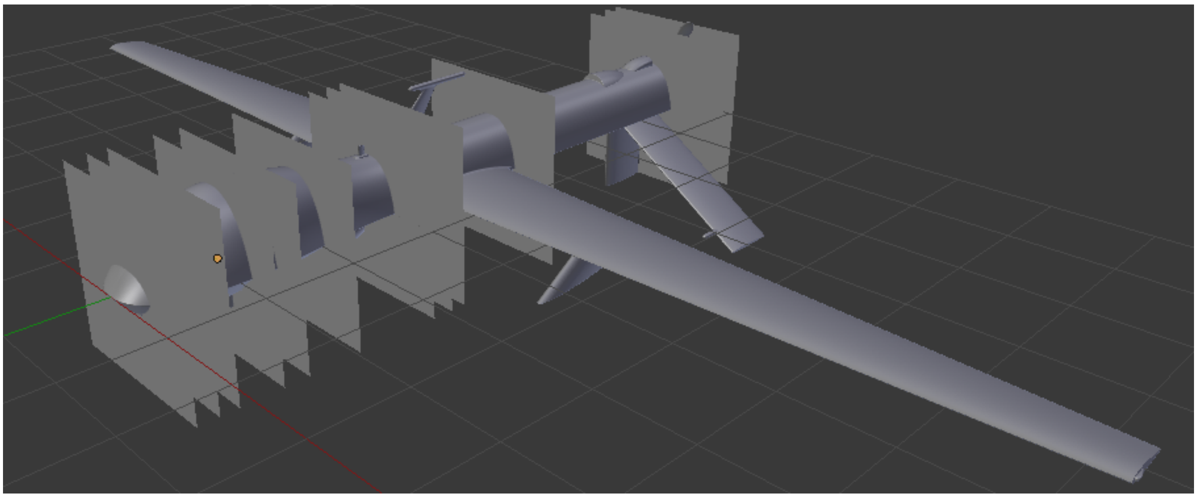

Figure 5.2: A Predator CAD model taken from GrabCAD, with 10 planes intersecting it at strategic locations along the fuselage length [16].

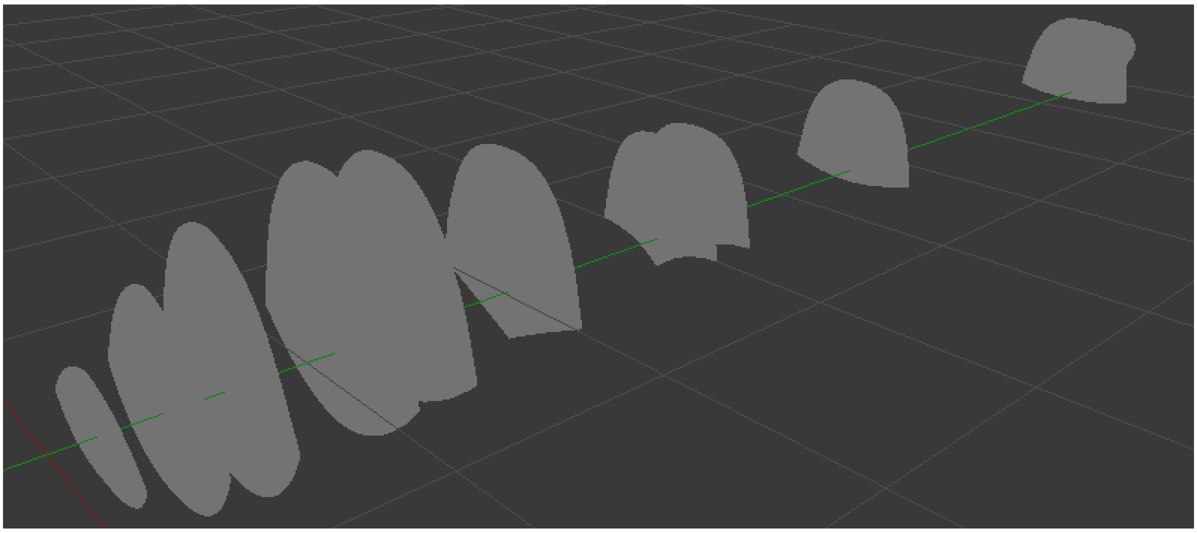

Figure 5.3: Predator fuselage cross-sections resulting from the intersection of the CAD model and 10 planes [16].

5.4. Aerodynamics

The case-study-specific parameters of the aerodynamics module include the selection of the airfoil and the PANAIR panel code mesh selection, determined through a mesh convergence study.

5.4.1. Airfoil selection

The Predator UAV features the Drela GW-19/GW-25 airfoil at the wing root and the Drela GW-27 airfoil at the wing tip, as confirmed by their designer Mark Drela of MIT [137]. These airfoils are proprietary to General Atomics and are thus not publicly available. The only piece of information about them found by the current author was by Drela, stating that the GW airfoils have considerable camber on the top surface [137]. This is logical, as the Predator is a reconnaissance UAV and as such it operates at low velocities and thus low dynamic pressures. In the absence of further GW airfoil information and based on Drela's high camber suggestion, the NACA 4412 airfoil has been selected for use in this study. The NACA 4412 is a conventional NACA 4-series airfoil which features a relatively high camber, at 4% maximum camber. This airfoil has previously been used in literature to model the Predator UAV wing, namely by Naidu and Adali [138], who optimised the wingbox of the Predator UAV. The authors also cited the airfoil's high camber as a reason for selection. Due to its high camber and its use in a similar study of the same aircraft, it is deemed appropriate for use in this study as well. The NACA 4412 features a maximum lift coefficient of $C_{l,max} = 1.6$, also taken in this study as the maximum lift coefficient [138].

5.4.2. Panel code mesh selection

To ensure the results of the PANAIR panel code are accurate, a highly-refined mesh is desirable. On the other hand, a highly-refined mesh may prove prohibitively computationally expensive, considering PANAIR will be run repeatedly throughout each optimisation run. A balance must thus be struck between selecting a mesh which is refined enough to provide results to an acceptable degree of accuracy, while still allowing the optimisation to be run within an acceptable time-frame. This balancing act is done by means of a mesh convergence study. The discipline analyses are run for six meshes, each with an increasing degree of fidelity, and the aircraft MTOW is compared. The mesh which is deemed to provide the most appropriate balance between accuracy and computational efficiency is then selected. It should be noted that this PANAIR panel code mesh convergence study applies to the six PANAIR runs per objective evaluation involved in determining the two drag polars. The single PANAIR run per objective evaluation for determining the C_p distribution in order to size the wing is given a different mesh refinement, as is discussed in Section 5.5.2.

As was explained in Section 4.5.2, the refinement of the wing mesh is controlled by selecting the number of panels in the chord-wise and span-wise directions, while that of the fuselage mesh is controlled by selecting the number of panels in the longitudinal direction for the front and aft sections, and the number of panels in the circumferential direction - a total of five mesh control parameters. Table 5.2 provides the number of panels for these five mesh control parameters, across six meshes of increasing fidelity. The total number of panels for the half-model is also given, along with the resulting MTOW obtained when executing a complete run of the discipline analyses using each mesh refinement.

Figures 5.4 and 5.5 show the convergence of the MTOW with an increasing number of panels and PANAIR run time respectively, over the six meshes. Full convergence appears to occur in the high and very high mesh refinements, with the very high refinement producing an MTOW of $758.9kg$. However, this requires a run time of around 30 minutes just for the generation of two drags polars within a single run of the discipline analyses, a duration which is not acceptable. In comparison, the high refinement mesh is only 0.4% off in terms of MTOW, using only 50% of the computational time, while the medium-high refinement mesh is only 2.9% off in terms of MTOW, using only 30% of the computational time. The medium, low-medium and low mesh refinements are not deemed acceptable, as their values of MTOW are greater than 3% compared to the very high refinement mesh. As a result, the two candidate meshes which provide the best balance between accuracy and computational efficiency are the medium-high and high-fidelity meshes, at error levels of 2.9% and 0.4% respectively.

Although the six increasingly-refined meshes presented thus far give a good idea of the level of fidelity required, further improvements to the computational efficiency may be made by selectively improving the mesh fidelity in regions of the aircraft model which substantially affect the MTOW, while reducing the fidelity in regions which do not have a major effect on MTOW. A sensitivity study has thus been conducted, to determine the sensitivity of MTOW to the refinement of each of the five mesh control parameters separately. The sensitivity study showed that the MTOW is highly-sensitive to the number of wing panels in the chord-wise direction but also the number of panels in the longitudinal direction of the forward part of the fuselage. As a result, a new mesh refinement has been generated, which places a high importance on these two mesh control parameters. This new mesh is given on the right side of Table 5.2. In terms of its resulting MTOW, it is within 0.2% of the very high refined mesh, requiring only 23% of its computational run time. At 6.5 minutes per run, this mesh allows the MDO to run within the time-frame of a few days, which is acceptable. As this mesh performs better than the two candidate meshes mentioned previously, it is selected for use in this case study.

Table 5.2: PANAIR panel code mesh convergence study for the PANAIR runs involved in generating the drag polars.

Mesh Control Parameters	Low Refined	Low-Med Refined	Med Refined	Med-High Refined	High Refined	Very High Refined	Selected Mesh
W: Chord-wise	16	20	22	25	28	30	30
W: Span-wise	8	10	12	16	18	22	10
F: Forward long.	10	12	14	16	18	20	20
F: Aft long.	6	8	10	12	16	20	4
F: Circumferential	6	8	10	12	14	16	10
Number of panels	640	1,040	1,448	2,072	2,744	3,560	1,680
PANAIR run time [s]	81	118	248	555	933	1,721	393
W_{MTOW} [kg]	885.9	830.2	805.9	780.6	761.8	758.9	760.3
Difference in W_{MTOW} to very high refined	16.7%	9.4%	6.2%	2.9%	0.4%	-	0.2%

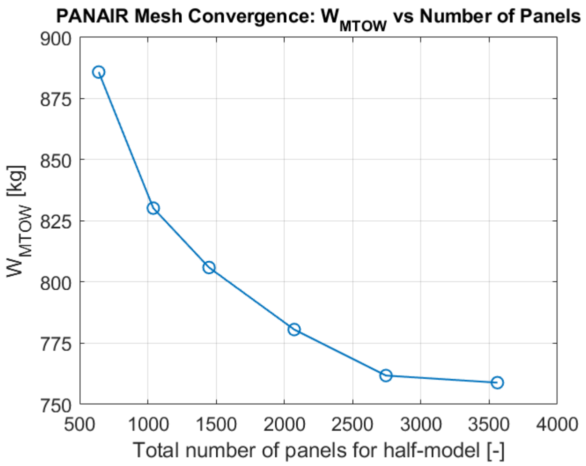

Figure 5.4: Convergence of the MTOW with an increase in the number of panels.

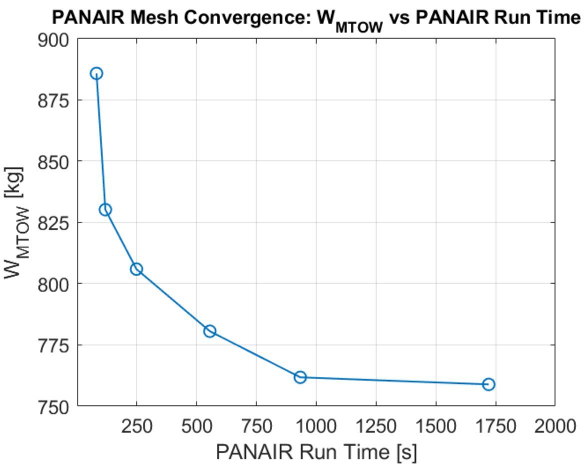

Figure 5.5: Convergence of the MTOW with an increase in the PANAIR run-time.

5.5. Weights

The case-study-specific parameters of the weights module include the selection of the wing sizing condition through a V-n diagram, and the FEM mesh selection, determined through a mesh convergence study.

5.5.1. FEM wing sizing condition selection

When sizing the aircraft wing structure, it is not possible to simulate the entire range of loads the wing may experience throughout its operational life. For this reason, a specific flight condition must be selected for the analysis, which is expected to produce the critical loading scenario [139]. This flight condition may be selected with the help of a V-n diagram. A V-n diagram is a plot of load factor $n = \frac{L}{W \cdot g}$ against indicated speed V and aids in outlining the expected safe operational flight envelope. The appropriate critical loading scenario may then be determined from the boundaries of this envelope. V-n diagrams typically have two components: the manoeuvre envelope, which deals with operational limits and the gust envelope, which deals with loads arising from wind gusts.

Figure 5.6 shows the manoeuvre envelope for the baseline Predator UAV, which is the case study of this research. The manoeuvre envelope has been constructed for a fictitious condition, where the aircraft is at $W = W_{MTOW}$, meaning it is fully loaded with payload and fuel, but has not spent any fuel. Furthermore, despite it being loaded with fuel, it is assumed no inertia relief due to fuel loading is present. Therefore, the fuel weight loading described in Section 4.7.2 is deactivated. This fictitious condition has been used to ensure a more conservative loading condition is applied, in order to guarantee the structural integrity of the wing.

Three limits are shown in the manoeuvre envelope of Figure 5.6: the aerodynamic limit, the structural limit and the aeroelastic limit. The aerodynamic limit demarcates the boundary within which the wings generate lift and outside of which stall occurs; it is essentially a limit of $C_{L,max}$ and is given by Equation 5.1. As described in Section 5.4, the NACA 4412 airfoil is selected for the case study and has a $C_{l,max}$ of 1.6, which is reflected in the aerodynamic limit of Figure 5.6. The structural limit indicates the maximum load factor n which the wing structure can safely withstand during a manoeuvre, before sustaining damage. This value is generally prescribed by the relevant aviation regulation authorities for manned aircraft. For UAVs however, no such regulatory requirement exists and its selection is often left to the designer [27]. Gundlach [27] provides various maximum load factors of manned aircraft based on their intended application, which he suggests may also be used for their unmanned counterparts. For long-endurance reconnaissance aircraft, he prescribes a maximum load factor of $n = 3$. This value is also in the middle of the range suggested by Raymer [90] for general aviation aircraft, namely $2.5 < n < 3.8$. A maximum load factor of $n = 3$ is thus applied in this framework and is reflected in the structural limit line of Figure 5.6. The aeroelastic limit defines the maximum velocity the aircraft can travel before aeroelastic phenomena such as flutter begin to pose a risk to the airframe [139]. This speed is known as the dive speed V_D and is taken as $132kt$ indicated, for reasons elaborated upon below.

$$n = \frac{0.5 \cdot \rho \cdot V^2 \cdot S \cdot C_{L,max}}{W \cdot g} \tag{5.1}$$

Although there is no regulatory reason to adhere to them in the design of UAVs, the Federal Aviation Administration's (FAA) Code of Federal Regulations (CFR) Title 14 Part 23 contain a comprehensive method for the construction of the gust envelope, for aircraft below $12,500lb$ [140]. This method is used here as a guideline, rather than as a requirement, to construct the gust envelope.

The first step in the process is to determine the design airspeeds, namely the design cruise speed V_C and design dive speed V_D. The CFR prescribes the use of Equations 5.2 and 5.3, both in imperial units, for their determination respectively.

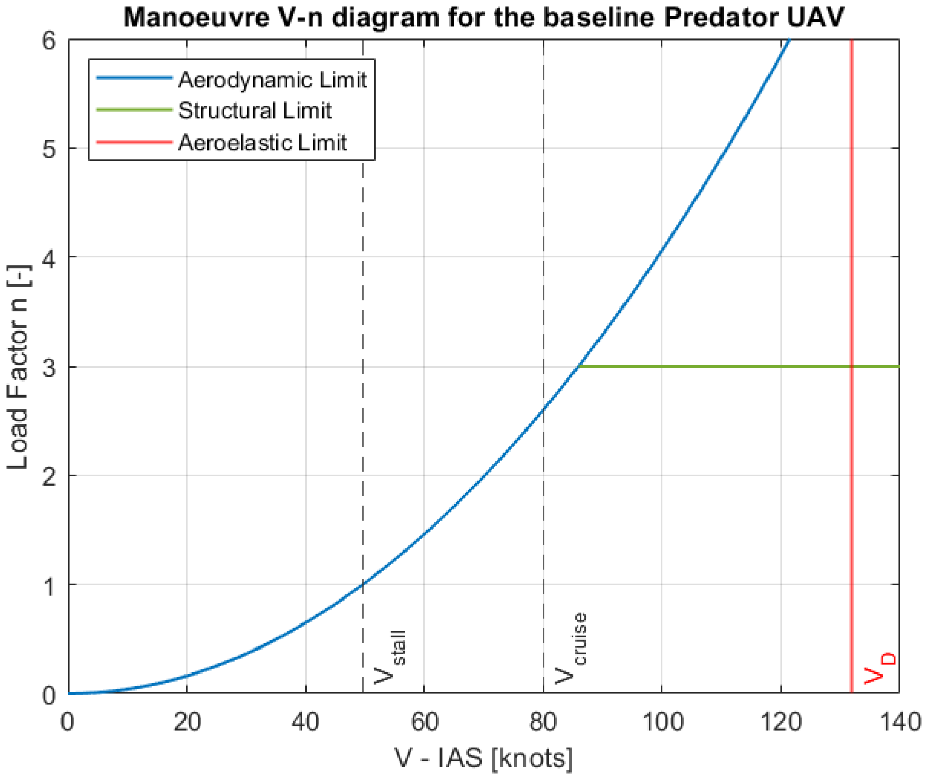

Figure 5.6: The manoeuvre envelope for the baseline Predator UAV. $C_{L,max} = 1.6$, $n_{max} = 3$ and $V_D = 132kt$.

$$V_C = 33\sqrt{\frac{W}{S}} \quad [kt] \tag{5.2}$$

$$V_D = 1.40 \cdot V_C \quad [kt] \tag{5.3}$$

However, taking the baseline Predator UAV data of $W_{MTOW} = 745kg = 1642lb$ and $S = 11.45m^2 = 123.25ft^2$ results in a design cruise speed of $V_C = 120kt$, which exceeds the aircraft's maximum level flight speed of $V_{max} = 110kt$, as specified by Jane's [17]. This is not surprising, as these regulations do not specifically consider reconnaissance aircraft which by virtue of their intended application operate at very low speeds. As a result, the CFR guidelines on setting the design airspeeds cannot be used in this case. As an alternative, the aircraft's loiter speed of $V_{loiter} = 65kt$ could be taken, as loiter accounts for approximately 95% of the mission duration. However, the current author deems this number quite low, considering the structural integrity of the wing is at stake. For a more conservative approach, the aircraft's original cruise speed of $V_{cruise} = 80kt$ is set as the design cruise speed V_C.

For the dive speed, Peery [141] suggests its value may be set between 1.2 and 1.5 times the maximum level speed. As the Predator UAV already has a relatively high maximum speed compared to its cruise and loiter speeds (40% and 70% higher respectively), a dive speed factor of 1.2 times the maximum speed is deemed sufficient in this case, hence $V_D = 132kt$.

The second step in the generation of the gust envelope is the computation of the gust load factors, given by Equations 5.4 to 5.6 in imperial units [140].

$$n = 1 + \frac{K_g \cdot U_g \cdot V \cdot C_{L_\alpha}}{498 \cdot \frac{W}{S}} \tag{5.4}$$

$$K_g = \frac{0.88 \cdot \mu_g}{5.3 + \mu_g} \tag{5.5}$$

$$\mu_g = \frac{2 \cdot \frac{W}{S}}{\rho \cdot c \cdot C_{L_\alpha} \cdot g} \tag{5.6}$$

Here, K_g is termed the 'gust alleviation factor', which accounts for the inertia of the aircraft and a non-instantaneous gust loading, while μ_g is termed the 'aircraft mass ratio' [139]. $\frac{W}{S}$ is the wing loading in psf, ρ is the air density in $slugs/ft^3$, c is the mean geometric chord in ft, C_{L_α} is the lift curve slope in rad^{-1}, g is the gravitational acceleration in ft/s^2, V is the indicated airspeed in kt and finally U_g is the gust velocity in ft/s. The CFR guidelines stipulate two gust scenarios: a gust with a speed of $U_g = 50ft/s$ at a flight speed of V_C and a gust with a speed of $U_g = 25ft/s$ at a flight speed of V_D [140]. Together with Equations 5.4 to 5.6, this allows for the generation of the gust envelope, which has been superimposed onto the manoeuvre envelope in Figure 5.7.

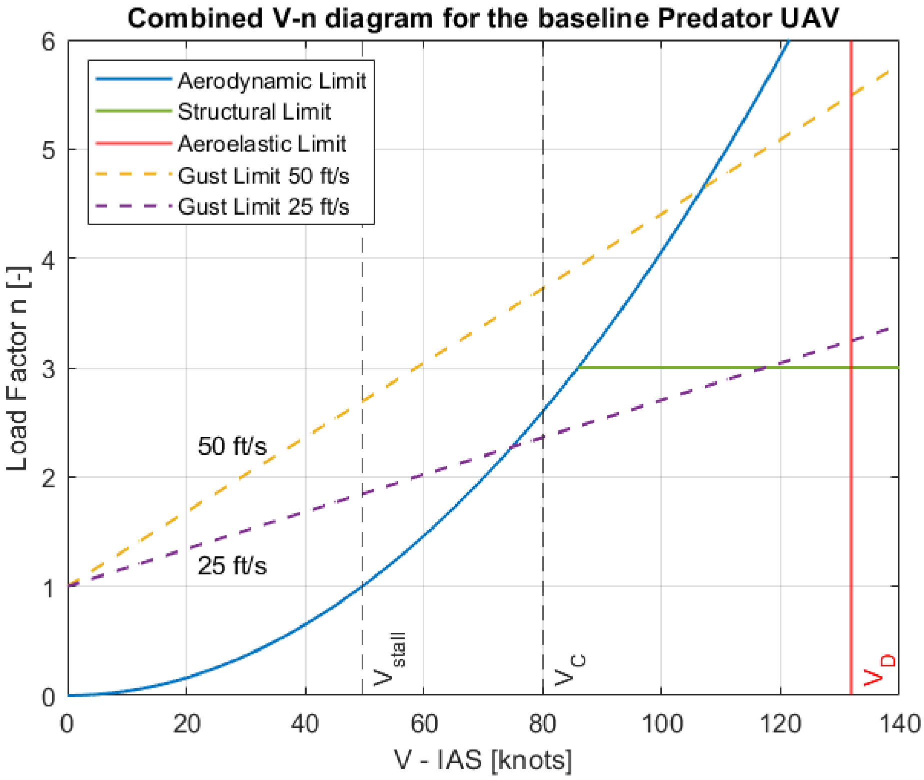

Figure 5.7: The combined manoeuvre and gust envelopes for the baseline Predator UAV. $C_{L,max} = 1.6$, $n_{max} = 3$ and $V_D = 132kt$.

The intersection of the $50ft/s$ gust loading factor line with the V_C line and the intersection of the $25ft/s$ gust loading factor line with the V_D line represent the two edge conditions set by the CFR. Drawing a straight line between the two intersection points, to encompass gust loadings across a variety of intermediate flight speeds, yields the final flight envelope, shown in Figure 5.8. The critical loading scenario is uniquely identifiable in this case, as it represents the single highest maximal load factor the aircraft is expected to experience. It comes about as a result of potential gust loads, rather than manoeuvre loads, meaning the wing must be sized not for $n = 3$ but rather for $n = 3.6$, at an indicated flight speed of $V_\infty = 94kt$.

This critical flight scenario is translated into a wing sizing condition for the FEA by first using $n = 3.6$ in the generation of the C_p pressure coefficient distribution when running PANAIR, followed by dimensionalising this pressure coefficient distribution through Equation 4.44 using $V_\infty = 94kt$. This pressure differential distribution is then fed to CalculiX, where it is applied to the model using the *DLOAD card.

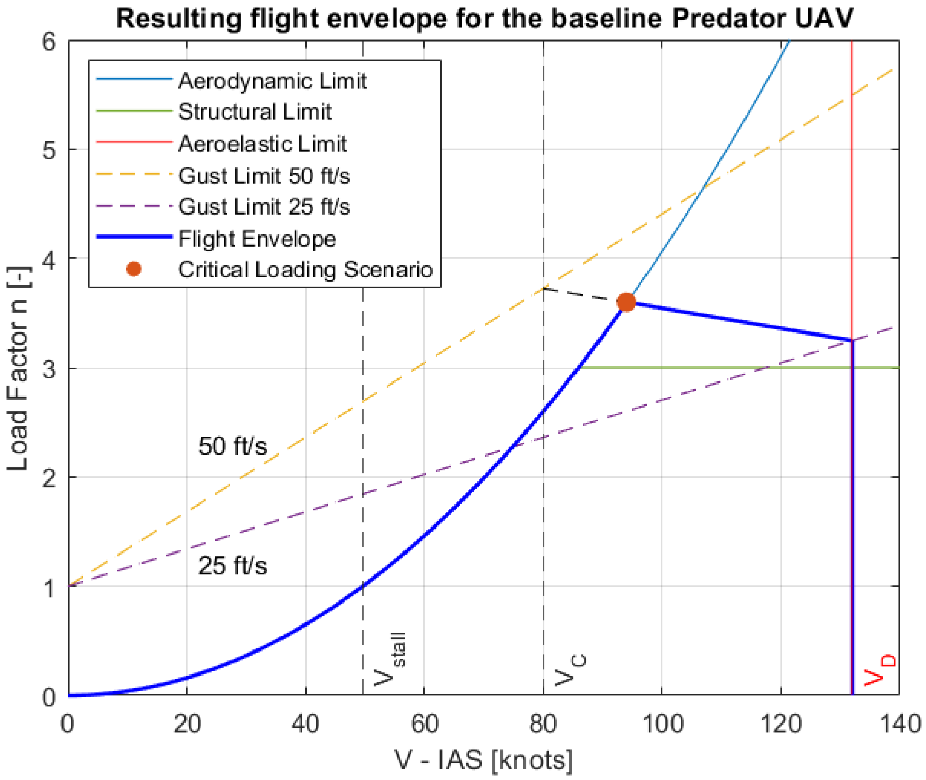

Figure 5.8: The resulting flight envelope for the baseline Predator UAV, with the critical loading scenario at $V = 94kt$, $n = 3.6$. $C_{L,max} = 1.6$, $n_{max} = 3$ and $V_D = 132kt$.

5.5.2. FEM mesh selection

Similarly to the PANAIR mesh convergence study, a convergence study for the FEM is required. As explained in Section 4.5.2, the mesh used for the PANAIR run which generates the C_p distribution is fed to the FEM to be reconstructed as the external wing surface mesh of CalculiX. As a result, the C_p-generating PANAIR run and CalculiX share the same mesh and the FEM mesh convergence study therefore incorporates the mesh convergence for both the C_p-generating PANAIR run and CalculiX. Although the same mesh refinement that was decided upon in the PANAIR mesh convergence study of Section 5.4.2 could be used, one would expect the FEM to require a less refined mesh for a given level of accuracy. This is because the output of the FEA, the wing structure weight, is expected by the author to be less sensitive to the the mesh refinement than the aerodynamic drag polars were.

The FEM mesh convergence study takes on the same form as the panel code mesh convergence study, with the results tabulated in Table 5.3. The convergence of W_{MTOW} is given, along with the stress aggregation function KS and the buckling load factor. The time variable is the sum of time taken for PANAIR to generate the C_p distribution and the time taken by CalculiX to execute the FEA. As predicted, the MTOW is much less sensitive to the FEA mesh refinement, with values all being within 0.09% of each other. Figures 5.9 and 5.10 show the convergence of the MTOW with an increasing number of panels and run time respectively, over the six meshes, using the same scale as Figures 5.4 and 5.5 for ease of comparison. The KS function shows a very low sensitivity to the mesh refinement, with the value of KS being very close to zero for all mesh refinements (KS values can typically range between -1 and 1 for oversized and undersized structures respectively). The buckling load factor shows less consistency than the KS function. It was determined during this research that the BLF in CalculiX is not a very stable parameter and only works under specific scenarios, namely when the number and size of FEM elements remain constant. This is further discussed in the result of Section 6.2. For the convergence study, however, the importance is on the convergence of the mass and KS function, which seem to behave very well across the refinement spectrum.

As was the case with the PANAIR mesh refinement, a sensitivity study has been conducted for each mesh control parameter in the FEA mesh. The study showed that all fuselage mesh control parameters had nearly no effect on W_{MTOW}, KS or the BLF. This is logical, as only the wing is modelled in the FEA. The very small effect of the fuselage refinement on the parameters likely stems from the C_p-generating PANAIR run. As a result of this insensitivity, the fuselage mesh has been left coarse, while the wing mesh has been refined to the highest extent. The resulting mesh is given on the right of Table 5.3 and shows virtually identical results to the very high refined mesh, requiring only 21% of its computational run-time. As a result, this mesh refinement has been selected for use in the FEA sizer.

Table 5.3: PANAIR C_p run + CalculiX FEM mesh convergence study.

Mesh Control Parameters	Low Refined	Low-Med Refined	Med Refined	Med-High Refined	High Refined	Very High Refined	Selected Mesh
W: Chord-wise	16	20	22	25	28	30	30
W: Span-wise	8	10	12	16	18	22	22
F: Forward long.	10	12	14	16	18	20	4
F: Aft long.	6	8	10	12	16	20	4
F: Circumferential	6	8	10	12	14	16	4
Number of panels	640	1,040	1,448	2,072	2,744	3,560	1,624
Run time [s]	48	76	153	304	505	916	190
KS aggregation function [-]	0.019	0.035	0.063	-0.021	-0.025	-0.015	-0.015
Buckling load factor [-]	2.48	0.66	0.63	0.70	1.10	1.02	1.01
W_{MTOW} [kg]	759.8	759.7	760.3	760.6	760.7	760.3	760.3
Difference in W_{MTOW} to very high refined	0.08%	0.09%	0.01%	0.03%	0.05%	-	0.00%

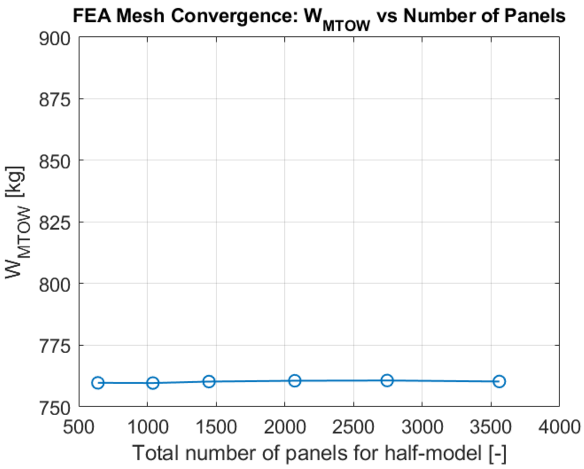

Figure 5.9: Convergence of the MTOW with an increase in the number of panels.

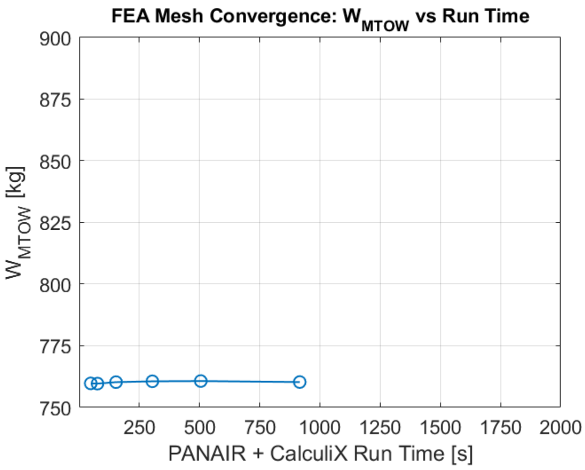

Figure 5.10: Convergence of the MTOW with an increase in the PANAIR and CalculiX run-time.

6

Results

This Chapter details the results of the investigation. Section 6.1 discusses the evaluation of the initial baseline configurations for all three propulsion types across the two levels of fidelity, prior to the execution of the MDO. Section 6.2 presents the optimised designs resulting from the MDO and compares and analyses them. Section 6.3 presents addition optimisation results at varying levels of loiter endurance, to analyse the effect of endurance on the optimised designs. Lastly, Section 6.4 provides an additional study on future battery technology levels required in order to achieve battery-powered MALE UAV flight.

6.1. Initial Configurations

Before the MDO may be run, the initial configuration must first be evaluated, in order to provide the optimiser with a starting point, which the optimal result will be compared against. This is done by setting the design variables to those of the real Predator UAV and running the discipline analyses in an iterative fashion until the coupling variables and the objective function converge. The converged coupling variables will inevitably be different from the true Predator values, as they represent the modelled output, rather than the values of the real UAV. This procedure is required for each of the three propulsion system types, for both fidelity levels, such that each of the six MDO runs are provided with a starting point.

As a reminder, the design variables consist of five planform variables, six wing structure sizing variables (only for the high-fidelity structural wing sizer case) and three or four target coupling variables (depending on the propulsion system), as was described in Section 4.2.2. The real Predator planform values are given in Table 5.1. The wing tip twist angle of the real Predator is not publicly available, hence has been set to 1^o. Naturally, these five planform variables remain constant throughout the convergence process. The real Predator target coupling variables, also given in Table 5.1, are input into the discipline analyses loop as the starting point for the convergence process. As they are coupling variables, their response values are updated at the end of each convergence iteration and are fed back into the next iteration as target values, until their convergence is achieved.

The only remaining design variables to be set are the six wing structure sizing variables, in the high-fidelity wing sizer case. Similarly to the planform design variables, these also remain constant throughout the convergence process. However, their true values from the real Predator UAV are not known. Rather than assuming their values, as has been done with the wing tip twist angle, they are derived by ensuring that they provide the initial configuration's wing with sufficient structural integrity to avoid stress-induced damage or buckling. This is done to ensure that the initial configuration (zeroth iteration of the high-fidelity MDO) is feasible, namely that it meets all the imposed constraints. This is achieved by first running a separate optimisation (prior to beginning the convergence process) which minimises the wing weight, while constraining the KS stress aggregation parameter and BLF of equations 4.4 and 4.6. Mathematically, this optimisation takes the form:

$$\begin{aligned} &\mathit{Minimise:} && J(\vec{x}) = W_W(\vec{x}) \\ &\mathit{Subject\ to:} && KS(g_j(\vec{x})) = g_{max}(\vec{x}) + \frac{1}{\rho}\ln\left[\sum_{j}^{n_g} e^{\rho(g_j(\vec{x}) - g_{max}(\vec{x}))}\right] \leq 0 \\ &&& 1 - BLF(\vec{x}) \leq 0 \\ &\mathit{where:} && \vec{x} = [t_{skin},\ t_{spar},\ t_{sparcap,r},\ t_{sparcap,t},\ t_{stringer,r},\ t_{stringer,t}] \end{aligned} \tag{6.1}$$

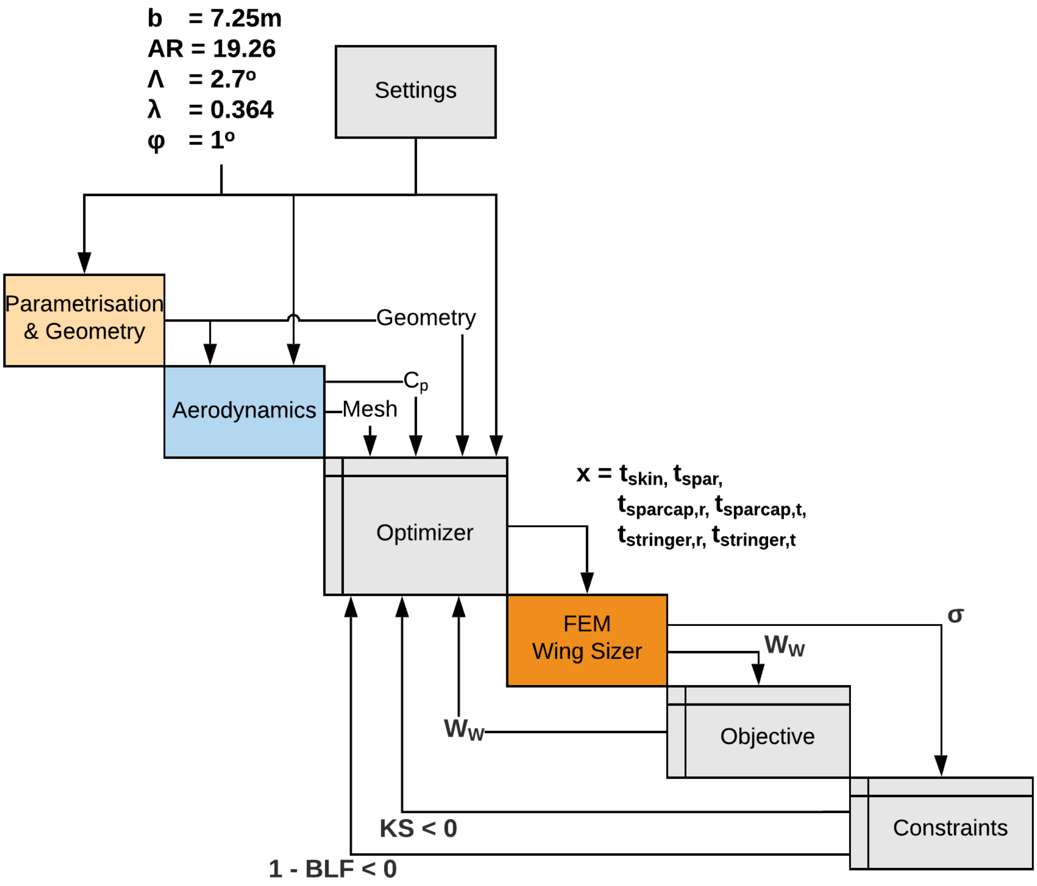

Figure 6.1: Design Structure Matrix of the separate wing structure sizing optimisation, to provide the initial configurations with a structurally-effective wing.

The DSM of the initial configuration wing structure sizing optimisation for the high-fidelity runs is given in Figure 6.1. As may be seen, the five planform variables are set as constants, with their values being those of the real Predator aircraft. The parametrisation & geometry and aerodynamics modules are run in the same way as in the MDO, as detailed in Sections 4.4 and 4.5 respectively. The geometry, outer wing mesh and C_p distribution are then passed to the optimiser, which takes the six (normalised) wing structure sizing variables as its design variables. The 'FEM wing sizer' rectangle shown in Figure 6.1 is not a full module - it is the high-fidelity section of the 'Weights' module shown in the MDO DSM of Figure 4.2. The FEM wing sizer is run in the same way as in the MDO, as detailed in Section 4.7.2. The optimiser runs the FEM wing sizer according to the optimisation problem given in Equation 6.1, until a wing structure with a minimal weight that meets the KS stress aggregation parameter and BLF constraints is determined. Once the initial wing structure sizing variables are determined in this fashion, they are entered as constants into the framework and the convergence process to determine the high-fidelity MDO starting point is run.

Table 6.1 presents the planform design variables (set to the real Predator values) and the converged coupling variables of the low-fidelity initial configurations for the reciprocating engine, fuel cell and battery cases. The equivalent table for the high-fidelity initial configurations is given in Table 6.2, which also includes the six wing structure sizing design variables which were derived through the separate optimisation scheme described above. The wing structure sizing variables seem reasonable and realistic, with the skin, tip sparcaps and tip stringers being very thin, while the sparcaps and stringers at the root have considerable thickness of around $1cm$. With these optimised thickness values, the wing structure has a minimal weight of $113kg$ for the given real Predator planform, while meeting both the stress and buckling constraints. The initial configuration wing with the optimised sizing variables is shown in Figure 6.2.

Table 6.1: Planform design variables and converged coupling variables of the low-fidelity initial configurations with varying propulsion systems. 'Div.' denotes diverged.

	Planform Variables					Coupling Variables				
	b_s [m]	AR [-]	Λ_{LE} [^{o}]	λ [-]	ϕ [^{o}]	W^*_{OEW} [kg]	W^*_f [kg]	P^*_p [kW]	P^*_{FC} [kW]	Q^*_b [Ah]
Reciprocating	7.425	19.26	2.7	0.364	1.0	448.5	229.4	114.5	-	-
Fuel Cell	7.425	19.26	2.7	0.364	1.0	358.1	46.3	62.4	69.6	-
Battery	7.425	19.26	2.7	0.364	1.0	Div.	-	Div.	-	Div.

Table 6.2: Planform & wing structure sizing design variables and converged coupling variables of the high-fidelity initial configurations with varying propulsion systems. 'Div.' denotes diverged.

	Planform Variables					wing structure sizing Variables						Coupling Variables				
	b_s [m]	AR [-]	Λ_{LE} [^{o}]	λ [-]	ϕ [^{o}]	t_{skin} [mm]	t_{spar} [mm]	$t_{sparcap,r}$ [mm]	$t_{sparcap,t}$ [mm]	$t_{stringer,r}$ [mm]	$t_{stringer,t}$ [mm]	W^*_{OEW} [kg]	W^*_f [kg]	P^*_p [kW]	P^*_{FC} [kW]	Q^*_b [Ah]
Reciprocating	7.425	19.26	2.7	0.364	1.0	0.85	1.78	10.47	0.75	10.31	0.85	466.0	194.3	106	-	-
Fuel Cell	7.425	19.26	2.7	0.364	1.0	0.85	1.78	10.47	0.75	10.31	0.85	398.3	37.1	62	68	-
Battery	7.425	19.26	2.7	0.364	1.0	0.85	1.78	10.47	0.75	10.31	0.85	Div.	-	Div.	-	Div.

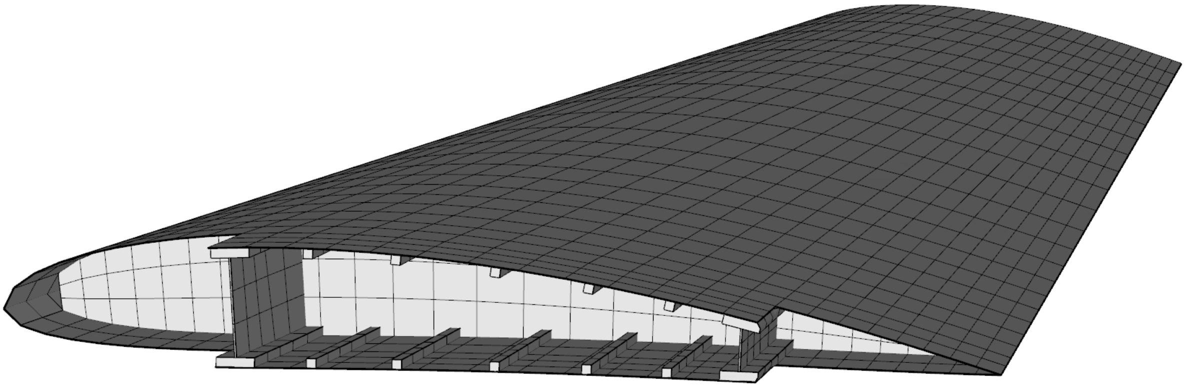

Figure 6.2: FEM wing with the optimised wing structure sizing variables for the high-fidelity initial configurations.

In order to analyse the differences between the low-fidelity and high-fidelity modelling and the effects of the different propulsion systems on the initial Predator configuration, the six sets of coupling variable results of Tables 6.1 and 6.2 are analysed and compared below. This analysis is conducted first by comparing the results of the different levels of fidelity, followed by comparing the results of the different propulsion systems.

6.1.1. Comparison of initial configurations by fidelity level

Table 6.3 compares the converged coupling variables of the initial configurations of the low-fidelity and high-fidelity methods, across all three propulsion systems.

Table 6.3: Converged coupling variables of the initial configurations of all three propulsion systems, compared between low-fidelity and high-fidelity results. 'Div.' denotes diverged.

	Reciprocating				Fuel Cell					Battery		
	W^*_{MTOW} [kg]	W^*_{OEW} [kg]	W^*_f [kg]	P^*_p [kW]	W^*_{MTOW} [kg]	W^*_{OEW} [kg]	W^*_f [kg]	P^*_p [kW]	P^*_{FC} [kW]	W^*_{OEW} [kg]	P^*_p [kW]	Q^*_b [Ah]
Low-fidelity	777.9	448.5	229.4	114.5	504.4	358.1	46.3	62.4	69.6	Div.	Div.	Div.
High-fidelity	760.3	466.0	194.3	105.6	535.4	398.3	37.1	61.6	68.5	Div.	Div.	Div.
Difference	-2.3%	+3.9%	-15.2%	-7.8%	+6.1%	+11.2%	-19.9%	-1.2%	-1.5%	-	-	-

In the reciprocating engine case, the W_{MTOW} of the low-fidelity and high-fidelity cases match very closely, within 2.3% of each other. However, this is a result of the high-fidelity case producing a 3.9% heavier W_{OEW}, while producing a 15.2% lighter W_f. The same trend is identifiable for the fuel cell-powered aircraft. Here, the W_{OEW} of the high-fidelity model is 11.2% higher than the low-fidelity model, while the W_f is 19.9% lower, resulting in a W_{MTOW} which is 6.1% higher in the high-fidelity case. The increased W_{OEW} in the high-fidelity cases is attributed to an increase in the wing weight, as may be seen in the weight breakdown of Figures 6.3 and 6.4. For both the reciprocating engine and fuel cell aircraft, the wing generated by the FEA optimisation produces a heavier wing than the class II empirical methods. This suggests that either the empirical relations are under-sizing the wing or the stress and/or buckling constraints set in the optimisation of Figure 6.1 may be too conservative.

The fuel weight W_f changes in the opposite direction to the W_{OEW} with an increase in fidelity, reducing by 15.2% and 19.9% for the reciprocating engine and fuel cell cases respectively. This is also visible in the weight breakdown of Figures 6.3 and 6.4. As the engine models are the same between the high-fidelity and low-fidelity runs, this fuel weight difference can only be attributed to the high-order aerodynamic panel code used in the high-fidelity run, which seems to be calculating a more aerodynamically-efficient aircraft. To verify this, Figure 6.5 shows the drag coefficient C_D of the low-fidelity and high-fidelity cases, for the flight condition at altitude. As can be seen, the high-fidelity C_D curve sits below the low-fidelity C_D curve for angles of attack below $\alpha = 6^o$. As the majority of flight time is spent below this angle of attack, the high-order PANAIR panel code predicts that the aircraft produces less drag than the aerodynamic relations do. As a result, the fuel rate is lower in the high-fidelity case, leading to an overall lower W_f. With the PANAIR implementation having shown a very close fit with the wind tunnel data of the validation case (Appendix A), it is safe to assume that the high-fidelity results are more accurate.

Although the same trend in W_{OEW} and W_f is seen across the low-fidelity and high-fidelity cases for both propulsion types - namely an increase in W_{OEW} and a decrease in W_f with an increase in modelling fidelity - the W_{MTOW} seems to have a different direction between the two propulsion systems. The W_{MTOW} decreases in the reciprocating engine case, while it increases in the fuel cell case, when the modelling fidelity is increased. This observation is explained as follows: As will be analysed in the next section, the fuel cell aircraft uses considerably less fuel than the reciprocating engine aircraft. Hence, although the fuel cell aircraft sees a 19.9% decrease in its W_f between the two fidelity levels, the overall contribution of this decrease to the M_{MTOW} is not enough to outweigh the increase in W_{OEW}, resulting in a +6.1% increase in W_{MTOW}. On the other hand, the reciprocating engine aircraft carries considerably more fuel, which means the 15.2% reduction in W_f between the low and high-fidelity cases has a larger net impact on the W_{MTOW}.

Engine/motor peak power P_p seems to be relatively insensitive to the fidelity changes in the aerodynamic and wing weight disciplines, with only a 7.8% decrease for the reciprocating engine peak power and a 1.2% decrease in the motor peak power. Similarly, the fuel cell peak power change is nearly negligible, at 1.5%.

In both the low and high-fidelity cases, the aircraft with the battery-powered electric motor did not yield a solution. Its coupling variables of W_{OEW}, P_p and Q_b all diverged until the simulation eventually terminated. The driving factor in this divergence was the battery weight, which continually increased as the battery capacity increased across each convergence loop iteration. This indicates that the specific energy of the battery as modelled in the framework is too low for the 24-hour flight of the modelled Predator. This is in agreement with the findings of Section 2.2.2 of the literature study, which states: *"...UAVs like MALEs and HALEs, which at best would have endurances of only a few hours on purely battery-powered systems"*. This result also means that the optimisation cannot be undertaken for the battery case, as the initial point is not defined. In lieu of optimisation results for the battery case, an additional study has been conducted for the battery case, to determine the level of battery specific energy that would be required in order for a purely battery-driven MALE UAV to complete the prescribed mission. This additional study is described separately in Section 6.4.

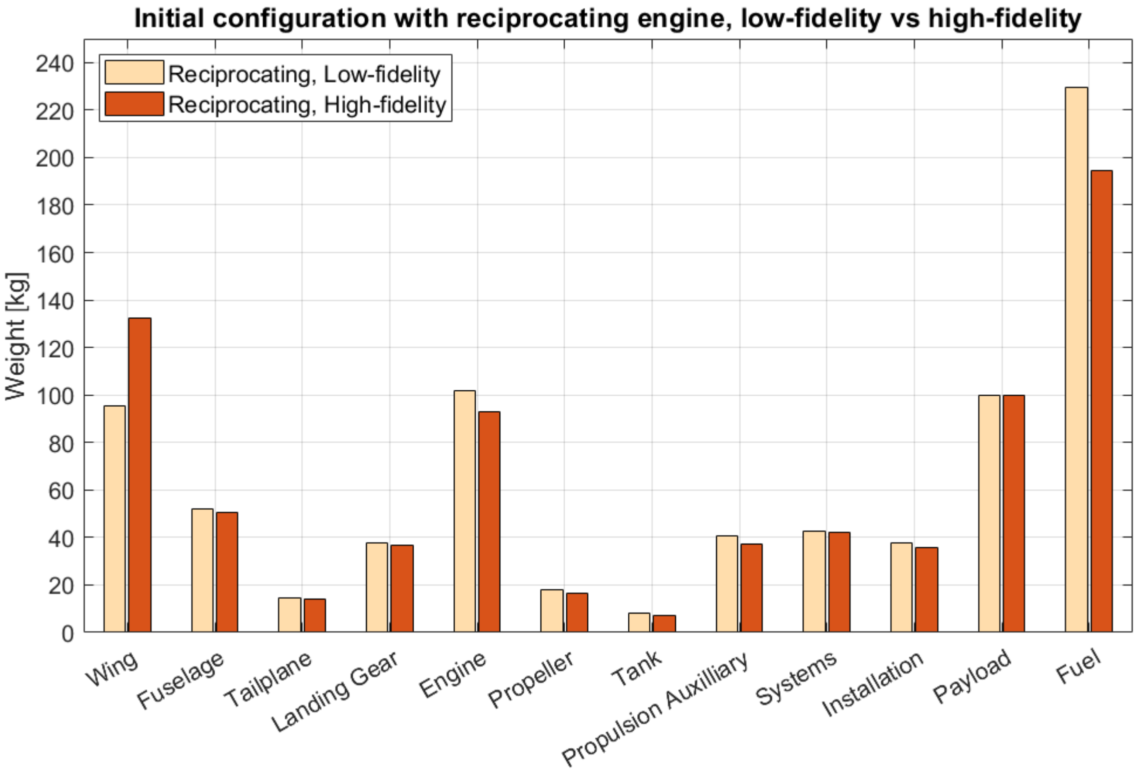

Figure 6.3: Weight breakdown of the initial configuration with reciprocating engine, for the low-fidelity and high-fidelity modelling.

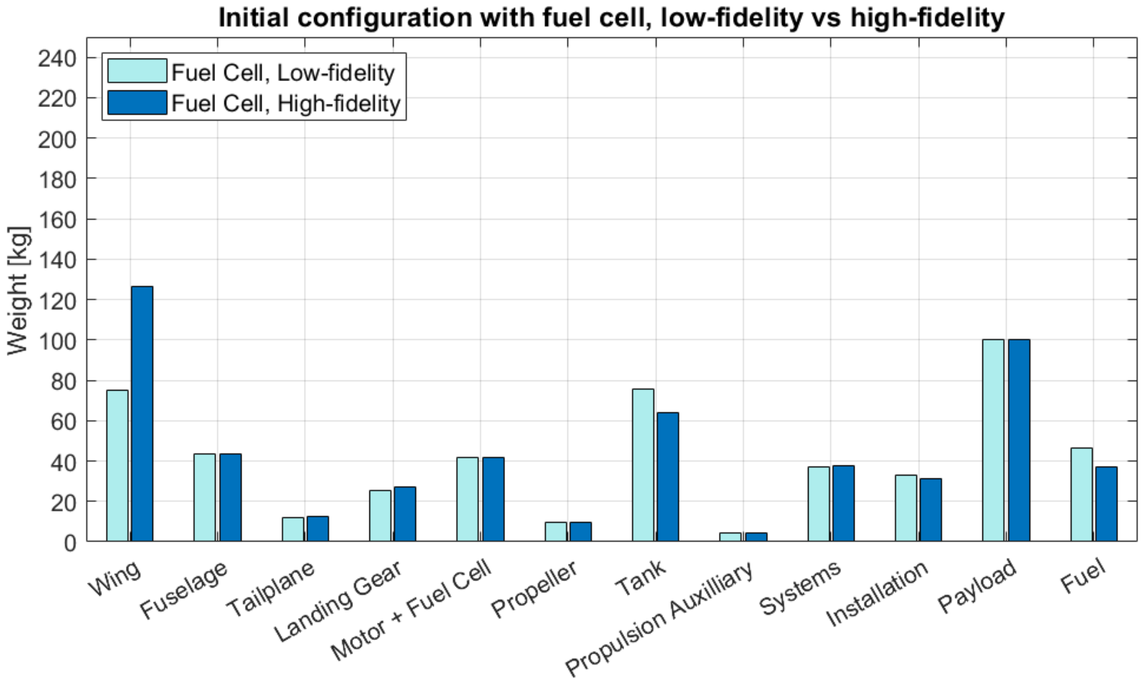

Figure 6.4: Weight breakdown of the initial configuration with fuel cell, for the low-fidelity and high-fidelity modelling.

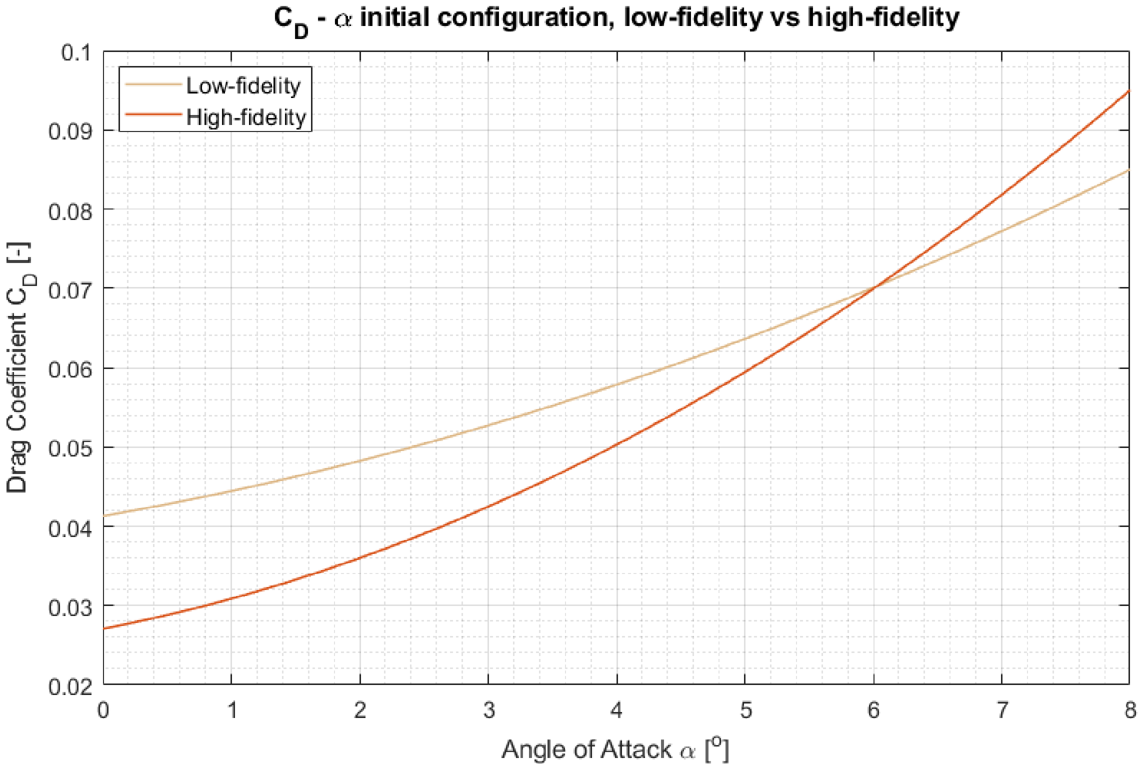

Figure 6.5: Drag coefficient C_D for the low-fidelity and high-fidelity aerodynamic modelling cases, in the flight condition at altitude.

6.1.2. Comparison of initial configurations by propulsion system

Table 6.4 compares the converged coupling variables of the initial configurations for the different propulsion systems, across both levels of fidelity.

Table 6.4: Converged coupling variables of the initial configurations of both fidelities, compared between propulsion systems.

	Low-fidelity					High-fidelity				
	W^*_{MTOW} [kg]	W^*_{OEW} [kg]	W^*_f [kg]	P^*_p [kW]	P^*_{FC} [kW]	W^*_{MTOW} [kg]	W^*_{OEW} [kg]	W^*_f [kg]	P^*_p [kW]	P^*_{FC} [kW]
Reciprocating	777.9	448.5	229.4	114.5	-	760.3	466.0	194.3	105.6	-
Fuel Cell	504.4	358.1	46.3	62.4	69.6	535.4	398.3	37.1	61.6	68.5
Difference	-35.2%	-20.2%	-79.8%	-45.5%	-	-29.6%	-14.5%	-80.9%	-41.7%	-

The modelled aircraft with the hydrogen fuel cell is significantly lighter in terms of W_{MTOW} than its standard reciprocating engine counterpart, for both the low and high-fidelity methods. Both levels of fidelity show similar weight saving for the fuel cell case, with the low-fidelity method showing a 35.2% reduction in W_{MTOW} and the high-fidelity method showing a 29.6% reduction in W_{MTOW}. For both fidelity levels, the majority of the weight saving stems from a significantly reduced fuel weight, in the order of approximately 80% reduction. This observation is in line with theory - as outlined in Section 2.2.2 of the literature study, hydrogen features a substantially higher specific energy than gasoline, by a factor of three. This is reflected in the weight breakdown diagrams of Figures 6.6 and 6.7, which compare the weights of the reciprocating engine case against the fuel cell case, for the low-fidelity and high-fidelity methods respectively. Both levels of fidelity see a substantial decrease in the fuel weight when switching to the hydrogen fuel cell system, thanks to hydrogen's very high specific energy.

This weight reduction is somewhat counteracted by an increase in the fuel tank weight, which is approximately 10 times heavier for the hydrogen case than for the gasoline case. This is also expected, as the LH_2 hydrogen storage tank situated within the fuselage is considerably more complex and heavy than a conventional gasoline fuel tank, as a result of hydrogen's very low energy density. One would actually expect the LH_2 tank to weigh more than 10 times the gasoline fuel tank - however, it should be noted that the LH_2 tank in the modelled Predator is considerably smaller than the gasoline fuel tank, as much less fuel is required for the fuel cell case. Thus, the substantial weight of the LH_2 tank truly becomes apparent when considering it is 10 times heavier than its gasoline counterpart, for storing only 20% of the gasoline fuel weight. Despite the substantially heavier LH_2 tank, the fuel weight reduction is so large that it outweighs it, leading to an overall reduction in W_{MTOW} for both levels of fidelity.

Another noteworthy weight change is that of the electric motor and fuel cell weight, as compared to the reciprocating engine. As listed in Table 6.4, both levels of fidelity see a reduction in the peak electric motor power by nearly 50% as compared to the engine power. This explains why the electric motor and fuel cell weigh around half the weight of the reciprocating engine, as shown in the weight breakdown diagrams of Figures 6.6 and 6.7.

Because of the weight reductions of the fuel and propulsion system, knock-on weight reductions are noticeable in the airframe components due to the snowball effect. This is the reason why the W_{OEW} sees a decrease of 20.2% and 14.5% for the low-fidelity and high-fidelity cases respectively, when switching from the reciprocating engine to the hydrogen fuel cell. This is visible across multiple airframe components, including the wing, fuselage, tailplane and landing gear. The propeller also sees a reduction in weight, due to the fact that its diameter has dropped from approximately $1.8m$ in the reciprocating engine cases, to about $1.57m$ in the fuel cell cases, because of the lower power requirement. These weight reductions lead to further weight reductions in the fuel weight, which is also partly why the hydrogen fuel weight reduction is so significant. These results are a good example of how making a significant design change, such as incorporating a hydrogen fuel cell propulsion system, leads to significant weight reductions across both W_f and W_{OEW}, through the snowball effect.

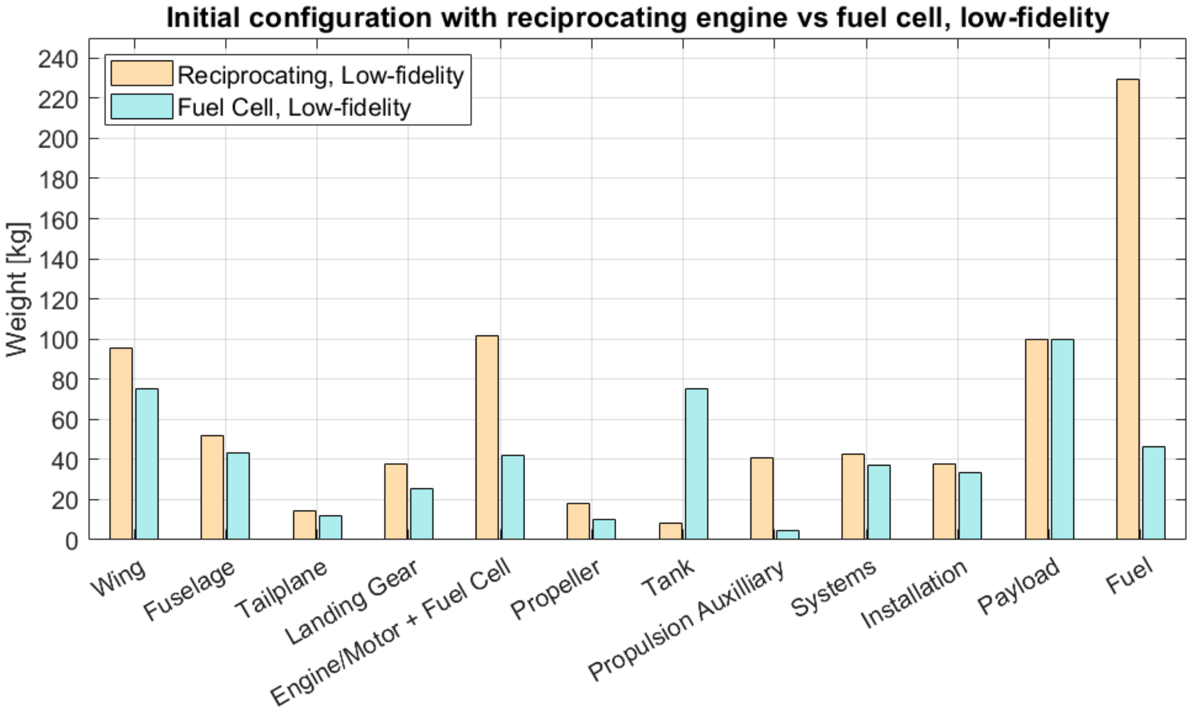

Figure 6.6: Weight breakdown of the initial configuration with reciprocating engine vs fuel cell, for the low-fidelity modelling.

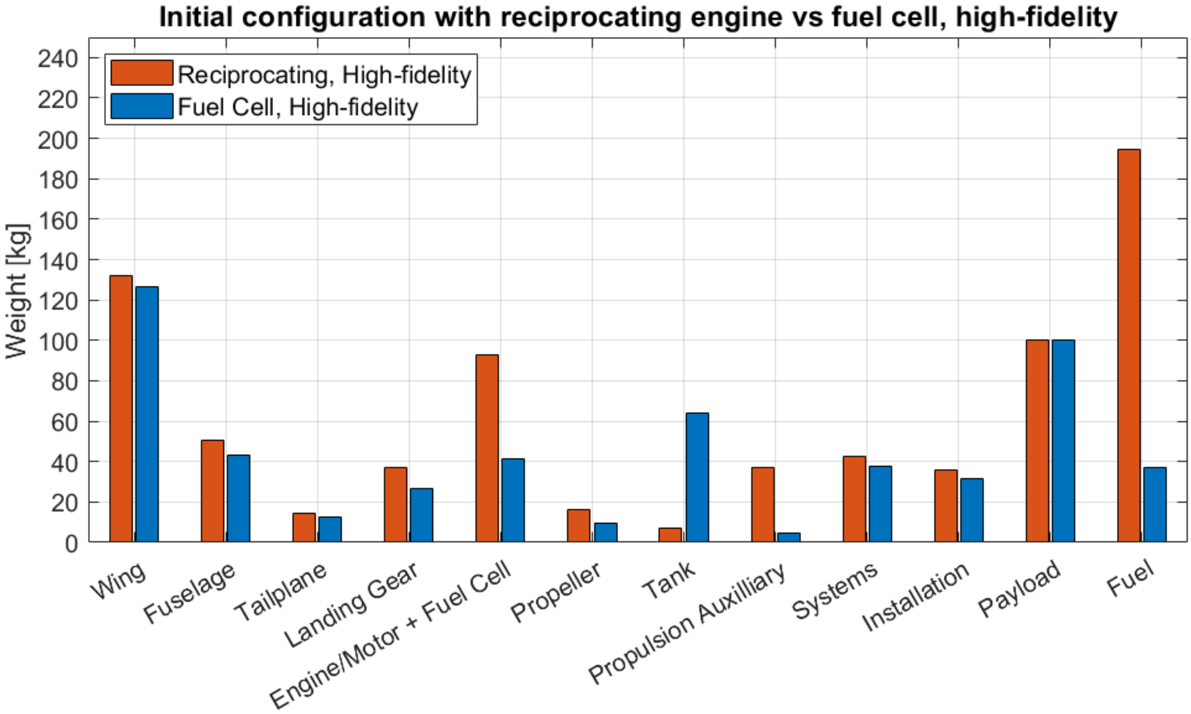

Figure 6.7: Weight breakdown of the initial configuration with reciprocating engine vs fuel cell, for the high-fidelity modelling.

6.1.3. Validation of initial configurations with real MALE UAV data

Having compared the initial configuration results by fidelity level and by propulsion system, it will help put these result into context by comparing them with real UAV data of the MALE class. Compared to the true Predator aircraft ($W_{OEW} = 350kg$), the W_{OEW} of both the low and high-fidelity reciprocating engine aircraft models are higher, at $436.1kg$ and $466.0kg$ respectively. This is expected, however, as there are multiple differences between the true aircraft and the modelling of this study. The most significant differences include the wing and propulsion modelling. As was detailed in Section 4.7.2, the wing has been modelled as an isotropic material, namely aluminium 2024-T3, due to CalculiX's limitations in the modelling of anisotropic materials. This is in contrast to the true Predator, which incorporates CFRP to produce a lighter wing structure. Although the wing weight of the true Predator is not available and thus a direct comparison cannot be made, it is logical to assume that the true wing weight will be lower than the wing weight output by the model. This explains why the modelled aircraft has a heavier airframe than the real one.

Furthermore, the reciprocating engine of the real Predator, the Rotax 914, is a turbocharged engine, while the modelled 'rubber' reciprocating engine is not. This means that the modelled engine is oversized, to be able to produce the required power at altitude. Indeed, referring to the weight breakdown of the modelled aircraft with the reciprocating engine, Figure 6.3, the engine weight is approximately $100kg$, depending on the fidelity, whereas the turbocharged Rotax 914 weighs only $74kg$ [45]. Improving the propulsion modelling of the framework is outside the scope of the current investigation and turbocharging has thus not been added as a feature. Therefore, as a future recommendation, incorporating a different FEA software, which has the ability to effectively model anisotropic materials, together with upgrading the reciprocating engine model to include turbocharging, will allow the modelled aircraft to align more closely with the real Predator.

Although the case study selected for this investigation is the Predator UAV, the methods incorporated into the framework concern the design of MALE UAVs in general and are not tied to one specific aircraft. Hence, the aforementioned comparison with the real Predator is more of a sanity check on the differences between the model and reality, rather than a complete investigation of the accuracy of the framework. More pertinent to the investigation at hand would be to compare the modelled aircraft with general MALE UAV trends. Figure 6.8 gives a plot of W_{OEW} against W_{MTOW} for eight MALE UAVs, shown by the blue circles. The blue line is the linear regression line, with a goodness of fit of $R^2 = 0.9956$. Both the low-fidelity and high-fidelity models featuring the reciprocating engine are superimposed and show a very close following of the trend. On the other hand, both fuel cell cases deviate from the trend-line significantly, as a result of a higher W_{OEW} for their respective W_{MTOW}. This is the result of the fuel weight being disproportionately lighter in the case of hydrogen.

Figure 6.9 provides a plot of W_f against W_{MTOW} for the same MALE UAVs. The data is slightly more scattered than in Figure 6.8, with a lower goodness of fit of $R^2 = 0.9185$, however still shows a strong linear correlation between W_f and W_{MTOW}. The modelled aircraft with the reciprocating engine follows the trend-line closely, but only in the high-fidelity case. The low-fidelity case produces a W_f which is relatively high compared to the trend-line. Referring back to Table 6.3, the low-fidelity model produces a 15.2% high W_f than the high-fidelity model. As was described previously, this was the result of the differences in aerodynamic efficiency produced by the low-fidelity aerodynamics equations versus the high-order panel code. From the MALE UAV data, it becomes apparent that the high-fidelity panel code leads to a W_f which aligns more closely with other UAVs of the MALE class. This further suggests that the high-fidelity method is more accurate than the low-fidelity aerodynamic relations, in addition the the validation work given in Appendix A. This result highlights the importance of incorporating higher-fidelity methods in the framework, where permitted by computational resources, in order to achieve more accurate results. The hydrogen fuel cell cases are also shown in this diagram, with a very low W_f for their respective W_{MTOW}. The effect of the hydrogen fuel weight saving is very apparent in this plot, with both fuel cell aircraft carrying the same fuel mass as the smallest MALE UAVs, which are less than half their W_{MTOW}.

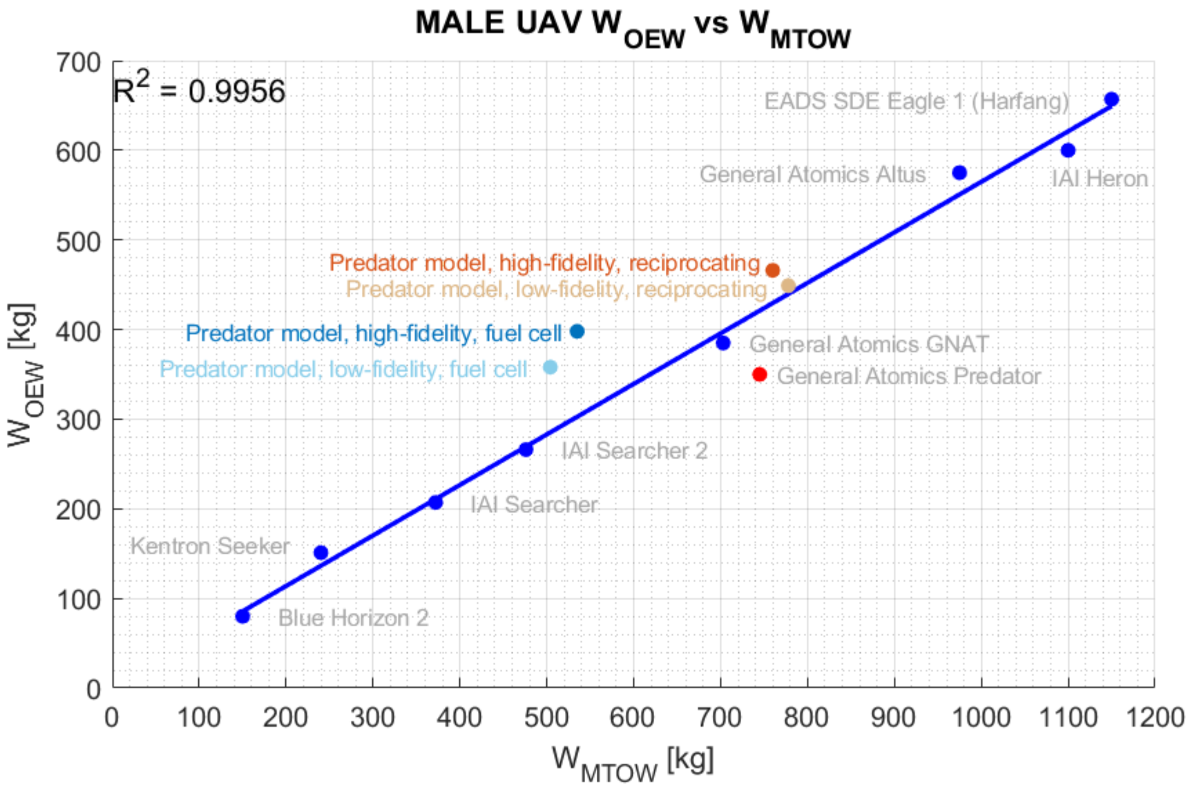

Figure 6.8: W_{OEW} vs W_{MTOW} for eight MALE UAVs, along with the respective linear trend-line. The low-fidelity and high-fidelity modelled Predator outputs, for the reciprocating engine and fuel cell cases, are also plotted. Data from [17].

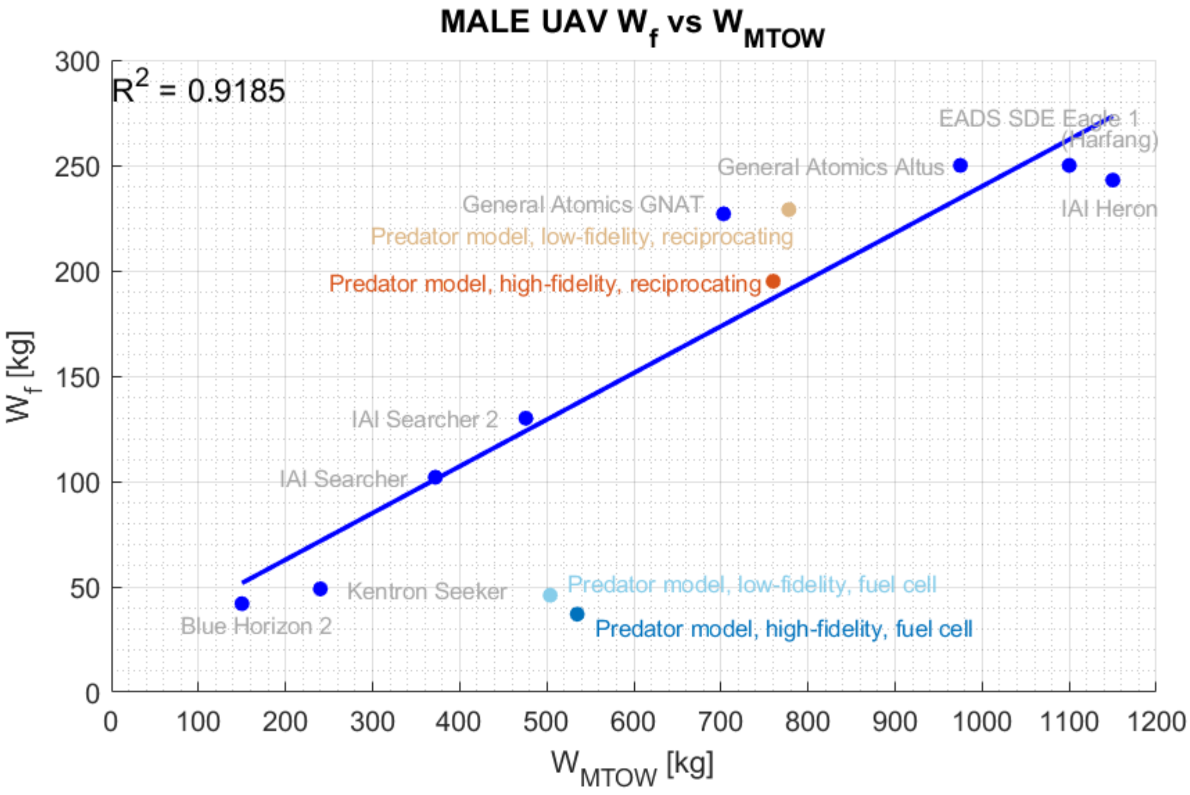

Figure 6.9: W_f vs W_{MTOW} for eight MALE UAVs, along with the respective linear trend-line. The low-fidelity and high-fidelity modelled Predator outputs, for the reciprocating engine and fuel cell cases, are also plotted. Data from [17].

6.2. Optimised Configurations

Using the initial configurations as a starting point, the MDO has been run for the optimisation problem specified in Section 4.2.2, reiterated below for the reader's convenience. This has been done for the reciprocating engine and fuel cell cases, at both low-fidelity (below on the left) and high-fidelity (below on the right).

$$
\begin{array}{lcc}
\mathit{Minimise}: & J(\vec{x}) = W_{MTOW}(\vec{x}) = W_{OEW}(\vec{x}) + W_f(\vec{x}) + W_{PL} & J(\vec{x}) = W_{MTOW}(\vec{x}) = W_{OEW}(\vec{x}) + W_f(\vec{x}) + W_{PL} \\
\mathit{Subject\ to}: & CV_i(\vec{x}) = CV_i^{*}(\vec{x}) & CV_i(\vec{x}) = CV_i^{*}(\vec{x}) \\
 & \frac{W_{MTOW}(\vec{x})}{S(\vec{x})} = \frac{W_{OEW}(\vec{x})+W_f(\vec{x})+W_{PL}}{S(\vec{x})} \leq \frac{W_{MTOW,ref}}{S_{ref}} & \frac{W_{MTOW}(\vec{x})}{S(\vec{x})} = \frac{W_{OEW}(\vec{x})+W_f(\vec{x})+W_{PL}}{S(\vec{x})} \leq \frac{W_{MTOW,ref}}{S_{ref}} \\
 & V_{required}(\vec{x}) \leq V_{available}(\vec{x}) & V_{required}(\vec{x}) \leq V_{available}(\vec{x}) \\
 & & KS(g_j(\vec{x})) = g_{max}(\vec{x}) + \frac{1}{\rho} \ln \left[\sum_{j}^{n_g} e^{\rho(g_j(\vec{x}) - g_{max}(\vec{x}))} \right] \leq 0 \\
 & & 1 - BLF(\vec{x}) \leq 0 \\
\mathit{where}: & \vec{x} = [b,\ AR,\ \Lambda_{LE},\ \lambda,\ \phi,\ CV_i] & \vec{x} = [b,\ AR,\ \Lambda_{LE},\ \lambda,\ \phi,\ CV_i,\ \ldots \\
 & & t_{skin},\ t_{spar},\ t_{sparcap,r},\ \ldots \\
 & & t_{sparcap,t},\ t_{stringer,r},\ t_{stringer,t}] \\
\mathit{for}: & CV_i = [W_{OEW},\ W_f,\ P_p] \quad \mathit{if\ reciprocating} & CV_i = [W_{OEW},\ W_f,\ P_p] \quad \mathit{if\ reciprocating} \\
 & CV_i = [W_{OEW},\ W_f,\ P_p,\ P_{p,FC}] \quad \mathit{if\ fuel\ cell} & CV_i = [W_{OEW},\ W_f,\ P_p,\ P_{p,FC}] \quad \mathit{if\ fuel\ cell} \\
 & CV_i = [W_{OEW},\ Q_b,\ P_p] \quad \mathit{if\ battery} & CV_i = [W_{OEW},\ Q_b,\ P_p] \quad \mathit{if\ battery}
\end{array}
$$

During trial runs, it was discovered that while the low-fidelity MDO runs behaved well, the high-fidelity MDO runs were not converging. More specifically, the buckling equality constraint $1 - BLF(\vec{x}) \leq 0$ was not being satisfied by the end of the optimisation runs. The issue was traced to the buckling analysis of CalculiX, which seemed to be unstable when implemented in the MDO framework. Inconsistencies were noted in the BLF between optimisation iterations, when the five wing planform design variables took on new values and generated a new wing shape. On the other hand, when the CalculiX buckling analysis was run as part of the initial configuration wing structure sizing optimisation (Figure 6.1), where the five wing planform variables were kept constant, the buckling analysis was very well-behaved. This leads the author to believe that the buckling analysis of CalculiX behaves well in an optimisation where the wing thickness variables are being varied and the wing planform variables are held constant, but not when both the wing thickness variables and planform variables are being varied at the same time. This is likely due to the CalculiX buckling analysis being significantly affected by changes in the size and shape of the FEA mesh elements, due to the planform changing. Therefore, in order to maintain the buckling analysis of CalculiX in a well-behaved manner, the wing planform variables must remain constant, while the wing thickness variables are allowed to vary. This ultimately meant that the buckling analysis could not be directly included in the MDO, as the planform variables would constantly be in variation across different iterations.

To overcome this issue, the buckling evaluation was removed from the high-fidelity optimisation and was imposed a posteriori, on the optimised aircraft. The buckling evaluation was removed by replacing the *BUCKLE card with the *STATIC card in the CalculiX input file, to disable the buckling analysis and only execute a static analysis in the MDO, while the buckling constraint $1 - BLF(\vec{x}) \leq 0$ was also disabled. Upon repeating the MDO trials without the buckling evaluation, the optimisations converged well. To ensure the wing of the optimised aircraft met the buckling criteria, the optimised configurations of the MDO were then passed through the same wing optimisation scheme that was used to size the initial configuration wing, given in Figure 6.1. However, rather than setting the real Predator planform variables as before, the optimised planform variables were set and kept constant, while the six wing structure sizing variables were used as the design variables of the optimisation. Naturally, the starting point of these six design variables in the new optimisation were set as the output values of the MDO.

The two-step optimisation method described above imposes the limitation that it is highly unlikely the same (local) optimum would be achieved as in the case of a single optimisation with the buckling constraint enabled. Therefore, the results of the two-step method will most likely be sub-optimal. Had the buckling analysis of CalculiX been more stable, it could have been incorporated directly into the MDO, and this would have yielded a further improved minimum. However, the described implementation still allows the optimiser to search for a locally-optimal configuration in terms of both the planform and wing structure sizing variables, and then perform another optimisation still within the design space vicinity of the first optimisation, to ensure the wing also satisfies the buckling constraints. The results are thus still very much reliable - they will just most likely not yield as much of a weight reduction as in the ideal single optimisation case. The new optimisation problem takes the below form, where the low-fidelity optimisation problem (left) remains the same, while the high-fidelity optimisation problem (right) has the buckling constraint removed and a subsequent wing structure sizing optimisation added.

$$
\begin{array}{lll}
\mathit{Minimise:} & J(\vec{x}) = W_{MTOW}(\vec{x}) = W_{OEW}(\vec{x}) + W_f(\vec{x}) + W_{PL} & J(\vec{x}) = W_{MTOW}(\vec{x}) = W_{OEW}(\vec{x}) + W_f(\vec{x}) + W_{PL} \\
\mathit{Subject\ to:} & CV_i(\vec{x}) = CV_i^*(\vec{x}) & CV_i(\vec{x}) = CV_i^*(\vec{x}) \\
 & \frac{W_{MTOW}(\vec{x})}{S(\vec{x})} = \frac{W_{OEW}(\vec{x})+W_f(\vec{x})+W_{PL}}{S(\vec{x})} \leq \frac{W_{MTOW,ref}}{S_{ref}} & \frac{W_{MTOW}(\vec{x})}{S(\vec{x})} = \frac{W_{OEW}(\vec{x})+W_f(\vec{x})+W_{PL}}{S(\vec{x})} \leq \frac{W_{MTOW,ref}}{S_{ref}} \\
 & V_{required}(\vec{x}) \leq V_{available}(\vec{x}) & V_{required}(\vec{x}) \leq V_{available}(\vec{x}) \\
 & & KS(g_j(\vec{x})) = g_{max}(\vec{x}) + \frac{1}{\rho}\ln\left[\sum_j^{n_g} e^{\rho(g_j(\vec{x})-g_{max}(\vec{x}))}\right] \leq 0 \\
\mathit{where:} & \vec{x} = [b,\ AR,\ \Lambda_{LE},\ \lambda,\ \phi,\ CV_i] & \vec{x} = [b,\ AR,\ \Lambda_{LE},\ \lambda,\ \phi,\ CV_i,\ \ldots \\
 & & t_{skin},\ t_{spar},\ t_{sparcap,r},\ \ldots \\
 & & t_{sparcap,t},\ t_{stringer,r},\ t_{stringer,t}] \\
\mathit{for:} & CV_i = [W_{OEW},\ W_f,\ P_p]\quad \mathit{if\ reciprocating} & CV_i = [W_{OEW},\ W_f,\ P_p]\quad \mathit{if\ reciprocating} \\
 & CV_i = [W_{OEW},\ W_f,\ P_p,\ P_{p,FC}]\ \mathit{if\ fuel\ cell} & CV_i = [W_{OEW},\ W_f,\ P_p,\ P_{p,FC}]\ \mathit{if\ fuel\ cell} \\
 & CV_i = [W_{OEW},\ Q_b,\ P_p]\quad \mathit{if\ battery} & CV_i = [W_{OEW},\ Q_b,\ P_p]\quad \mathit{if\ battery}
\end{array}
$$

$$\Big\downarrow \text{ followed by}$$

$$
\begin{array}{ll}
\mathit{Minimise:} & J(\vec{x}) = W_W(\vec{x}) \\
\mathit{Subject\ to:} & KS(g_j(\vec{x})) = g_{max}(\vec{x}) + \frac{1}{\rho}\ln\left[\sum_j^{n_g} e^{\rho(g_j(\vec{x})-g_{max}(\vec{x}))}\right] \leq 0 \\
 & 1 - BLF(\vec{x}) \leq 0 \\
\mathit{where:} & \vec{x} = [t_{skin},\ t_{spar},\ t_{sparcap,r},\ \ldots \\
 & t_{sparcap,t},\ t_{stringer,r},\ t_{stringer,t}]
\end{array}
$$

The results of the four MDO runs are presented and analysed from four perspectives. First, in Section 6.2.1 the optimised designs are presented and compared against the initial designs. These results are given in the Tables 6.5 to 6.8, where the tables corresponding to the low-fidelity runs contain a single set of optimised results, while the tables corresponding to the high-fidelity runs contain two sets of optimised results - one set of results for the optimisation without the buckling constraint and one set of results for the optimisation including the a posteriori wing structure sizing for buckling, as described above. Second, these optimised designs are analysed in more detail in Section 6.2.2, where they are compared against each other by fidelity level, to determine how changing the fidelity level of the aerodynamics and wing structure sizing methods affects the optimised designs. Third, in Section 6.2.3 the optimised designs are compared against each other by propulsion system, to determine the effects of changing the propulsion system on the optimised designs. Following this three-step analysis, in Section 6.2.4 the optimised designs are presented together with the real MALE UAV data shown previously in Section 6.1.3.

6.2.1. Comparison of initial and optimised configurations

Table 6.5: Design variables and objective function value of the initial vs optimised configurations, for the low-fidelity reciprocating engine run.

	Objective	Planform Variables					Coupling Variables		
	W_{MTOW} [kg]	b_s [m]	AR [-]	Λ_{LE} [^{o}]	λ [-]	ϕ [^{o}]	W^*_{OEW} [kg]	W^*_f [kg]	P^*_p [kW]
Initial	777.9	7.43	19.26	2.70	0.36	1.00	448.5	229.4	114.5
Optimised	766.6	8.56	24.39	1.68	0.13	1.15	446.3	220.3	109.8
Difference	-1.5%	+14.3%	+26.6%	-37.9%	-65.2%	+15.2%	-0.5%	-4.0%	-4.1%

Beginning our analysis with the low-fidelity, reciprocating engine aircraft, Table 6.5 shows a very modest reduction in the W_{MTOW} of just $11.3kg$, or 1.5% as compared to its initial configuration. This is achieved through a 0.5% reduction in the W_{OEW} and a 4.0% reduction in the W_f, which would suggest that the W_f is the driving factor behind the W_{MTOW} reduction. The optimiser has increased the wing semi-span b_s by 14.3% and the aspect ratio AR by a significant 26.6%. The optimiser has also reduced the taper ratio λ of the wing by 69.1%. Therefore, in minimising the W_{MTOW}, the optimiser seems to have travelled in the direction of a more slender wing, in order to improve the aerodynamic efficiency of the aircraft, which is why the W_f sees a more substantial reduction. The leading edge sweep angle Λ_{LE} may seem to have decreased by a significant proportion, at -37.9%, however because its actual magnitude was very small to begin with it is still relatively unchanged and nearly negligible. This is expected, as the aircraft operates in the low subsonic regime, meaning high sweep angles are ineffective aerodynamically.

The slenderness of the wing is visible in Figure 6.14, where the initial and optimised wing planforms are plotted. The wing of the low-fidelity, reciprocating engine model is visibly more slender than the initial wing, through its longer semi-span, nearly identical root chord and significantly smaller tip chord. One would actually expect the wing weight to increase in this case, as a result of its longer semi-span. Indeed, referring to the weight breakdown of Figure 6.10, the new wing is heavier by about $5kg$. However, this is counteracted by a reduced engine, auxiliary propulsion and installation weight, as a result of the improvements in aerodynamic efficiency. Therefore, it seems the decrease in the W_{OEW} has not come about as a result of an inherently lighter structure - indeed, the wing weight has actually increased. Rather, the improvements brought about by the slender wing have had enough of a knock-on effect on the propulsion weights, that the W_{OEW} has reduced. Therefore, the benefits of a more slender wing seem to outweigh the weight penalty of having a longer wing in this case.

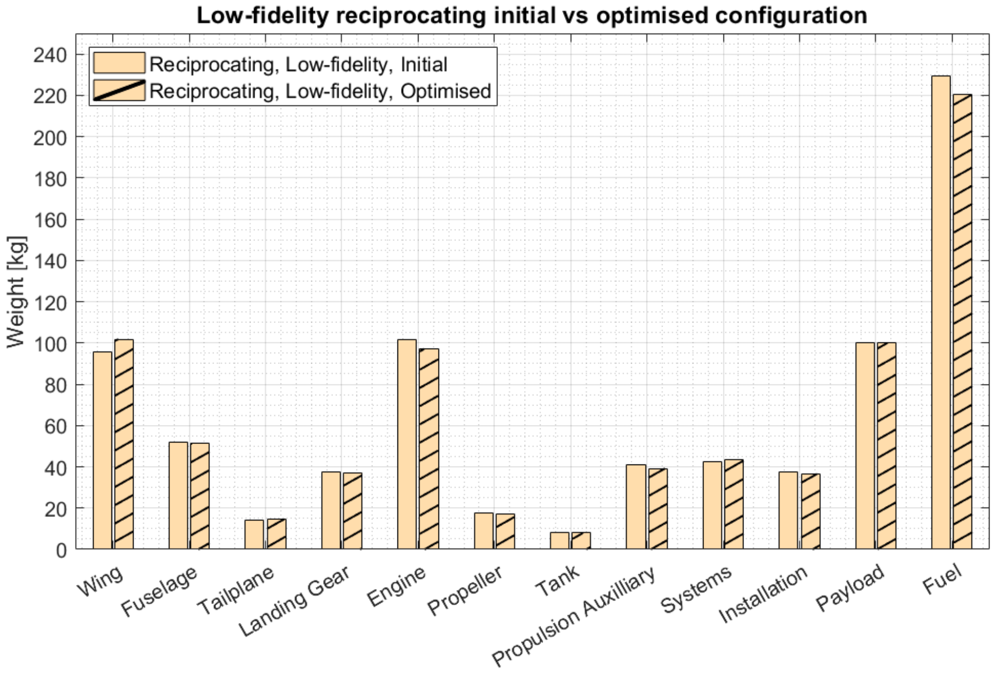

Figure 6.10: Weight breakdown of the low-fidelity, reciprocating engine aircraft: initial vs optimised.

Table 6.6: Design variables and objective function value of the initial vs optimised configurations (before and after a posteriori wing buckling optimisation), for the high-fidelity reciprocating engine run. The last row gives the difference between the initial configuration and optimised configuration with the buckling constraint.

	Objective	Planform Variables					wing structure sizing Variables						Coupling Variables		
	W_{MTOW} [kg]	b_s [m]	AR [-]	Λ_{LE} [^{o}]	λ [-]	ϕ [^{o}]	t_{skin} [mm]	t_{spar} [mm]	$t_{sparcap,r}$ [mm]	$t_{sparcap,t}$ [mm]	$t_{stringer,r}$ [mm]	$t_{stringer,t}$ [mm]	W^*_{OEW} [kg]	W^*_f [kg]	P^*_p [kW]
1) Initial	760.3	7.43	19.26	2.70	0.36	1.00	0.85	1.78	10.47	0.75	10.31	0.85	466.0	194.3	105.6
2) Optimised	679.1	7.19	19.44	1.71	0.20	1.53	0.57	2.00	8.18	2.83	9.79	2.96	403.1	171.0	92.1
3) Optimised w. buckling	733.8	7.19	19.44	1.71	0.20	1.53	0.81	0.79	11.2	0.70	8.8	0.76	443.3	190.5	103.1
Difference 1) vs 3)	-3.5%	-3.1%	+0.9%	-36.8%	-46.5%	+53.1%	-4.4%	-55.9%	+6.7%	-6.9%	-14.9%	-9.7%	-4.9%	-2.0%	-2.4%

The two sets of optimisation results for the high-fidelity, reciprocating engine model are presented in Table 6.6 and compared to their initial configuration. The optimisation without the buckling constraint results in a substantially reduced W_{MTOW}, however this increases again when the a posteriori buckling constraint is imposed. The resulting difference in W_{MTOW} is -3.5%, a modest decrease similar to that of the low-fidelity case. Here, however, the reduction seems to be driven by a 4.9% lighter W_{OEW}, rather than the 2.0% lighter W_f. To confirm this, we look to the design variable changes, where a reduction in the semi-span b_s of 3.1% is seen. The aspect ratio AR increases slightly by 0.9%, while the taper ratio λ has reduced by 46.5%. Visualising these planform changes in Figure 6.14, it can be seen that the opposite to the low-fidelity case has occurred here. The wing has reduced in length, increased in aspect ratio and reduced in its tip chord, for approximately the same root chord. By virtue of the relationship between the aspect ratio and span, $AR = b^2/S$, these changes result in a planform area S of $10.6m^2$, which is 7.8% smaller than the $11.5m^2$ of the initial wing. One would thus expect the weight of the wing to reduce by a comparable amount. Indeed, referring to the weight breakdown of Figure 6.11, the wing weight reduces by about 9.8% between the initial configuration and the final optimised configuration. Therefore, in contrast to the low-fidelity case, the optimiser in the high-fidelity case seems to have travelled in the direction of a lighter W_{OEW}, by reducing the wing's semi-span and area and therefore its weight. Furthermore, because of these reductions, the structure need not be as strong as in the initial configuration and thus most of the wing structure sizing variables have also reduced, ranging from 4.4% to 55.9% reductions in thickness, further reducing the wing weight.

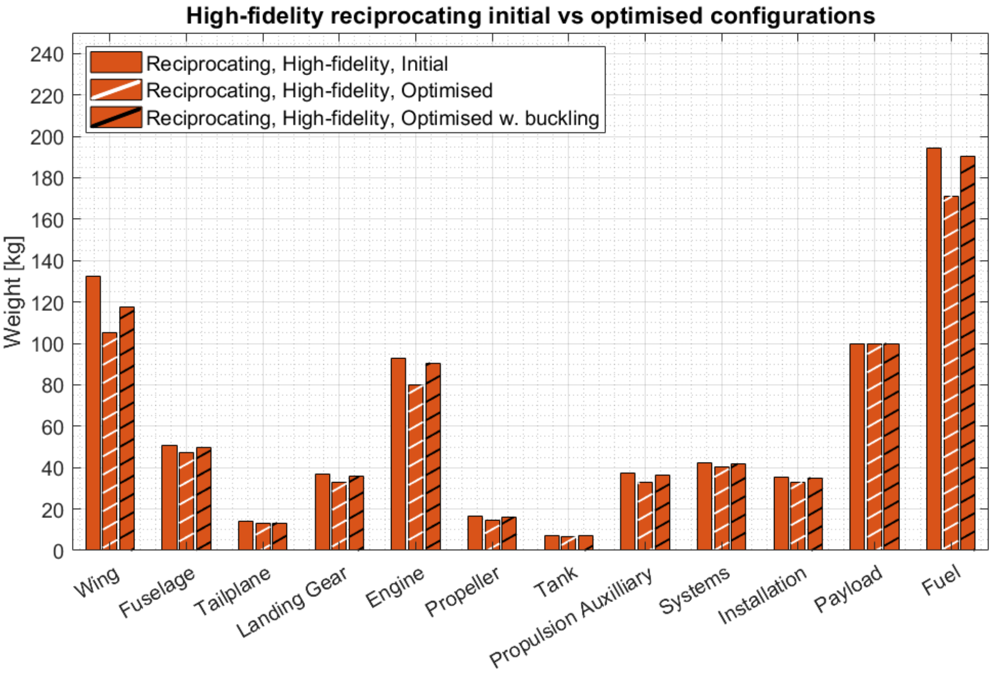

Figure 6.11: Weight breakdown of the high-fidelity, reciprocating engine aircraft: initial vs optimised vs optimised with a posteriori buckling constraint.

Table 6.7: Design variables and objective function value of the initial vs optimised configurations, for the low-fidelity fuel cell run.

	Objective	Planform Variables					Coupling Variables			
	W_{MTOW} [kg]	b_s [m]	AR [-]	Λ_{LE} [^{o}]	λ [-]	ϕ [^{o}]	W^*_{OEW} [kg]	W^*_f [kg]	P^*_p [kW]	P^*_{FC} [kW]
Initial	504.4	7.43	19.26	2.70	0.36	1.00	358.1	46.3	62.4	69.6
Optimised	460.0	5.48	16.96	2.83	0.11	0.99	317.5	42.7	56.9	63.4
Difference	-8.8%	-26.2%	-11.9%	+5.0%	-69.1%	-1.1%	-11.3%	-7.9%	-8.9%	-8.8%

Moving on to the fuel cell propulsion system, Table 6.7 presents the results of the low-fidelity, fuel cell case. Here, the W_{MTOW} has reduced significantly, by $44.4kg$, or 8.8% of the initial configuration. Looking at the coupling variables, it initially seems that both W_{OEW} and the W_f have contributed significantly to this lower W_{MTOW}, at 11.3% and 7.9% reductions respectively. However, it should be noted that the absolute magnitude of W_f in the fuel cell case is substantially lower than its reciprocating engine counterpart and thus a 7.9% reduction in W_f is only really a $3.6kg$ reduction, out of the $44.4kg$ reduction in W_{MTOW}. Therefore, most of the weight saving has stemmed from a reduction in the W_{OEW} in this case. This observation is expected, for two reasons. Firstly, the W_f in the fuel cell case is nearly an entire order of magnitude lower than the W_{OEW}, meaning the optimiser has found more net weight reductions by focusing on reducing the W_{OEW}. Secondly, the design variables of the initial configuration are those used in the real Predator, which has been designed around a reciprocating engine. It is therefore expected that the fuel cell optimal point is much further away to the initial point in the design space, than the reciprocating optimal point is. As a result, one would expect a significantly different planform would emerge in the optimal fuel cell case.

Indeed, the key design variables have changed significantly, where the semi-span b_s has decreased by about $2m$, or 26.2%, while the aspect ratio AR has decreased by 11.9%. The taper ratio λ has also reduced substantially, by 69.1%, while the leading-edge sweep Λ_{LE} and the tip twist angle ϕ have remained relatively constant, at 5.0% and -1.1% respectively. The optimiser has thus elected to provide a much smaller wing, both in span and area. This is visible in the planform comparison of Figure 6.14, where the low-fidelity, fuel cell wing shows a dramatic decrease in span and area as compared to the initial wing. The optimised wing's area has decreased to $7.1m^2$, down 38.3% from the original wing's $11.5m^2$ area. Referring to the weight breakdown of the initial and optimised fuel cell configuration of Figure 6.12, the shrinkage of the wing has resulted in a $20kg$ wing weight reduction, or 26% from the initial configuration. This wing weight reduction seems to have a knock-on effect on all other airframe component weights, which together are what bring the W_{OEW} down. Furthermore, because of the lighter W_{OEW}, less fuel is required and hence why the 7.9% reduction in W_f is observed.

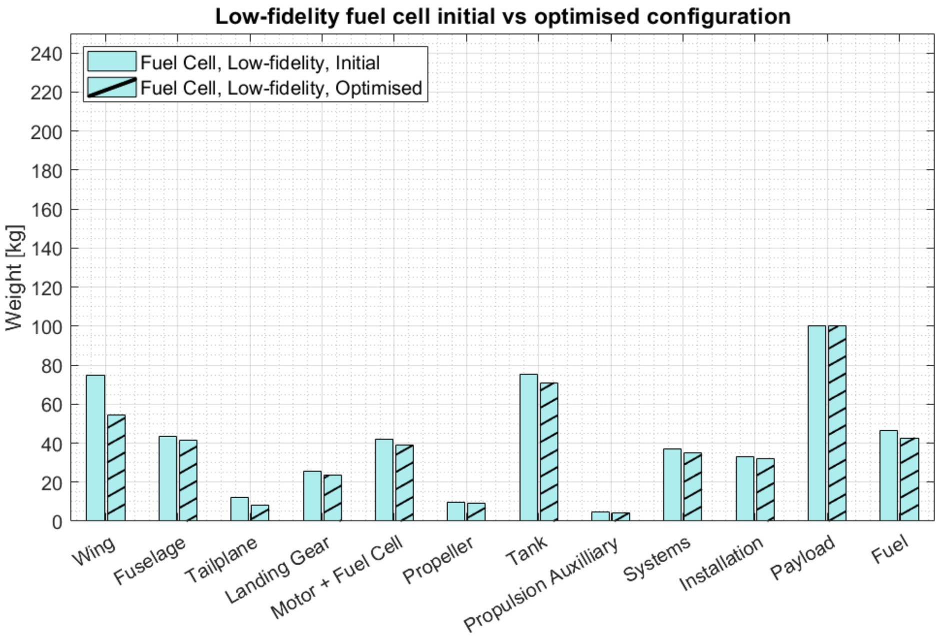

Figure 6.12: Weight breakdown of the low-fidelity, fuel cell aircraft: initial vs optimised.

The W_f reduction also has its own knock-on effects. Firstly, a lighter and less powerful motor and fuel cell stack is now required. Both the motor peak power and fuel cell peak power show a nearly identical reduction of 8.8% and 8.9% respectively, which is also reflected in their 7.7% weight reduction. Secondly, the hydrogen tank has seen a 5.9% weight reduction; however, it still very much dominates the aircraft weight (along with the payload) in comparison to the other components shown in Figure 6.12, as its $71kg$ weight represents 16% of the W_{MTOW} or 22% of the W_{OEW}.

Table 6.8: Design variables and objective function value of the initial vs optimised configurations (before and after a posteriori wing buckling optimisation), for the high-fidelity fuel cell run. The last row gives the difference between the initial configuration and optimised configuration with the buckling constraint.

	Objective	Planform Variables					wing structure sizing Variables						Coupling Variables			
	W_{MTOW} [kg]	b_s [m]	AR [-]	Λ_{LE} [^{o}]	λ [-]	ϕ [^{o}]	t_{skin} [mm]	t_{spar} [mm]	$t_{sparcap,r}$ [mm]	$t_{sparcap,t}$ [mm]	$t_{stringer,r}$ [mm]	$t_{stringer,t}$ [mm]	W^*_{OEW} [kg]	W^*_f [kg]	P^*_p [kW]	P^*_{FC} [kW]
1) Initial	535.4	7.43	19.26	2.70	0.36	1.00	0.85	1.78	10.47	0.75	10.31	0.85	398.3	37.1	61.6	68.5
2) Optimised	428.1	5.24	16.35	2.94	0.39	0.98	0.51	1.59	6.71	0.74	7.29	0.84	293.4	34.7	50.9	56.8
3) Optimised w. buckling	429.0	5.24	16.35	2.94	0.39	0.98	0.50	0.55	5.77	0.52	10.42	0.52	294.1	34.8	51.0	57.0
Difference 1) vs 3)	-19.9%	-29.5%	-15.1%	+8.8%	+7.2%	-2.1%	-40.9%	-69.4%	-44.9%	-30.2%	+1.1%	-38.0%	-26.2%	-6.2%	-17.3%	-16.9%

The optimisation results of the final case, the high-fidelity models with the fuel cell propulsion system, are given in Table 6.8. As with the high-fidelity reciprocating engine case, the first set of results, found on the second row, are without the buckling constraint, while the second set of results, found on the third row, include the a posteriori wing buckling optimisation. In the main optimisation, the W_{MTOW} falls substantially, from $535.4kg$ to $428.1kg$, a reduction of $107.3kg$. The second optimisation barely changes this, only slightly increasing the W_{MTOW} to $429.0kg$. This small increase in W_{MTOW} between the two optimisations stems from the fact that the wing weight has barely changed during the a posteriori optimisation with the buckling constraint, as is visible in the weight breakdown of Figure 6.13. This is in contrast to the reciprocating engine high-fidelity case, where the a posteriori buckling optimisation brought about a substantial increase in the wing weight. Referring to the second and third row of the wing structure sizing variables of Table 6.8, we see that although the wing weight has barely changed between the two optimisations, the wing structure sizing variables have changed substantially. It seems that in the a posterior buckling optimisation, the optimiser has saved weight by reducing the thicknesses of the non-buckling-supporting structure, while increasing the thickness of the stringers, from $7.29mm$ to $10.42mm$. These two opposing weight changes seem to cancel each other out, therefore producing a wing structure which meets the buckling constraint, while still maintaining a very similar weight.

The final W_{MTOW} value is $429.0kg$, which represents a 19.9% reduction compared to its initial configuration. This is double the percentage change observed in the low-fidelity fuel cell optimisation and the reason for this will be investigated in the upcoming Section 6.2.2. Turning to the coupling variables, the W_{OEW} has reduced by $104.2kg$, or 26.2%, while the W_f has reduced by only $2.3kg$, or 6.2%. As was the case with the low-fidelity fuel cell run, we see that the reduction in the W_{OEW} is nearly entirely responsible for the reduction in W_{MTOW}. Looking at the planform design variables, this W_{OEW} reduction is the result of a significantly smaller wing. The semi-span b_s has reduced by nearly 30%, while the aspect ratio has reduced by 15%. Interestingly, the optimised design variables of the high-fidelity case match very closely with those of the low-fidelity case of Table 6.7, except for the taper ratio, which has increased slightly in the high-fidelity case. The planform is visualised in Figure 6.14, where we see it has the lowest semi-span of all cases and is within $0.24m$ of the low-fidelity case. Unlike the other cases, which retained a relatively constant root chord, this case shows a decrease in the root chord, while showing the largest tip chord of the optimised cases. With an area of just $6.7m^2$, 42% lower than the initial wing, the high-fidelity, fuel cell optimisation produces the smallest wing of the group.

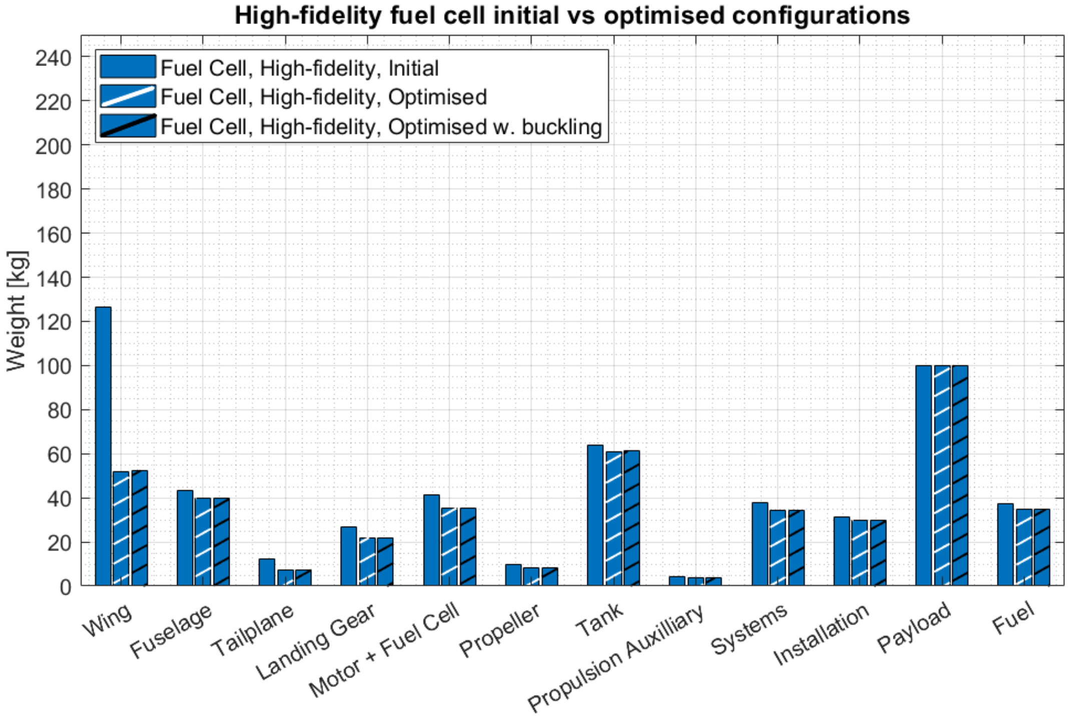

Figure 6.13: Weight breakdown of the high-fidelity, fuel cell aircraft: initial vs optimised vs optimised with a posteriori buckling constraint.

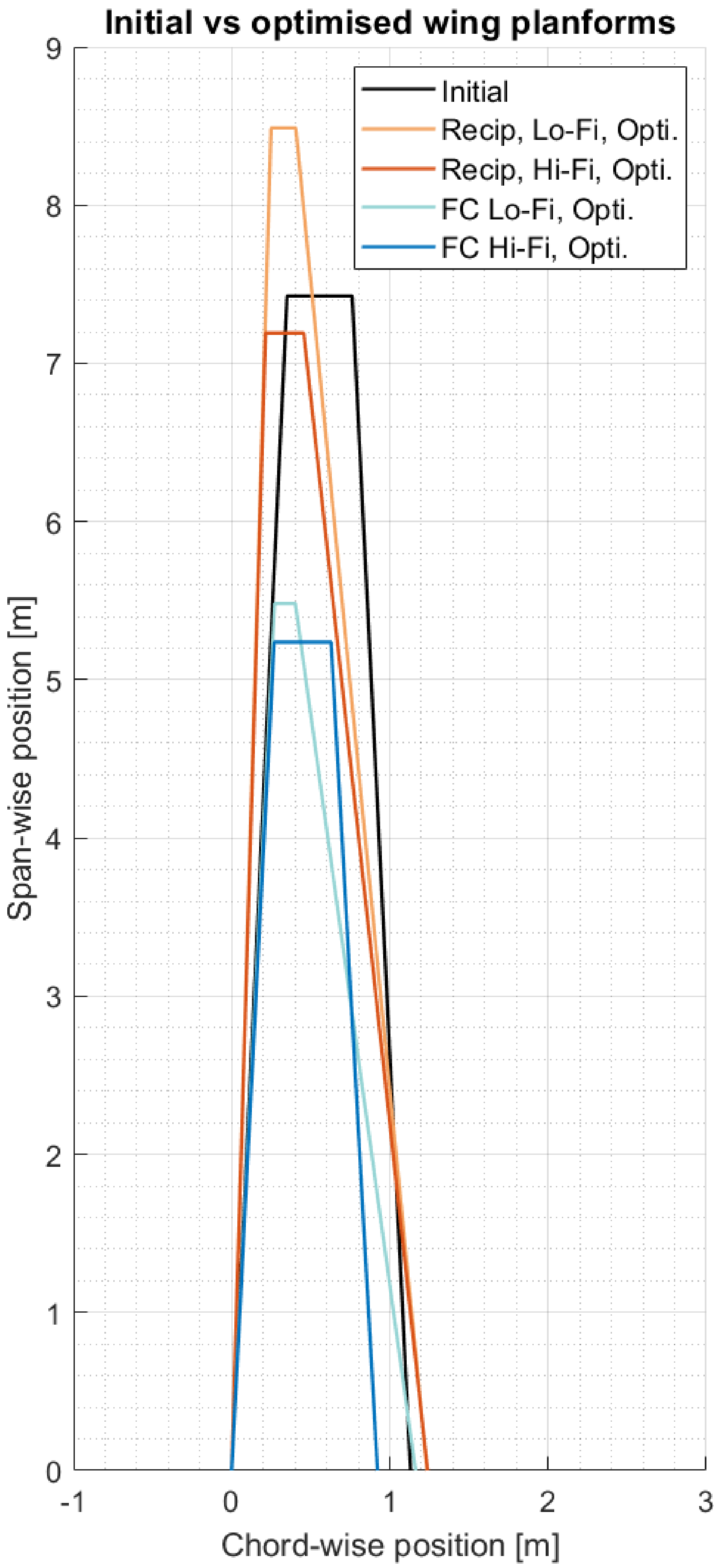

Figure 6.14: Wing planforms of the initial configuration vs optimised configurations.

6.2.2. Comparison of optimised configurations by fidelity level

The four sets of optimisation results provided above are now examined in more detail, to compare the low-fidelity against the high-fidelity results. The two reciprocating engine cases are first discussed, followed by the two hydrogen fuel cell cases.

Reciprocating engine cases

Beginning with the reciprocating engine cases, Figure 6.15 shows the normalised planform and coupling design variables at the end of the low-fidelity and high-fidelity optimisations. No wing structure sizing design variables are shown, as they do not exist for the low-fidelity case. The horizontal line at $y = 1$ represents the initial point of the normalised design variables at the beginning of the optimisation. It was deduced earlier that the low-fidelity case showed a minor W_{MTOW} reduction of 1.5%, as a result of the optimiser moving towards a more slender wing. This was achieved by increasing the semi-span b_s and aspect ratio AR, while reducing the taper ratio λ and sweep angle Λ_{LE}, seen in Figure 6.15. As is also visible in Figure 6.15, the net effect of this was a small decrease in W_f due to improved aerodynamic efficiency and a nearly negligible decrease in W_{OEW}, due to an increased wing weight counteracted by a decreased engine weight (as seen in Figure 6.10). Contrary to this, the high-fidelity case showed a small decrease in b_s, a very slight increase in AR and a significant decrease in both λ and Λ_{LE} resulting in a smaller wing (as seen in Figure 6.14) and thus a lighter wing (as seen in Figure 6.11). The net effect of this, together with respective reductions in component thicknesses, was a slightly reduced W_{OEW} and a nearly negligible change in W_f.

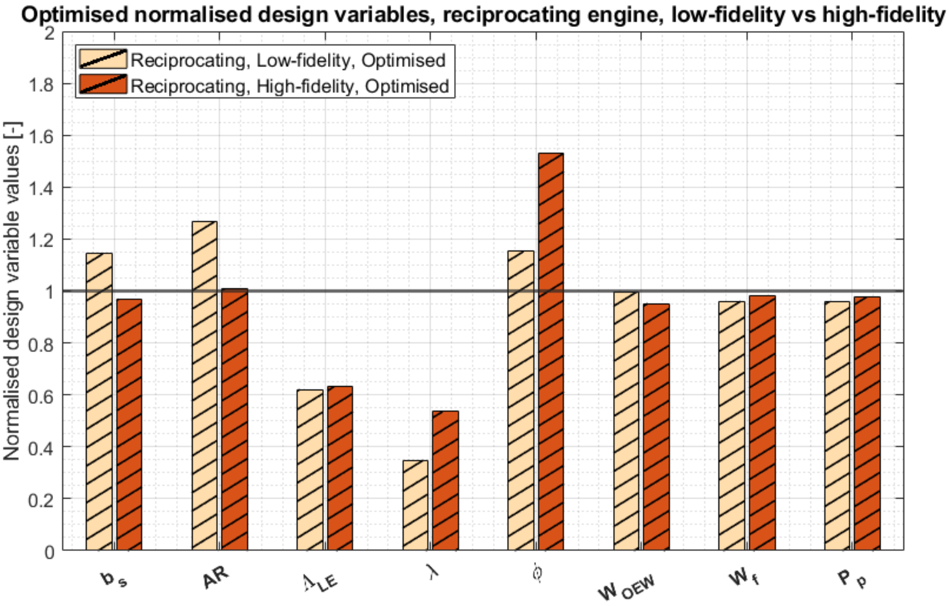

Figure 6.15: Optimised values of the normalised design variables for the reciprocating engine case, low-fidelity vs high-fidelity.

To summarise, the optimiser has travelled in the direction of better aerodynamic efficiency at the expense of a heavier wing in the low-fidelity case, while opting for a lighter wing in the high-fidelity case. This raises the question as to why the optimiser has followed two different paths in the optimisations of the two levels of fidelity. To help analyse this observation, the low-fidelity aerodynamics and class II wing weight estimation methods are revisited.

Beginning with the wing weight estimation methods, the average of Equations 4.42 and 4.43 has been taken as the wing weight in this framework. The equations are repeated below for convenience and are referred to here as those of 'Gerard' and 'Raymer' respectively.

$$W_w = 0.0038 \cdot (n \cdot W_{MTOW})^{1.06} \cdot AR^{0.38} \cdot S^{0.25} \cdot (1+\lambda)^{0.21} \cdot \left(\frac{t}{c}\right)_r^{-0.14} \quad [\text{kg}] \tag{6.2}$$

$$W_w = 1.35 \cdot S^{0.694} \cdot AR^{0.5} \cdot \left(\frac{t}{c}\right)_r^{-0.4} \cdot (1+\lambda)^{0.1} \quad [\text{kg}] \tag{6.3}$$

In order to analyse the effect of the planform design variables on these relations, the wing area S is substituted with the definition of the aspect ratio AR, $AR = \frac{b^2}{S}$, to give:

$$W_w = 0.0038 \cdot (n \cdot W_{MTOW})^{1.06} \cdot AR^{0.13} \cdot b^{0.5} \cdot (1+\lambda)^{0.21} \cdot \left(\frac{t}{c}\right)_r^{-0.14} \quad [\mathrm{kg}] \tag{6.4}$$

$$W_w = 1.35 \cdot \frac{b^{1.388}}{AR^{0.194}} \cdot \left(\frac{t}{c}\right)_r^{-0.4} \cdot (1+\lambda)^{0.1} \quad [\mathrm{kg}] \tag{6.5}$$

From the new form of these equations, it becomes clear that in the equation of Gerard, the wing weight increases with an increase in the aspect ratio, span and taper ratio. On the other hand, in the equation of Raymer, the wing weight increases with an increased span and taper but decreases with an increased aspect ratio. To visualise these relationships, Figures 6.16 and 6.17 show the normalised responses of the wing weights against a change in the normalised planform design variables. Here, each normalised design variable is individually varied while the rest remain constant, in order to show the sensitivity of the wing weight to each design variable. The baseline normalised wing weight ($y = 1$) represents the weight when the design variables are set to those of the true Predator ($x = 1$). The tip twist angle ϕ does not impact the low-fidelity runs and is thus not shown here.

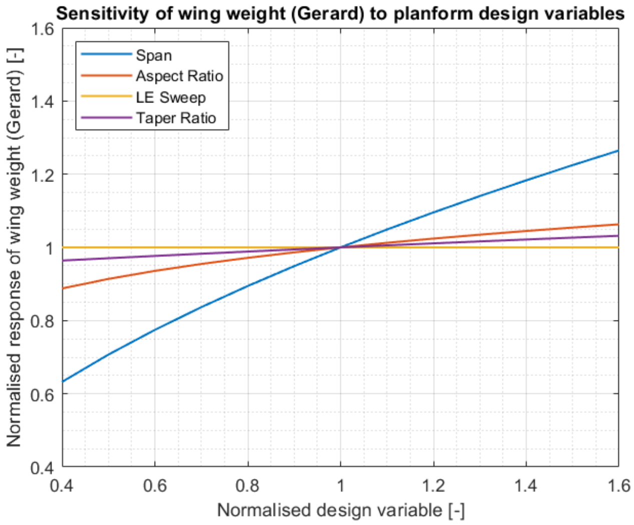

Figure 6.16: Sensitivity of the normalised wing weight responses (Gerard) to changes in the normalised planform design variables.

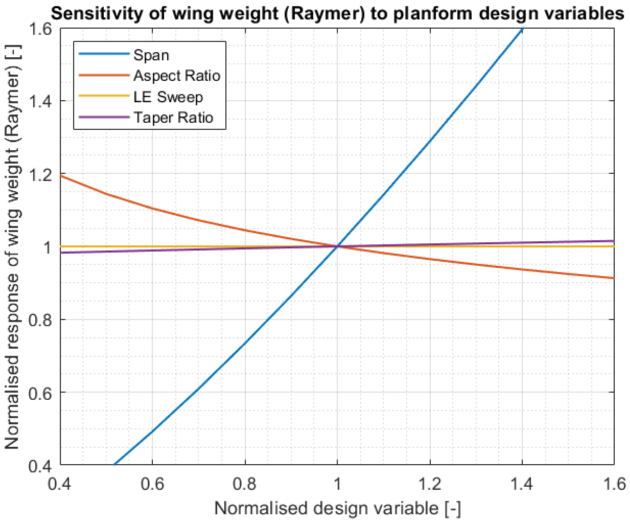

Figure 6.17: Sensitivity of the normalised wing weight responses (Raymer) to changes in the normalised planform design variables.

For both class II methods, the wing weight is most sensitive to the wing span. This is logical, as a longer wing leads to a larger moment arm which requires a stiffer and heavier structure. Next is the aspect ratio, where an increase in the aspect ratio leads to an increase in the wing weight of Gerard but a decrease in the wing weight of Raymer. Next, both wings weights are relatively insensitive to the taper ratio, with both cases increasing only slightly with an increase in taper ratio. This is in line with theory, as a larger taper ratio leads to a larger tip chord, which increases the lift distribution at the tip, creating a larger bending moment and thus requiring a stiffer structure. Lastly, both equations are completely insensitive to sweep.

As the current framework takes the average of both equations, as described in Section 4.7.1, Figure 6.18 shows the sensitivity of the total wing weight to the normalised design variables. The sensitivity of the wing weight to the span, taper ratio and sweep mirrors that of both equations. The sensitivity to the aspect ratio follows the case of Raymer, as the wing weight in this case is more sensitive to the aspect ratio as compared to the case of Gerard. Relating these sensitivities back to the optimisation results, from a weights perspective the optimiser would want to substantially reduce the wing span, while increasing the aspect ratio, in order to drive down the wing weight. Through the relation $AR = \frac{b^2}{S}$, this would result in a shorter wing with a smaller area.

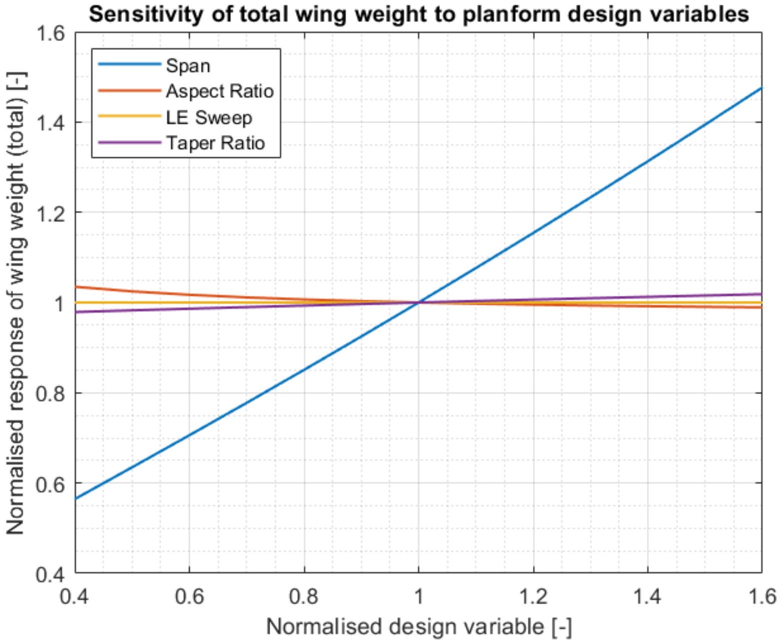

Figure 6.18: Sensitivity of normalised total wing weight responses to changes in normalised planform design variables.

Moving to the low-fidelity aerodynamics relations, the induced drag given in Equation 4.12 was:

$$C_{D,i} = \frac{{C_L}^2}{\pi ARe} \tag{6.6}$$

Figure 6.19 provides the normalised response of the induced drag $C_{D,i}$ to the normalised design variables and includes the effects of the Oswald factor e. Here, a clear inverse relationship exists between the induced drag and both the span and aspect ratio. This is in line with theory, as a longer and more slender wing leads to a reduction in the induced drag. Relating these sensitivities back to the optimisation results, from an aerodynamics perspective the optimiser would want to substantially increase both the wing span and the aspect ratio, in order to drive down the induced drag and thus reduce fuel burn. Through the relation $AR = \frac{b^2}{S}$, this would result in a longer and more slender wing with a relatively unchanged wing area.

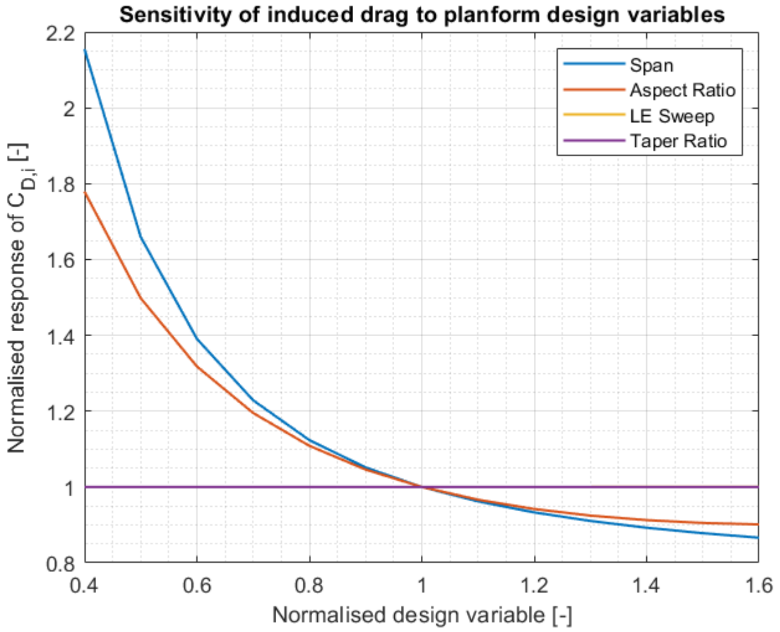

Figure 6.19: Sensitivity of normalised induced drag responses to changes in the normalised planform design variables.

The sensitivities of the low-fidelity methods to the design variables can now help explain the optimisation path taken in the low-fidelity run and why it differs from the high-fidelity optimisation path. The class II wing weight estimation methods are sensitive to span and aspect ratio, pushing the optimiser to traverse in the path of a shorter wing with a higher aspect ratio. Similarly, the aerodynamics relations are also sensitive to span and aspect ratio, however the span has an inverse relationship to induced drag, meaning a longer wing with a higher aspect ratio is desired. Therefore, both low-fidelity methods promote a higher aspect ratio, which explains why the optimiser has increased the aspect ratio by a substantial 26%. However, there is a competing requirement on the span. Ultimately, the optimiser has traversed on a path of a longer span, which suggests that the resulting reduction in induced drag has a larger effect on the fuel weight W_f than the resulting increase in the wing weight. Indeed, referring to the weight breakdown of Figure 6.10, the fuel weight has reduced by about twice as much as the wing weight has increased.

To understand why the optimiser has placed more importance on fuel weight, we look ahead to the results of the upcoming Section 6.3 on the effect of endurance. A lower induced drag has a profound effect on the fuel saved over a long endurance, 24-hour loiter mission. Figure 6.20, which plots the semi-span b_s resulting from repeating the MDO at various loiter endurances, proves this by showing that the optimised value of the span actually decreases at lower endurances, as the fuel savings brought about by a longer span begin to diminish over a shorter mission, making the wing weight increase more dominant in the selection of the optimisation path. The 'break-even' point, where the optimiser switches from opting from a shorter wing to a longer wing, seems to occur at an endurance of around 18 hours. Concluding the low-fidelity analysis then, aerodynamic consideration are more dominant than wing weight considerations at the high endurance of 24 hours.

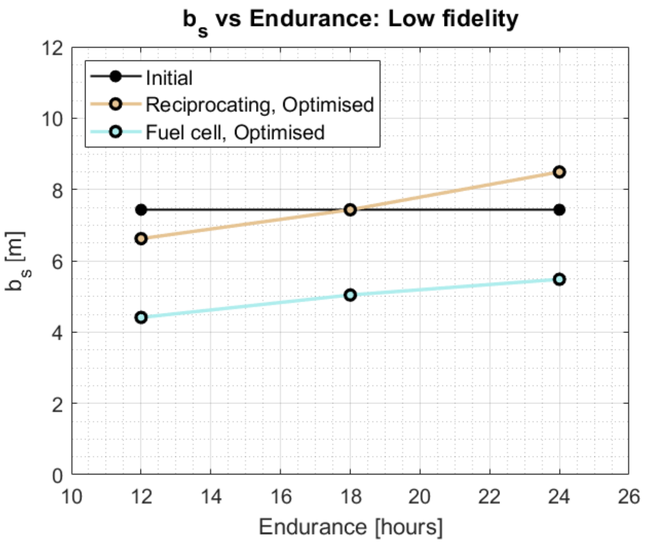

Figure 6.20: The effect of endurance on the optimised b_s, low-fidelity cases.

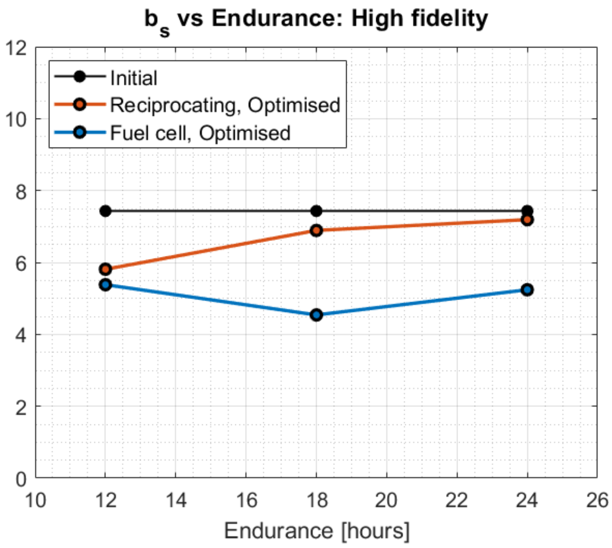

Figure 6.21: The effect of endurance on the optimised b_s, high-fidelity cases

Having analysed the low-fidelity methods, we turn our attention to the high-fidelity case, where the optimiser has opted to slightly reduce the wing semi-span b_s and increase the aspect ratio AR, in an effort to reduce the wing weight and thus the W_{OEW}. This suggests that in the high-fidelity case the reduction in wing weight is more sensitive to the semi-span than the induced drag is. As was mentioned earlier and shown in Figure 6.20, this same situation occurred in the low-fidelity case at lower values of endurance, when the wing weight reduction became more dominant than any improvements in induced drag. With this in mind, we refer to Figure 6.21, which shows the equivalent variation of the optimised value of the semi-span against endurance, now for the high-fidelity case. The same trend is observed as with the low-fidelity case, wherein the optimised semi-span reduces at lower endurances, as the reduction in wing weight becomes more dominant than the increase in induced drag. The high-fidelity line seems to be shifted down as compared to the low-fidelity line, suggesting that the 'break-even' point is at a higher endurance.

In summary then, it seems as though the difference observed in the optimisation path between the two levels of fidelity is not the result of the low and high fidelity methods behaving differently - as proven by the fact that the optimised semi-span values follow a similar relationship with endurance in Figures 6.20 and 6.21. Rather, the 'break-even' point of opting for a longer wing instead of a shorter wing takes place at a higher endurance in the high-fidelity case, or in other words, the semi-span vs endurance line is 'shifted downwards' in the high-fidelity case, as compared to the low-fidelity case. This suggests that in the high-fidelity case, the reduction in wing weight by reducing the span remains more dominant than the corresponding increase in induced drag for up to around a 24-hour loiter endurance, as opposed to an 18-hour loiter endurance in the low-fidelity case. The wing weight is thus more sensitive to the semi-span in the high-fidelity case.

This increased sensitivity to the wing weight in the high-fidelity case may be attributed to two things. Firstly, the high-fidelity optimisation's ability to control the internal structure of the wing. With six additional wing weight-related design variables at its disposal, the optimiser in the high-fidelity case has more control over the wing weight and is thus biased towards travelling in the direction of a lighter wing. The second reason for this difference may be a result of the separation of the buckling optimisation from the main MDO. By removing the buckling constraint, the optimiser was allowed to travel in a region of the design space where it could find a much lighter wing, by reducing the wing structure sizing variables. This may have biased the optimiser in seeing a steeper gradient in the direction of a lower W_{OEW} and preferring that over a more aerodynamically efficiency wing. Although the buckling constraint was later imposed on the optimised result, the MDO had already travelled to a local minimum by that point, meaning it had already settled on an optimal planform. Had the buckling functionality of CalculiX been more robust, it would have been possible to include the buckling constraint in the main MDO and another local minimum, which was not biased towards a lighter wing, may have been obtained. Having said this, even if this theory has indeed taken place, the current high-fidelity results are still very much valid - an aircraft with a 3.5% smaller W_{MTOW} has been found, which is actually better than the 1.5% reduction in W_{MTOW} of the low-fidelity results. It is simply important to caveat this result with the knowledge that the local minimum that has been obtained may have been biased by the optimisation separation and that a different local minimum may have been obtained if the buckling constraint worked as intended in the main MDO. To verify this, as a recommendation of this study, a FEA package with a more robust buckling analysis could be implemented in place of CalculiX and the results compared against the current ones.

Hydrogen fuel cell cases

Moving on to the fuel cell cases, Figure 6.22 gives the normalised planform design variables and coupling variables at the end of the low-fidelity and high-fidelity optimisations. From the diagram, it becomes clear that the design variables between the two levels of fidelity have arrived at very similar values. The exception to this is the taper ratio λ, where it has reduced substantially in the low-fidelity case but increased slightly in the high-fidelity case. For both levels of fidelity, the optimiser has taken a similar path towards a smaller, shorter and lighter wing. This has resulted in a much lighter W_{OEW} and a slightly reduced W_f (as previously discussed, the small absolute magnitude of W_f means any reduction in the normalised W_f of Figure 6.22 is in reality very small in absolute terms).

The fact that both levels of fidelity have arrived at a similar design indicates that the low and high-fidelity models are in agreement and behaving consistently. Referring again to Figures 6.20 and 6.21, one notices the same trend in the semi-span vs endurance lines of the hydrogen cases as in the reciprocating engine cases - namely, that the optimised semi-span is higher for longer endurances than it is for shorter endurances (except for the high-fidelity case at 12 hours of endurance, which seems to have terminated on a different minimum than expected). Furthermore, what is also visible is the same 'downwards shift' of the high-fidelity line as compared to the low-fidelity line. As both of these observations are seen in both the reciprocating engine and hydrogen fuel cell cases, this suggest that the low and high-fidelity methods are behaving consistently between the reciprocating engine and fuel cell cases.

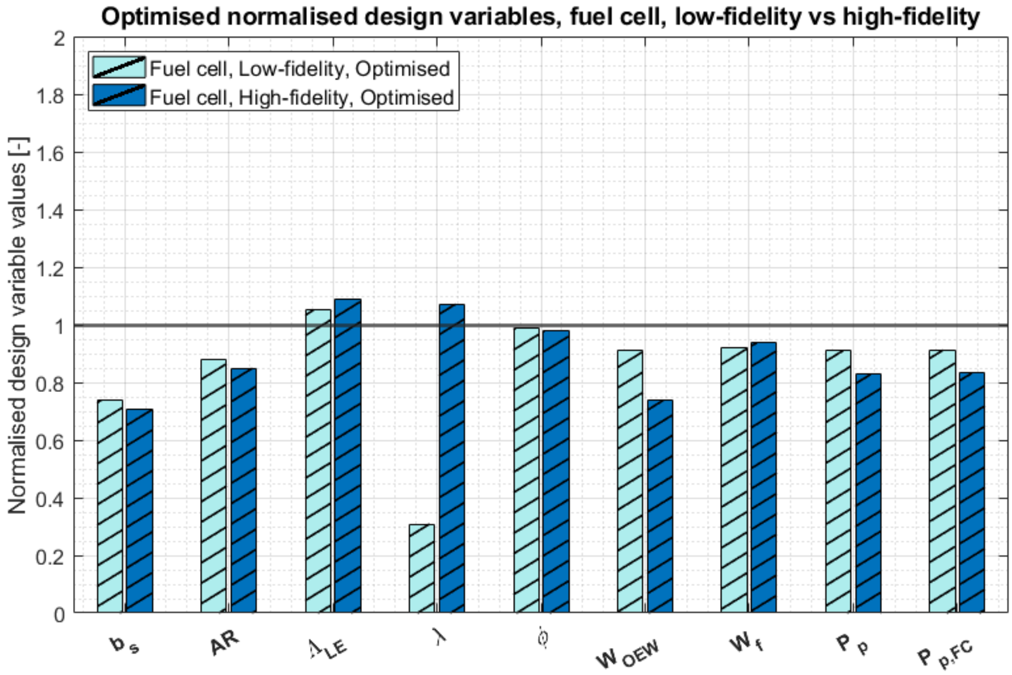

Figure 6.22: Optimised values of the normalised design variables for the fuel cell case, low-fidelity vs high-fidelity.

Why then do both levels of fidelity reach the same optimised design in the hydrogen fuel cell case, while they reach different designs in the reciprocating engine case? This is simply because the optimised values of semi-span in the reciprocating engine cases remain very close to the initial value of $7.43m$ (horizontal black line in Figures 6.20 and 6.21) and thus the 'downwards shift' of the high-fidelity line crosses the initial value. In the case of the hydrogen fuel cell runs, the optimised semi-span values are all much smaller than the initial value and hence the 'downwards shift' of its high-fidelity run does not have any major effect. In other words, the effects imparted by changing propulsion system are much larger than the effects imparted by changing the level of fidelity.

The reason why the optimised designs stay very close to the initial design in the reciprocating engine case is simply because the initial design is that of the real Predator UAV, which is a reciprocating engine-driven aircraft. It is thus expected that the MDO would not result in a substantially different design, as the same type of propulsion system is modelled. The hydrogen fuel cell case, on the other hand, is expected to produce a much different optimal design, as the initial Predator has not been designed around this type of propulsion system.

Finally, having analysed the differences in the optimised planform variables of the two levels of fidelity, the differences in the resulting weights must also be analysed. Although the hydrogen fuel cell optimal planform designs of the low and high-fidelity cases are very similar and have both resulted in a lighter W_{OEW}, the W_{OEW} of the high-fidelity case seems to have reduced more than the low-fidelity case. This is reflected in the fact that the low-fidelity optimisation resulted in a 8.8% reduction in W_{MTOW}, while the high-fidelity optimisation resulted in a 19.9% reduction in W_{MTOW}, according to Tables 6.7 and 6.8 respectively. This observation is explained with the help of the normalised weight breakdown of Figure 6.23. Here, $y = 1$ represents the normalised weights of the initial configurations. As can be seen, the weight which differs most between the low and high-fidelity results is the wing weight. The optimiser in the high-fidelity case has managed to reduce the wing weight by more than in the low-fidelity case. This is a result of a) the optimiser having six additional wing structure sizing design variables at its disposal, which has allowed it to not only reduce the wing weight through a smaller planform but also through a correspondingly thinner wing structure and b) the class II wing weight estimation methods not being applicable to the optimised hydrogen fuel cell-powered aircraft, which are vastly different cases than the data points used to develop said estimation methods. This is also proven by the fact that the relation of Gerard was developed for wing spans between $13.4m < b < 26.4m$, which is larger than the $8.8m$ to $10.9m$ optimised spans of the low-fidelity fuel cell cases. This showcases the strength of higher-fidelity, physics-based approaches in an optimisation framework, where planform designs are expected to change drastically and even to design points outside the realms of applicability of a given empirical relation.

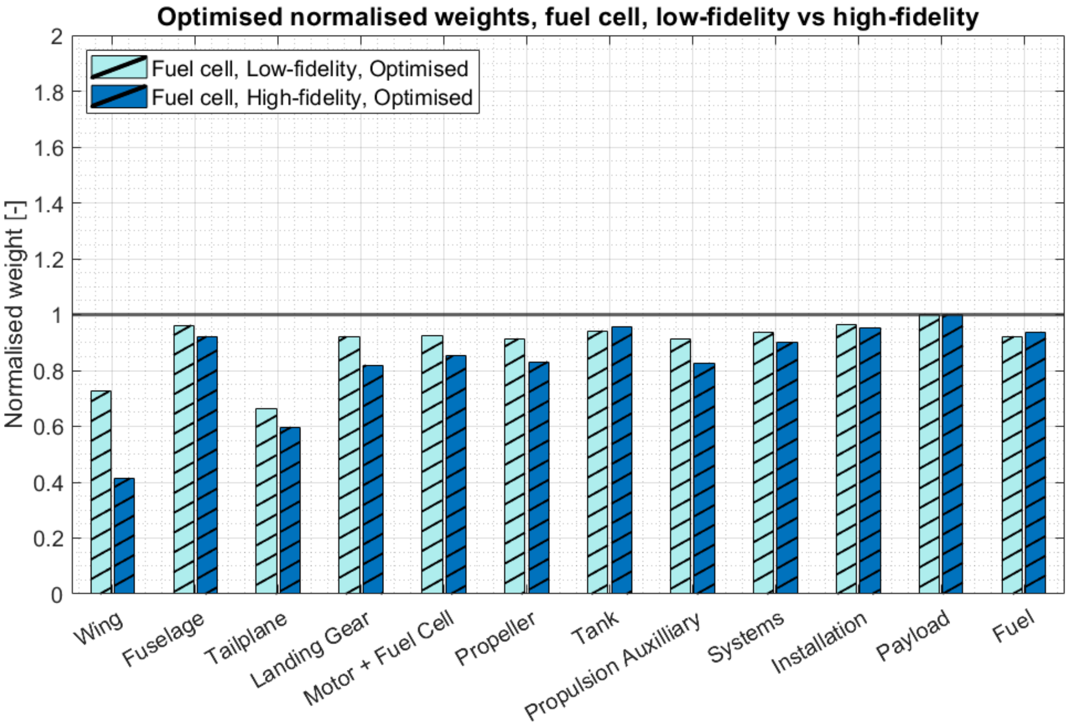

Figure 6.23: Normalised weight breakdown of the optimal configurations with fuel cell, for the low-fidelity and high-fidelity modelling.

6.2.3. Comparison of optimised configurations by propulsion system

Having compared the results by fidelity level, they are now compared by propulsion system in this section. Beginning with the low-fidelity cases, Figure 6.24 shows the normalised design variables at the end of the optimisations of the reciprocating engine and fuel cell cases. All planform design variables have changed in opposite directions with respect to their initial values, except for the taper ratio λ. The wing semi-span b_s and the aspect ratio AR have increased in the reciprocating engine case, while the same parameters have both decreased for the fuel cell case. As was mentioned previously, the low-fidelity reciprocating engine optimisation has tended towards a longer and more slender wing, in an effort to improve the aerodynamic characteristics of the wing and thus reduce the fuel weight required. This is also understood by referring to the coupling variables in Figure 6.24, where the W_{OEW} is nearly unchanged and nearly all of the weight reduction has stemmed from the decrease of W_f. In contrast, the optimiser in the fuel cell case has tended towards a shorter and less slender wing, in an effort to reduce the wing weight. These results are logical, as the $W_f = 229.4kg$ fuel weight of the reciprocating engine model's initial configuration constitutes around 30% of the total $W_{MTOW} = 777.9kg$, while on the other hand the fuel cell model's initial configuration features a W_f of just $46.3kg$, which is a mere 9% of its $504.4kg$ W_{MTOW}. As a result, more weight reduction is realised for the reciprocating engine case by achieving a lower fuel weight, while a structural wing weight reduction is more beneficial in the fuel cell case.

The leading-edge sweep Λ_{LE} reduces slightly for the reciprocating engine case and increases slightly for the fuel cell cases. However, as was mentioned previously, these changes are negligible considering the initial value of 2.7^o. The taper ratio decreases nearly equally for both cases, to a normalised value of about 0.35 or a non-normalised value of 0.12 based on an initial non-normalised taper ratio of 0.36. As was discussed in Section 6.2.2, the decrease in taper ratio for the reciprocating engine case is likely a result of the optimiser tending towards a more slender wing for improved wing aerodynamics. In the fuel cell case, however, the decrease in taper ratio is likely another design variable the optimiser utilised in order to reduce the overall wing area and thus achieve a lighter wing. Lastly, the twist angle ϕ sees nearly no change in either case, as it has no effect on the low-fidelity aerodynamic method, which does not capture its effects.

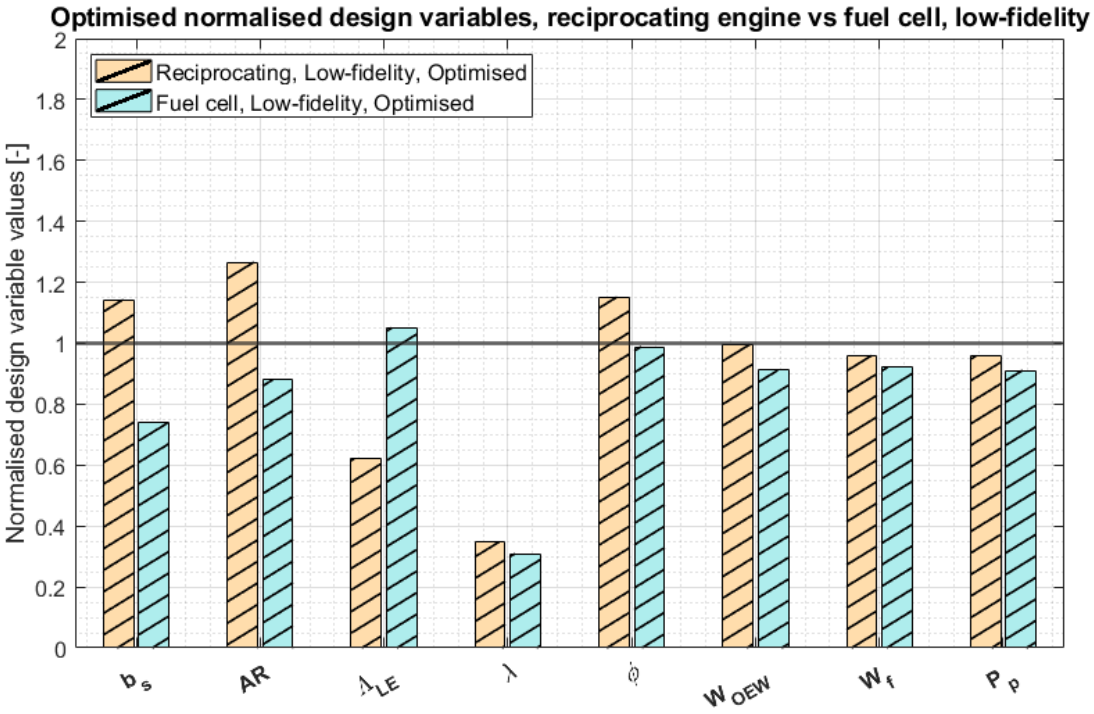

Figure 6.24: Optimised values of the normalised design variables for the reciprocating engine and fuel cell cases, low-fidelity.

Moving on to the high-fidelity optimisations, Figure 6.25 shows the normalised design variables at the end of the optimisations of the reciprocating engine and fuel cell cases. As was discussed in Section 6.2.2, the optimiser tends towards a smaller and lighter wing for both the high-fidelity reciprocating engine case and the high-fidelity fuel cell case. This is also evident in the design variable changes of Figure 6.25. Here, b_s reduces for both cases, albeit much more for the fuel cell aircraft and only slightly for the reciprocating engine aircraft. Similarly, AR changes only slightly in the reciprocating engine case, whereas a more substantial change is seen for the fuel cell case. Furthermore, the taper ratio for the reciprocating engine case reduces substantially, while it increases slightly in the fuel cell case (although this is the effect of the root chord decreasing in this case). The effect of these three design variables results in a wing area of $10.6m^2$ and $6.7m^2$ respectively, which is 7.8% and 42% lower than the initial wing area of $11.5m^2$. Together with the wing weight reduction from smaller planforms, reductions in the structural thickness variables lead to further reductions in the wing weight, as was discussed in Section 6.2.2. Ultimately, by referring to the coupling variables of Figure 6.25, a reduction in W_{OEW} is the dominant form of decrease in W_{MTOW}.

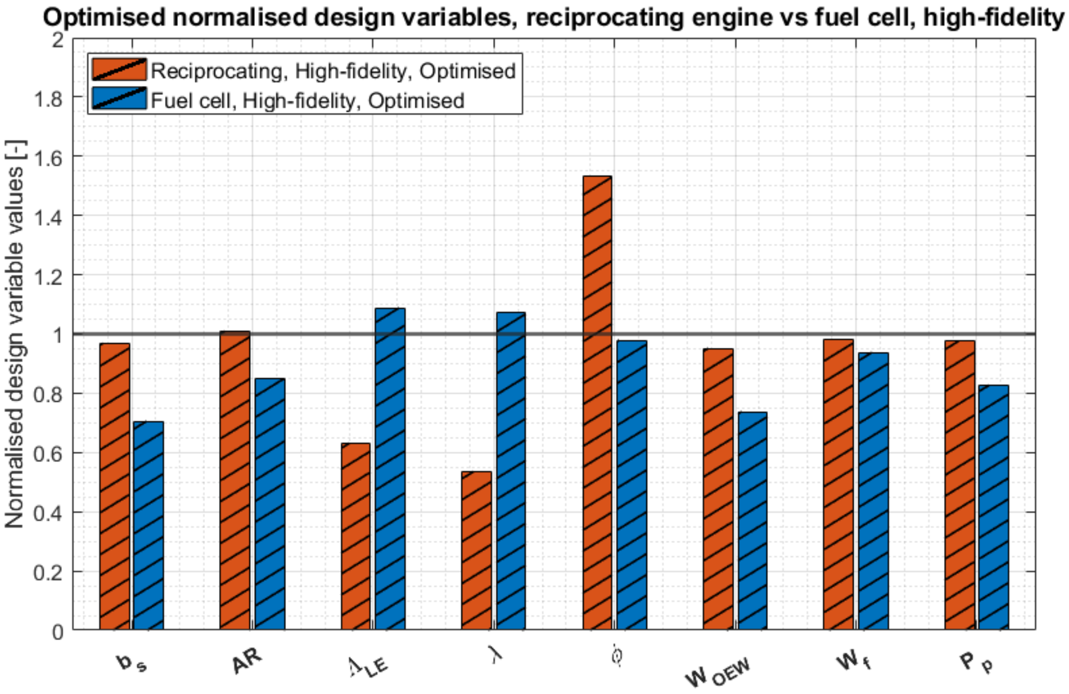

Figure 6.25: Optimised values of the normalised design variables for the reciprocating engine and fuel cell cases, high-fidelity.

6.2.4. Comparison of optimised configurations with real MALE UAV data

As was done with the initial configurations, it is interesting to see how the optimised configurations compare against other UAVs of the MALE class. Figures 6.26 and 6.27 are the same W_{OEW} vs W_{MTOW} and W_f vs W_{MTOW} plots of Figures 6.8 and 6.9, respectively, but with the four optimised configurations added. In agreement with the results analysed so far, the low-fidelity reciprocating engine case shows very little change in its W_{OEW} vs W_{MTOW}, as the small 1.5% W_{MTOW} reduction was achieved through improving the aerodynamic efficiency. This is why its plot of W_f vs W_{MTOW} sees more of a reduction. While it aligns very well with the trend-line in the W_{OEW} vs W_{MTOW} plot, it is still significantly above the W_f vs W_{MTOW} trend-line, as was the case for its initial configuration. This reinforces the earlier suggestion that the low-fidelity aerodynamic model does not accurately capture the aircraft's aerodynamic performance. The high-fidelity reciprocating optimal configuration, on the other hand, aligns closely with both trend-lines. Both its W_{OEW} and W_f have decreased along the respective trend-lines, rather than away from them, suggesting that the high-fidelity optimisation behaves well in comparison to general MALE UAV trends.

Moving on to the fuel cell cases, the low-fidelity optimal configuration sees a substantial decrease in its W_{OEW}, as its weight savings stemmed from a lighter wing weight. Its W_{OEW} is still substantially above the trend-line, because of the disproportionately low hydrogen fuel weight required. The high-fidelity fuel cell case sees a very dramatic decrease in its W_{OEW} (again along the W_{OEW} vs W_{MTOW} trend-line), even more so than the low-fidelity case. This is due to the substantial wing weight reduction, achieved through the addition of the wing structure sizing variables. All four fuel cell configurations align very well with respect to each other in the W_{OEW} vs W_{MTOW} plot of Figure 6.26, and show a similar gradient to the trend-line, albeit at a vertical offset from the trend-line because of their high specific energy hydrogen fuel. On the other hand, in the W_f vs W_{MTOW} plot of Figure 6.27, the optimised configurations have moved horizontally to the left from their initial configurations, as a result of their W_{MTOW} reducing dramatically through W_{OEW} but their absolute W_f remaining relatively constant.

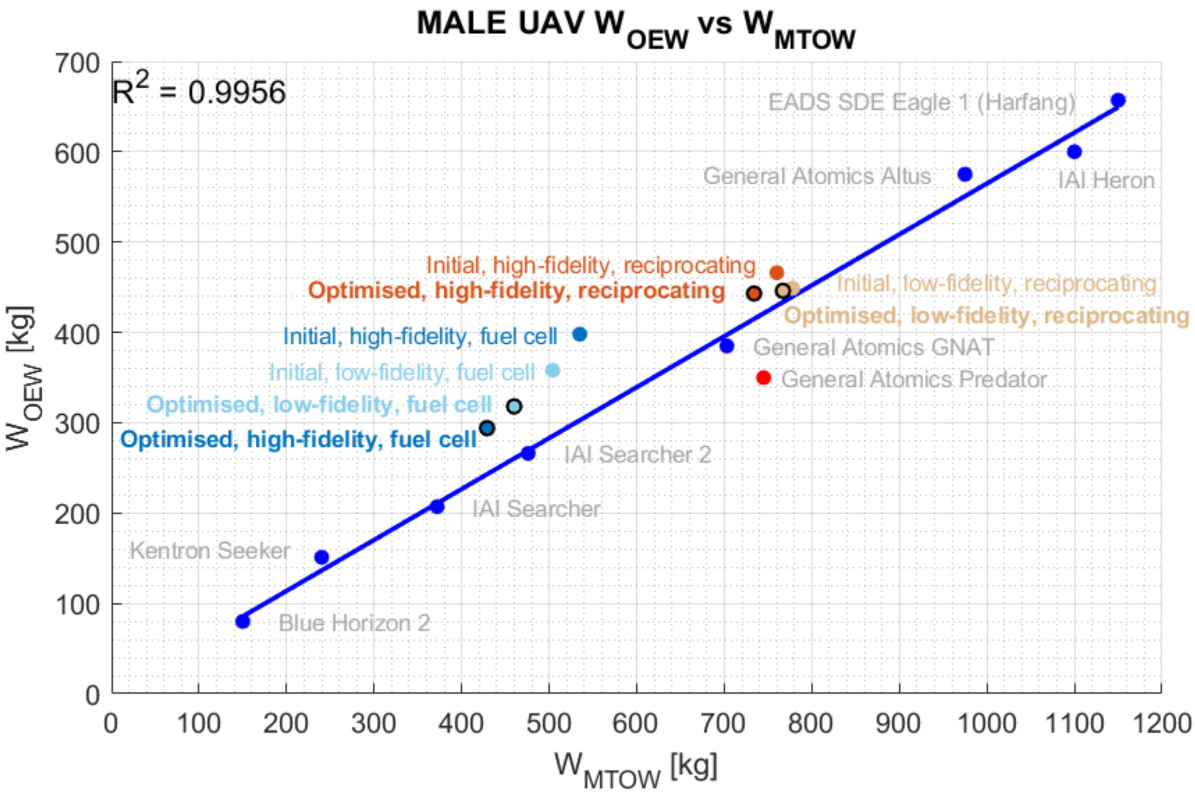

Figure 6.26: W_{OEW} vs W_{MTOW} for eight MALE UAVs, along with the respective linear trend-line. The initial and optimised low-fidelity and high-fidelity modelled Predator outputs, for the reciprocating engine and fuel cell cases, are also plotted. Data from [17].

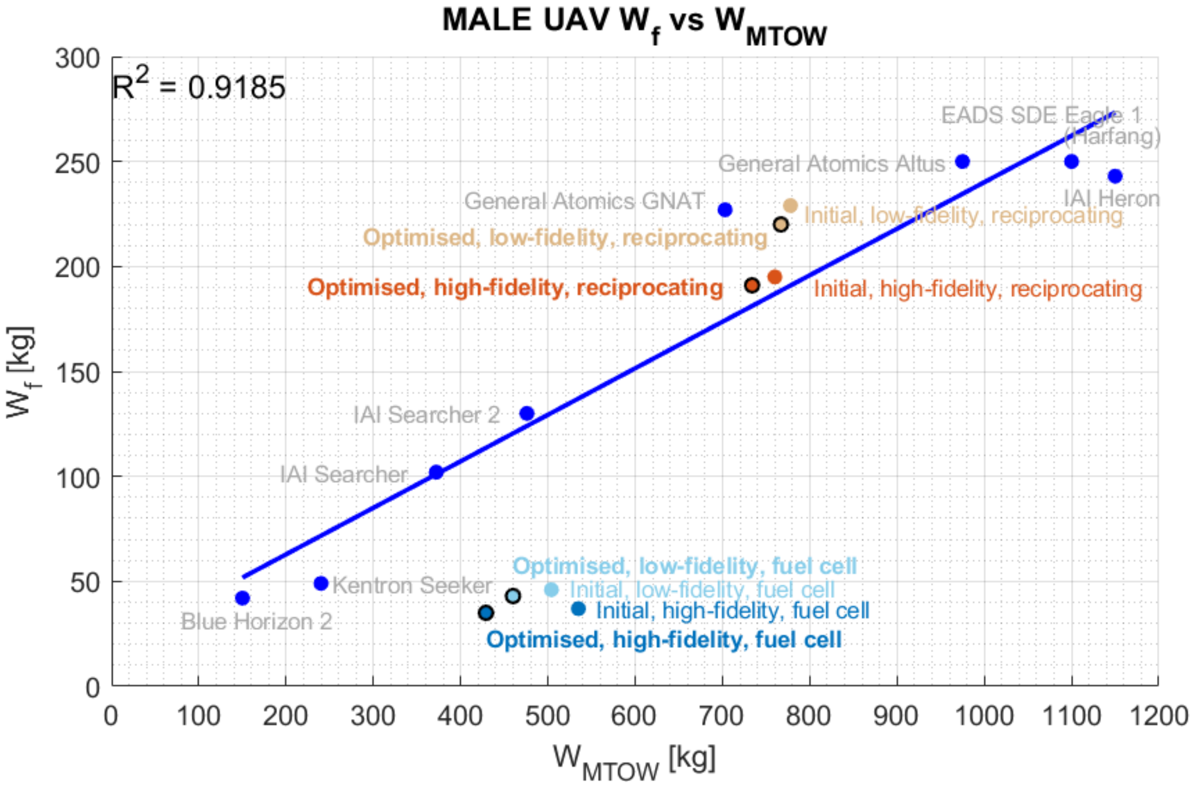

Figure 6.27: W_f vs W_{MTOW} for eight MALE UAVs, along with the respective linear trend-line. The initial and optimised low-fidelity and high-fidelity modelled Predator outputs, for the reciprocating engine and fuel cell cases, are also plotted. Data from [17].

6.3. Effect of Endurance

An aircraft's take-off weight, W_{MTOW}, is one of its key defining characteristics. In this framework, W_{MTOW} has been used as the objective function of the optimisations. When discussing the MALE UAV class, another key parameter of interest is that of aircraft endurance. The results analysed so far have only concerned a single endurance of 24 hours, which is the typical endurance of many large-scale MALE UAVs. In order to investigate the effect of endurance on the optimised shape of a MALE UAV, the optimisations have been repeated for endurances of 12 and 18 hours, to produce an analysed endurance range of 12-24 hours, which is the typical endurance window for most MALE UAVs. These additional optimisations concern both the low-fidelity and high-fidelity methods, for the reciprocating engine and hydrogen fuel cell propulsion system models. This resulted in a total of 12 sets of optimisation results, including the results of the 24 hours endurance runs presented thus-far. Similarly to the 24-hour endurance case, the battery initial configurations did not converge even at lower endurance values and thus no MDO runs could be conducted for them. In response to this, an additional study on battery-powered propulsion is presented in the upcoming Section 6.4.

Figures 6.28 and 6.29 show the variation of W_{MTOW} with endurance for the low and high-fidelity methods respectively. In these plots, the converged W_{MTOW} values of the initial configurations are presented, along with the optimised W_{MTOW} values. Beginning with the reciprocating engine cases, both plots show an approximately linear decrease in W_{MTOW} with a reduction in endurance for the initial and optimised configurations, as one would expect. Furthermore, the reduction in W_{MTOW} between the initial and optimised configurations becomes more pronounced when reducing the endurance. This is also expected, as the initial configuration of the Predator was designed for an endurance of at least 24 hours and thus at lower endurances optimal configurations will be further from their initial point within the design space. The low-fidelity and high-fidelity results are very much in agreement, however the high-fidelity results show more of an optimised reduction in W_{MTOW} at lower endurances. This same trend is seen in the W_{OEW} vs endurance plots of Figures 6.30 and 6.31, which points to this being the result of the optimiser having the freedom to not only reduce the wing size through the planform variables but also generate a corresponding reduction in the wing structure sizing variables, as a smaller wing requires a less stiff structure. Indeed, when analysing the wing weights across the difference endurances, it becomes clear that the wing weight reduction is responsible for this trend.

Moving on to the fuel cell results within the same figures, linear reductions of W_{MTOW} with a reduction in endurance are also noted. However, the gradient of reduction is not as steep as the reciprocating engine cases. This is the result of the hydrogen fuel weight being significantly lower than the weight of gasoline and as a result decreasing by a smaller absolute amount between different endurances. This is seen in Figures 6.32 and 6.33, in which the W_f is plotted against endurance. While both gasoline and hydrogen fuel weights have reduced by more than 50% between the 24-hour and 12-hour endurances, the gasoline weight has reduced by approximately $100kg$, while the hydrogen weight by only about $20kg$. The W_{MTOW} trends of the high-fidelity fuel cell case show a slightly heavier initial configuration than the low-fidelity case, as a result of the increased W_{OEW}/W_f ratio discussed earlier. On the other hand, the high-fidelity optimised configuration trend shows a stronger W_{MTOW} reduction from the initial configuration than the low-fidelity optimised trend, again as a result of the optimiser being able to vary the wing component thicknesses but also because of the fact that the optimiser has traversed to short spans for which the class II weight estimation methods are not valid, as was discussed in Section 6.2.2.

Figures 6.34 through 6.43 present the variation of the optimised design variables with endurance. Figures 6.34 and 6.35 show the variation in optimised semi-span b_s with endurance. These results have already been analysed in Section 6.2.2 and aided in the comparison of the two levels of fidelity. The aspect ratio AR trends in Figures 6.36 and 6.37 show a gradual reduction with a smaller endurance in the low-fidelity cases. In the high-fidelity cases, the reciprocating engine runs seem to remain relatively close to the initial aspect ratio, while the fuel cell cases see a major reduction at 18 hours of endurance and then a bounce back to approximately 20 at 12 hours of endurance. As seen in Figures 6.38 and 6.39, the leading-edge sweep angle Λ_{LE} in all cases remains relatively constant, around 3^o, showing no sensitivity to endurance, due to the aircraft flying in the low subsonic regime. In Figure 6.40 the taper ratio λ remains relatively constant across the endurance window, while in Figure 6.41 it tends to increase with a reduction in endurance. The straight-line behaviour in the low-fidelity case is attributed to the fact that the low-fidelity aerodynamic method is not able to accurately capture the effects of changing the taper ratio and thus the optimiser seems to reduce the taper ratio such that the wing weight is minimised in accordance with the sensitivity given in Figure 6.18. Finally, the tip twist angle ϕ sees nearly no change in the low-fidelity case of Figure 6.42, while also remaining relatively constant, but still changing, in the high-fidelity case. The lack of change in the low-fidelity case is the result of the low-fidelity aerodynamic methods not capturing the effects of the twist angle at all - the design variable is in effect not used. On the other hand, in the high-fidelity case these effects are captured but ϕ is relatively insensitive to endurance.

While all the optimisation results presented here have W_{MTOW} as the objective function, with the endurance varying as a constant between individual runs, it would also be interesting in future work to reformulate the optimisation problem and have the maximisation of endurance as the objective function. Therefore, a future recommendation of this work is to modify the optimisation scheme and alter the mission definition in such as way as to facilitate the endurance being the objective function. This will allow for the generation of new optimal designs which may then be compared against the designs presented in the current study.

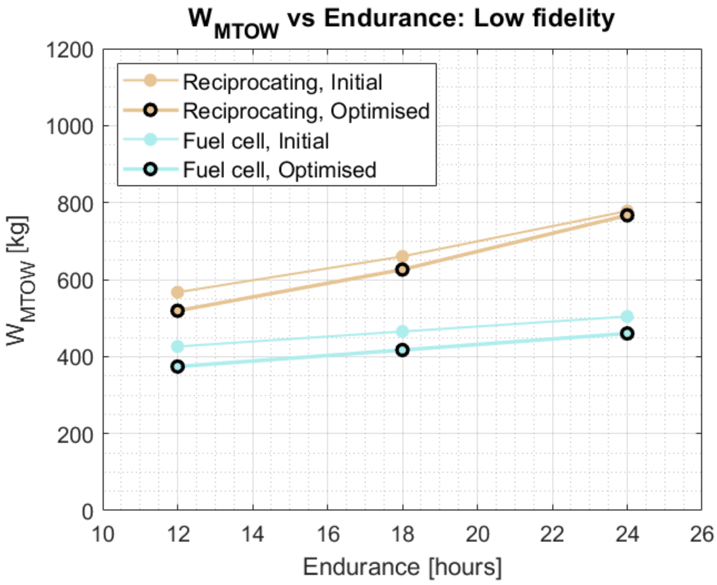

Figure 6.28: The effect of endurance on W_{MTOW}, low-fidelity cases.

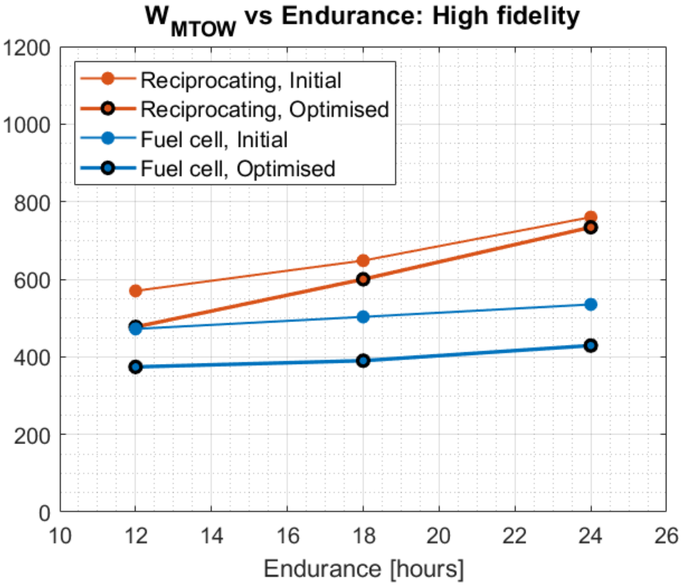

Figure 6.29: The effect of endurance on W_{MTOW}, high-fidelity cases

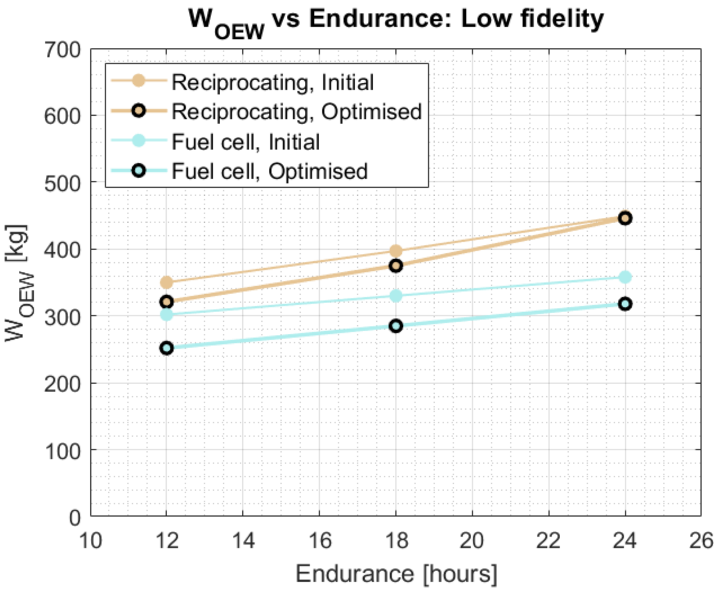

Figure 6.30: The effect of endurance on W_{OEW}, low-fidelity cases.

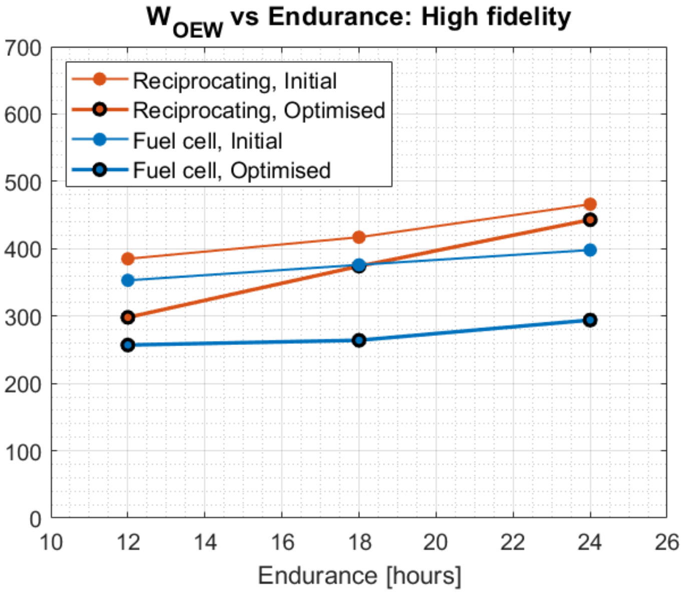

Figure 6.31: The effect of endurance on W_{OEW}, high-fidelity cases

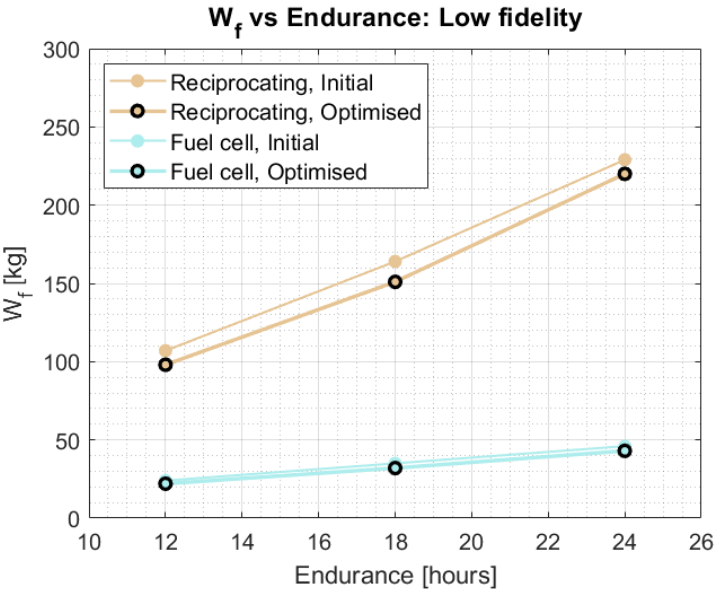

Figure 6.32: The effect of endurance on W_f, low-fidelity cases.

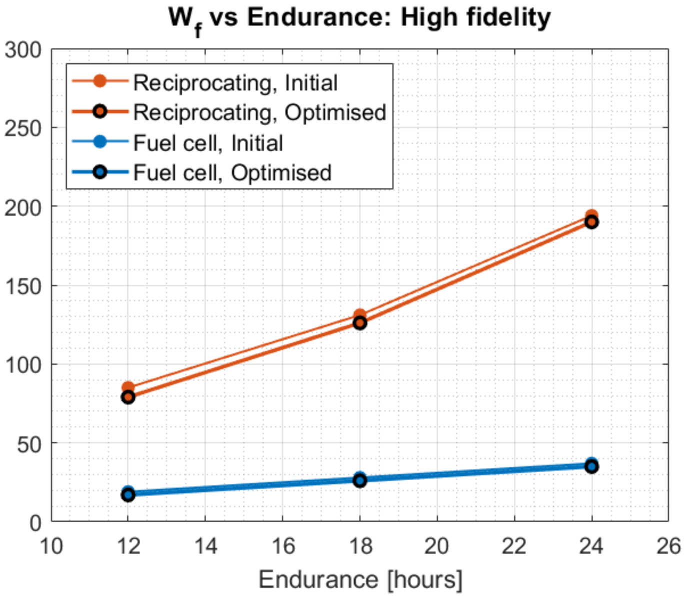

Figure 6.33: The effect of endurance on W_f, high-fidelity cases

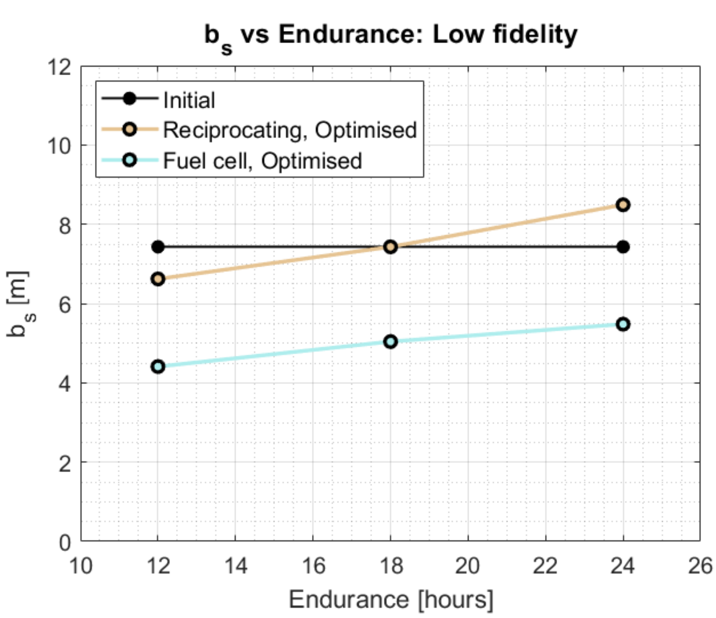

Figure 6.34: The effect of endurance on the optimised b_s, low-fidelity cases.

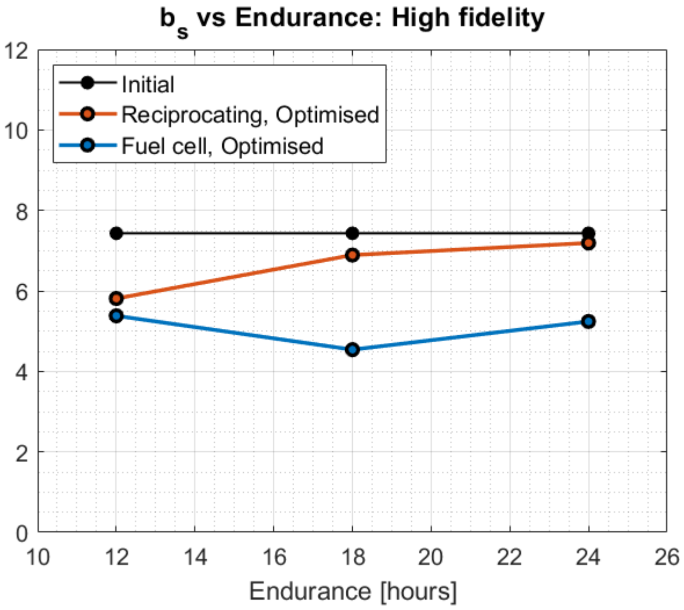

Figure 6.35: The effect of endurance on the optimised b_s, high-fidelity cases

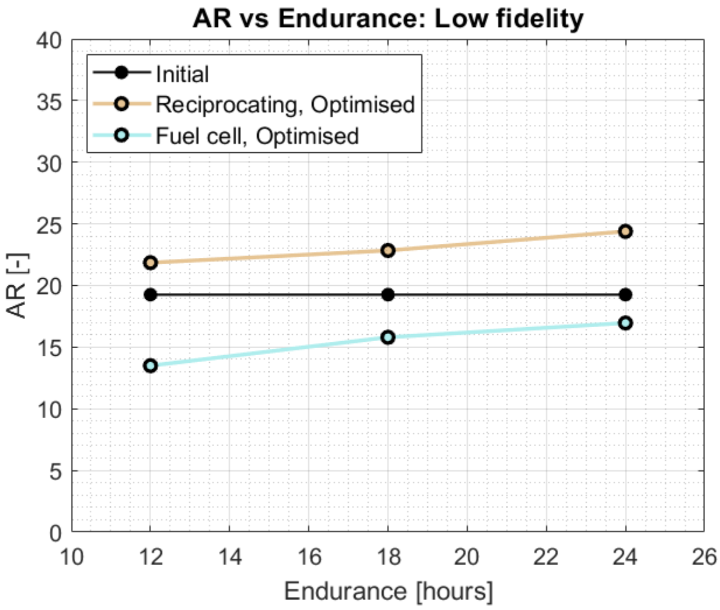

Figure 6.36: The effect of endurance on the optimised AR, low-fidelity cases.

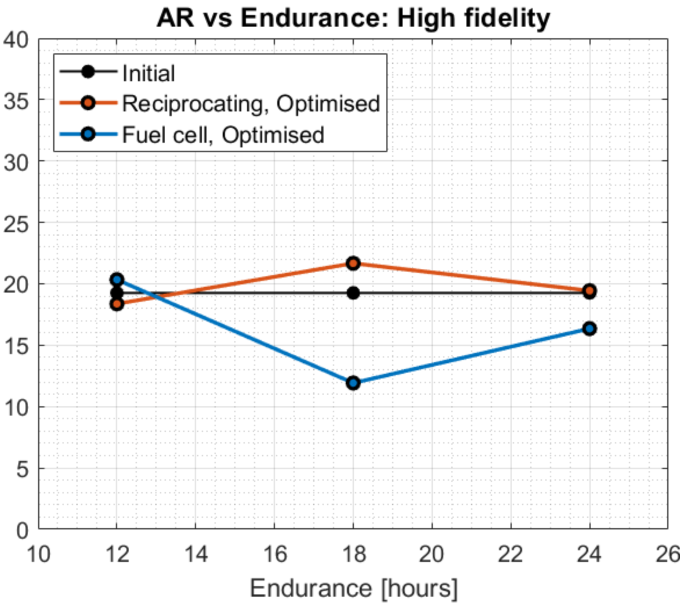

Figure 6.37: The effect of endurance on the optimised AR, high-fidelity cases

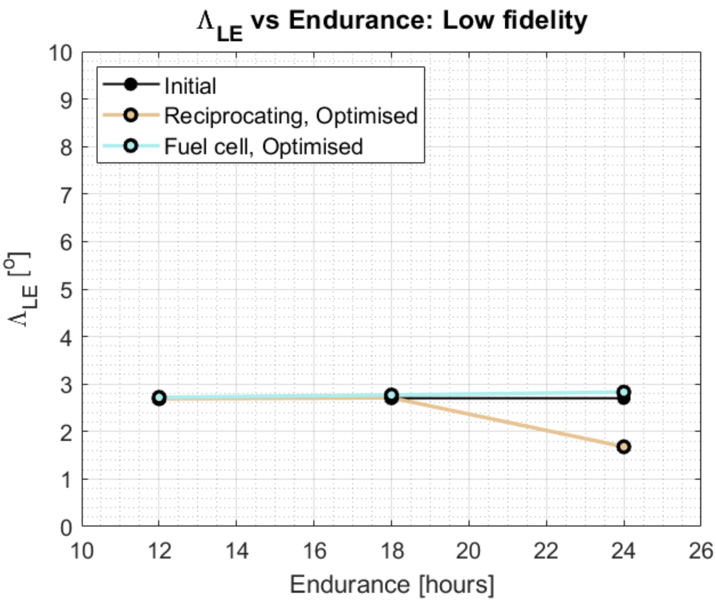

Figure 6.38: The effect of endurance on the optimised Λ_{LE}, low-fidelity cases.

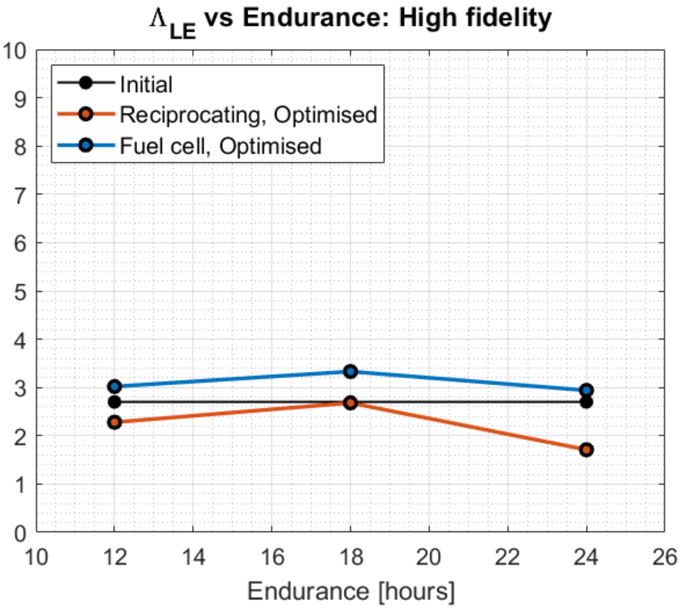

Figure 6.39: The effect of endurance on the optimised Λ_{LE}, high-fidelity cases

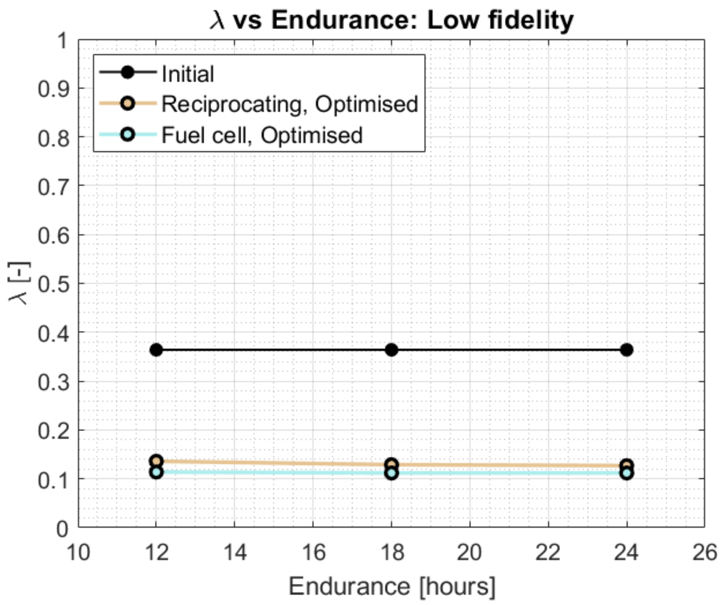

Figure 6.40: The effect of endurance on the optimised λ, low-fidelity cases.

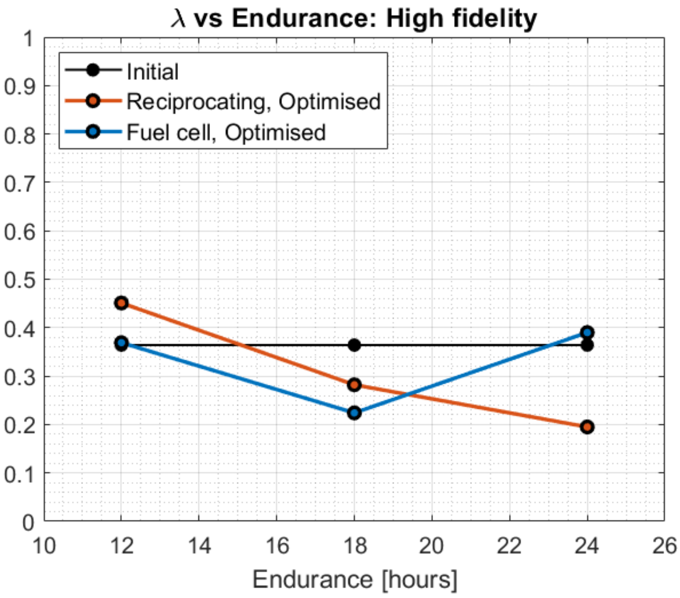

Figure 6.41: The effect of endurance on the optimised λ, high-fidelity cases

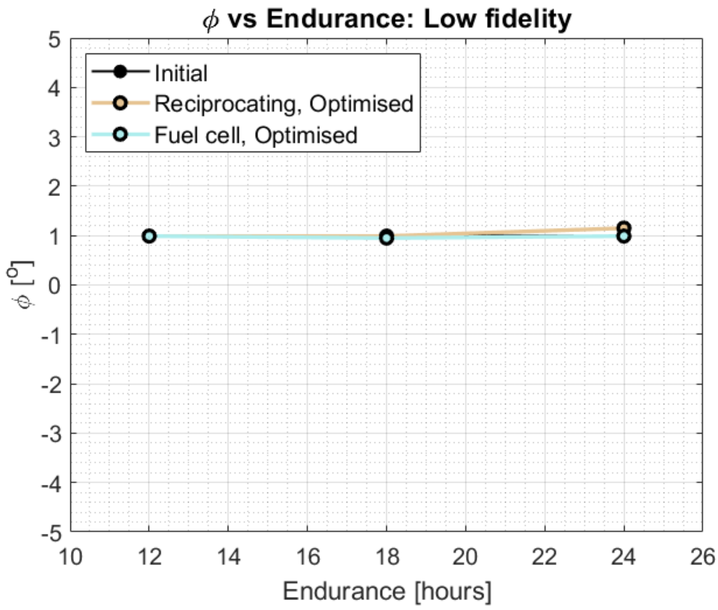

Figure 6.42: The effect of endurance on the optimised ϕ, low-fidelity cases.

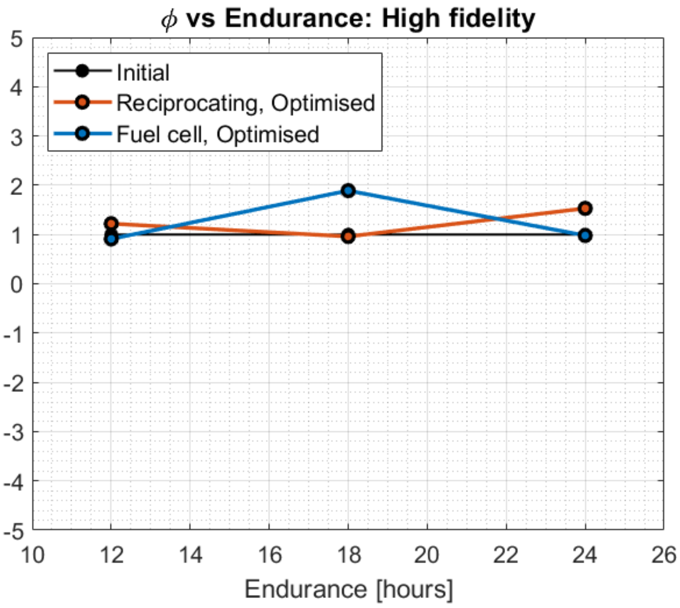

Figure 6.43: The effect of endurance on the optimised ϕ, high-fidelity cases

6.4. Additional Battery Study

As discussed in Section 6.1, the low and high-fidelity battery cases did not yield a solution for the initial configuration. This was the result of the required battery capacity increasing continuously during the convergence process, resulting in a battery weight with exponential growth. As was further mentioned in Section 6.1, this outcome follows the findings of Chapter 2: Literature Study - namely that batteries are severely disadvantaged by a significantly lower specific energy than hydrogen or hydrocarbon fuels. These findings suggest that a feasible design space does not currently exist for battery-powered MALE UAVs with current battery technologies. In this section, further analysis is conducted to expand the explored design space, in order to identify the level of battery technology improvement required for a feasible design to emerge.

As a first attempt in expanding the design space, the specific energy is maintained at current levels, while the mission loiter duration is progressively lowered from 24 hours down to zero hours, to determine whether a lower endurance would yield a feasible design at current specific energy levels. Although the rate of weight increase did reduce throughout the convergence process as the endurance was lowered, the W_{MTOW} still ultimately diverged for all endurances down to zero hours. Lowering the loiter duration to zero hours results in a total flight time of approximately 90 minutes from all other non-loiter mission phases. Hence, current battery specific energy levels did not yield a feasible design for a 90-minute flight at $20,000 ft$, with no loiter phase.

In a second attempt, the loiter duration is maintained at zero hours, while the specific energy of the battery is increased progressively until a feasible design emerges for a 90-minute flight. When increasing the specific energy, it is important to remember the contribution of the battery cell and battery system characteristics to the effective specific energy. In future, it is expected that both the cell specific energy and the system-to-cell efficiency factor will improve, as battery cell technology improves and battery/thermal management systems become lighter. To capture the effects of improvements in both the cell specific energy and the system-to-cell efficiency factor (which was taken as 0.84 in this study, as described in Section 4.8.4), the C-rate vs specific energy data provided by Verstraete and shown in Figure 4.40 is replaced with an effective specific energy on a battery system level, which includes the system-to-cell efficiency factor. Therefore, for the remainder of this report, the term 'specific energy' refers of the specific energy of the battery on the system level, not on the cell level, and implicitly includes the system-to-cell efficiency factor.

This second attempt, with no loiter, resulted in a converged design only for system specific energy values of $230 Wh/kg$ and higher. At $230 Wh/kg$, the resulting W_{MTOW} was $1215 kg$, with a W_{OEW} of $611 kg$ and a battery weight W_{bat} of $604 kg$. This nearly 50% battery weight fraction is substantially higher than the fuel weight fraction of 26% - 30% for the reciprocating engine case, showcasing just how heavy the battery would need to be in order to fly for just 90 minutes. Making direct comparisons of this result to existing battery-powered aircraft like the Airbus E-Fan and Pipistrel Alpha Electro is not appropriate, as these aircraft are designed for much lower altitudes than the $20,000 ft$ of a MALE UAV. However, considering that these two aircraft have system-level specific energies of $174 Wh/kg$ and $198 Wh/kg$ respectively (as calculated in Section 4.8.4), endurances of about 60 minutes and substantially shorter high-power climb phases, it is within reason to suggest that the electric Predator with $230 Wh/kg$ can achieve 90 minutes of flight time while featuring a more intensive climb phase.

A system-level specific energy of $230 Wh/kg$ required for the simulated 90-minute medium-altitude, *short-endurance* flight, may be possible in the near future, as current battery-powered aircraft like the E-Fan and Alpha Electro already feature about 76% to 86% of this specific energy respectively, while battery systems see a yearly increase in system-level specific energy of roughly $8 Wh/kg$ per year [131] (in the automotive industry, assuming here that battery systems for aeronautical applications will follow similar trends). However, considering the W_{MTOW} of $1215 kg$ resulting from just a 90-minute medium-altitude flight, $230 Wh/kg$ seems to be nowhere near sufficient for medium-altitude, *long-endurance* flight.

Having now identified a baseline for which a battery-powered Predator UAV may exist (albeit for only a 90-minute flight with zero loiter flight), a third attempt at identifying feasible battery-powered designs is undertaken by varying both the endurance and the system-level specific energy. In a first stage, this is done for specific energies of $230Wh/kg$ to $350Wh/kg$, technology levels which may well be achievable in the future, and for loiter durations of zero to 60 minutes, representing medium-altitude, short-endurance flight. In a second stage, this is extended to theoretical specific energies of $1000Wh/kg$ to $3000Wh/kg$, which will most probably never be achieved with lithium-ion technology, and for loiter durations of 6 to 24 hours, to determine which theoretical specific energy would be needed to enable medium-altitude, long-endurance flight.

Figure 6.44 shows the resulting W_{MTOW} against loiter durations of zero to 60 minutes, incremented in 15 minute intervals, with specific energy levels varying from $230Wh/kg$ to $350Wh/kg$. As was mentioned previously, the configuration of $230Wh/kg$ and no loiter - hence only a 90-minute flight time - resulted in a W_{MTOW} of $1215kg$ and is shown in the top left of the figure. This represents the lower limit of specific energy required for the framework to converge to a feasible (although very heavy) design. Any increase in the loiter duration by 15 minutes or more at this specific energy level resulted in weight divergence. Increasing the specific energy from $230Wh/kg$ to $250Wh/kg$ allowed for a maximum loiter time of 15 minutes, while 45 minutes was achieved with a specific energy level of $300Wh/kg$. The only specific energy level which enabled a 60-minute loiter duration (hence 2.5 hours of total flight time) was $350Wh/kg$. This suggests that in order for the Predator to achieve a mere 1 hour loiter time at high altitude with batteries, as opposed to 24 hours with a reciprocating engine, the specific energy levels need to increase from the current $198Wh/kg$ to $350Wh/kg$, or 75%, and will result in an overall heavier aircraft. This showcases just how far battery technology is from allowing even moderate-endurance electric flight.

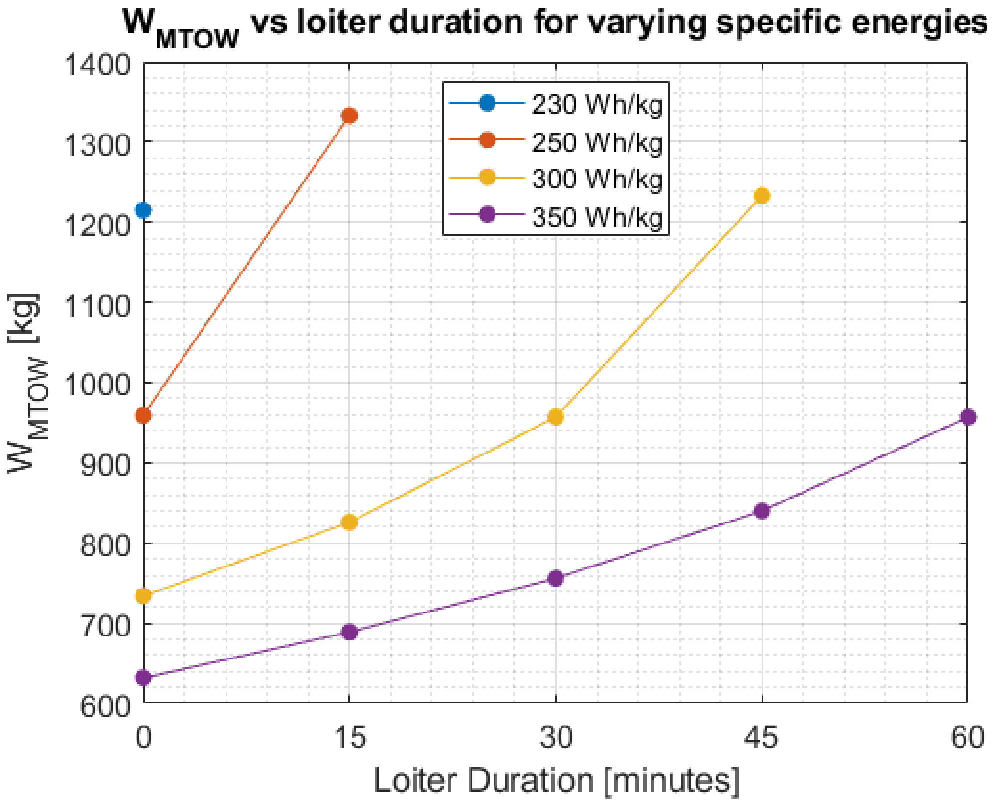

Figure 6.44: Resulting W_{MTOW} against loiter duration for varying levels of lithium-ion battery system specific energy.

Figures 6.45 and 6.46 show the resulting W_{MTOW} against loiter durations of zero to 24 hours, incremented in six hour intervals, with theoretical specific energy levels varying from $1000Wh/kg$ to $3000Wh/kg$. Beginning with the case of no-loiter flight, all five levels of specific energy result in a very light W_{MTOW}, between $309kg$ and $376kg$. Increasing the loiter time results in an increased W_{MTOW}, with the gradient of each curve becoming less steep as the theoretical specific energy increases. Only

6 hours are achievable with a $1000Wh/kg$ specific energy level, while 12 hours is the maximum loiter duration achieved at the $1500Wh/kg$ level. At a specific energy level of $2000Wh/kg$, only 18 hours is achieved, while 24-hour loiter is only achievable with $2500Wh/kg$ and above. Therefore, the first battery case which may be compared to the 24-hour MALE Predator featuring a reciprocating engine is for a battery system with a specific energy of $2500Wh/kg$. While this specific energy allows for 24-hour loiter, the W_{MTOW} is much heavier than the reciprocating engine case, at $1184kg$ compared to $777kg$. Furthermore, system-level specific energy levels of $2500Wh/kg$ represent a nearly 13-fold increase in current levels and while medium-altitude, long-endurance flight seems to theoretically be achievable at this level, it would still result in a substantially heavier design. The final theoretical specific energy level of $3000Wh/kg$ also leads to a design capable of 24-hour loiter but at a W_{MTOW} of $778kg$, which is comparable to the $777kg$ of the 24-hour reciprocating engine model.

In conclusion then, in order for a battery system to allow for the same 24-hour MALE mission as the current reciprocating engine Predator UAV, at a comparable W_{MTOW}, a system-level specific energy of $3000Wh/kg$ would be required. This is about 15 times higher than current technology levels and will most probably be infeasible in future without major paradigm shifts in electrical energy storage technology.

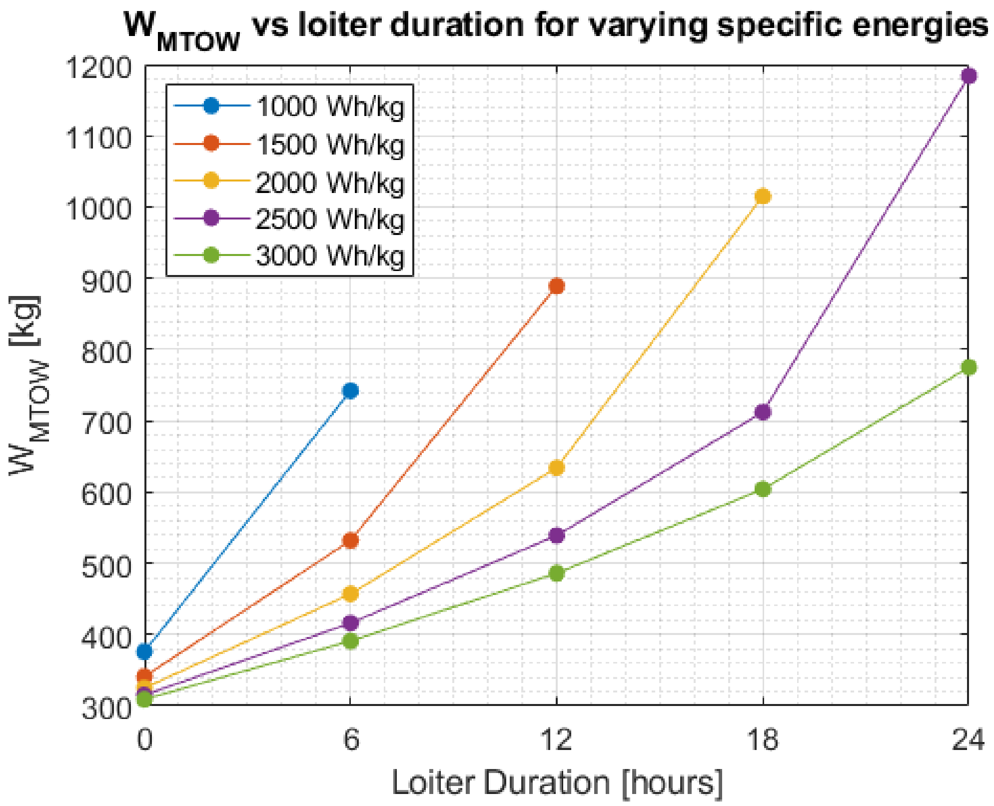

Figure 6.45: Resulting W_{MTOW} against loiter duration for varying levels of lithium-ion battery system specific energy.

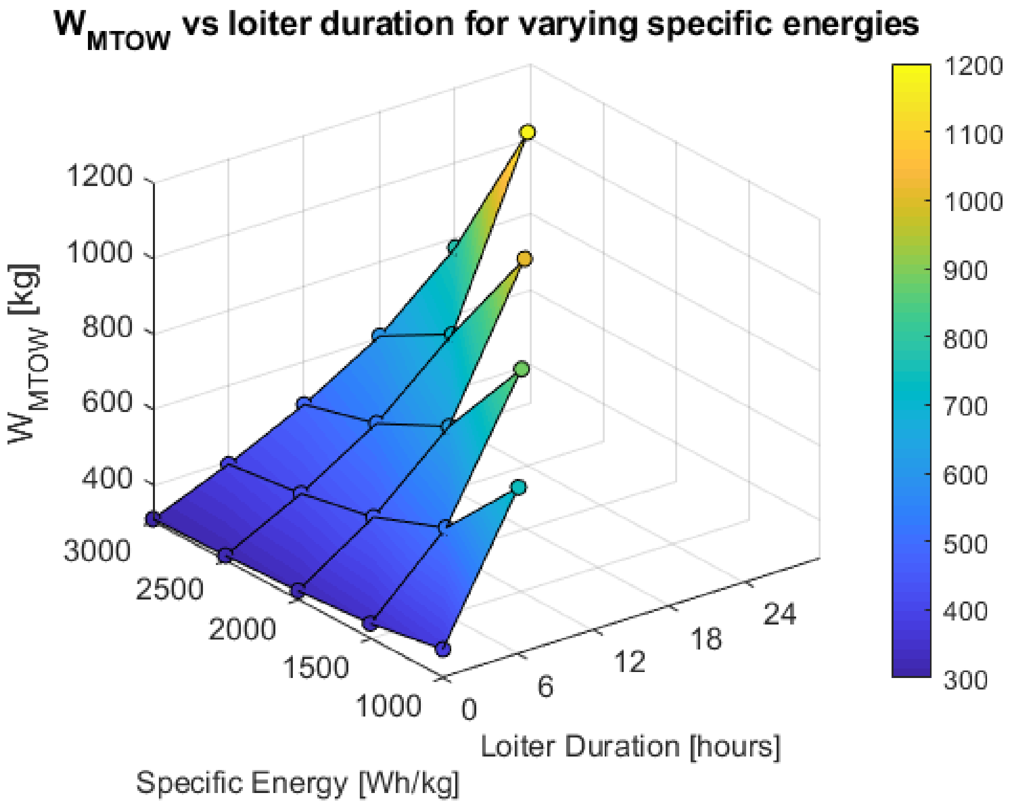

Figure 6.46: Resulting W_{MTOW} against loiter duration for varying levels of lithium-ion battery system specific energy.

7

Discussion

In this chapter the findings of the current investigation are put into context and used to help answer the three research sub-questions presented in Chapter 3. As part of this, the findings are assessed and compared against those found in existing literature, where applicable.

7.1. Research Sub-question 1

What are the effects on the optimised shape of a MALE UAV resulting from improving the fidelity of the aerodynamics and structural wing weight models?

Throughout this work, all MDO runs have been repeated for two levels of modelling fidelity of the aerodynamic and structural weight estimation methods. The low-fidelity runs include aerodynamics relations and class II empirical weight estimation methods, while the high-fidelity runs incorporate the PANAIR higher-order aerodynamic panel code and the CalculiX finite element solver for the weight estimation of the wing. Maintaining the low-fidelity methods while upgrading to the high-fidelity methods has allowed for the comparison of the two. Here, the effect of modelling fidelity on relevant aircraft system-level design parameters under consideration, namely the objective function, coupling variables and design variables, is discussed.

In order to understand the effect of the models' varying fidelity on the optimised aircraft, their effect on the initial configuration, where the planform is the same between the two fidelity levels, has first been analysed. Figures 6.3 and 6.4 of Section 6.1.1 showed the weight breakdown comparison between the low and high-fidelity results, for the initial runs of reciprocating engine and hydrogen fuel cell cases respectively. As was discussed in Section 6.1.1, the same differences were observed when moving from the low-fidelity to high-fidelity methods for both propulsion types. These included a heavier wing and a lower fuel weight in the high-fidelity method, for the same initial planform. The heavier wing indicates that the high-fidelity wing structural sizing optimisation, which was undertaken prior to the MDO in order to produce a feasible initial wing, has produced a wing which is heavier than the output of the class II weight estimation methods. This may be explained as follows. First, the class II weight estimation method may be under-sizing the wing weight for this particular application, keeping in mind that these empirical relations have not been developed from MALE UAV data but rather from general aviation aircraft and sailplanes. Secondly, the V-n diagram given in Chapter 5: Case Study may have produced a sizing condition which is too conservative. After all, the aircraft weight during the sizing condition was taken as W_{MTOW} and it was assumed no inertia relief was present, giving a final load factor of $n = 3.6$. For long-endurance reconnaissance UAVs, Gundlach [27] quoted the load factor of equivalent manned aircraft as being $n = 3$, and even then, he did specify that *"using an analogous approach to manned aircraft can be overly constraining for UAS applications."* [27].

The lower fuel weight in the high-fidelity case indicates that the aerodynamic panel code is calculating the aircraft drag to be lower than the aerodynamic relations of the low-fidelity method. Indeed, it was shown in the drag polar of Figure 6.5 that the panel code yielded a lower drag polar in the angle of attack range encountered during the mission. This results in a lower fuel rate and thus a lower required fuel weight. This also had a knock-on effect on the engine weight and tank weight, as they both reduced. This is particularly impactful in the hydrogen fuel cell case, as the fuel tank accounts for a significant proportion of the aircraft weight.

Having discussed the fidelity effects on the initial configurations, we now continue our discussion with the optimised configurations. Focusing first on the design variables, the planform diagrams of Figure 6.14, together with the normalised design variables changes of Figures 6.15 (reciprocating engine) and 6.22 (fuel cell) from Section 6.2.2 showed that there were indeed differences in the optimal planform shapes between the two levels of fidelity but mostly for the reciprocating engine case. As described in Section 6.2.2, the low-fidelity reciprocating engine optimisation run resulted in a more slender wing, with an increased semi-span b_s and aspect ratio AR, as the optimiser seemingly travelled in the direction of better aerodynamic efficiency. In contrast, the high-fidelity run resulted in a wing with minimal planform changes, which remained very similar to the planform of the initial configuration and was made only slightly smaller, as the optimiser seemingly travelled in the direction of a lower wing weight. In contrast, the low and high-fidelity runs of the hydrogen fuel cell case aligned, by resulting in a much shorter semi-span b_s and smaller aspect ratio AR.

The reason as to why the optimiser travelled towards different designs in the two reciprocating engine cases, while travelling towards a similar design in the two hydrogen fuel cell cases has been discussed in detail in Section 6.2.2 and is summarised briefly here. First, the sensitivity of the low-fidelity class II wing weight estimation methods, along with the low-fidelity aerodynamic relations, have been analysed with respect to the planform design variables. This sensitivity analysis showed that while both the wing weight estimation methods and the aerodynamic relations desired a wing with a higher aspect ratio, they had conflicting requirements on the semi-span. Ultimately, the aerodynamic relations were more sensitive to changes in the semi-span, which is why the optimiser tended towards a more slender wing in the low-fidelity reciprocating engine case, for a loiter endurance of 24 hours. However, when repeating the optimisation runs at lower endurances of 18 and 12 hours, Figure 6.20 showed that the optimised value of the semi-span b_s actually reduced from the initial value, leading to a smaller and lighter wing, similar to the result of the high-fidelity optimisation for a loiter endurance of 24 hours. A clear linear relationship between semi-span and endurance emerged in Figures 6.20 and 6.21, where the positive effect of increasing the semi-span on the aerodynamics outweighs the negative effects on the wing weight, at higher endurances. The 'break-even' point for this switch in importance occurred at around 18 hours of endurance in the low-fidelity case and somewhere above 24 hours endurance in the high-fidelity case. Therefore, the high-fidelity trend line was essentially shifted downwards with respect to its low-fidelity counterpart. As both 24-hour optimisation runs of the reciprocating engine case resulted in wing semi-spans which were still very close to the initial value of $7.43m$ semi-span, this downward shift caused the high-fidelity optimisation to result in a smaller wing.

On the other hand, the same semi-span vs endurance relationship was observed in the hydrogen fuel cell case, as was the downward shift in of the line in the high-fidelity case. However, because the very high specific energy of hydrogen lead to an overall decrease in the UAV W_{MTOW}, the semi-span in both low and high-fidelity cases reduced substantially below the initial value of $7.43m$, Therefore, the effects of the high-fidelity's downward shift were not as noticeable. In other words, the effects imparted by changing the propulsion system are much more significant than the effects imparted by changing the level of fidelity. Ultimately, the resulting optimal design was very similar between the two levels of fidelity. The semi-span b_s values were within 4.4% of each other, the aspect ratio AR values 3.6%, the leading-edge sweep Λ_{LE} 3.9% and the tip twist angle ϕ 1.0%, demonstrating that the two levels of fidelity behaved consistently.

Having analysed the differences imparted by the two levels of fidelity, a relevant question arises around whether the additional computational resources required for the higher-fidelity aerodynamic and wing weight models are justified in the determination of an optimal design. To answer this question, we refer back to Section 6.3, where the effect of endurance was investigated. When looking at the aircraft weights, it was observed that the low and high-fidelity results were in close alignment when the aircraft being optimised reflected the true Predator design - namely, one using a conventional reciprocating engine, at a loiter endurance of 24 hours. In this case, the increase in computational resources required for the high-fidelity methods does not seem to be justifiable, as the results are very similar. However, as the aircraft being optimised begins to tend away from the true Predator aircraft, namely through either a lower loiter endurance or through the incorporation of a hydrogen fuel cell propulsion system, differences in the results of the low and high-fidelity optimised configurations begin to appear. When incorporating either of these changes, the high-fidelity models typically produced an optimal design with a lower W_{MTOW} and W_{OEW} than the low-fidelity models. This was attributed in Section 6.3 to two things. Firstly, the high-fidelity methods provide the optimiser with more control over the thickness of the wing structure, allowing it to reduce the wing size not only through the planform variables but also through a corresponding reduction in the structural sizing variables. Secondly, in the case of the hydrogen fuel cell runs, the optimal wing designs were both much smaller than the original wing, with wing spans which were outside the applicable design space of one of the class II methods. In such cases then, where the optimal design begins to deviate substantially from the initial design, it seems more justifiable to use higher-fidelity methods.

The answer to this question then, according to the result presented in this study, is that it seems more justifiable to opt for higher-fidelity methods when aspects of the mission or design under investigation differ considerably from those of the initial configuration. For example, if the initial point of the MDO is based on a real aircraft designed for a 24-hour endurance using a reciprocating engine, utilising higher-fidelity tools becomes more important when this MDO is being used to investigate designs with a very different mission, or one that incorporates a novel propulsion system.

7.1.1. Key limitations

The limitations pertinent to the current research sub-question involve limitations of the high-fidelity methods employed. Firstly, the fact that the wing buckling optimisation had to be separated from the MDO has likely caused the optimiser to reach a different minimum than would have been reached in an ideal single-step optimisation. This is because although the buckling constraint was imposed on the optimised wing design, the MDO had already travelled to a local minima by the point. Therefore, the planform design variables have not been influenced by the buckling constraint. While the high-fidelity results are still very much valid, with a lighter design having been achieved, it is important to caveat this result with the fact that a different optimised design would most probably have emerged, had an ideal single-step optimisation been possible.

7.2. Research Sub-question 2

Does a feasible design space exist for MALE UAVs with electric propulsion systems?

Based on the results of the current investigation, the short answer to this sub-question is: yes, a feasible design space does exist for MALE UAVs with electric propulsion systems. However, this is only true for fuel cell-powered MALE UAVs and not for battery-powered MALE UAVs with current or near future battery technology levels.

7.2.1. Battery-powered propulsion

The results of this investigation suggest that long endurance flight seems to be infeasible for purely battery-powered MALE UAVs. Not only did the framework not converge for a configuration with current specific energy levels and a 24-hour loiter mission, but it also did not converge even when the loiter duration was reduced to zero minutes (leaving a mere 90-minute flight from the other mission phases). To obtain a feasible design for a mission without loiter, the battery-system specific energy had to be increased to $230Wh/kg$, which represents approximately a 15% increase from current levels. This is most likely feasible in the near future, however, at this low level of endurance, the aircraft can no longer be classified as a medium-altitude long-endurance UAV and would most likely be of little use to operators of MALE UAVs.

To achieve feasible designs for missions which included a loiter phase, the specific energy had to be increased continuously. For a 24-hour loiter mission, the minimum required theoretical specific energy was found to be $2500Wh/kg$, which still resulted in a much heavier aircraft than the baseline Predator with a reciprocating engine. In order to obtain a design with a comparable W_{MTOW}, the theoretical specific energy required was found to be $3000Wh/kg$, which represents a 15-fold increase from current technology levels and is most likely not feasible in future without major paradigm shifts in electrical energy storage technology.

These findings are in agreement with existing aircraft designs which are fully powered by batteries. The Airbus E-Fan, for example, is of similar size to the Predator UAV and can only achieve a maximum of 60 minutes of flight time [132]. Similarly, the Pipistrel Alpha Electro, an electric trainer aircraft, also has a maximum endurance of just 60 minutes [133]. In conclusion then, pure battery power is not sufficient for moderate endurances, let alone the high endurance of a MALE UAV, and will most likely never be, given the nearly 15-fold increase in specific energy that would be required.

While infeasible for use alone, battery systems may still very well play a role in MALE UAV flight, in conjunction with an energy source. Hybrid propulsion systems which feature batteries as the energy storage method together with energy sources like solar panels, for example, could very well pave the way for electric MALE flight. This would make logical sense - batteries are a great method to store electrical energy, however, due to their low specific energy, it is not practical nor feasible to carry this energy throughout the entire long-endurance mission. Rather, using solar panels to provide the batteries with charge during the day, for consumption at night, would allow for long-endurance missions.

Hybrid electric design concepts have been explored in literature and show promise. For example, the NASA Pathfinder was one of the first major studies of high-altitude, long-endurance solar-powered UAV flight. Its subsequent iterations, the Pathfinder Plus and Centurion, ultimately lead to the development of the Helios in the early 2000s, which was designed for a 20-hour endurance at an altitude of $30.5km$ [142]. More recently, in 2012 the $1600kg$ Solar Impulse set a world record as the first solar-powered manned aircraft to conduct an intercontinental flight, from Switzerland to Morocco. It used 11,628 photovoltaic panels, from which energy was stored in the $400kg$ lithium-ion battery system for night-time operation [142].

It should be noted, however, that most solar-battery hybrid aircraft designed to date have been of the

HALE type and not of the MALE type. High-altitude flight has the benefit of higher solar irradiance, making it a more suitable candidate for long-endurance solar-powered flight. This may explain why there is scarce research around solar-powered MALE aircraft. Incorporating a solar-battery hybrid model into the current framework would have helped fill this gap of knowledge in the field. It would also have been more useful in terms of gaining a more practical understanding of the potential of using batteries for energy storage, as the pure-battery approach followed in the current investigation was unlikely to provide a competitive design. However, the modelling of a solar-battery hybrid was outside the scope of the current investigation and was left as an additional task in the case that time permitted. For this reason, a recommendation of the current study is the incorporation of a solar power system model into the current battery model, in order to obtain more practical results around the use of batteries as an energy storage solution.

7.2.2. Hydrogen fuel cell-powered propulsion

In contrast to the battery-powered aircraft model, the fuel cell-powered aircraft model showed that a feasible design space does exist for electric MALE UAVs using liquid hydrogen. This is in line with the findings of the preceding study of Verstraete [13]. The current results show that replacing a reciprocating engine with a hydrogen fuel cell system drastically reduces the W_{MTOW} of the MALE UAV by around 30%. While a reduction in the W_{OEW} of around 14% does contribute to this, the majority of the W_{MTOW} reduction is driven by a much lighter W_f load, which reduces by about 80% with respect to the reciprocating engine-powered initial configuration. To put these results into context, they must be evaluated against similar studies in literature. Naturally, it is not appropriate to compare the results of this investigation to the preceding study of Verstraete, as many of the same propulsion system models are shared between the two studies.

Comparing these findings to results in literature is not straight forward, as the current author did not find any work on the modelling of large UAVs fuelled by liquid hydrogen. Moving up in size to general aviation and regional short-range transport aircraft, only three studies were found which compare aircraft modelled with liquid hydrogen to their equivalent modelled with conventional aviation fuel [143] [144] [145]. Only one of these was modelled with fuel cells rather than a hydrogen-fuelled internal combustion engine [145]. Moving up in size to large long-range transport aircraft, only three studies were found which compare aircraft modelled with liquid hydrogen to their equivalent modelled with kerosene [146] [147] [23]. None of these were modelled with fuel cells but rather all with internal combustion engines. As a result, none of these studies are directly applicable to the evaluation and comparison of the current work. Nevertheless, these studies may still be used to identify trends, which may then be roughly compared to the current results.

The six aforementioned studies comparing hydrogen-powered aircraft to kerosene-powered aircraft are divided on the effects of hydrogen on the aircraft weight. On the one hand, Cálão [143], Vonhoff [145] and Verstraete [23] report an increase in W_{MTOW} and energy consumed when replacing conventional kerosene-powered engines with liquid hydrogen. More specifically, Cálão [143] used the XMDO platform of Airbus to model a twin-turboprop regional aircraft, closely resembling the ATR 72, as both kerosene-fuelled and liquid hydrogen-fuelled. The hydrogen-fuelled variant showed a 7.5% increase in W_{MTOW} and a 12.9% increase in energy consumption, as a result of the heavier airframe weight and reduced aerodynamic performance resulting from an increased fuselage wetted area. Vonhoff [145] modelled a hydrogen-fuelled variant of the Cessna 208 Caravan, this time with a fuel cell rather than a combustion engine. The hydrogen fuel cell variant resulted in an even heavier aircraft, with a 49% higher W_{MTOW} than the kerosene reference model, as a result of a 84% increase in W_{OEW} due to the heavy fuel tank and power system.

On the other hand, Seeckt [144], Brewer [146] and Verstraete [147] [148] claim that the liquid-hydrogen variants of their reference aircraft result in a lighter and more efficient design. More specifically, Seeckt [144] modelled the kerosene-fuelled ATR 72 regional aircraft, together with a LH_2-burning variant, using the PrADO framework. Despite having a 7.1% heavier W_{OEW}, the hydrogen variant resulted in a 9.8% reduced W_{MTOW} as a result of the significant reduction in W_f. What is interesting to note is that while both Cálão and Seeckt modelled a very similar (if not the same) aircraft, they both obtained significantly different results in terms of the effect of using hydrogen, highlighting the variation surrounding hydrogen propulsion modelling.

In the large transport aircraft class, Brewer [146] compared a 400-passenger subsonic reference aircraft against a LH_2 variant, with fuel tanks forward and aft of the passenger compartment. The LH_2 variant resulted in a W_{MTOW} reduction of 25%, as a result of a 68% reduction in fuel weight W_f. The W_{OEW} remained nearly constant, as the increase in tank and fuselage weight was counteracted by a decrease in wing weight. Furthermore, the LH_2 variant required 11% less energy utilisation. Brewer attributed the improved design characteristics delivered by the hydrogen variant to the large amount of fuel required for the long-range transport aircraft, stating: *"In those airplane designs where the mission does not require much fuel it is apparent there will be less performance advantage to switching fuels."* [146].

Verstraete echoes and further proves Brewer's argument, in two studies modelling similarly-sized long-range transport aircraft [147] [23]. Both aircraft saw approximately a 30% reduction in W_{MTOW}, as a result of a 68% reduction in W_f and a nearly constant W_{OEW}, along with an approximately 11% reduction in energy utilisation, results which match those of Brewer almost exactly. Furthermore, in [23], Verstraete also modelled a medium-range and short-range transport aircraft using both kerosene and hydrogen, to compare against the long-range aircraft. In contrast to the long-range aircraft, the medium-range hydrogen variant only saw a 6% decrease in W_{MTOW} as compared to its kerosene reference, coupled with a very significant increase in W_{OEW} of 28% and an increase in the energy utilisation of about 5%. Following the same trend, the short-range hydrogen aircraft actually saw an 11% increase in W_{MTOW} as compared to its kerosene reference, with a significant 36% increase in W_{OEW} and an 18% increase in energy utilisation.

From these results found in literature, a trend begins to emerge. Whether or not hydrogen leads to a lighter and more efficient aircraft or heavier and less efficient aircraft does not seem to depend strictly on the aircraft size but rather on the designed range/endurance. Indeed, from small regional aircraft all the way up to large transport aircraft, cases where switching to hydrogen led to a heavier design occurred when the aircraft was designed for a short-range - in other words, where the fuel weight W_f was not the dominant weight. For example, Vonhoff's [145] kerosene-fuelled Cessna 208 Caravan featured a fuel fraction of merely 17%, while Verstraete's [23] kerosene-fuelled short-range large transport aircraft featured a fuel fraction of only 15%, with both of these aircraft resulting in a heavier design when switching to hydrogen. On the other hand, Verstraete's kerosene-fuelled medium and long-range transport aircraft featured a fuel fraction of 29% and 39% respectively, while Brewer's featured a fuel fraction of 31%, all three of which showed an improved design when switching to hydrogen. In comparison, the initial configuration reciprocating engine models of the current study featured a fuel fraction of 30% and 26% for the low-fidelity and high-fidelity cases respectively, which align with the fuel fractions of Verstraete's and Brewer's kerosene-fuelled aircraft.

In summary, switching to hydrogen as a fuel source seems to become more advantageous as the designed fuel fraction of the aircraft increases. This makes logical sense - in order to counteract the increased weight of the liquid hydrogen fuel tank, the amount of fuel required should be significant, such that hydrogen's high specific energy may reduce a large portion of the overall aircraft weight. This makes long-endurance vehicles, such as MALE UAVs, particularly well-positioned to utilise hydrogen. Indeed, other authors share this line of thought, with González-Espasandín et al. [4] highlighting that fuel cells are well-suited for low-manoeuvrability, long-endurance UAVs designed for surveillance missions, which effectively describes the majority of the MALE UAV category.

These findings in literature help explain the results of the current investigation. Both the initial and optimised configurations of the hydrogen fuel cell variant showed a significant reduction in W_{MTOW}, driven primarily by a substantial reduction in W_f. This is the result of the modelled Predator aircraft being designed for a long-endurance mission and thus featuring a substantial fuel fraction (26% - 30%), which allows a larger portion of the W_{MTOW} to benefit from hydrogen's high specific energy. This may also be why the current result differ substantially from those of Vonhoff [145], who also modelled an aircraft powered by hydrogen fuel cells. In Vonhoff's case, the fuel fraction was only 17%, as a result of a mere $317km$ range at a cruise speed of $96m/s$, leading to a calculated endurance of approximately just under

1 hour. This is in stark contrast to the MALE UAV modelled here, which features nearly double the fuel fraction and a 24-hour endurance, making hydrogen fuel cell propulsion a much more attractive option.

7.2.3. Key limitations

While the results presented here make the case for hydrogen propulsion in MALE UAVs, they should be put into context with regards to the relevant limitations of the study. The incorporation of liquid hydrogen in aircraft presents an array of challenges, not the least of which is the cryogenic hydrogen storage, including boil-off requirements. The empirical models presented in Section 4.8.3 implicitly account for these characteristics but only within the design space of those specific tanks used in the development of said models. The effect of tank geometry, for example, is not accounted for through these relations, which is significant considering that the boil-off is related to the surface area and thus the shape of the tank. With hydrogen storage technology playing a pivotal role in the feasibility of hydrogen propulsion in aviation, it may be the case that empirical relations may not suffice and higher-fidelity models which explicitly incorporate the thermodynamics of the hydrogen storage system are required to accurately capture the performance of the storage system.

The scope of the current investigation, however, only included the enhancement of the modelling fidelity of other disciplines, in an attempt to bring them up to the level of modelling fidelity of the propulsion systems and did not include any subsequent enhancement of the propulsion system modelling fidelity, unless time permitted. The current work has now brought the fidelities of the aerodynamics and wing weight models to a higher level than those of the propulsion system models. Therefore, the next logical step would be to increase the modelling fidelity of the propulsion system models and importantly the hydrogen storage models, in order to capture the considerations discussed above. As a result, one of the key recommendations of this study for future work is the enhancement of the propulsion system modelling fidelity, particularly in the case of the hydrogen propulsion models, in order to verify the claims of the current study and be able to more confidently claim that hydrogen propulsion is indeed beneficial for MALE UAVs.

7.3. Research Sub-question 3

If a feasible design space does exist, what are the effects on the optimised shape of a MALE UAV resulting from electric propulsion systems?

With the fuel cell-powered UAV being the only modelled electric aircraft having shown a feasible design space, it is the only modelled aircraft this research sub-question is applicable to. The results of the optimised configurations show that all relevant aircraft system level design parameters under consideration, namely the objective function, coupling variables and design variables, are dramatically affected when the aircraft design is optimised with a hydrogen fuel cell propulsion system.

The effects on the objective W_{MTOW} and coupling variables W_{OEW} and W_f have been discussed in Section 7.2 for the baseline configuration, wherein significant weight reductions were observed as a result of hydrogen's high specific energy. For the optimised configuration, further weight savings were achieved for the hydrogen variant and to a larger extent than the reciprocating engine optimal design. More specifically, the hydrogen variants saw a reduction in W_{MTOW} of 8.8% and 19.9% for the low-fidelity and high-fidelity cases respectively, between the initial and optimised configurations. On the other hand, the reciprocating engine variants saw a W_{MTOW} reduction of just 1.5% and 3.5% respectively, between their initial and optimised configurations. The fact that the weight improvements in the reciprocating engine cases were only small is expected, as the real Predator has been designed around a reciprocating engine. It is therefore logical to assume that the original aircraft is already close to an optimal design, for its specific propulsion system. On the other hand, the hydrogen variant's optimal point is much further away to the initial point in the design space than the reciprocating engine optimal point is. As a result, one would expect that allowing the optimiser to alter the design variables would result in more significant weight changes for the hydrogen variant than the reciprocating engine variant.

For the weight parameters then, it is concluded that a hydrogen fuel cell propulsion system not only results in a lighter design than its reciprocating engine counterpart for the same planform configuration, but also allows for greater weight savings when the planform is allowed to vary through a MDO. This result also demonstrates the power of MDO, which in this case has uncovered significant weight savings when applied to novel electric propulsion MALE configurations.

Moving on to the design variables, from the planform diagrams of Figure 6.14, together with the normalised design variables changes of Figures 6.24 (low-fidelity) and 6.25 (high-fidelity), the most prominent effect of the fuel cell propulsion system is the vastly reduced size of the wing. The optimised semi-span b_s reduced by around 26% and 29% compared to the initial configuration, for the low and high-fidelity cases respectively, while the area reduced by 38% and 42% respectively. As was discussed in Section 7.2, the use of hydrogen as a fuel dramatically reduced the fuel weight W_f and thus decreased the W_{MTOW}. With the aircraft being significantly lighter, the wing loading reduced dramatically during the optimisation, which allowed the optimiser to decrease the wing area accordingly without violating the wing loading constraint.

Comparisons of this result with results in literature are again limited to the studies given in Section 7.2. In the cases where the incorporation of hydrogen as a fuel led to a decrease in W_{MTOW} compared to the kerosene baseline, the resulting wing deceased in size. More specifically, Brewer [146] reported a wing span reduction of about 10%, with a wing area reduction of approximately 20%. Verstraete [147] [23] reported a wing area reduction of 31% and 44% for the two long-range transport aircraft modelled with LH_2, along with a reported smaller span, for which values have not been given. Furthermore, in [23], Verstraete showed that the medium-range hydrogen variant, which only saw a 6% decrease in W_{MTOW}, had a wing area reduction of just 12%, much less than the long-range hydrogen variant.

On the other hand, in studies where the hydrogen variants resulted in a heavier design, the wing size increased. More specifically, in [23] Verstraete reported that the short-range hydrogen variant, which resulted in a 11% heavier design, saw a wing area increase of 36%. Furthermore, Vonhoff [145], who reported that the Cessna 208 hydrogen variant resulted in a W_{MTOW} increase of 49%, also reported an increase in wing size. No specific values were given but based on the planform diagram he provided, both span and area seem to have increased significantly as a result.

It can thus be said that the design effects of a hydrogen propulsion system observed in the current study align with the those results in literature for which a lighter aircraft design was observed. More specifically, design effects of a smaller, lighter wing are observed in the current study, similarly to the studies of Brewer [146] and Verstraete [147] [23]. Had the hydrogen variants of the current study resulted in a heavier design, as observed by Vonhoff [145] and Verstraete [23] (for the short-range aircraft), the expectation would be that a larger wing would be required, in order to maintain the minimal wing loading constraint.

7.3.1. Key limitations

The design effects observed in this study are very much dependent on the accuracy of the hydrogen storage and propulsion models. In the case that the current models do not accurately describe the true characteristics of a hydrogen fuel cell propulsion system, a more detailed model may suggest that the hydrogen tank weight exceeds any weight benefit from the hydrogen's high specific energy, as was the case for Vonhoff [145]. This may ultimately mean that the wing size and weight would increase when optimised through a MDO, contrary to the results observed in the current study. This again highlights the limitation of the current study around the fidelity of the hydrogen storage and propulsion models and further prompts the current author to recommend the implementation of higher-fidelity models in future iterations of the framework.

8

Conclusions and Recommendations

The conclusions of the current investigation are presented in Section 8.1, while its limitations along with relevant recommendations are provided in Section 8.2.

8.1. Conclusions

The Medium-Altitude Long-Endurance (MALE) Unmanned Aerial Vehicle (UAV) is seeing growing importance in today's world, both in civil and military applications. Its large size, comparable to that of general aviation aircraft, and its long endurance, in the order of days, allow it to carry heavy payload and instrumentation for extended periods of time, without the need for a human pilot. However, it is still primarily powered by hydrocarbon fuels and its design is very much constrained by existing general aviation reciprocating engines, which are designed for a different set of requirements. Electric propulsion solutions are beginning to show promise on larger-scale aircraft, however limited work has been conducted to investigate how these novel propulsion solutions will affect the aircraft-level design of MALE UAVs.

This study has focused on the investigation of the design effects imparted on the optimised shape of a MALE UAV from the incorporation of electric propulsion systems, namely hydrogen fuel cells and battery systems, while in parallel investigating how the results change when varying the fidelity of the aerodynamics and structural wing weight models. A Multidisciplinary Design Optimisation (MDO) framework has been developed which incorporates the modelling of three types of propulsion systems, namely a reciprocating engine, hydrogen fuel cell and battery. The aerodynamics module features a low-fidelity method based on aerodynamics relations and a medium/high-fidelity method based on the PANAIR higher-order panel code. Moreover, the structural wing weight module features low-fidelity class II wing weight estimation methods and a high-fidelity finite element analysis (FEA)-based structural wing sizer. Design optimisations for the minimisation of the maximum take-off weight of the General Atomics Predator UAV have been conducted using the three propulsion system models, across the two levels of modelling fidelity of the aerodynamics and structural wing weight methods.

The following conclusions have been drawn from the current study:

1. The initial (pre-optimised) configuration of the hydrogen fuel cell variant shows a reduction in the maximum take-off weight W_{MTOW} of about 30% as compared to the initial configuration of the baseline aircraft with a reciprocating engine. This is driven primarily by a corresponding reduction in the fuel weight W_f of 80%, despite a 10-fold increase in the fuel tank weight. This is aligned with results in literature where incorporating hydrogen as a fuel in long-range or long-endurance missions resulted in a lighter design. This highlights the potential of hydrogen as a fuel for MALE UAVs, as it has been shown to be increasingly beneficial at higher endurances.
2. As the initial configuration of the battery variant did not converge, due to an excessively heavy battery, this suggests that current battery specific energy levels do not suffice for the long-endurance missions which characterise MALE UAV flight.

3. In order for the battery variant to deliver the same 24-hour endurance as the baseline Predator UAV with a reciprocating engine, at a similar W_{MTOW}, a theoretical specific energy of $3000Wh/kg$ would be required, making the idea of purely battery-powered MALE flight seem highly unlikely.

4. The optimised configuration of the reciprocating engine-powered aircraft does not change substantially with respect to its initial configuration. The W_{MTOW} reduces by only 1.5% and 3.5% for the low and high-fidelity cases respectively.

5. The optimised configuration of the hydrogen fuel cell variant, on the other hand, changes substantially, with an 8.8% and 19.9% reduction in W_{MTOW} compared to its initial configuration, for the low and high-fidelity cases respectively. This equates to a 40.9% and 43.6% reduction in W_{MTOW} compared to the initial configuration of the reciprocating engine-powered aircraft, for the low and high-fidelity cases respectively. This weight reduction is achieved through a substantially smaller and lighter wing, with a planform area reduction of 38.3% and 42.0% respectively, a semi-span reduction of 26.2% and 29.5% respectively and an aspect ratio reduction of 11.9% and 15.1% respectively, compared to the baseline design. This demonstrates the substantial design changes which hydrogen fuel cell propulsion solutions allow on a MALE UAV, namely a much lighter and smaller aircraft, for the same endurance and performance as the baseline reciprocating engine-powered aircraft.

6. In the optimised configurations of the hydrogen fuel cell-variant, the hydrogen fuel tank becomes the dominant airframe component in terms of weight, representing about 22% of the operational empty weight W_{OEW}.

7. Incorporating a high-fidelity aerodynamics method based on the PANAIR higher-order panel code results in the calculation of a more aerodynamically-efficient design as compared to low-fidelity aerodynamics relations.

8. Incorporating a high-fidelity wing structural sizing method based on the CalculiX finite element analysis solver allows for a greater wing weight reduction during a MDO, as compared to low-fidelity class II wing weight estimation methods, as it allows for the reduction of the wing weight not only through a planform reduction but also through a correspondingly thinner structure. Furthermore, such physics-based methods remains applicable even when the optimiser traverses to a region of the design space where the class II methods do not apply.

9. The choice of using computationally-costly high-fidelity aerodynamics and structural wing weight models in an iterative MDO framework becomes more justified when the aircraft design being optimised is substantially different from the baseline configuration, such as for example when incorporating a different mission or a novel propulsion system.

10. The linear buckling analysis of the CalculiX FEA package is not appropriate for use in a MDO framework where the number, size or shape of the mesh elements are under the control of the optimiser.

11. The wing planform variables with the most influence on the design of a MALE UAV when optimised through a MDO are the semi-span b_s, the aspect ratio AR and to a lesser extent the taper ratio λ. The leading edge sweep angle Λ_{LE} and the tip twist angle ϕ do not show to have a significant impact on the optimised planform design of a MALE UAV.

8.2. Recommendations

Although this study incorporates multiple improvements with respect to the preceding study of Verstraete, it is not without limitations of its own. These are summarised below, together with corresponding recommendations.

1. **Incorporating propulsion models of higher fidelity**: While the initial purpose of increasing the fidelity of the aerodynamics and structural wing weight modelling was to bring them more in line with the fidelity of the propulsion system models, the propulsion system models now have a lower fidelity than the models of the other two disciplines. However, it is the propulsion systems which are being compared in this framework and as such the study would have benefited from an increase in the fidelity of their models as well. Due to time limitations, however, this was set outside the scope of the study but it does remain as one of the most significant limitations. This is of particular importance in the modelling of the hydrogen storage method, which plays a pivotal role in the feasibility and performance of hydrogen propulsion solutions in aircraft. Therefore, the primary recommendation for future studies is the inclusion of propulsion models of a higher fidelity, to ensure more detailed effects of novel propulsion systems are accurately captured within the MDO framework.

2. **Extending the framework to include hybrid propulsion solutions**: Within the scope of the current study was the investigation of only two electric propulsion solutions, namely hydrogen fuel cells and battery systems. No hybrid electric propulsion solutions were modelled, such as a battery system with an energy source like solar panels. A recommendation of this work is the incorporation of hybrid propulsion systems, which will allow for a more varied comparison of electric propulsion solutions and will demonstrate more practical applications of battery systems.

3. **Extending the framework to include more design disciplines**: Implementing the design disciplines of stability and control, cost and any application-specific considerations were not included within the scope of this study. They remain key disciplines (particularly stability and control from a technical perspective) and their inclusion in the framework will most definitely have an impact on the optimised MALE designs. A recommendation is to extend the current MDO framework by modelling these disciplines and determine how different the feasibility of electric propulsion systems are as compared to the findings of the current investigation.

4. **Incorporating more robust commercial software packages**: Due to the requirement of using open source modelling software, limitations arose in the implementation of certain disciplines. These include the lack of a tailplane model in ESP, the lack of an option for modelling composite materials in CalculiX when using tie constraints but most significantly the instability of the buckling analysis of CalculiX, which forced a two-step optimisation that has most likely led to a different optimised solution than would have been obtained through an ideal single-step optimisation. Should the study be extended in future, the use of commercial software packages in recommended, as these are more likely to have more varied functionality and come with more extensive documentation.

5. **Improving the accuracy and design variable scope of the investigation through more computational resources**: Highly-iterative workflows such as MDO are computationally-costly. Computational resources available to the author were limited during this investigation. This imposed limitations in a number of disciplines, which include not executing the PANAIR panel code at every discrete mission segment, limiting the number of wing structure sizing design variables from 18 down to six and not including fuselage design parameters as design variables. In future studies, access to more computational resources will allow for accurate calculations of the drag polar at each discrete mission segment, while also allowing the number of mission segments to increase. Furthermore, it will also be possible to include a wider variety of design variables in the MDO, including more wing structural sizing variables and fuselage design variables. The latter would be particularly useful, in order to gain a more complete understanding of the design effects of electric propulsion solutions on the wider aircraft design.

6. **Replacing the gradient-based optimisation algorithm with a global optimisation algorithm**: The current MDO framework makes use of a gradient-based optimisation algorithm. This has a consequence of the optimised points most likely being local and not global. The use of a global optimisation algorithm will allow for the possible determination of a global optimum and is recommended for future studies.

Finally, aside from addressing the aforementioned limitations, it would be interesting in future studies to reformulate the optimisation problem such that the objective function becomes the maximisation of endurance, rather than the minimisation of W_{MTOW} as has been done in this investigation. This will allow for the generation of new optimal designs which may then be compared against the results presented in the current study.

A

Appendix A: Panel Code Validation

Appendix A contains the validation of the PANAIR panel code. As was described in Chapter 4: Methodology, during the undertaking of the current study, Clar [98] also developed a MDO platform which also incorporated PANAIR. Clar undertook an extensive validation exercise of the PANAIR panel code, which showed a very close match with wind tunnel data for the NACA RM L51F07 wing-body configuration for Mach numbers of $M = 0.6$ and $M = 0.8$ [18]. As the PANAIR pre and post-processing scripts used in the current framework were originally developed by Clar, it would logically follow that his validation work would apply in the current study. Nevertheless, implementing the scripts into the current framework must be done correctly and although Clar has validated PANAIR, it would give the current study further credence to validate the implementation here. After all, the current study involves comparing varying levels of modelling fidelity - hence, ensuring their correct implementation is important.

In the current validation exercise, the same wing-body configuration is used, namely the NACA RM L51F07 [18]. The NACA study was undertaken for Mach numbers of $0.6 \leq M \leq 1.2$. As the current study focuses on the low-subsonic flow regime, the current validation exercise is executed for the lowest Mach number available, namely $M = 0.6$. Figure A.1 shows the NACA model, with all dimensions given in inches [18]. The fuselage and wing were modelled in the current framework using the method described in Section 4.4 of Chapter 4: Methodology, namely through the fitting of superellipses for the fuselage and through the use of the CST method for the wing. The CST parameters were optimised for the shape of the NACA 65A006 airfoil, the coordinates of which were not found in the NACA RM L51F07 report but were sourced from the Public Domain Aeronautical Software website [149].

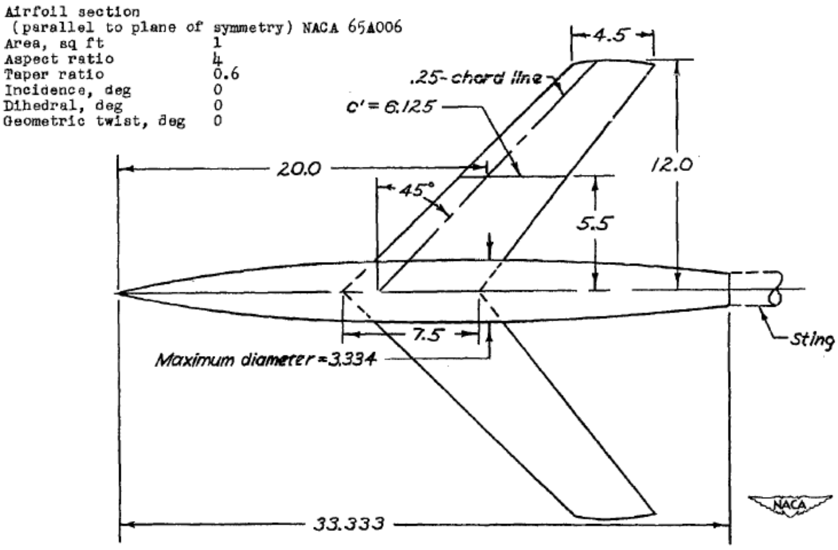

Figure A.1: NACA RM L51F07 report wing-body configuration. All dimensions are given in inches [18].

After creating the solid body model in ESP, as described in Chapter 4: Methodology, the model was meshed in SALOME, as is shown in Figure A.2. The mesh was then passed to PANAIR, where it was evaluated at nine angles of attack, namely $\alpha = [-2, 0, 2, 4, 6, 8, 10, 12, 14]$, at sea-level altitude and a Mach number of $M = 0.6$.

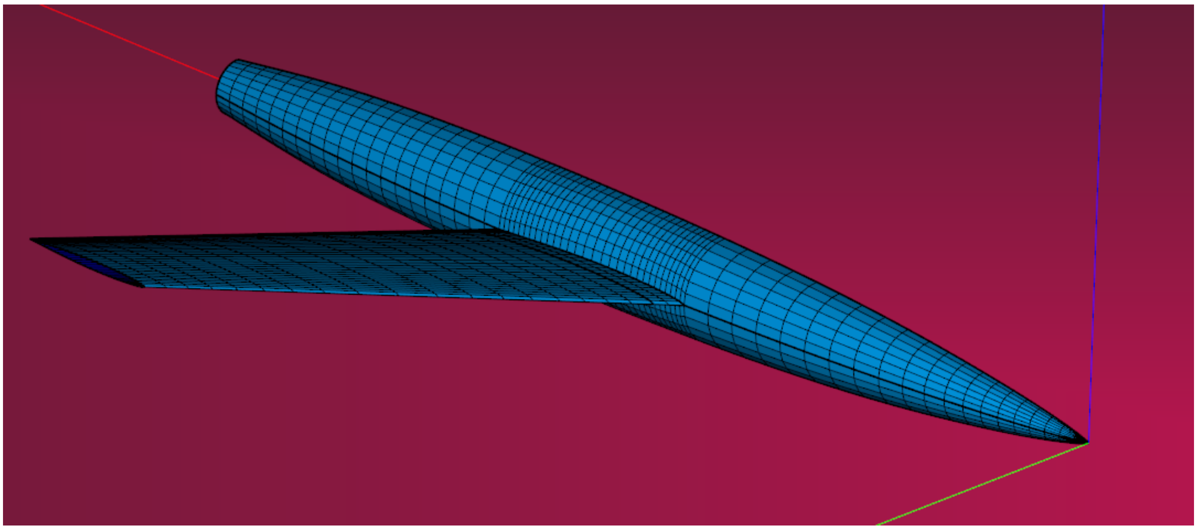

Figure A.2: The NACA RM L51F07 wing-body configuration meshed in SALOME.

Plots of the lift coefficient C_L and inviscid drag coefficient C_D at the nine angles of attack as obtained in PANAIR are given in Figures A.3 and A.4 respectively. The wind tunnel data points at the same angles of attack are superimposed for comparison. The PANAIR lift curve is in very good agreement with the wind tunnel data from $\alpha = -2^o$ to $\alpha = 10^o$. After $\alpha = 10^o$, the PANAIR C_L curve begins to diverge from the wind tunnel data, as the wind tunnel points decrease in comparison. This is expected and is attributed to the initiation of flow separation from the wing in the real case, something which is not captured in the inviscid flow modelling of PANAIR. The $C_L - \alpha$ relationship as provided by PANAIR is thus valid for angles of attack less than about 10^o.

In the drag $C_D - \alpha$ plot of Figure A.4, PANAIR aligns very well with the wind tunnel data between $\alpha = -2^o$ to $\alpha = 8^o$. After $\alpha = 8^o$, PANAIR under-predicts the drag by an increasing margin. Viscous effects present in the flow separation regime are much more evident in the wind tunnel data of this figure, which highlights PANAIR's inability to capture these effects. Nevertheless, PANAIR seems to accurately capture inviscid drag for angles of attack less than about 8^o. In the current framework, the vast majority of flight time takes place below $\alpha = 8^o$, rendering PANAIR a very valid tool for the application at hand.

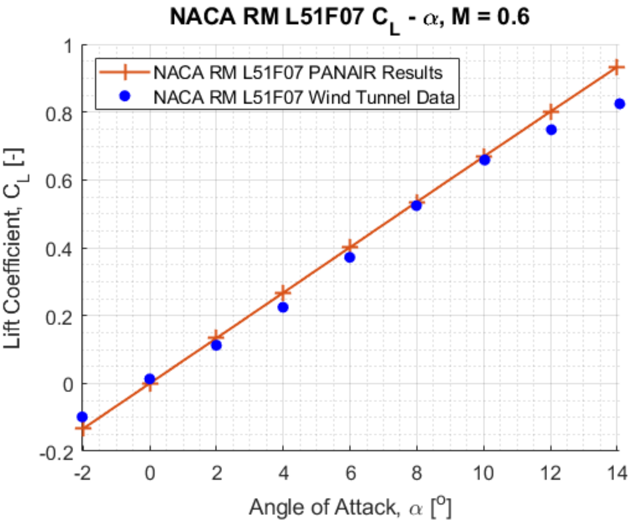

Figure A.3: PANAIR C_L results vs wind tunnel data for the NACA RM L51F07, $M = 0.6$. Wind tunnel data from [18].

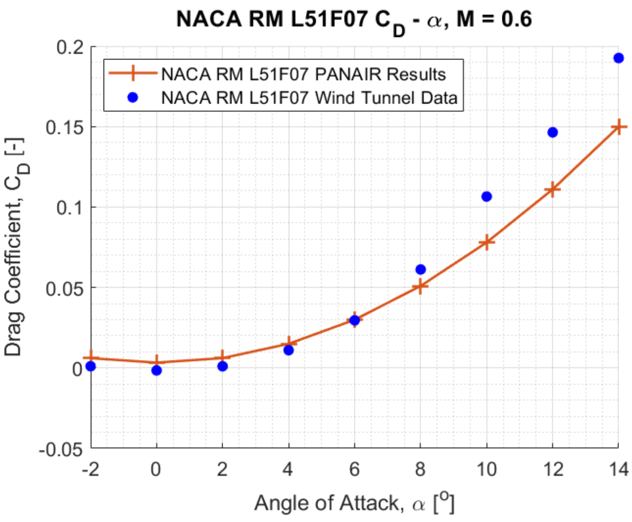

Figure A.4: PANAIR inviscid drag C_D results vs wind tunnel data for the NACA RM L51F07, $M = 0.6$. Wind tunnel data from [18].

To look closer at how PANAIR behaves in the expected flight regime, the pressure coefficient C_p distribution over the wing as output by PANAIR is compared against the wind tunnel data. C_p wind tunnel data is provided in the NACA report for semi-span positions of $y/b_s = 0.2, 0.4, 0.6, 0.8$ and 0.95, corresponding to the pressure orifices of the physical aircraft model. Here, the PANAIR C_p distribution over the wing is compared to the wind tunnel points at three semi-span locations, namely $y/b_s = 0.2, 0.6$ and 0.95, for two angles of attack, namely $\alpha = 0^o$ and $\alpha = 4^o$. The C_p plots are given in Figure A.6, with the semi-span location increasing from left to right and the angle of attack increasing from top to bottom.

In the case of $\alpha = 0^o$, the expectation is that the pressure coefficient C_p distributions for the upper and lower wing surfaces are identical, considering the airfoil is symmetric and the wing aerodynamics are not asymmetrically affected by the interaction of the fuselage, as the fuselage is perfectly circular. Indeed, PANAIR meets this expectation, with the upper and lower C_p curves overlapping, while also aligning with the wind tunnel data very well. For the case of $\alpha = 4^o$, where lift is now generated, the PANAIR and wind tunnel C_p distributions align very well, even near the leading and trailing edges, indicating that PANAIR is accurately capturing the pressure variations over lifting bodies.

Finally, the pressure coefficient C_p distribution over the fuselage is compared. The NACA report provides C_p distribution data in the fuselage length-wise direction along lines A-F of Figure A.5. Because of symmetry, locations A, B and C are compared here, again for two angles of attack, $\alpha = 0^o$ and $\alpha = 4^o$. The results are provided in Figure A.7, with the location letter increasing from left to right and the angle of attack increasing from top to bottom.

As is clearly visible in Figure A.7, the PANAIR results line up very well with the wind tunnel data. Both data sets show an increase in the magnitude of C_p in the region $0.4 \leq x/L \leq 0.7$, namely in the length-wise position of the wing. This increase is progressively more pronounced in orifice locations B and C, as these locations are closer to the wing as shown in Figure A.5. The only small variation in the PANAIR data as compared to the wind tunnel data is near the rear of the fuselage, where PANAIR seems to be slightly under-predicting the C_p distribution. This is most likely attributed to the fact that the physical wind tunnel model was attached to a sting at its rear side, which held it in place in the wind tunnel, as is seen in the drawing of Figure A.1. The PANAIR model did not incorporate the modelling of a string and hence the aerodynamic properties near the rear differ slightly. Overall however, the PANAIR results align very well with the wind tunnel data over the fuselage, further validating the use of PANAIR as a high-order panel code, while also validating the implementation into the current framework.

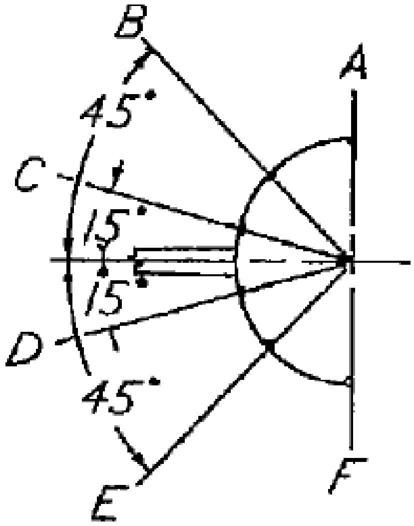

Figure A.5: Front view of the NACA RM L51F07 wing-body configuration, with pressure orifices of the fuselage along lines A-F.

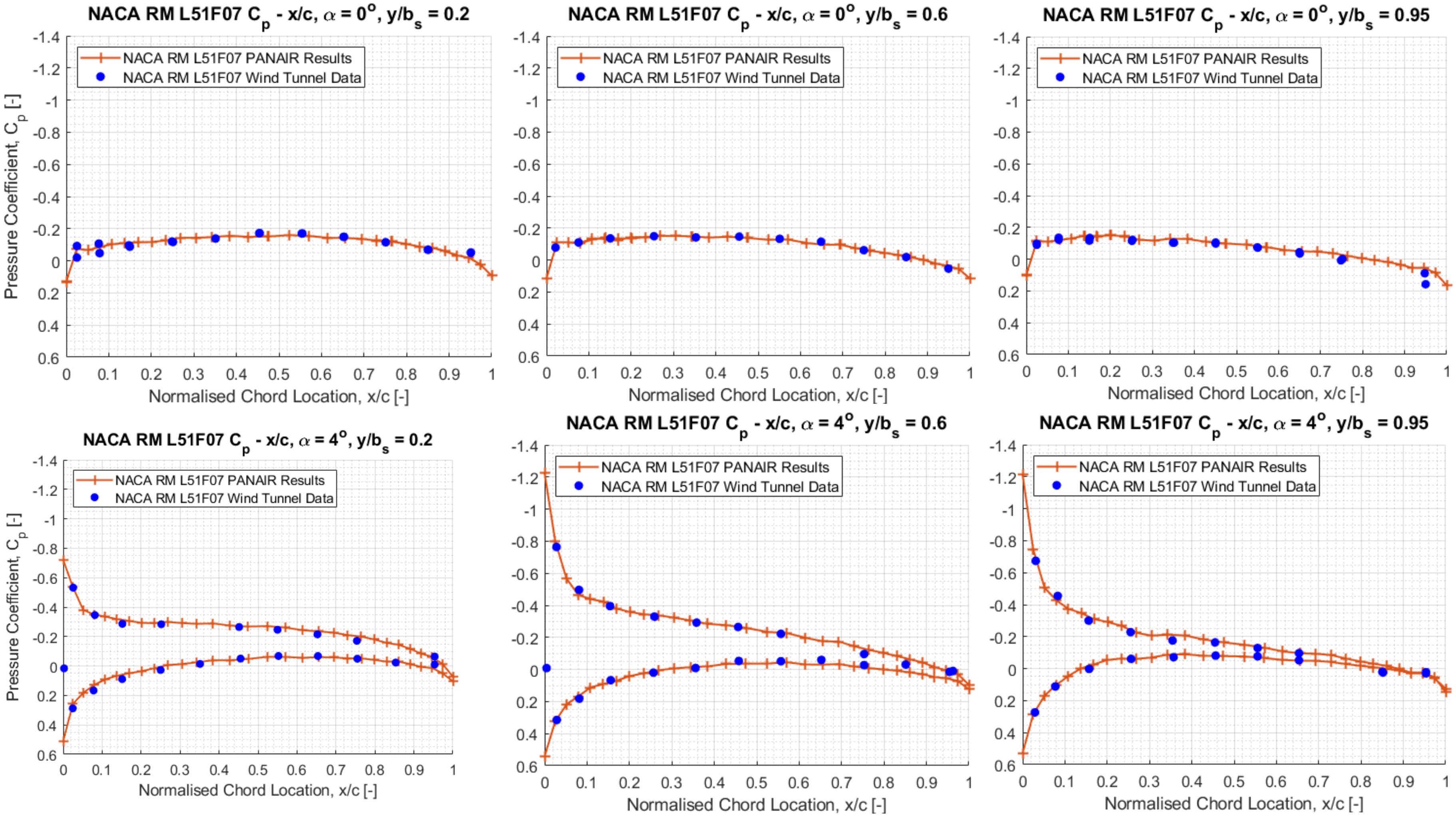

Figure A.6: PANAIR results vs wing tunnel data of pressure coefficient C_p over the wing at three semi-span locations: $y/b_s = 0.2, 0.6, 0.95$ (left to right) at two angles of attack: $\alpha = 0^o, 4^o$ (top and bottom). Wind tunnel data from [18].

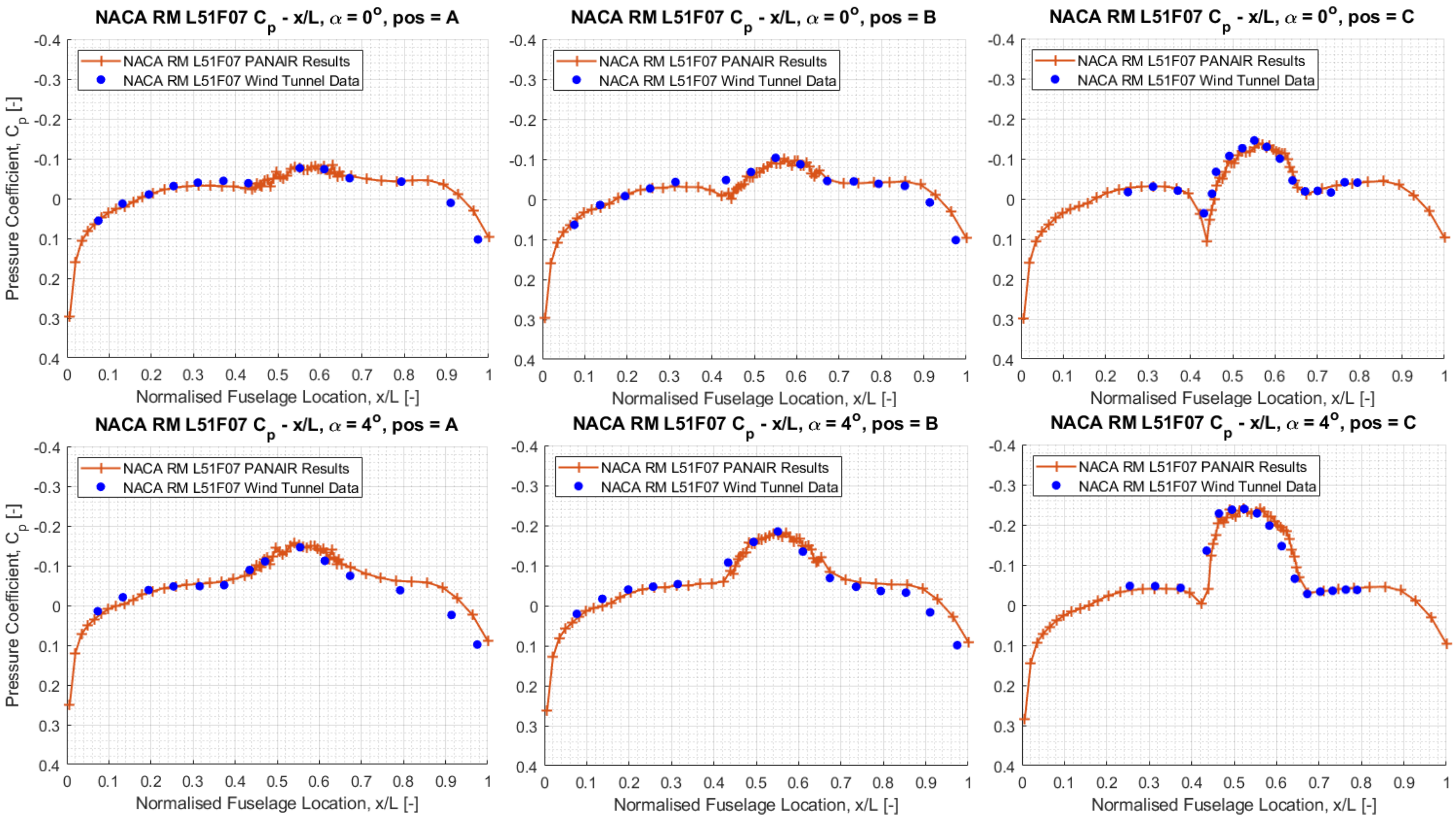

Figure A.7: PANAIR results vs wing tunnel data of pressure coefficient C_p over the fuselage at three circumferential positions: $pos = A, B, C$ (left to right) at two angles of attack: $\alpha = 0^o, 4^o$ (top and bottom). Wind tunnel data from [18].

As was alluded to previously, the purpose of the current validation exercise is two-fold: to independently prove that PANAIR accurately captures the main aerodynamic behaviours of the problem at hand in a specific flow regime, while also proving that its implementation in the framework is free from errors. While the second point has entirely been proven by the validation work shown so far, the first point is only partially proven. This is because the minimum Mach number included in the NACA RM L51F07 report was 0.6, which is indeed in the subsonic regime but still relatively far from the low subsonic regime of MALE UAV flight ($M \approx 0.1$). To achieve a more complete validation, comparing PANAIR against real data in a flow regime closer to that of a MALE UAV would be beneficial. While no low speed data was found in the $M = 0.1$ flow regime, Sepuldeva and Smith [19] validated PANAIR for the Boeing 1303 large UAV, at a Mach number of $M = 0.3$. The lift and drag curves provided in Figure A.8 and A.9 respectively show a very good match with wind tunnel data, for angles of attack where the flow is fully attached ($\alpha < 10^o$).

With the validation of PANAIR against the NACA RM L51F07 wing-body configuration, the implementation of PANAIR in the current framework has been validated while also proving PANAIR as an accurate tool in the mid-subsonic flow regime. Furthermore, PANAIR's low speed performance has further been validated through the work of Sepuldeva and Smith [19]. Together, these pieces of evidence validate the use of PANAIR in the current framework and for the current application at hand.

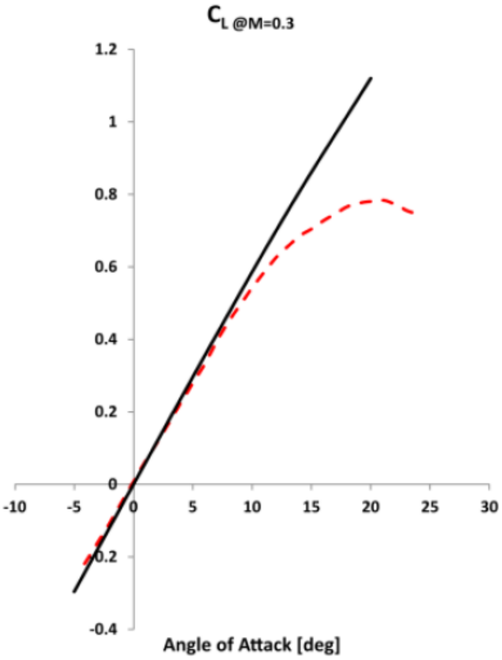

Figure A.8: PANAIR C_L results vs wind tunnel data for the Boeing 1303 UAV, $M = 0.3$ [19].

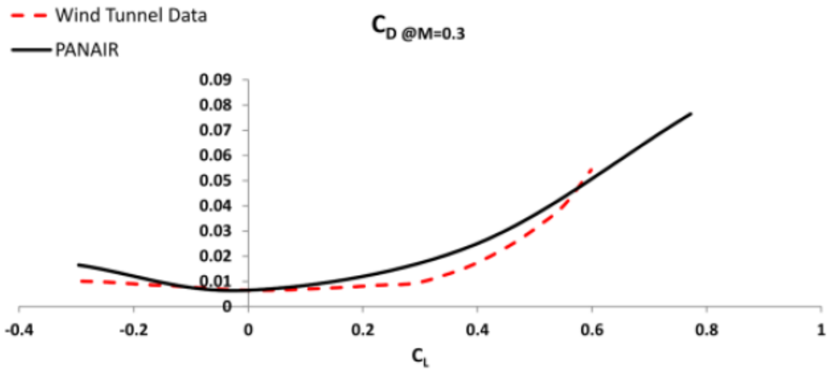

Figure A.9: PANAIR C_D results vs wind tunnel data for the Boeing 1303 UAV, $M = 0.3$ [19].

B

Appendix B: FEA Verification

Appendix B contains the verification of the finite element method of this study. Figures B.1, B.2 and B.3 show a simple plate meshed with S4, S4R and S8R elements respectively, as modelled in both CalculiX (left) and Abaqus (right). No S8 meshing case is seen, as Abaqus does not offer full integration S8 elements. A *DLOAD distributed pressure load is applied, while three sides are clamped. The plate thickness is $12.7mm$. The peak von Mises stresses are compared in Table B.1.

From the stress distributions presented in Figures B.1 to B.3, it becomes immediately clear that CalculiX best matches Abaqus for the S8R element type, with S4 a close second. CalculiX gives a spurious stress distribution for the S4R case. This is most likely due to the fact that S4R element only contain a single integration point in CalculiX, which is located in the middle of the element thickness, hence on the neutral axis. As a result, bending is not appropriately captured with this element type in CalculiX, as compared to Abaqus which seems to correct for this.

Referring to Table B.1, the difference between the performance of S4 and S8R elements becomes clear. Where the S4 case has a peak von Mises stress difference of 5.2% between the results of CalculiX and Abaqus, the S8R element case is nearly identical, at a difference of 0.2%. This difference may be explained as follows: according to Dhondt [12] and as was described in Section 4.7.2, vendors of FEA packages often modify the linear shape functions of elements, while CalculiX does not. Abaqus seems to have modified shape functions for the S4 elements with linear shape functions, creating a variation in its results with CalculiX.

With CalculiX S4R elements containing only a single integration point and S4 elements not having modified shape functions, the S8R shape function does indeed seem to be the most reliable 2-D shell element in CalculiX.This verifies Dhondt's claim that *"if you are setting off for a long journey and you are allowed to take only one element type with you, that's* [S8R] *the one to take"* [12].

Table B.1: Peak von Mises stresses for the plate modeled in CalculiX and Abaqus, using S4, S4R and S8R elements at a thickness of $12.7mm$.

	Peak von Mises Stress Calculix [Pa]	Peak von Mises Stress Abaqus [Pa]	Difference [%]
S4	$4.90 \cdot 10^3$	$5.17 \cdot 10^3$	5.2
S4R	$5.15 \cdot 10^3$	$4.93 \cdot 10^3$	4.5
S8R	$5.45 \cdot 10^3$	$5.46 \cdot 10^3$	0.2

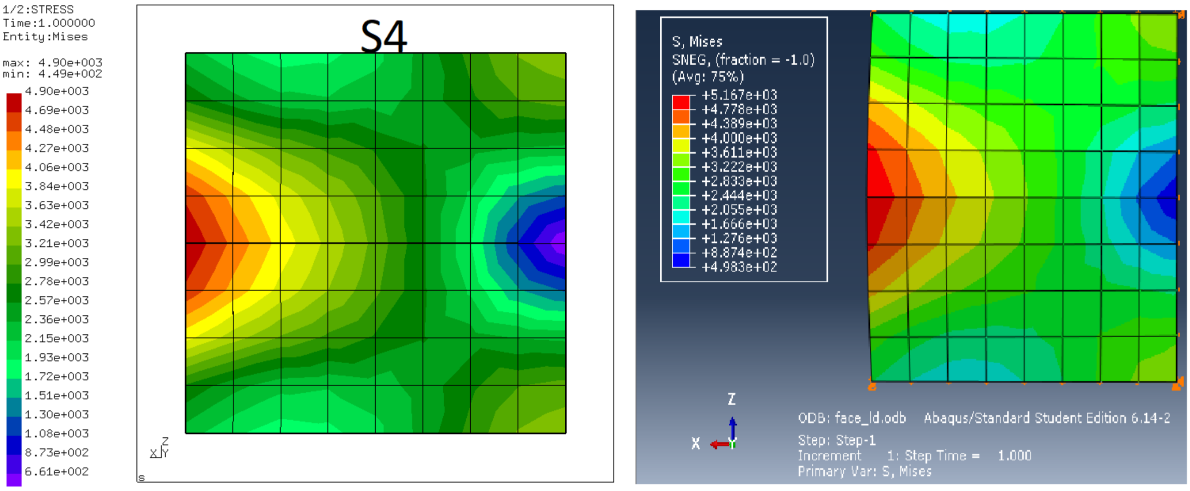

Figure B.1: Von Mises stress distribution on a plate composed of S4 elements in CalculiX (left) and Abaqus (right).

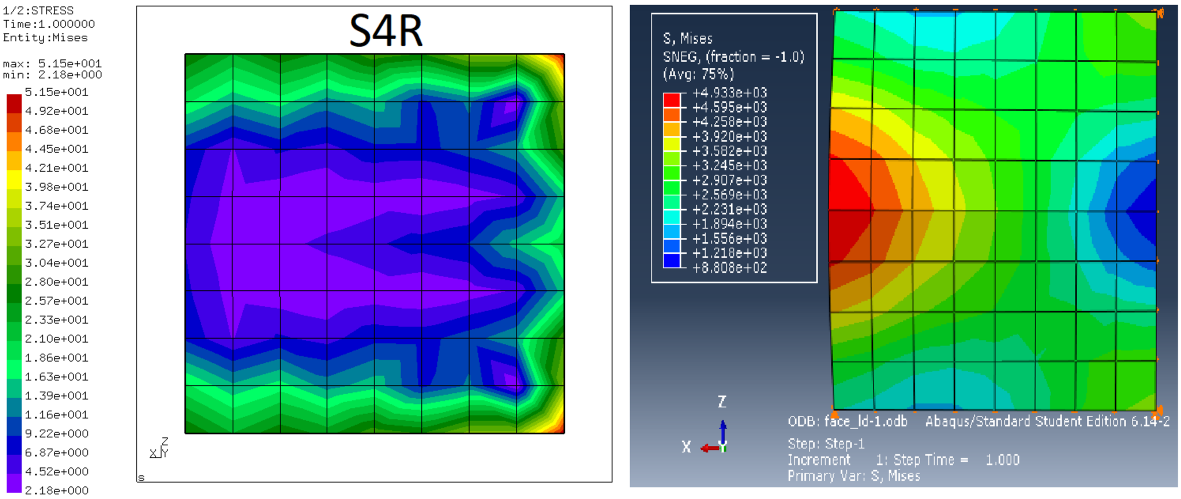

Figure B.2: Von Mises stress distribution on a plate composed of S4R elements in CalculiX (left) and Abaqus (right).

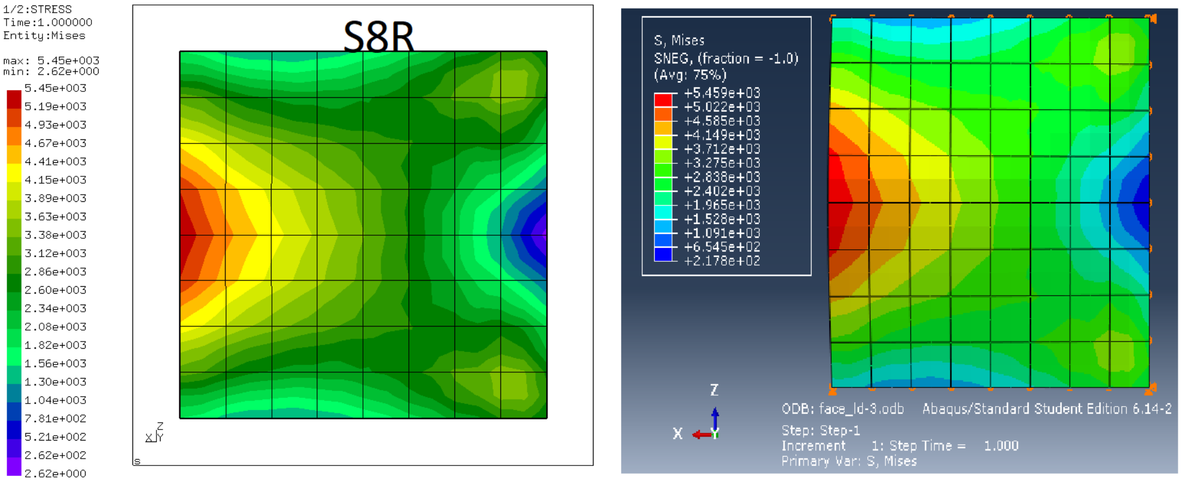

Figure B.3: Von Mises stress distribution on a plate composed of S8R elements in CalculiX (left) and Abaqus (right).

As wing component thicknesses are included as design variables in this study, their values will differ throughout the optimisation runs. The aforementioned verification was conducted at a plate thickness of $12.7mm$, which is on the higher end of expected thicknesses. To verify the choice of the S8R element for lower thicknesses, the panel verification analysis was repeated with a thickness of $0.25mm$. The pressure was reduced accordingly. Figure B.4 gives the results for both CalculiX (left) and Abaqus (right). The stress distribution produced by CalculiX once again matches that of Abaqus, while their peak von Mises stresses are identical. This verifies that using S8R elements in CalculiX matches the modelling of Abaqus for very thin components.

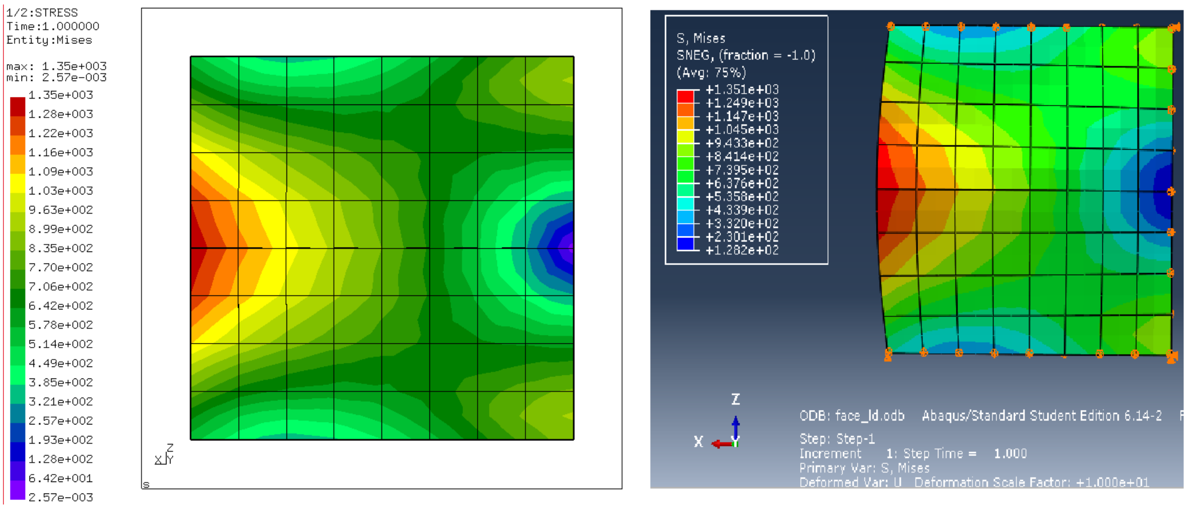

Figure B.4: Von Mises stress distribution on a thin plate composed of S8R elements in CalculiX (left) and Abaqus (right).

For the verification of the *TIE card in CalculiX, a simple wing skin-spar cap-spar web model is created, shown in Figure B.5. The spar caps are tied to the skin, while the spar web is tied to the opposite face of the spar caps. In this way, the spar caps act as slaves to the skin, while the spar web acts as the slave to the spar caps. In Figure B.5, the stress distribution of the model in CalculiX (left) closely matches that in Abaqus (right), when both colour-maps are set to the same range. The peak von Mises stress in CalculiX reaches $5.18 \cdot 10^2$, while its counterpart in Abaqus reaches $5.56 \cdot 10^2$, a difference of 6.8%. This difference may be attributed to the way CalculiX implements its tie constraint functionality compared to Abaqus. Although not negligible, the difference in the accuracy of the *TIE functionality is deemed acceptable, as CalculiX unfortunately offers no alternative for the creation of a model containing tapered components.

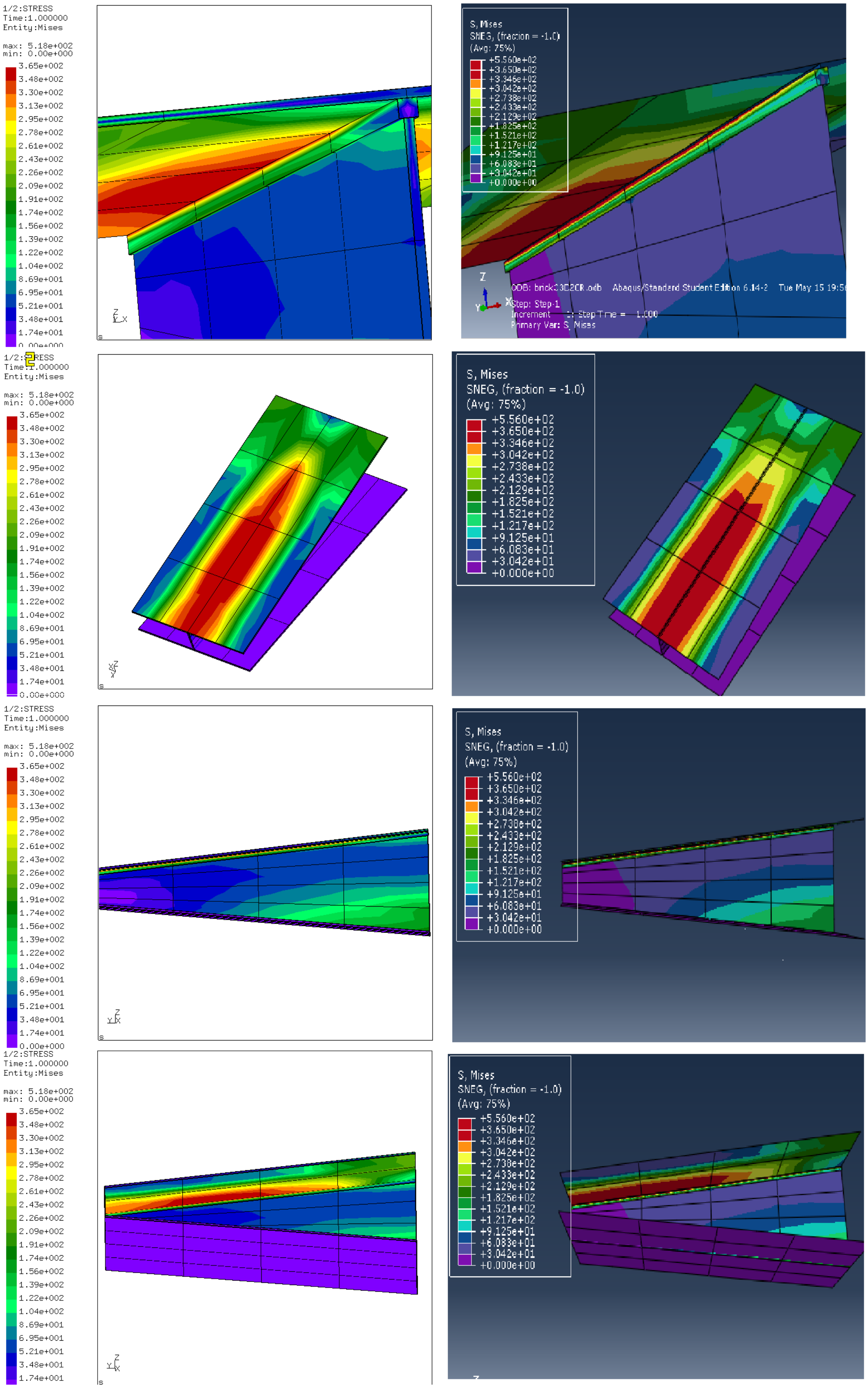

Figure B.5: Von Mises stress distribution on a skin-spar cap-spar web model with tie constraints in CalculiX (left) and Abaqus (right).

C

Appendix C: Optimisation History

Appendix C contains figures which display the optimisation history of the objective function, design variables, inequality constraints and equality constraints of the main MDO runs presented in the report. All given parameters are the normalised parameters which have been optimised. Figures include any second subsequent MDO runs conducted in order to ensure convergence to a minimum - their iterations are joined here to the iterations of the first runs, to show the full iteration count to convergence.

C.1. Reciprocating engine, low-fidelity

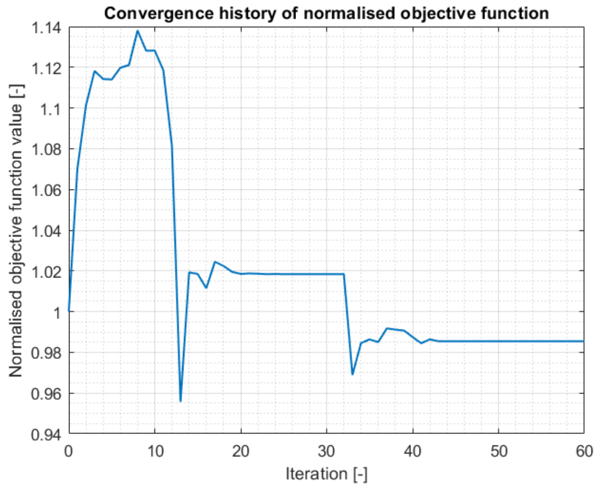

Figure C.1: Normalised objective function value history, reciprocating engine, low-fidelity.

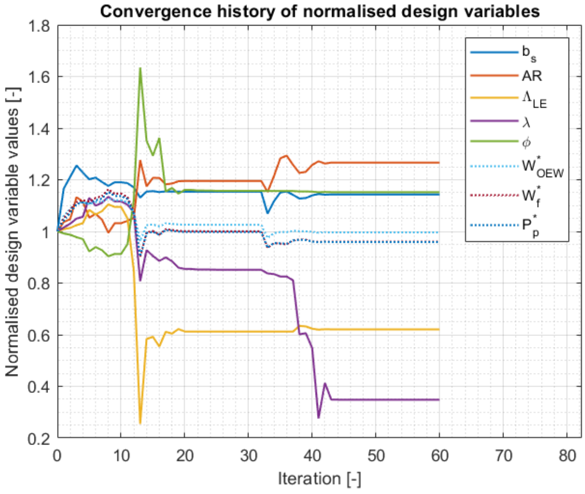

Figure C.2: Normalised design variable value history, reciprocating engine, low-fidelity.

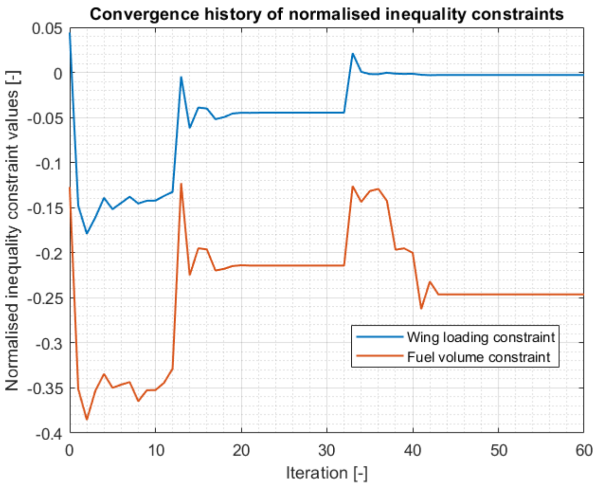

Figure C.3: Normalised inequality constraint history, reciprocating engine, low-fidelity.

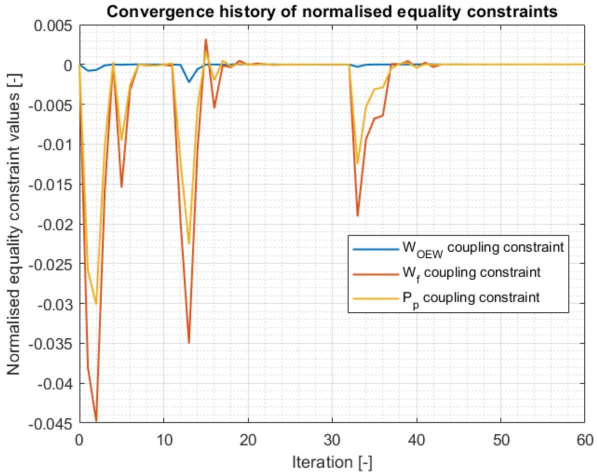

Figure C.4: Normalised equality constraint history, reciprocating engine, low-fidelity.

C.2. Reciprocating engine, high-fidelity

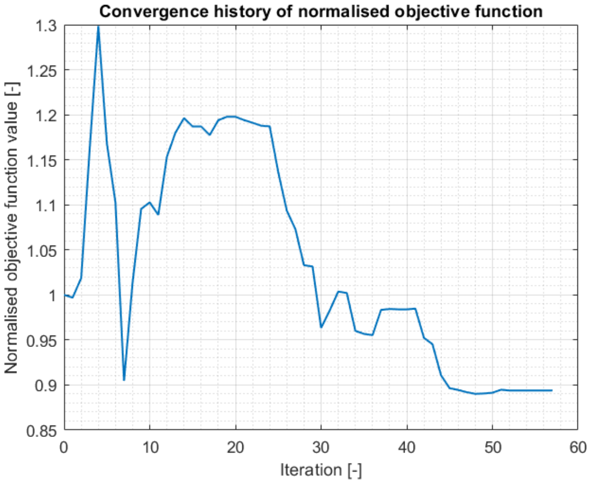

Figure C.5: Normalised objective function value history, reciprocating engine, high-fidelity.

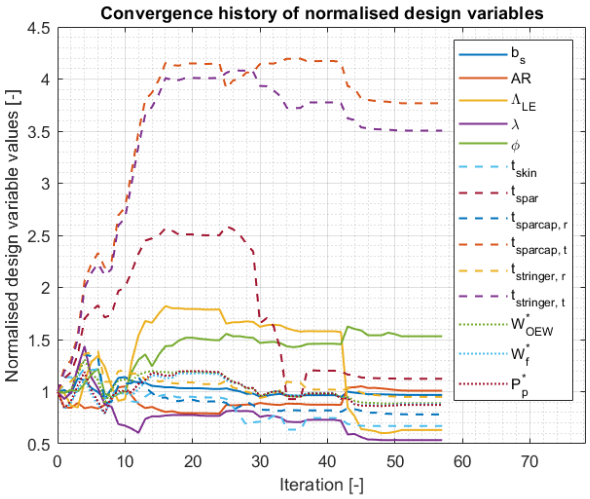

Figure C.6: Normalised design variable value history, reciprocating engine, high-fidelity.

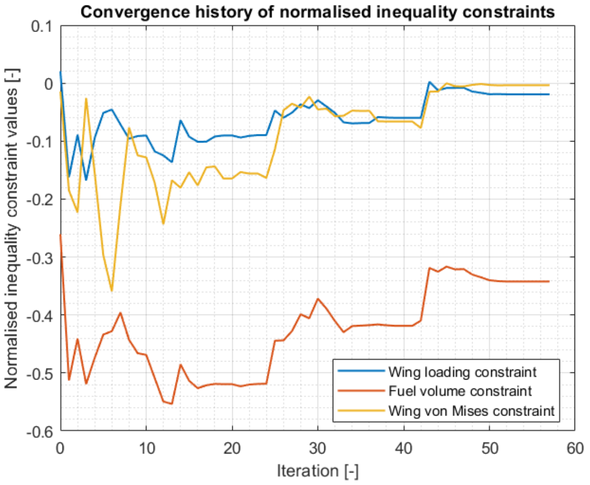

Figure C.7: Normalised inequality constraint history, reciprocating engine, high-fidelity.

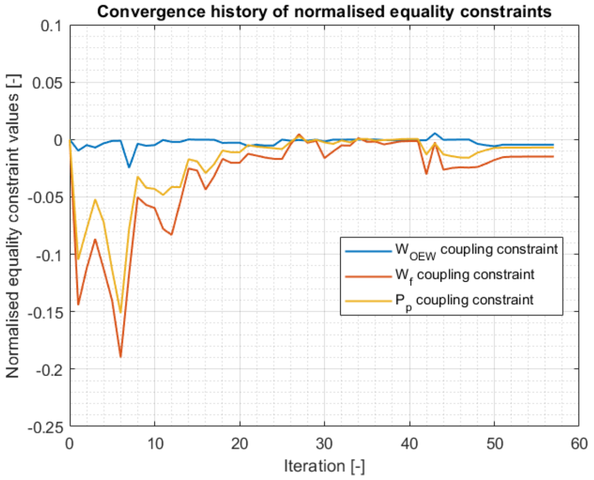

Figure C.8: Normalised equality constraint history, reciprocating engine, high-fidelity.

C.3. Hydrogen fuel cell, low-fidelity

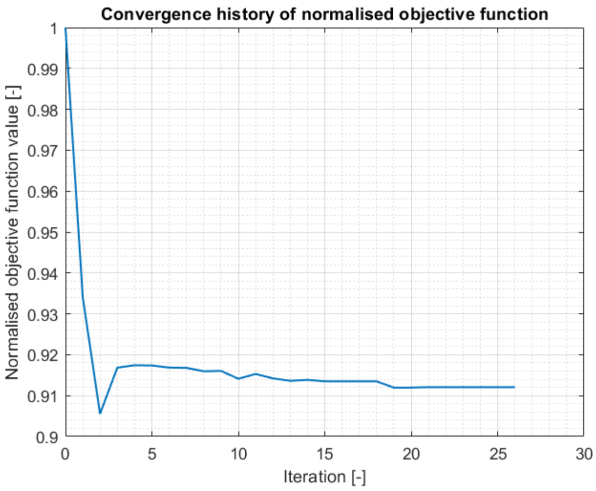

Figure C.9: Normalised objective function value history, hydrogen fuel cell, low-fidelity.

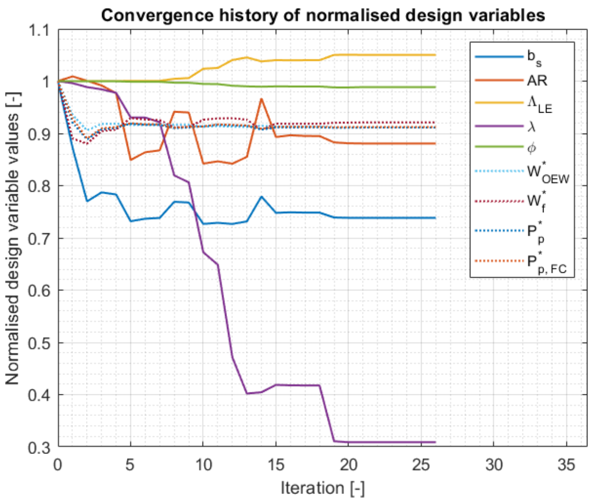

Figure C.10: Normalised design variable value history, hydrogen fuel cell, low-fidelity.

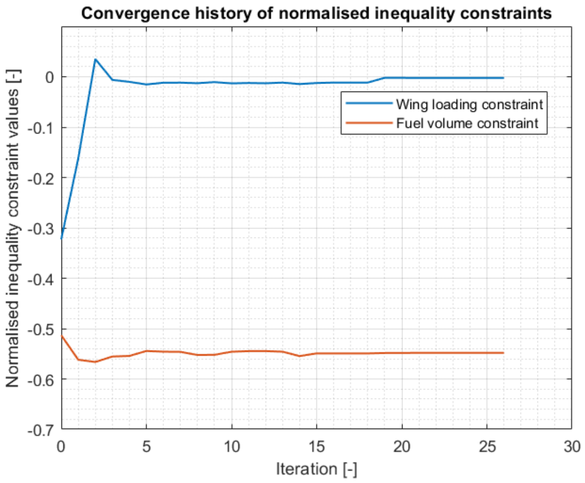

Figure C.11: Normalised inequality constraint history, hydrogen fuel cell, low-fidelity.

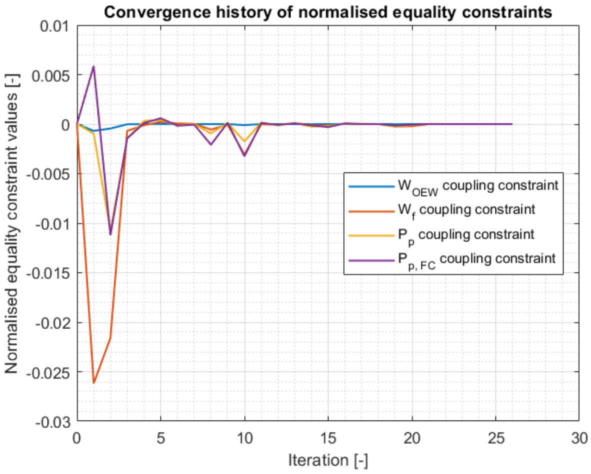

Figure C.12: Normalised equality constraint history, hydrogen fuel cell, low-fidelity.

C.4. Hydrogen fuel cell, high-fidelity

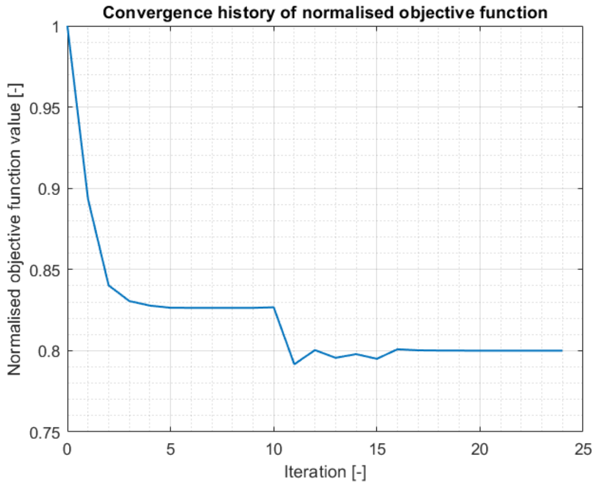

Figure C.13: Normalised objective function value history, hydrogen fuel cell, high-fidelity.

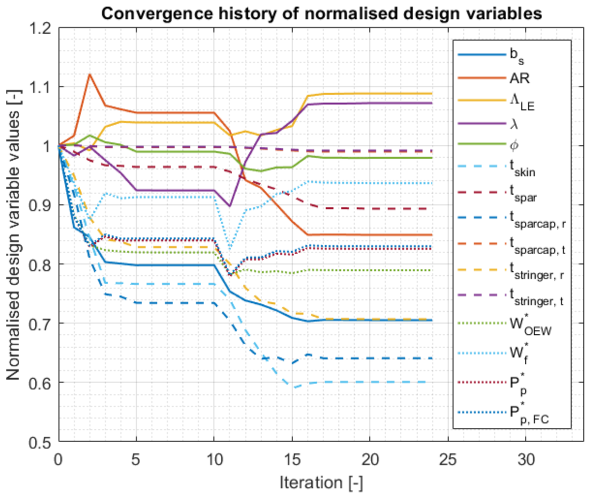

Figure C.14: Normalised design variable value history, hydrogen fuel cell, high-fidelity.

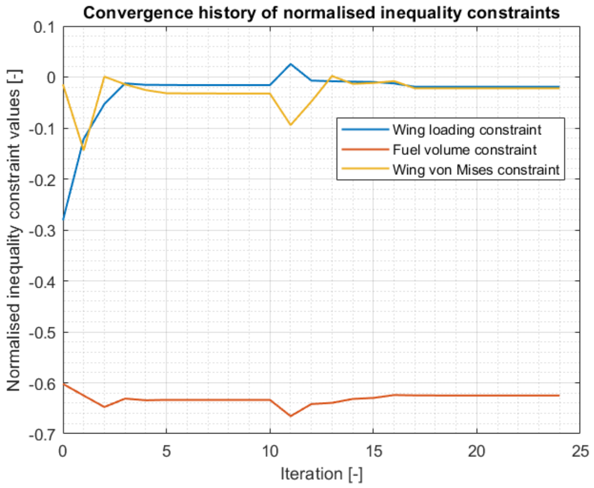

Figure C.15: Normalised inequality constraint history, hydrogen fuel cell, high-fidelity.

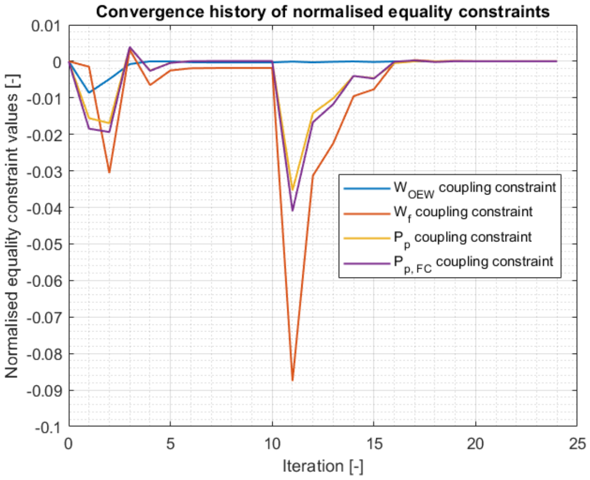

Figure C.16: Normalised equality constraint history, hydrogen fuel cell, high-fidelity.

Bibliography

[1] Northrop Grumman, *Photo Release – Northrop Grumman, L-3 MAS to Join Forces on Unmanned System for Canadian Security,* http://news.northropgrumman.com/news/releases/photo-release-northrop-grumman-l-3-mas-to-join-forces-on-unmanned-system-for-canadia (2012).

[2] P. G. Fahlstrom and T. J. Gleason, *Introduction to UAV Systems*, 4th ed. (Wiley, 2012).

[3] A. Marcellan, *An Exploration into the Potential of Microturbine Based Propulsion Systems for Civil Unmanned Aerial Vehicles*, Master's thesis, Delft University of Technology (2015).

[4] O. González-Espasandín, T. J. Leo, and E. Navarro-Arévalo, *Fuel Cells: A Real Option for Unmanned Aerial Vehicles Propulsion,* The Scientific World Journal **2014** (2014), 10.1155/2014/497642.

[5] C. Griffis, J. Schneider, T. Wilson, and P. Pierpont, *Unmanned Aircraft System Propulsion Systems Technology Survey*, Tech. Rep. (Embry-Riddle Aeronautical University, 2009).

[6] S. M. Batill, M. A. Stelmack, and X. Q. Yu, *Multidisciplinary Design Optimization of an Electric-Powered Unmanned Air Vehicle,* Aircraft Design **2**, 1 (1999).

[7] B. A. Moffitt, T. H. Bradley, D. Mavris, and D. E. Parekh, *Design Space Exploration of Small-Scale PEM Fuel Cell Long Endurance Aircraft,* in *6th AIAA Aviation Technology, Integration and Operations Conference (ATIO)*, September (American Institute of Aeronautics and Astronautics, Wichita, 2006) pp. 1–16.

[8] S. Rajagopal and R. Ganguli, *Multidisciplinary Design Optimization of Long Endurance Unmanned Aerial Vehicle Wing,* Computer Modeling in Engineering & Sciences **81**, 1 (2011).

[9] S. R. Powell, *Applications and Enhancements of Aircraft Design Optimization Techniques*, Ph.D. thesis, University of Southampton (2012).

[10] A. Azamatov, J.-w. Lee, and Y.-h. Byun, *Comprehensive aircraft configuration design tool for Integrated Product and Process Development,* Advances in Engineering Software **42**, 35 (2011).

[11] Deust, *h-Method & p-Method,* https://deust.wordpress.com/2014/11/30/h-method-p-method/ (2014).

[12] G. Dhondt, *CalculiX CrunchiX USER'S MANUAL version 2.14,* http://www.dhondt.de/ccx_2.14.pdf (2018).

[13] D. Verstraete, *Multi-disciplinary optimisation of medium altitude long endurance UAVs,* 31st Congress of the International Council of the Aeronautical Sciences, ICAS 2018 , 1 (2018).

[14] R. A. McDonald, *Electric motor modeling for conceptual aircraft design,* 51st AIAA Aerospace Sciences Meeting including the New Horizons Forum and Aerospace Exposition 2013 , 1 (2013).

[15] D. Verstraete, *Propulsion Technologies for Unmanned Aerial Vehicles [unpublished document]*, Tech. Rep. (The University of Sydney).

[16] S. Aniyi, *GrabCAD,* https://grabcad.com/library/mq-1b-predator-1 (2016).

[17] Jane's Information Group, *Jane's Unmanned Aerial Vehicles and Targets,* (2001).

[18] D. Loving and B. Estabrook, *Transonic-wing investigation in the Langley 8-foot high-speed tunnel at high subsonic Mach numbers and at a Mach number of 1.2*, Tech. Rep. (National Advisory Committee for Aeronautics, Washington, 1951).

[19] E. Sepulveda Palacios and H. Smith, *Impact of mission requirements on the design of low observable UCAV configurations,* Aircraft Engineering and Aerospace Technology **91**, 1295 (2019).

[20] P. van Blyenburgh, *UAVs: an Overview,* Air & Space Europe **1**, 43 (1999).

[21] K. Dalamagkidis, *Classification of UAVs,* in *Handbook of Unmanned Aerial Vehicles*, edited by K. P. Valavanis and G. J. Vachtsevanos (Springer, 2015) Chap. 5, pp. 83–91.

[22] National Research Council, *Uninhabited Air Vehicles: Enabling Science for Military Systems* (National Academies Press, 2000).

[23] D. Verstraete, A. Gong, D. D. Lu, and J. L. Palmer, *Experimental Investigation of the Role of the Battery in the AeroStack Hybrid, Fuel-Cell-Based Propulsion System for Small Unmanned Aircraft Systems,* International Journal of Hydrogen Energy **40**, 1598 (2015).

[24] T. H. Bradley, B. A. Moffitt, T. F. Fuller, D. N. Mavris, and D. E. Parekh, *Comparison of Design Methods for Fuel-Cell-Powered Unmanned Aerial Vehicles,* Journal of Aircraft **46**, 1945 (2009).

[25] S. Kumar Das and S. Roy, *Finite element analysis of aircraft wing using carbon fiber reinforced polymer and glass fiber reinforced polymer.* IOP Conference Series: Materials Science and Engineering **402** (2018), 10.1088/1757-899X/402/1/012077.

[26] U. Zerbst, M. Madia, and H. T. Beier, *A model for fracture mechanics based prediction of the fatigue strength: Further validation and limitations,* Engineering Fracture Mechanics **130**, 65 (2014).

[27] J. Gundlach, *Designing Unmanned Aircraft Systems: A Comprehensive Approach* (American Institute of Aeronautics and Astronautics, 2012).

[28] Cambridge Dictionary, *UAV Meaning in the Cambridge English Dictionary,* `http://dictionary.cambridge.org/dictionary/english/uav?q=UAV`.

[29] T. H. Cox, I. Somers, and D. J. Fratello, *Earth Observations and the Role of UAVs: A Capabilities Assessment*, Tech. Rep. (National Aeronautics and Space Association, 2006).

[30] P. van Blyenburgh, *UAV Systems: Global Review,* in *ICAO Exploratory Meeting on UAV Systems* (Amsterdam, 2006).

[31] H. Bendea, P. Boccardo, S. Dequal, F. G. Tonolo, D. Marenchino, and M. Piras, *Low Cost UAV for Post-Disaster Assessment,* The International Archives of the Photogrammetry, Remote Sensing and Spatial Information Sciences **XXXVII**, 1373 (2008).

[32] L. R. N. Newcome, *Unmanned Aviation A Brief History of Unmanned Aerial Vehicles* (American Institute of Aeronautics and Astronautics, 2004).

[33] R. Austin, *Unmanned Aircraft Systems: UAVs Design, Development and Deployment*, 1st ed., edited by I. Moir, A. Seabridge, and R. Langton (Wiley, 2010).

[34] S. Kahvecioglu and H. Oktal, *Turkish UAV Capabilities as a New Competitor in the Market,* International Journal of Intelligent Unmanned Systems **2**, 183 (2014).

[35] Airbus Defence and Space, *European MALE RPAS (Medium Altitude Long Endurance Remotely Piloted Aircraft System) Programme takes off,* `https://airbusdefenceandspace.com/wp-content/uploads/2016/09/press-release-male-rpas-28092016-eng.pdf` (2016).

[36] Jane's 360, *Kronshtadt, Rosboronexport partner for Orion-Eh UAV | Jane's 360,* `http://www.janes.com/article/72468/kronshtadt-rosboronexport-partner-for-orion-eh-uav` (2017).

[37] K. Herrick, *Development of the Unmanned Aerial Vehicle Market: Forecasts and Trends,* Air & Space Europe **2**, 25 (2000).

[38] S. Tsach, D. Penn, and A. Levy, *Advanced Technologies and Approaches for Next Generation UAVs,* in *23rd Congress of the International Council of the Aeronautical Sciences* (Toronto, 2002) pp. 1–10.

[39] S. Tsach, A. Peled, D. Penn, B. Keshales, and R. Guedj, *Development Trends for Next Generation of UAV Systems,* in *AIAA Infotech@Aerospace 2007 Conference and Exhibit* (Rohnert Park, 2007) p. 2762.

[40] K. Nonami, *Prospect and Recent Research and Development for Civil Use Autonomous Unmanned Aircraft as UAV and MAV,* Journal of System Design and Dynamics **1**, 120 (2007).

[41] A. V. Koldaev, *Non-Military UAV Applications,* in *Aero India International Seminar 2007*, February (2007).

[42] P. A. Newman, *Uninhabited Aerial Vehicles: Current and Future Use,* in *Observing Systems for Atmospheric Composition* (Springer, 2007) Chap. 8, pp. 106–118.

[43] V. G. Ambrosia, S. Wegener, T. Zajkowski, D. V. Sullivan, S. Buechel, F. Enomoto, B. Lobitz, S. Johan, J. Brass, and E. Hinkley, *The Ikhana Unmanned Airborne System (UAS) Western States Fire Imaging Missions: From Concept to Reality (2006–2010),* Geocarto International **26**, 85 (2011).

[44] T. H. Cox, C. J. Nagy, M. A. Skoog, and I. A. Somers, *Civil UAV Capability Assessment*, Tech. Rep. December (NASA, 2004).

[45] M. Rozenkranc and J. Ernst, *TACTICAL UAV ENGINES INTEGRATION IN IAI,* in *2nd AIAA "Unmanned Unlimited" Conf. and Workshop & Exhibit* (American Institute of Aeronautics and Astronautics, San Diego, 2003).

[46] P. Dagaut and M. Cathonnet, *The Ignition, Oxidation, and Combustion of Kerosene: A Review of Experimental and Kinetic Modeling,* Progress in Energy and Combustion Science **32**, 48 (2006).

[47] V. S. Kolosnitsyn and E. V. Karaseva, *Lithium-Sulfur Batteries: Problems and Solutions,* Russian Journal of Electrochemistry **44**, 506 (2008).

[48] Z. Guo, X.-k. Chen, Z.-x. Hou, and J. Guo, *Development of a Solar Electric Powered UAV for Long Endurance Flight,* in *11th AIAA Aviation Technology, Integration, and Operations (ATIO) Conference*, September (Virginia Beach, 2011) pp. 1–13.

[49] G. Marsh, *Best Endurance Under the Sun,* Renewable Energy Focus **11**, 24 (2010).

[50] P. Panagiotou, I. Tsavlidis, and K. Yakinthos, *Conceptual Design of a Hybrid Solar MALE UAV,* Aerospace Science and Technology **53**, 207 (2016).

[51] J. Larminie and A. Dicks, *Fuel Cell Systems Explained*, 2nd ed. (Wiley, 2003) p. 418.

[52] O. Z. Sharaf and M. F. Orhan, *An Overview of Fuel Cell Technology: Fundamentals and Applications,* Renewable and Sustainable Energy Reviews **32**, 810 (2014).

[53] G. Romeo, F. Borello, G. Correa, and E. Cestino, *ENFICA-FC: Design of Transport Aircraft Powered by Fuel Cell & Flight Test of Zero Emission 2-Seater Aircraft Powered by Fuel Cells Fueled by Hydrogen,* International Journal of Hydrogen Energy **38**, 469 (2013).

[54] A. L. Dicks, *PEM Fuel Cells: Applications,* in *Comprehensive Renewable Energy*, Vol. 4 (Elsevier Ltd, 2012) pp. 203–245.

[55] T. H. Bradley, B. A. Moffitt, D. Mavris, and D. E. Parekh, *Aviation: Fuel Cells,* in *Encyclopedia of Electrochemical Power Sources*, edited by J. Garche, C. K. Dyer, P. T. Moseley, Z. Ogumi, D. A. J. Rand, and B. Scrosati (Elsevier Ltd, 2009) 1st ed., pp. 186–192.

[56] D. Verstraete, K. Lehmkuehler, A. Gong, J. R. Harvey, G. Brian, and J. L. Palmer, *Characterisation of a Hybrid, Fuel-Cell-Based Propulsion System for Small Unmanned Aircraft,* Journal of Power Sources **250**, 204 (2014).

[57] D. Verstraete, J. R. Harvey, and J. L. Palmer, *Hardware-in-the-Loop Simulation of Fuel-Cell-Based Hybrid-Electrical UAV Propulsion,* in *28th International Congress of the Aeronautical Sciences* (Brisbane, 2012) pp. 2662–2674.

[58] A. Gong and D. Verstraete, *Experimental Characterization of a Fuel Cell Hybrid Electrical UAV Propulsion System,* in *52nd Aerospace Sciences Meeting*, January (American Institute of Aeronautics and Astronautics, National Harbor, Maryland, 2014) pp. 114–124.

[59] A. Gong, J. L. Palmer, G. Brian, J. R. Harvey, and D. Verstraete, *Performance of a Hybrid, Fuel-Cell-Based Power System During Simulated Small Unmanned Aircraft Missions,* International Journal of Hydrogen Energy **41**, 11418 (2016).

[60] K. E. Swider-Lyons, J. A. MacKrell, J. A. Rodgers, G. S. Page, M. Schuette, and R. O. Stroman, *Hydrogen Fuel Cell Propulsion for Long Endurance Small UAVs,* in *AIAA Centennial of Naval Aviation Forum "100 Years of Achievement and Progress"*, September (American Institute of Aeronautics and Astronautics, Virginia Beach, 2011) pp. 1–11.

[61] N. Lapeña-Rey, J. Mosquera, E. Bataller, and F. Ortí, *First Fuel-Cell Manned Aircraft,* Journal of Aircraft **47**, 1825 (2010).

[62] P. Rathke, J. Kallo, J. Schirmer, T. Stephan, W. Waiblinger, and J. Weiss-Ungethüm, *Antares DLR-H2 – Flying Test Bed for Development of Aircraft Fuel Cell Systems,* ECS Transactions **51**, 229 (2013).

[63] A. Sóbester and A. Keane, *Multidisciplinary Design Optimization of UAV Airframes,* in *47th AIAA/ASME/ASCE/AHS/ASC Structures, Structural Dynamics, and Material Conference*, May (American Institute of Aeronautics and Astronautics, Newport, 2006) pp. 1–13.

[64] S. Rajagopal, R. Ganguli, A. Pillai, and A. Lurdharaj, *Conceptual Design of Medium Altitude Long Endurance UAV using Multi Objective Genetic Algorithm,* in *48th AIAA/ASME/ASCE/AHS/ASC Structures, Structural Dynamics, and Material Conference*, April (American Institute of Aeronautics and Astronautics, Honolulu, 2007) pp. 1–13.

[65] S. Gano and J. Renaud, *Optimized Unmanned Aerial Vehicle with Wing Morphing for Extended Range and Endurance,* in *9th AIAA/ISSMO Symposium on Multidisciplinary Analysis and Optimization*, September (American Institute of Aeronautics and Astronautics, Atlanta, 2002) pp. 1–9.

[66] A. Ciarella, C. Tsotskas, M. Hahn, N. Werter, R. D. Breuker, C. Beaverstock, M. Friswell, Y. Yang, S. Ozgen, A. Antoniadis, P. Tsoutsanis, and D. Drikakis, *A Multi-Fidelity, Multi-Disciplinary Analysis and Optimization Framework for the Design of Morphing UAV wings,* in *16th AIAA/ISSMO Multidisciplinary Analysis and Optimization Conference*, June (American Institute of Aeronautics and Astronautics, Dallas, 2015) pp. 1–21.

[67] V. Jagdale, A. Patil, B. Stanford, and P. Ifju, *Conceptual Design of a Bendable UAV Wing Considering Aerodynamic and Structural Performance,* in *50th AIAA/ASME/ASCE/AHS/ASC Structures, Structural Dynamics, and Material Conference*, May (American Institute of Aeronautics and Astronautics, Palm Springs, 2009) pp. 2641 – 2650.

[68] M. Berci, V. Toropov, R. Hewson, and P. Gaskell, *Multidisciplinary Multifidelity Optimisation of a Flexible Wing Aerofoil for Small UAV,* in *12th AIAA Aviation Technology, Integration, and Operations (ATIO) Conference and 14th AIAA/ISSMO Multidisciplinary Analysis and Optimization Conference*, September (American Institute of Aeronautics and Astronautics, Indianapolis, 2012) pp. 1–21.

[69] L. Gonzalez, R. Walker, K. Srinivas, and J. Periaux, *Multidisciplinary Design Optimisation of Unmanned Aerial Systems (UAS) using Meta Model Assisted Evolutionary Algorithms,* in *16th Australasian Fluid Mechanics Conference*, December (Gold Coast, 2007) pp. 471–474.

[70] D. S. Lee, L. F. Gonzalez, J. Periaux, and K. Srinivas, *Robust Multi-Objective Aerostructural Optimisation using Advanced Evolutionary Algorithms,* in *47th AIAA Aerospace Sciences Meeting including the New Horizons Forum and Aerospace Exposition* (Orlando, 2009).

[71] D. S. Lee, K. Srinivas, L. F. Gonzalez, and J. Periaux, *Uncertainty Based MDO of UAS Using HAPMOEA,* in *Computational Fluid Dynamics 2008* (Seoul, 2009) pp. 649–654.

[72] H. Tianyuan and Y. Xiongqing, *Aerodynamic/Stealthy/Structural Multidisciplinary Design Optimization of Unmanned Combat Air Vehicle,* Chinese Journal of Aeronautics **22**, 380 (2009).

[73] N. V. Nguyen, S. M. Choi, W. S. Kim, J. W. Lee, S. Kim, D. Neufeld, and Y. H. Byun, *Multidisciplinary Unmanned Combat Air Vehicle system design using Multi-Fidelity Model,* Aerospace Science and Technology **26**, 200 (2013).

[74] B. Moffitt, T. Bradley, D. Parekh, and D. Mavris, *Design and Performance Validation of a Fuel Cell Unmanned Aerial Vehicle,* in *44th AIAA Aerospace Sciences Meeting and Exhibit* (American Institute of Aeronautics and Astronautics, Reno, 2006) pp. 1–20.

[75] B. A. Moffitt, T. H. Bradley, D. Mavris, and D. E. Parekh, *Reducing Uncertainty of a Fuel Cell UAV Through Variable Fidelity Optimization,* in *7th AIAA Aviation Technology, Integration and Operations Conference (ATIO)*, September (American Institute of Aeronautics and Astronautics, Belfast, 2007) pp. 1–19.

[76] J. Y. Hung, L. F. González, and R. A. Walker, *Mission Optimisation and Multi-Disciplinary Design of Hybrid Unmanned Aerial Systems (UAS) using Advanced Numerical Techniques,* in *27th International Congress of the Aeronautical Sciences*, September (Nice, 2010) pp. 1–11.

[77] D. E. Bryson, C. R. Marks, R. M. Miller, and M. P. Rumpfkeil, *Multidisciplinary Design Optimization of Quiet, Hybrid-Electric Small Unmanned Aerial Systems,* Journal of Aircraft **53**, 1959 (2016).

[78] R. M. Ajaj, M. I. Friswell, and E. I. Flores, *On the Effectiveness of Active Aeroelastic Structures for Morphing Aircraft,* Aeronautical Journal **117**, 1167 (2013).

[79] R. M. Ajaj, M. I. Friswell, E. I. Saavedra Flores, A. T. Isikveren, and H. Chaouk, *Variable Wing Span using the Compliant Spar Concept,* in *54th AIAA/ASME/ASCE/AHS/ASC Structures, Structural Dynamics and Materials Conference* (American Institute of Aeronautics and Astronautics, Boston, 2013) pp. 1–25.

[80] P. S. Prakasha, P. D. Ciampa, L. Boggero, and M. Fioriti, *Assessment of Airframe-Subsystems Synergy on Overall Aircraft Performance in a Collaborative Design Environment,* in *17th AIAA/ISSMO Multidisciplinary Analysis and Optimization Conference*, June (American Institute of Aeronautics and Astronautics, Washington, 2016).

[81] B. Morrisey and R. McDonald, *Multidisciplinary Design Optimization of an Extreme Aspect Ratio HALE UAV,* in *9th AIAA Aviation Technology, Integration, and Operations Conference (ATIO)*, September (American Institute of Aeronautics and Astronautics, Hilton Head, 2009) pp. 1–15.

[82] J. R. R. A. Martins and A. B. Lambe, *Multidisciplinary Design Optimization: A Survey of Architectures,* AIAA Journal **51**, 2049 (2013).

[83] D. Steenhuizen, G. La Rocca, and A. Elham, *AE4205 MDO for Aerospace Applications Lecture 4 - Part A - Remarks on Optimization Efficiency,* Delft University of Technology (2015).

[84] E. J. Cramer, J. E. Dennis, Jr., P. D. Frank, R. M. Lewis, and G. R. Shubin, *Problem Formulation for Multidisciplinary Optimization,* SIAM Journal on Optimization **4**, 754 (1994).

[85] J. R. R. A. Martins and N. M. K. Poon, *On Structural Optimization Using Constraint Aggregation,* Proceedings of 6th World Congress on Structural and Multidisciplinary Optimization , 1 (2005).

[86] MathWorks, *fmincon,* `https://www.mathworks.com/help/optim/ug/choosing-the-algorithm.html` (2020).

[87] B. Kulfan and J. Bussoletti, *"Fundamental" Parameteric Geometry Representations for Aircraft Component Shapes,* in *11th AIAA/ISSMO Multidisciplinary Analysis and Optimization Conference* (American Institute of Aeronautics and Astronautics, Portsmouth, 2006).

[88] R. Haimes and J. F. Dannenhoffer, *The Engineering Sketch Pad: A Solid-Modeling, Feature-Based, Web-Enabled System for Building Parametric Geometry,* in *21st AIAA Computational Fluid Dynamics Conference* (San Diego, 2013) pp. 1–21.

[89] R. Cummings, W. Mason, S. Morton, and D. McDaniel, *Drag: An Introduction,* in *Applied Computational Aerodynamics* (Cambridge University Press, 1997) Chap. 5, pp. 1–62.

[90] D. Raymer, *Aircraft Design: A Conceptual Approach*, 2nd ed. (American Institute of Aeronautics and Astronautics, 1992).

[91] D. Scholz, *Drag Prediction,* https://www.fzt.haw-hamburg.de/pers/Scholz/HOOU/AircraftDesign_13_Drag.pdf (2015).

[92] S. Sartorius, *Oswald efficiency estimation function,* https://uk.mathworks.com/matlabcentral/fileexchange/38800-oswald-efficiency-estimation-function (2020).

[93] R. Shevell, *Fundamentals of Flight*, 2nd ed. (Prentice Hall, 1989) pp. 1–438.

[94] Public Domain Aeronautical Software (PDAS), *PANAIR Predicting Subsonic Or Supersonic Linear Potential Flows About Arbitrary Configurations Using A Higher Order Panel Method,* http://www.pdas.com/panair.html (2017).

[95] T. Derbyshire and K. W. Sidwell, *PANAIR Summary Document*, Tech. Rep. (Boeing Military Airplane Company, Seattle, 1982).

[96] Larry L. Erickson, *Panel Methods - An Introduction*, Tech. Rep. (NASA, Moffett Field, 1990).

[97] Open Cascade, *SALOME The Open Source Integration Platform for Numerical Simulation,* https://www.salome-platform.org/ (2018).

[98] T. Clar, *Development and Application of a Multidisciplinary Design Optimisation Sizing Platform for the Conceptual Design of Hypersonic Long-Range Transport Aircraft*, Master's thesis, Delft University of Technology (2019).

[99] Public Domain Aeronautical Software (PDAS), *Input Pre-Processor for PanAir,* https://www.pdas.com/panin.html (2017).

[100] C. B. Craidon, *A DESCRIPTION OF THE LANGLEY WIREFRAME GEOMETRY STANDARD (LaWGS) FORMAT*, Tech. Rep. (NASA, 1985).

[101] A. Magnus and M. Epton, *PANAIR - A Computer Program for Predicting Subsonic or Supersonic Linear Potential Flows About Arbitrary Configurations Using A Higher Order Panel Method, Vol. I. Theory Document*, Tech. Rep. 3 (Boeing Military Airplane Company, Seattle, 1980).

[102] K. Sidwell, P. Baruah, and J. Bussoletti, *PANAIR - A Computer Program for Predicting Subsonic or Supersonic Linear Potential Flows About Arbitrary Configurations Using A Higher Order Panel Method, Vol. II. User's Manual*, Tech. Rep. 3 (Boeing Military Airplane Company, Seattle, 1980).

[103] D. Raymer, *Aircraft Design: A Conceptual Approach, Fifth Edition*, 5th ed. (American Institute of Aeronautics and Astronautics, Inc., Washington, DC, 2012).

[104] M. Drela, *XROTOR Download Page,* https://web.mit.edu/drela/Public/web/xrotor/ (2011).

[105] W. H. Gerard, *Prediction of Sailplane Wing Weight for Preliminary Design,* Weight Engineering (1998).

[106] A. Elham, G. La Rocca, and M. J. Van Tooren, *Development and implementation of an advanced, design-sensitive method for wing weight estimation,* Aerospace Science and Technology **29**, 100 (2013).

[107] G. Dhondt and K. Wittig, *CALCULIX A Free Software Three-Dimensional Structural Finite Element Program,* `http://www.calculix.de/` (2018).

[108] J. Roskam, *Airplane Design Part III: Layout Design of Cockpit, Fuselage, Wing and Empennage: Cutaways and Inboard Profiles* (DARcorporation, Lawrence, 1986).

[109] Y. L. Kuo, W. L. Cleghorn, K. Behdinan, and R. G. Fenton, *The h-p-r-refinement finite element analysis of a planar high-speed four-bar mechanism,* Mechanism and Machine Theory **41**, 505 (2006).

[110] F. Dorbath, B. Nagel, and V. Gollnick, *A Knowledge Based Approach for Automated Modelling of Extended Wing Structures in Preliminary Aircraft Design,* Deutscher Luft- und Raumfahrtkongress , 1 (2011).

[111] Y. C. Lin, Y. C. Xia, Y. Q. Jiang, H. M. Zhou, and L. T. Li, *Precipitation hardening of 2024-T3 aluminum alloy during creep aging,* Materials Science and Engineering A **565**, 420 (2013).

[112] G. Kreisselmeier and R. Steinhauser, *Computer Aided Design of Control Systems* (IFAC, 1980) pp. 113–117.

[113] E. Torenbeek, *Development and application of a comprehensive, design-sensitive weight prediction method for wing structures of transport category aircraft*, Tech. Rep. (Delft University of Technology, Delft, 1992).

[114] D. Howe, *The prediction of aircraft wing mass,* Proceedings of the Institution of Mechanical Engineers, Part G: Journal of Aerospace Engineering **210**, 135 (1996).

[115] Z. Yi and W. Heping, *A STUDY OF STRUCTURE WEIGHT ESTIMATING FOR HIGH ALTITUDE LONG ENDURENCE (HALE) UNMANNED AERIAL VEHICLE (UAV),* in *25th International Congress of the Aeronautical Sciences* (Hamburg, 2006) pp. 1–6.

[116] J. Roskam, *Airplane Design Part V: Component Weight Estimation* (DARcorporation, Lawrence, 1985).

[117] S. Menon and C. P. Cadou, *Scaling of miniature piston-engine performance, Part 1: Overall engine performance,* Journal of Propulsion and Power **29**, 774 (2013).

[118] K. B. Wipke, M. R. Cuddy, and S. D. Burch, *ADVISOR 2.1: A user-friendly advanced powertrain simulation using a combined backward/forward approach,* IEEE Transactions on Vehicular Technology **48**, 1751 (1999).

[119] J. T. Lowry, *Performance of Light Aircraft* (American Institute of Aeronautics and Astronautics, 1999).

[120] J. F. Gundlach, *Multi-Disciplinary Design Optimization of Subsonic Fixed-Wing Unmanned Aerial Vehicles Projected Through 2025*, Ph.D. thesis, Virginia Polytechnic Institute and State University (2004).

[121] R. MacNeill and D. Verstraete, *Propeller optimisation for an electrically-powered tactical UAS,* 31st Congress of the International Council of the Aeronautical Sciences, ICAS 2018 , 1 (2018).

[122] magniX, *magni250,* `https://www.magnix.aero/products` (2019).

[123] F. Anton, *eAircraft : Hybrid-elektrische Antriebe für Luftfahrzeuge,* `https://www.bbaa.de/fileadmin/user_upload/02-preis/02-02-preistraeger/newsletter-2019/02-2019-09/02_Siemens_Anton.pdf` (2019).

[124] A. Noth, *Design of Solar Powered Airplanes for Continuous Flight*, Ph.D. thesis, ETH Zurich (2008).

[125] J. Larminie and J. Lowry, *Electric Vehicle Technology Explained: Second Edition*, 1st ed. (Wiley, 2003).

[126] UQM, *PowerPhase 125 ®,* https://wiki.neweagle.net/ProductDocumentation/EV_Software_and_Hardware/Traction_Inverters/UQM/PowerPhase_125_DataSheet.pdf.

[127] C. O. Rößler, *Conceptual Design of Unmanned Aircraft with Fuel Cell Propulsion System*, Ph.D. thesis, Technical University Munich (2012).

[128] I. L. Sarioglu, B. Czapnik, E. Bostanci, O. P. Klein, H. Schröder, and F. Küçükay, *Optimum design of a fuel-cell powertrain based on multiple design criteria,* Journal of Power Sources **266**, 7 (2014).

[129] S. K. Mital, J. Z. Gyekenyesi, S. M. Arnold, R. M. Sullivan, J. M. Manderscheid, and P. L. N. Murthy, *NASA-TM-2006-214346*, Tech. Rep. (NASA, Cleveland, 2006).

[130] N. Thapa, S. Ram, S. Kumar, and J. Mehta, *All electric aircraft: A reality on its way,* Materials Today: Proceedings **43**, 175 (2021).

[131] H. Löbberding, S. Wessel, C. Offermanns, M. Kehrer, J. Rother, H. Heimes, and A. Kampker, *From cell to battery system in BEVs: Analysis of system packing efficiency and cell types,* World Electric Vehicle Journal **11**, 1 (2020).

[132] Airbus Group, *E-Fan: The New Way to Fly,* http://company.airbus.com/service/mediacenter/download/?uuid=48b1bd2c-a428-4c65-82e5-ed3e923bd142 (2015).

[133] Pipistrel, *Aircraft Information: Pipistrel Alpha Electro,* (2017).

[134] Pipistrel, *Light Sport Aircraft Acceptance Report*, Tech. Rep. (Civil Aviation Authority of New Zealand, 2020).

[135] Samsung SDI, *Introduction of INR18650,* (2014).

[136] The Blender Foundation, *Blender,* https://www.blender.org/ (2017).

[137] M. Drela, *RCGroups,* https://www.rcgroups.com/forums/showthread.php?1227417-Predator-Airfoil/page3 (2010).

[138] Y. Naidu and S. Adali, *Design and Optimization of a Medium Altitude Long Endurance UAV Wingbox Structure,* Research and Development (R&D) Journal of The South African Institution of Mechanical Engineering , 22 (2014).

[139] F. Perini, *Structural design, manufacturing and testing of a new wing for the CSIR's Modular UAS in composite materials*, Master's thesis, University of Bologna (2012).

[140] Federal Aviation Administration, *Code of Federal Regulations, Title 14, Parts 1 to 59, Aeronautics and Space,* (2001).

[141] D. J. Peery, *Aircraft Structures* (Dover Publications Inc., Mineola, 2011).

[142] X. Zhu, Z. Guo, and Z. Hou, *Solar-powered airplanes: A historical perspective and future challenges,* Progress in Aerospace Sciences **71**, 36 (2014).

[143] M. N. Cálão, *On the Use of Hydrogen as the Future Aviation Fuel*, Master's thesis, Instituto Superior Técnico (2018).

[144] K. Seeckt, *Conceptual Design and Investigation of Hydrogen-Fueled Regional Freighter Aircraft*, Master's thesis, KTH Royal Institute of Technology (2010).

[145] G. L. M. Vonhoff, *Conceptual Design of Hydrogen Fuel Cell Aircraft*, Master's thesis, Delft University of Technology (2021).

[146] G. D. Brewer, *AVIATION USAGE OF LIQUID HYDROGEN FUEL– PROSPECTS AND PROBLEMS,* International Journal of Hydrogen Energy **1**, 65 (1976).

[147] D. Verstraete, *Long range transport aircraft using hydrogen fuel,* International Journal of Hydrogen Energy **38**, 14824 (2013).

[148] D. Verstraete, *On the energy efficiency of hydrogen-fuelled transport aircraft,* International Journal of Hydrogen Energy **40**, 7388 (2015).

[149] Public Domain Aeronautical Software (PDAS), *Appendix I - Profiles,* `http://www.pdas.com/profiles.html` (2010).